UNIVERSITY OF CALIFORNIA
RIVERSIDE

Exploring the Relationship Between Thermal Conductivity and Phonon Dynamics by Ultrafast Pump-Probe and Scattering Techniques

A Dissertation submitted in partial satisfaction
of the requirements for the degree of

Doctor of Philosophy

in

Materials Science and Engineering

by

Songrui Hou

December 2023

Dissertation Committee:
- Dr. Chen Li, Co-Chairperson
- Dr. Richard B. Wilson, Co-Chairperson
- Dr. Xi Chen
- Dr. Lorenzo Mangolini

The Dissertation of Songrui Hou is approved:

Committee Co-Chairperson

Committee Co-Chairperson

University of California, Riverside

ACKNOWLEDGEMENTS

I consider myself incredibly fortunate to have received extensive and exceptional guidance, advice, and mentorship from not just one, but two outstanding advisors, Prof. Richard Wilson and Prof. Chen Li. Their teachings have allowed me to see the world through the eyes of a scientist, and for that, I am deeply grateful.

Undertaking a Ph.D. during the COVID-19 pandemic presented numerous challenges for everyone involved. I would like to thank Prof. Bo Sun for his generous help when I was stranded in China due to the pandemic. His generous assistance went beyond research-related matters, providing me with constructive advice and inspiration. His help transformed what could have been an unexpected crisis into a meaningful and enlightening experience during my Ph.D. journey.

Working alongside my fellow lab mates at UCR has been an absolute privilege. I would like to express my sincere gratitude to all my colleagues from Prof. Wilson's and Prof. Li's groups. My heartfelt thanks go to Ramya Mohan, Samreen Khan, Victor Ortiz, Wonsik Lee, Qiyang Sun, Yaokun Su, and Xinping Shi for the enlightening scientific discussions we shared. I would like to extend a special thanks to Shuonan Chen, whose support was instrumental during my challenging times. I also want to acknowledge Kexin Liu for being my companion during the initial demanding stages of our Ph.D. journey.

Collaborations with colleagues from various research groups have enriched my academic experience, especially Prof. Zhifeng Ren’s group at the University of Houston. I would like to convey my appreciation to Prof. Fei Tian and Fengjiao Pan, who synthesized the groundbreaking sample, boron arsenide, for our research. I gained invaluable insights into the operation of diamond anvil cells through my association with Prof. Shanmin Wang's group at the Southern

University of Science and Technology of China. I extend my thanks to Xuefeng Zhou and Jian Chen for generously sharing their high-pressure expertise. I received generous assistance from Yufeng Wang, Yizhe Liu, Lu Zhao, and Qinshu Li during my stay at Tsinghua University, for which I am truly thankful.

I cherish the friendships and memories created over the past five years. I want to convey my appreciation to Terry Roberts and Asuncion Roberts for their assistance when I first arrived in the United States. I have enjoyed engaging in conversations and sharing drinks with friends, especially Kevin. Our Friday/Saturday meal adventures with Youming, Xunhao, Shucheng, and Qiang have been memorable. I am grateful for the companionship of Fanyun, and the friendships formed in Shenzhen, particularly with Liping, are treasured.

Lastly, I want to express my profound gratitude to my parents and sister for their unwavering love, trust, and support throughout my life. Their encouragement has been my driving force, and I am deeply thankful.

The text of this dissertation, in part, is a reprint of the material as it appears in “Thermal Conductivity of BAs under Pressure” (2022), “Response of Vibrational Properties and Thermal Conductivity of Perovskites to Pressure” (2023), “Spin-phonon interactions induced anomalous thermal conductivity in nickel (II) oxide” (2023). The co-authors, Richard B. Wilson and Chen Li, listed in that publication directed and supervised the research which forms the basis for this dissertation. Other co-authors provided technical expertise.

My research was supported as part of ULTRA, an Energy Frontier Research Center funded by the U.S. Department of Energy (DOE), Office of Science, Basic Energy Sciences (BES), under Award #DE-SC0021230, and by the National Science Foundation (NSF) under Awards #1847632 and #1750786.

DEDICATION

To my beloved father in Heaven, I hope you continue to find pride in me.

ABSTRACT OF THE DISSERTATION

Exploring the Relationship Between Thermal Conductivity and Phonon Dynamics by Ultrafast Pump-Probe and Scattering Techniques

by

Songrui Hou

Doctor of Philosophy, Graduate Program in Materials Science and Engineering

University of California, Riverside, December 2023

Dr. Richard B. Wilson and Dr. Chen Li, Co-Chairpersons

Comprehending the interplay between thermal conductivity and phonon dynamics in semiconductors and insulators holds significance for the field of phonon engineering. While substantial progress has been made in the theoretical understanding of this relationship over the last decade, many of these predictions lack empirical validation. This dissertation endeavors to bridge this experimental gap, focusing particularly on the validation of theoretical insights, with a special emphasis on boron arsenide (BAs), a recently discovered material exhibiting ultrahigh thermal conductivity.

Temperature-induced changes in phonon occupation impact thermal conductivity, making it a valuable probe for understanding phonon scattering in materials. Through systematic investigations of BAs samples across the temperature range of 300 to 600 K, we discovered a more pronounced temperature dependence ($1/T^2$) than theoretical predictions ($1/T^{1.7}$) in BAs sample with ambient thermal conductivity of 1500 W m^{-1} K^{-1}. This discrepancy indicates that existing calculations have underestimated the importance of four-phonon scattering in BAs.

Pressure renders a systematic tool to modulate phonon dispersion, offering insights into the correlation between changes in phonon dispersion and thermal conductivity. The Leibfried-Schlömann (LS) equation, a phenomenological model known for its predictive capabilities, has been successfully applied to elucidate the pressure dependence of thermal conductivity in numerous materials. My initial investigations focused on two perovskites, $SrTiO_3$ and $KTaO_3$, revealing that their thermal conductivity variations align with LS equation predictions. The distinct pressure sensitivities observed in $SrTiO_3$ and $KTaO_3$ underscore the pivotal role of phonon lifetime in determining pressure-induced alterations in thermal conductivity.

However, when applying the LS equation to BAs, a notable discrepancy emerged. While the LS equation projected a threefold increase in BAs's thermal conductivity at 30 GPa, our experimental findings demonstrated much less changes. Subsequently, I extended my investigations to GaN, which shares certain phonon dynamics similarities with BAs. Both BAs and GaN have a frequency gap in their phonon dispersion. GaN exhibited a stronger pressure dependence, aligning well with LS equation predictions. Furthermore, I conducted pressure-dependent measurements on diamond, where my data exhibited acceptable agreement with LS predictions. This comparative analysis among BAs, GaN, and diamond underscores the distinctive thermal characteristics of BAs.

Table of Contents

List of Figures

Chapter 1 Introduction

1.1 Motivation

Atoms vibrate collectively in crystals, and phonons are quantum mechanical quantization of the vibrational modes for interacting particles. To illustrate this, let us examine the elastic vibrations in a one-dimensional chain of atoms, with one atom located in the primitive cell. For atom s, when considering only interactions with its nearest neighbors, $s+1$ and $s-1$, the equation of motion of s is

$$F_s = M\frac{d^2u}{dt^2} = C(u_{s+1} - u_s) + C(u_{s-1} - u_s). \quad (1.1)$$

Here, F_s is the force applied on atom s, M is the mass of an atom, u is the displacement of an atom, and C is the force constant between nearest neighbors. By solving the equation (1.1), we get

$$\omega = (4C\ /\ M)^{1/2}\left|sin\frac{1}{2}Ka\right|. \quad (1.2)$$

This is the phonon dispersion relation $\omega(K)$. Here, ω is the frequency of the vibration, *i.e.*, phonon frequency, K is the wavevector of the vibration, *i.e.*, phonon wavevector, and a denotes the lattice constant. A plot of $\omega(K)$ is shown in Figure 1.1. Atoms can vibrate in the direction perpendicular or parallel to the phonon wavevector. Correspondingly, there are 3 phonon dispersions known as acoustic phonons. When the primitive cell has n atoms ($n > 1$), there emerge $3(n-1)$ more dispersion curves corresponding to the additional interactions of atoms within the primitive cell. These $3(n-1)$ phonon dispersions are recognized as optical phonon dispersions [1].

Phonons are the main heat carriers in nonmetallic materials. From the kinetic gas theory,

$$\Lambda = \sum_j \int_0^{\omega_m} \frac{1}{3} c_j(\omega) v_j^2(\omega) \tau_j(\omega)\, \mathrm{d}\omega \qquad (1.3)$$

Where Λ is the thermal conductivity of materials, $c_j(\omega)$ is the heat capacity of a phonon mode, $v_j(\omega)$ is the phonon group velocity, $\tau_j(\omega)$ is the phonon lifetime, and j labels the phonon polarization. Therefore, $v_j(\omega)$ is the average of group velocities along different directions. From equation (1.3), it is evident that thermal conductivity hinges on heat capacity, group velocity, and the lifetime of phonon modes. The heat capacity and group velocity of a phonon mode can be readily computed from the phonon dispersion.

$$c(\omega) = D(\omega)\hbar\omega \frac{\partial n(\omega)}{\partial T} \qquad (1.4)$$

$$v(\omega) = \frac{d\omega}{dK} \qquad (1.5)$$

Here, $D(\omega)$ is the phonon density of states, and n is the Bose-Einstein distribution. Note that $v(\omega)$ here represents the directionally averaged group velocity. The determination of phonon lifetimes is a complex yet theoretically achievable task with the help of phonon dispersion relationships and higher-order interatomic force constants [2]. So, the thermal conductivity of nonmetallic materials is intricately tied to their phonon dispersion relations. In experimental settings, temperature adjustments can modulate the distribution and occupation of phonon modes, even subtly altering the dispersion relation of certain materials [3,4]. Furthermore, the application of high pressure on the GPa scale has the remarkable capacity to significantly reshape the phonon dispersion [5,6]. Through the precise measurement of alterations in phonon dispersion and thermal conductivity in response to varying temperature or pressure, we gain a more profound

understanding of the fundamental mechanisms underlying how phonon dispersion dictates the thermal conductivity of nonmetallic materials.

This enhanced understanding of the physics at play holds great potential, offering insights into the discovery of materials with ultrahigh or ultralow thermal conductivity [7], enabling advancements in thermal management techniques [8], and facilitating the field of thermal conductivity engineering [6]. Additionally, the experimental data on thermal conductivity at elevated pressures holds particular significance for the geophysics community, aiding in comprehending the thermal balance and historical evolution of our planet Earth [6].

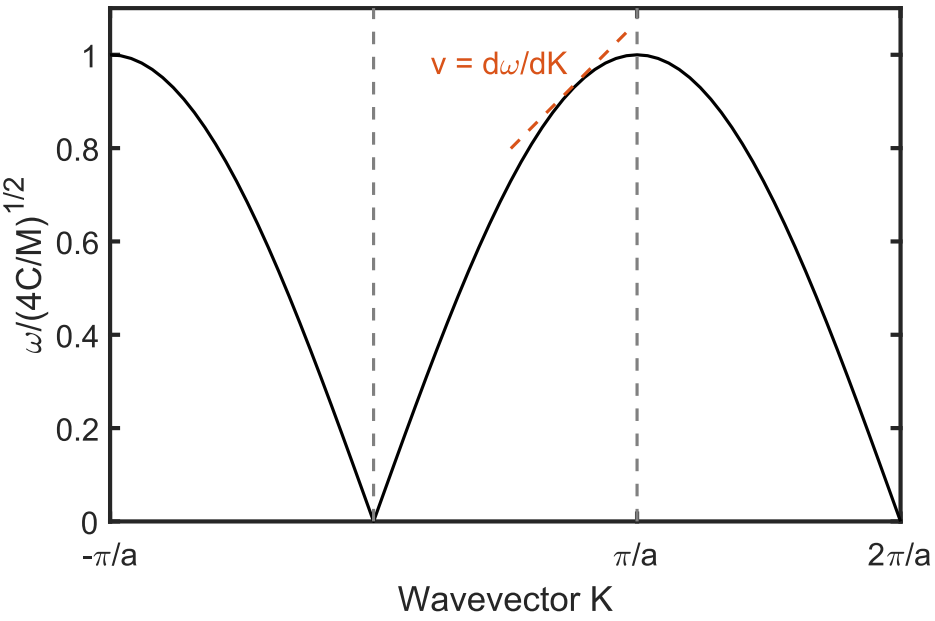

Figure 1.1. An example of an acoustic phonon dispersion relation.
This is a plot of equation (1.2). The phonon group velocity is the gradient of phonon dispersion, as shown in equation (1.5).

1.2 Typical behavior of Λ vs. T of Nonmetallic Materials

The temperature dependence of thermal conductivity for nonmetallic materials has been extensively examined. At low temperatures, thermal conductivity carried by phonons displays a $\Lambda \propto T^3$ dependence due to the T^3 dependence of heat capacity in this temperature range [1]. In extremely low temperature conditions, only low-frequency acoustic phonons are excited, and their group velocities $v(\omega)$ remain nearly constant as temperature changes. Additionally, phonon lifetime is predominantly governed by boundary scattering, $1 \,/\, \tau(\omega) \propto L/v(\omega)$, with L representing grain or crystal size, resulting in nearly constant phonon lifetime $\tau(\omega)$ as temperature changes. Consequently, the temperature dependence of phonon heat capacity becomes the primary determinant of thermal conductivity.

At higher temperatures, specifically above half of the Debye temperature, $\Lambda \propto 1 \,/\, T$ is observed for most nonmetallic materials. This behavior can be attributed to several factors: 1) Phonon heat capacity reaches the Dulong-Petit limit and remains constant at elevated temperatures; 2) for most materials, phonon group velocity does not change much since phonon dispersion does not change significantly as temperature changes. 3) phonon lifetime is limited by phonon-phonon scattering processes at high temperature. For the lowest-order phonon-phonon scattering which involves three phonons, the scattering rate is proportional to the total number density of excited phonons, which is proportional to temperature. So, $1 \,/\, \tau(\omega) \propto T$. At intermediate temperatures, things are more complicated because c, v, and τ have more complicated temperature dependence. The peak thermal conductivity in Figure 1.2 is determined by crystal size and/or imperfections in the crystal structure, such as grain boundaries, dislocations, and isotopes. Note that all the discussion above is about pure single crystals. With the presence of significant crystal disorder, Matthiessen's rule is used to account for different scattering channels.

$$\frac{1}{\tau} = \frac{1}{\tau_L} + \frac{1}{\tau_i} \qquad (1.6)$$

Where $1 / \tau_L$ and $1/\tau_i$ are scattering rates for phonon-phonon interaction and phonon-disorder scattering, respectively.

The discussion above focuses on typical nonmetallic materials. There are also materials with unusual behaviors. Unusual temperature dependence can be caused by a variety of factors, such as higher-order phonon-phonon scattering. In magnetic insulators, magnetic phase transitions can cause atypical temperature dependence. Our temperature-dependent studies on NiO and BAs will be discussed in Chapter 3 and 4.

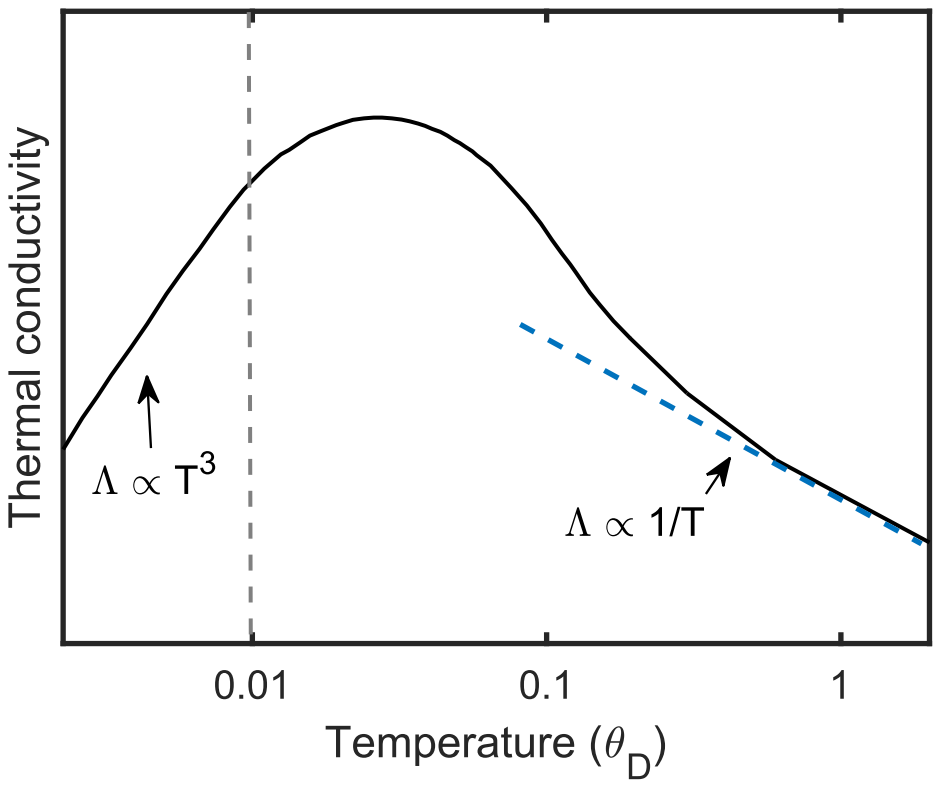

Figure 1.2. A schematic of the typical temperature-dependent thermal conductivity of nonmetallic materials.

At low temperature limit, $\Lambda \propto T^3$ due to the change of heat capacity. At high temperature limit, $\Lambda \propto 1/T$ due to the variation of phonon lifetime. Note that both the horizontal and vertical axis are plotted in log scale which can show the temperature dependence more clearly. θ_D represents the Debye temperature.

1.3 Typical behavior on Λ vs. P of Nonmetallic Materials

Compared to the temperature dependent studies, the GPa-scale experimental studies of Λ vs. P for nonmetallic materials are less explored. So far, there are only ~ 30 materials whose thermal conductivity has been measured up to 20 GPa [6]. However, it is a booming research area and receiving growing attention.

When applied GPa-scale pressure, materials will experience significant changes in phonon dispersion, resulting in changes in heat capacity, group velocity, and phonon lifetime. The Leibfried-Schlömann equation (LS) [9] is commonly used to explain observed trends for $\Lambda(P)$ in nonmetallic crystals. The LS equation approximates c, v, and τ in Eq. (1.3) using properties that can be extracted from the volume-pressure equation of states (*V-P* EOS) [10]. The volumetric heat capacity is assumed to be $C \propto 1/V$. The group velocity v is parameterized as $v = \sqrt{K_T/\rho} \propto \delta\theta$. Phonon mean free path ($l = v\tau$) is set to be $l \propto \delta \,/\, T\alpha\gamma$ [11]. Here, K_T is the isothermal bulk modulus defined as $K_T = -dP \,/\, d\,ln\,V$, and α is the volumetric thermal expansion coefficient which can be calculated by $\alpha = C\gamma \,/\, K_T$. Plugging these approximations into Eq. (1.3) yields

$$\Lambda = \frac{B\bar{M}\delta\theta^3}{T\gamma 2} \qquad (1.7)$$

Here *B* is a constant which we set according to the ambient thermal conductivity, $\bar{M}$ is the average mass of an atom in the crystal, δ^3 is the average volume occupied by one atom in the crystal, θ is the Debye temperature, *T* is temperature, and γ is the Grüneisen parameter. δ, θ, and γ are all pressure dependent. The evolution of δ, θ, γ with pressure depends on the first, second, and third derivatives of the *V-P* EOS. $\theta \propto \sqrt{\delta K_T}$, where K_T is the isothermal bulk modulus. The LS equation uses the "Slater γ", which is defined as $\gamma = \frac{1}{2}\frac{dK_T}{dP} - \frac{1}{6}$ [12]. The pressure dependent thermal conductivity calculated by the LS equation usually gives an almost linearly increasing

thermal conductivity at high pressure (see Figure 1.3). Our pressure dependent studies on $SrTiO_3$, $KTaO_3$, BAs, GaN, and diamond will be discussed in Chapter 5 - 7.

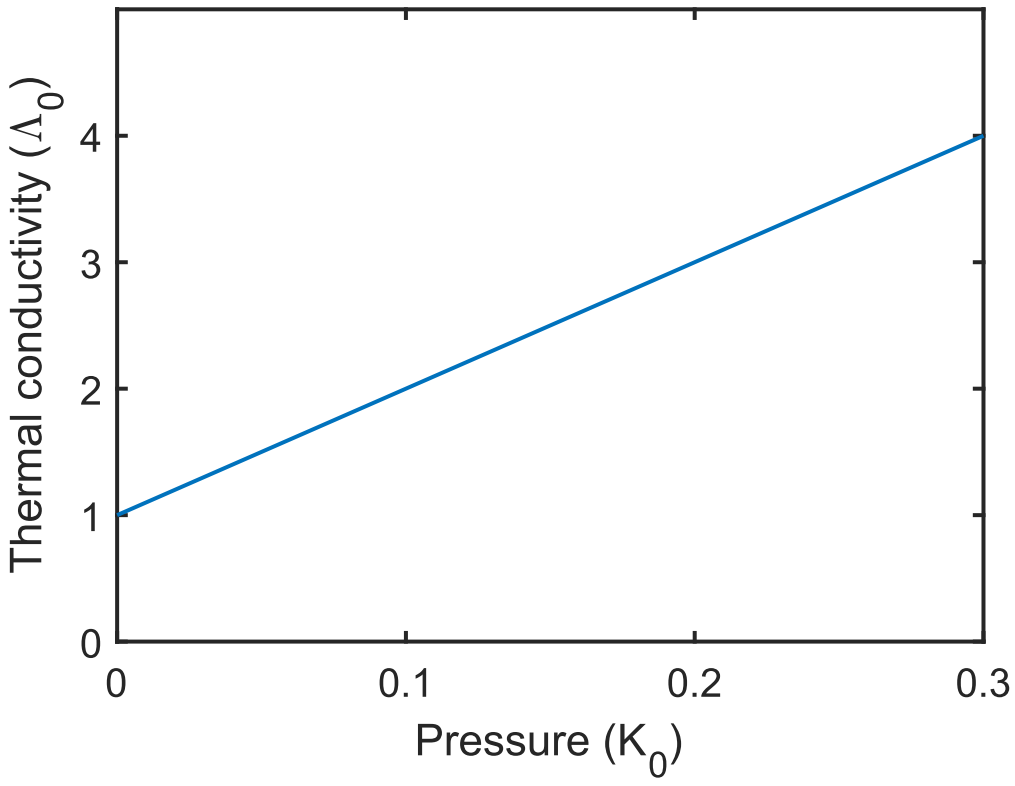

Figure 1.3. A schematic of the typical pressure-dependent thermal conductivity of nonmetallic materials.

Λ_0 represents the ambient thermal conductivity, and K_0 is the ambient bulk modulus.

Chapter 2 Experimental Methods

2.1 Time-domain thermoreflectance (TDTR)

TDTR is a well-established pump-probe technique. In TDTR measurements, a train of 783-nm-wavelength laser pulses emitted from a mode-locked Ti:sapphire oscillator is split into a pump beam and a probe beam. The pump beam is modulated at a MHz-frequency duty cycle (I used 10.7 MHz modulation frequency for most of my measurements). The probe beam monitors the temperature decay at the sample surface via temperature induced changes in reflectance (ΔR):

$$\Delta R = \frac{dR}{dT}\Delta T. \quad (2.1)$$

$dR\ /\ dT$ is thermoreflectance (also called thermos-optic coefficient). It has been found for most thin metal films, $dR\ /\ dT$ is a constant at tens of Kelvin temperature excursion [13,14]. Thus, we can detect ΔT through measuring ΔR. The reflected probe beam from the sample surface is collected by a silicon photodiode detector. A lock-in amplifier reads the micro-volt change in voltage output by the detector due to changes in reflected probe beam intensity. The amplifier outputs the in-phase signal V_{in} and out-of-phase signal V_{out} at the MHz pump modulation frequency.

To extract thermal properties from data we collect from TDTR measurements, we simulate the ratio $-V_{in}(t)/V_{out}(t)$ after 100 ps by a multilayer heat diffusion model in cylindrical coordinates [12]. The model assumes pump pulses with a Gaussian distribution in intensity heat up the surface of the semi-infinite sample at the modulation frequency, and heat flows continuously across each interface. In this model, interfaces are treated as 1-nm thin layers with 0.1 J cm^{-3} K^{-1} volumetric heat capacity, which can conduct heat but cannot significantly absorb heat. Figure 2.1 shows TDTR data and the sensitivity plots of a Si sample deposited with an 80-nm Al film as the transducer, denoted as Al/Si. The sensitivity is defined as

$$S_\alpha = \frac{\partial\, ln(-V_{in}/V_{out})}{\partial\, ln\, \alpha}, \qquad (2.2)$$

where α is one the parameters in the heat diffusion model. Figure 2.1(b) shows sensitivities of parameters of interests for 80 nm Al/Si sample. Most uncertainty of Al/Si comes from the thickness of Al because its high sensitivity to the ratio. For 100 ps < t < 500 ps, the sensitivity of h_{Al} is ≈ -0.9 and the sensitivity of Λ_{Si} is ≈ 0.5. Thus, if there is an ≈ 4% uncertainty in Al, it will propagate ≈ 7.2% uncertainty in Λ_{Si}.

Many parameters need to be determined for the heat diffusion model, including $1/e^2$ radius of laser w_0, thickness h, volumetric heat capacity C, and thermal conductivity Λ of each layer, interface conductance G between the transducer and the sample. Among these parameters, only Λ of the substrate and G are significant unknowns, and we can obtain other parameters from experiments or literature. Take Al/Si as an example. The laser spot size can be measured by beam-offset method [14] and camera method which analyzes the Gaussian distribution of images of laser beams. Al thickness can be measured simultaneously with TDTR using picosecond acoustics [15]. The heat capacity of Al can be found in literature [16]. For the thermal conductivity of Al, first we measure the conductivity of Al by the four-point probe method, then calculate the thermal conductivity of Al by Wiedemann-Franz law. Additionally, we fit the ratio after 100 ps when the ratio has little sensitivity to the thermal conductivity of Al as shown in Figure 2.1(b). In most cases the heat capacity of the sample has experimental or calculation data from literature. TDTR can also measure the thermal conductivity and heat capacity of the sample simultaneously by varying laser spot size and modulation frequency [17].

For the two significant unknowns, Λ of the substrate and G, we can determine them from a single TDTR scan. From the sensitivity plot in Figure 2.1(b), it can be noticed that the sensitivity of G changes significantly and goes from positive to negative as time increases. This means G mainly

affects the gradient of the ratio curve (see Figure 2.1(c)). While the sensitivity of Λ_{si} stays positive over time, which indicates it mainly affects the magnitude of the ratio curve (see Figure 2(d)). Thus, the interface conductance and the thermal conductivity of the substrate can be determined from a single TDTR scan simultaneously.

So far, we are talking about cases where the sample is exposed to air. Usually, we do not consider heat flowing into air due to its low thermal conductivity, ≈ 0.026 W m^{-1} K^{-1} [18], which is much lower than most solid materials. In high pressure TDTR measurements, the sample is surrounded by pressure medium. Under GPa-scale pressure, the thermal conductivity of pressure medium is 1-40 W m^{-1} K^{-1} [19, 20] and the heat conducted to the medium cannot be neglected. In this case, we need to use a bidirectional heat diffusion model to fit TDTR data [15]. Heat flows to both the pressure medium and the sample in parallel in the bidirectional model.

In the case of bidirectional heat conduction, heat tends to flow along the thermally conductive direction. Figure 2.2 demonstrates the sensitivity analyses with the substrate being muscovite mica and BAs of 500 W m^{-1} K^{-1}. Silicone oil (0.15 W m^{-1} K^{-1}) serves as the pressure medium and an 80-nm Al film as the transducer for both cases. All input parameters are the same except the heat capacity and thermal conductivity of the substrate. For mica, the properties of silicone oil have almost half of the sensitivities as those of mica since they two have comparable thermal conductivity (see Figure 2.2(a)). In comparison, for the BAs system, the sensitivity of silicone oil is close to 0. This indicates if we want to study the thermal conductivity of the substrate, we should choose a relatively low-thermal-conductivity pressure medium. If we want to study the thermal conductivity of the pressure medium, we should select a substrate with low thermal conductivity.

When analyzing TDTR data on materials of high thermal conductivity such as diamond and BAs single crystals, it is better to analyze the $-V_{in}\,/\,V_{out}(t<0)$ instead of $-V_{in}\,/\,V_{out}$ for the acquisition of thermal conductivity. Here $V_{out}(t<0)$ represents the average out-of-phase signal at negative delay time. Ideally, V_{out} in TDTR scans should remain almost constant versus delay time. When considering the spot size enlargement with delay time, $|V_{out}|$ is expected to decrease with delay time. However, in real scans, V_{out} sometimes shows weird behavior at positive delay time. Figure 2.3 shows two consecutive TDTR scans on diamond, *i.e.*, I collected the two scans at the same spot on the diamond sample back-to-back. It can be noticed that the V_{out} at positive delay time for the two scans are different from each other, leading to different $-V_{in}\,/\,V_{out}$ and subsequently different fitted thermal conductivity of diamond. The different V_{out} signals at $t>0$ may be related to the phase jitter of the lock-in amplifier. The V_{out} signals at negative delay time are consistent with each other and reproducible. So, to guarantee reproducibility, it is better to analyze $-V_{in}\,/\,V_{out}(t<0)$ for high-thermal-conductivity materials when fitting their thermal conductivity. Note that this is a universal problem for TDTR, but small artifacts in V_{out} do not cause significant errors for low-thermal-conductivity materials which have large V_{out} signals.

When fitting the interface conductance between the transducer and the substrate, it is better to analyze the $-V_{in}\,/\,V_{out}$ signal. We control the pump-probe delay time by the physical movement of retroreflectors. In our system, we delay the pump beam. The spot size (w_p) of the pump beam depends on the position of the retroreflector. Therefore, as delay time increases, the spot size of the pump beam changes. The change of spot size will change the power density ($P/\pi w_p^2$). Both V_{in} and V_{out} are proportional to the power density, so $-V_{in}\,/\,V_{out}$ is not related to power density at any delay time. However, $V_{out}(t<0)$ does not include the time-dependent variations due to the change of spot size. Therefore, $-V_{in}\,/\,V_{out}(t<0)$ at long delay time is not accurate, see

Figure 2.3(c). The sensitivity analysis (Figure 2.1(c)) shows the gradient of $-V_{in} / V_{out}$ *vs.* delay time depends on the interface conductance. Therefore, it is more accurate to analyze the $-V_{in} / V_{out}$ when acquiring the interface conductance.

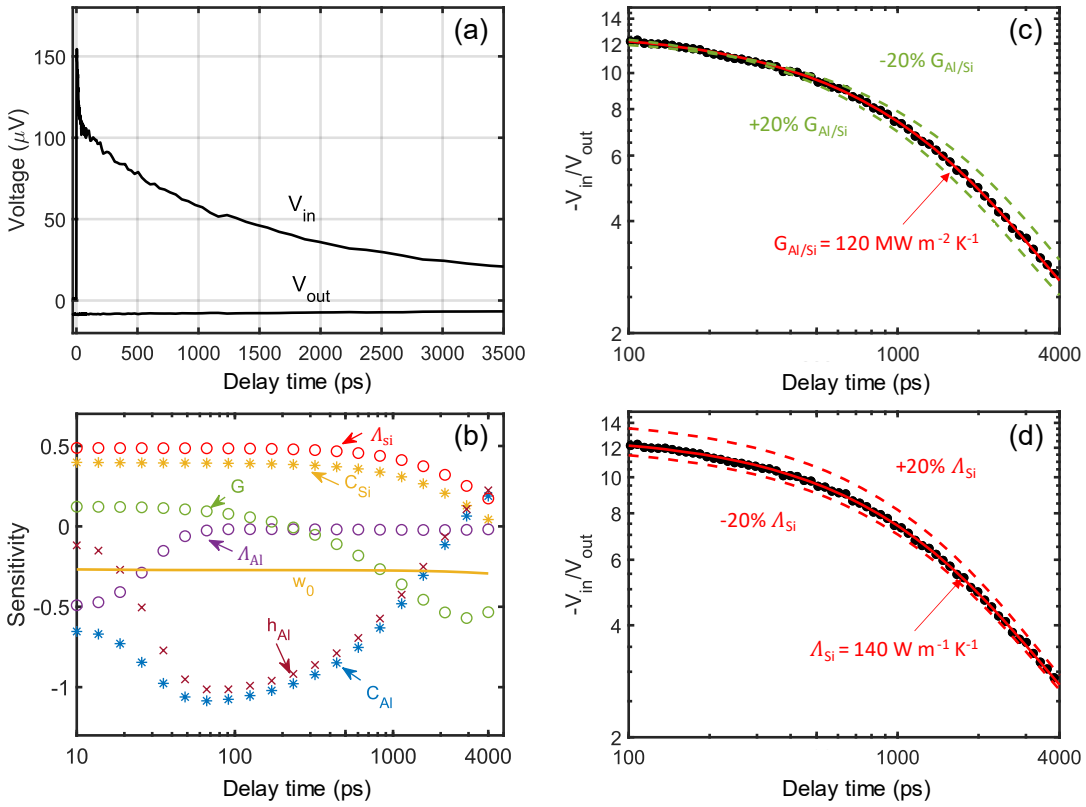

Figure 2.1. TDTR data on an 80-nm Al/Si sample and its sensitivity analysis.

(a) V_{in} and V_{out} versus delay time collected on an 80 nm Al/Si sample. (b) Sensitivity analysis of parameters of interests, where h means thickness, C stands for heat capacity, Λ is thermal conductivity, and G is interface conductance. (c) and (d) show how variations of G and Λ_{Si} affect the fitting curve. The G affects the gradient of the fitting, while Λ_{Si} affects the amplitude.

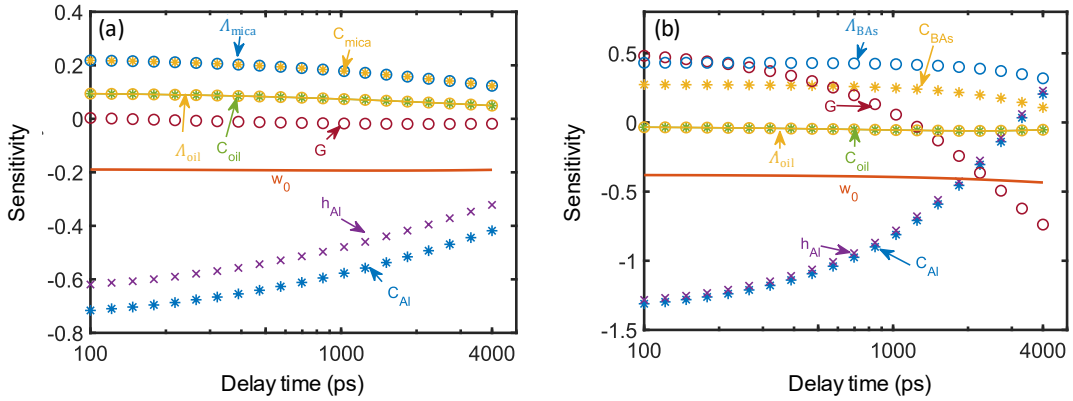

Figure 2.2. Sensitivity analyses of bidirectional heat diffusion.

(a) Sensitivity analysis of silicone oil/Al/mica. Λ_{mica} = 0.46 W m^{-1} K^{-1}. Thermal conductivity of silicone oil is comparable to that of mica. Heat flowing into silicone oil is not negligible, resulting in a large sensitivity of Λ_{oil}. (b) Sensitivity analysis of silicone oil/Al/BAs. Λ_{BAs} = 500 W m^{-1} K^{-1}. Thermal conductivity of silicone oil is much less than that of BAs. Heat flowing into silicone oil is negligible, resulting in $\Lambda_{oil} \approx 0$.

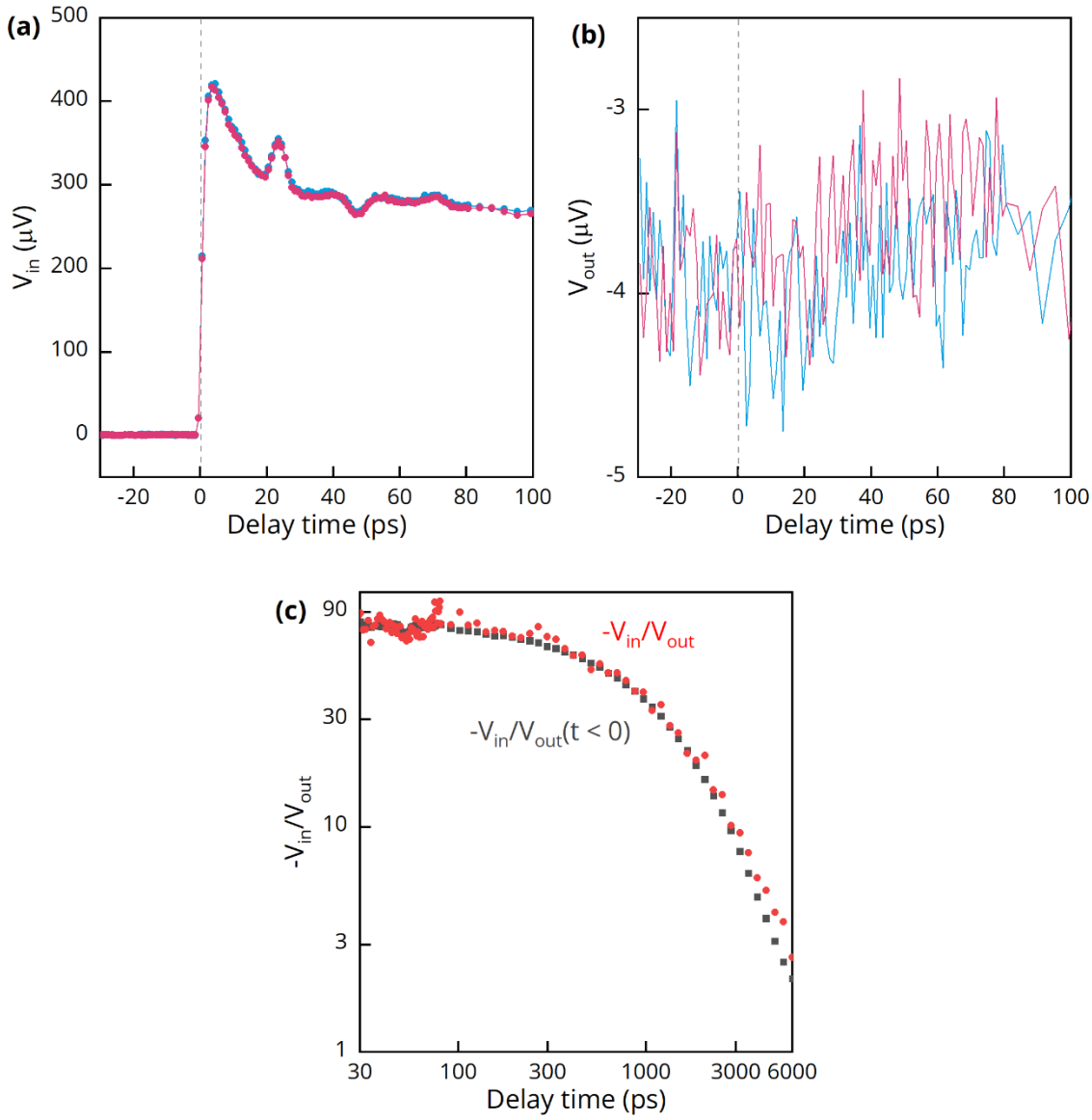

Figure 2.3. Two consecutive TDTR scans on an Al/diamond sample.

(a) In-phase signal versus delay time. V_{in} signals of the two back-to-back scans are consistent. (b) Out-of-phase signal versus delay time. At $t < 0$, V_{out} signals for the two scans are consistent. At $t > 0$, the two scans have an offset in the V_{out} signal, even though everything in experimental setups are the same. (c) Comparison between two ways of analyzing $-V_{in}/V_{out}$.

2.2 Diamond anvil cell (DAC)

Diamond anvil cells (DACs) operate by applying force to a pair of diamond culets with diameters in the range of hundreds of microns. This force generates high pressure, calculated as $P = F / A$, where P is the pressure, F is the applied force and A is the area of the culet. Note that DACs do not compress the sample inside directly. Instead, the sample is immersed in some pressure medium. Two diamond anvils compress the pressure medium, and the pressure medium transmits the pressure to the sample. Diamond, with its exceptional hardness, allows DACs to generate pressures exceeding 100 GPa [21, 22]. Diamond is a very hard and least-compressible material. These two properties can help minimize the deformation and failure of the anvils. (Hardness measures the ability to resist localized plastic deformation.) Moreover, the optical transparency of diamond, stemming from its 5.47 eV band gap, makes it suitable for laser-related experiments. I employ both symmetric DACs (procured from Syntek) and plate DACs (purchased from Almax easyLab) for conducting high-pressure measurements, see Figure 2.4. Symmetric DAC is a traditional design, and plate DAC is a relatively new design. In terms of functionality, they do not have much difference [16,17].

Figure 2.5(a) presents a schematic of a DAC. In this setup, a pair of diamonds oppose each other, separated by a gasket. The gasket serves two purposes: it safeguards the diamond anvils against breakage and creates a chamber for housing the sample. Our typical choice for gasket material is hardened stainless steel or Re. Re is stronger and stiffer than stainless steel, but Re is also more expensive. The sample is positioned in the center of the chamber along with a ruby sphere. The ruby sphere calibrates the pressure within the DAC by its fluorescence spectrum [23]. Figure 2.6(a) shows the fluorescence spectrum of a ruby at 4.6 and 16.2 GPa. When using silicone oil as the pressure medium, its Brillouin frequency can also serve as a pressure gauge when doing

TDTR measurements (Figure 2.6d). Details about Brillouin scattering will be discussed in Chapter 2.3.

The sample and ruby sphere are surrounded by pressure medium. There are various kinds of pressure mediums used in DAC measurements, such as Ar, He, Ne, N_2, H_2O, silicone oil, methanol-ethanol mixture, and sodium chloride (NaCl). For measurements using a laser, it is essential that the pressure medium be transparent at the wavelength of the laser. Different experiments have different requirements for the pressure medium. For TDTR experiments, a low thermal conductivity pressure medium is preferred to minimize heat flow into the medium (Figure 2.2). When conducting Raman scattering experiments, it is advisable to select a medium with no Raman peaks overlapping with the target materials. Additionally, hydrostaticity is a critical factor in high-pressure measurements, ensuring that pressure is uniformly distributed in all directions. Non-hydrostatic pressure conditions can result in sample strains due to pressure gradients within the DAC [18]. Also, the pressure measured by ruby fluorescence may not be the pressure experienced by the sample for non-hydrostatic conditions. It has been found that gaseous pressure media are more hydrostatic than liquid and solid media [18]. However, loading gaseous pressure media requires a complicated compressing system [19] which is not available in most labs or at UCR. Also, gaseous pressure media have relatively high thermal conductivity at high pressure [20], making them unsuitable for thermal transport studies of low-thermal-conductivity samples. Argonne National Lab and Oak Ridge National Lab provide gas loading service for outside researchers. The choice of pressure medium ultimately involves a trade-off between these various factors. Most experiments I have done employed silicone oil as the pressure medium.

In our experiments, we use a pair of diamonds with culet size of ≈ 300 μm in diameter. I usually pre-indent the stainless-steel gasket to be ≈ 30 μm in thickness. Then I drill a hole with ≈ 100 to 150 μm in diameter on the center of the gasket to serve as a sample chamber. I load samples with

lateral dimensions of 50 - 80 μm into the sample chamber along with ruby spheres of ~10 μm. Finally, I fill the chamber with pressure medium and apply pressure.

The maximum pressure of a DAC depends on the culet size of diamond anvils. Usually, anvils with 500 – 600 μm culet diameter can reach 20 – 30 GPa [10,21,22]. 400 μm anvils can reach 30 – 50 GPa [23–27]. 300 μm anvils can tolerate 50 – 60 GPa [17]. Anvils with culet size ≤ 200 μm can go beyond 100 GPa [17,25,28,29]. Table 2.1 shows the pressure maximum for different culet diameters suggested by Almax easyLab, a company selling equipment related to high-pressure research.

The pre-indentation thickness plays a crucial role in high-pressure measurements. Inadequate pre-indentation can lead to an unstable sample chamber under pressure. A “stable sample chamber” retains its shape under pressure, while an unstable chamber may rupture at high pressure. Figure 2.7 shows a sample chamber without sufficient pre-indentation. The area of the sample chamber (DAC hole) increases as pressure increases, leading to rupture at a pressure of 31.2 GPa. In contrast, Figure 2.8 shows a sample chamber with sufficient pre-indentation. In this case the DAC hole remains its shape even at 40.1 GPa. Based on my experience, a pre-indentation thickness of less than 35 μm is sufficient. An alternative way to determine the pre-indentation thickness is by measuring the pre-indentation pressure. The pre-indentation pressure should be at least half of the target maximum pressure. For example, if aiming for 40 GPa, a pre-indentation pressure of ≥ 20 GPa is required. The pre-indentation pressure can be measured by the Raman peak of diamond anvils versus pressure [30].

Sample thickness is another critical factor in high-pressure measurements, particularly in TDTR experiments. The sample within the DAC should not contact both diamond anvils, which is referred to as "bridging" in the high-pressure community. Bridging leads to extreme sample

strains and introduces optical artifacts from the diamond anvils. TDTR measures temperature through optical reflectance signals, and there will be two additional issues if bridging happens: 1) Heat can possibly flow into the diamond anvil, making the modelling of heat diffusion unreliable. 2) The reflected probe beam from the diamond anvils can cause optical artifacts in thermal-related signals. Both effects compromise the accuracy of measured thermal conductivity.

To prevent bridging, it's crucial that the sample's thickness remains less than the distance between the two diamond anvils. By assessing the DAC hole's area (A) through camera images (*e.g.*, Figures 2.6 and 2.7) in combination with the equation of state (EOS) for the pressure medium, we can estimate the distance (d) as a function of pressure, calculated as $d = V / A$. As depicted in Figure 2.9B, the estimated d for the scenarios shown in Figures 2.7 and 2.8 suggests that the sample's thickness should be less than 20 μm. In practice, I typically prepare the sample to be less than 10 μm in thickness, which has been tested to be sufficient for measurements up to 50 GPa.

Specifically, for silicone oil, with measured Brillouin frequency data, we can calculate the EOS of silicone oil using the following formula:

$$f = \frac{2Nv_l}{\lambda}, \quad (2.3)$$

$$\frac{N^2-1}{\rho(N^2+2)} = A \text{ (Lorentz-Lorenz relation)}, \quad (2.4)$$

$$P = 3K_0\left(\frac{1-\eta}{\eta^2}\right)e^{\frac{3}{2}(K_0'-1)(1-\eta)} \text{ (Vinet equation of states)}, \quad (2.5)$$

$$K = -V\left(\frac{\mathrm{d}P}{\mathrm{d}V}\right)_T. \quad (2.6)$$

Here, f is the Brillouin frequency of silicone oil from measurements, N is the index of refraction of silicone oil, v_l is the longitudinal group velocity, λ is the laser wavelength, ρ is the density of silicone oil, A is a constant, P is the pressure, K_0 is the ambient isothermal bulk modulus, $\eta =$

$(V\ /\ V_0)^{1/3}$, V is the volume, K_0' is the derivative of bulk modulus with respect to pressure, and K is the isothermal bulk modulus. The calculated EOS of silicone oil is shown in Figure 2.9A.

Note that the Lorentz-Lorenz (LL) relation is just a crude model to estimate the changes of refractive index induced by changes of density [1]. In real materials, it does not really work. For example, for diamond at 700 nm laser wavelength, the LL relation predicts its refractive index will increase from 2.407 to 2.42 at 9 GPa. The equation of states of diamond is from Ref. [30]. However, experiments show that N of diamond decreases from 2.407 to 2.4 at 9 GPa [31]. In the above, my goal is to derive the EOS of silicone oil from the Brillouin frequency data, so that I can estimate the distance between two diamond anvils at high pressure. Even if I assume N of silicone oil is a constant under pressure, the estimated distance will not be very different from the result obtained using the LL relation, see Figure 2.9. I did not apply the LL relation to any materials I studied (BAs, GaN, diamond, $SrTiO_3$, $KTaO_3$).

One way to identify when bridging occurs is if the sample's area increases as pressure rises. Based on the pressure-volume EOS of materials [32], volume should decrease as pressure increases. Given hydrostatic pressure, it is impossible for the sample's volume/area to increase as pressure increases. An increase in sample area suggests non-uniform pressure inside the DAC, with the sample likely undergoing plastic deformation [33]. Thermal conductivity of a material is sensitive to plastic deformation [34]. If plastic deformation happens at high pressure, the change in thermal conductivity may not be attributable to the material's intrinsic properties. Consequently, thermal conductivity results obtained under such conditions should be discarded.

A recent paper discussed measuring the transducer thickness using camera images [35]. However, their samples very likely experienced severe plastic deformation, making their results hard to

justify. In the following chapters, I will address how we account for the thickness of transducer at high pressure case by case.

Different from using silicone oil as the pressure medium, when employing a gaseous pressure medium, the DAC hole experiences significant shrinkage during compression, see Figure 2.11. Therefore, when using gaseous pressure medium, it is important to make sure that the lateral size of the sample is small enough so that the sample will not be crushed by the DAC hole shrinkage upon compression. The way to estimate the DAC hole shrinkage is by assuming d remains constant at high pressure, and the volume change is accommodated by the area change, $A = V / d$. The sample area should be less than the estimated A at the target pressure.

2.3 Forced Brillouin scattering.

Forced Brillouin scattering is a pump-probe laser technique for measuring the longitudinal group velocity of materials [36]. The schematic of forced Brillouin scattering is shown in Figure 2.6(b). When the pump beam heats the transducer surface, it launches a strain wave into the material for study. The strain wave front moves at the longitudinal sound velocity of sample. Both the strain wave and the transducer can reflect the subsequent probe beam. These two reflected probe beams interfere with each other and cause Brillouin oscillations in the in-phase voltage signal V_{in} [36]. When laser beams are perpendicular to the sample, the Brillouin frequency is

$$f = 2Nv_l / \lambda, \qquad (2)$$

Where N is the index of refraction of the sample, v_l is the longitudinal speed of sound of the sample, and λ is the excitation wavelength (783 nm in our experiments). We use the measured Brillouin frequency as a measure of the longitudinal speed of sound. Figure 2.6(c) shows data of a Brillouin

scattering scan. Additionally, the Brillouin frequency of silicone oil is an effective way of measuring the pressure in DAC [24].

There are two ways to do Brillouin scattering. One is to coat one side of the substrate with a metal transducer and shoot the laser beams from the uncoated side. This method works for materials that are transparent to the incident laser. I used this geometry for my high-pressure Brillouin scattering measurements. The other way is to coat the substrate with a 5-nm transducer (usually Pt) and shoot the laser from the coated side. I employed the latter geometry for temperature-dependent measurements.

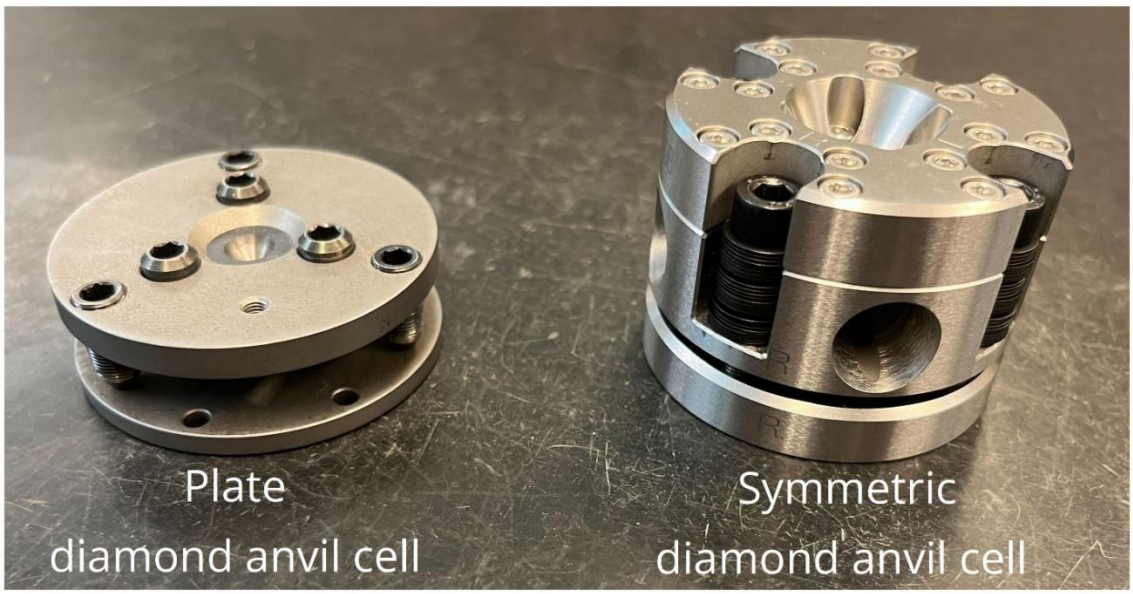

Figure 2.4. A photo of symmetric and plate diamond anvil cells.

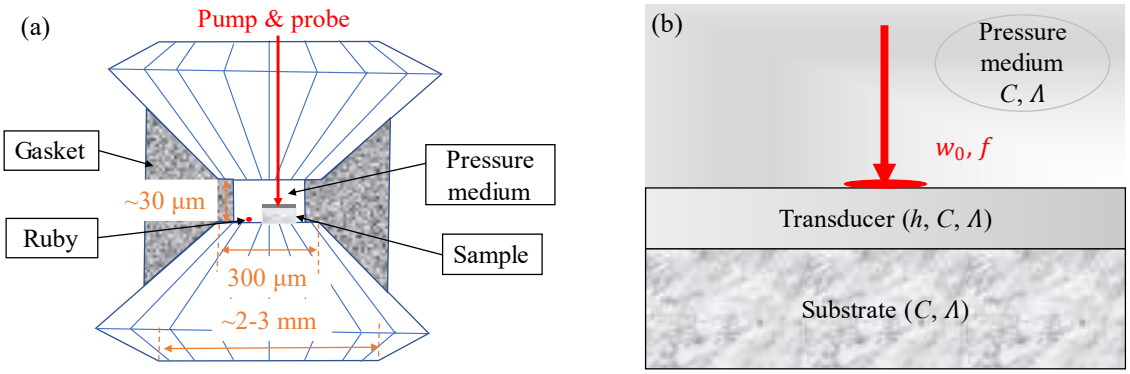

Figure 2.5. Schematics of DAC-assisted TDTR measurements.

(a) A schematic of a sample inside a DAC. (b) The sample geometry in DAC-assisted TDTR measurements. Pump and probe beams go through a diamond and the pressure medium, hitting on the transducer surface, and are reflected. Both (a) and (b) are not drawn to scales. Important scales in (a) are marked.

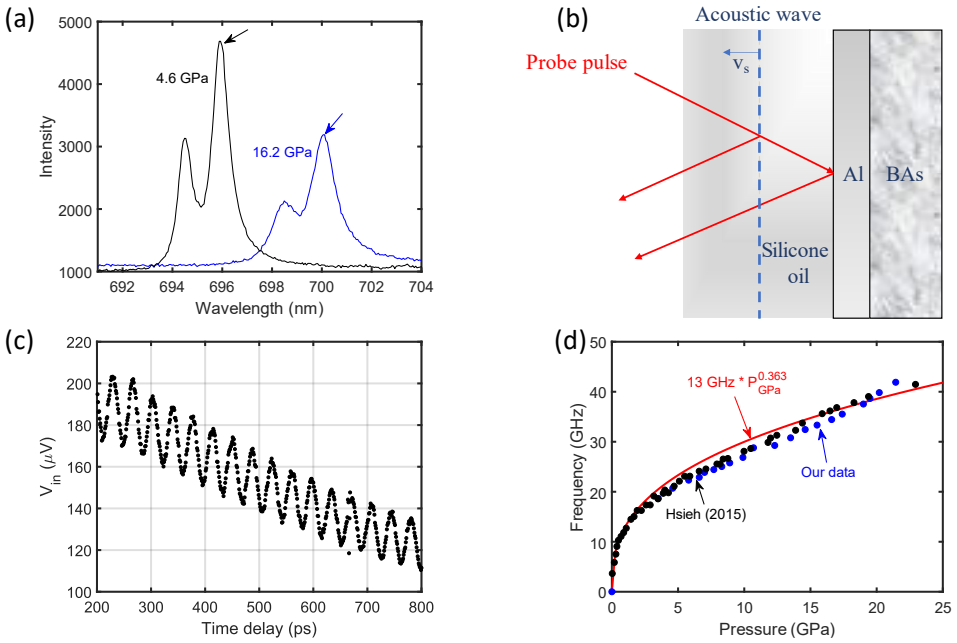

Figure 2.6. Measurements of pressure in a diamond anvil cell.

(a) An example of the red shift of ruby R1 line with increasing pressure. The arrows indicate the R1 lines at 4.6 and 16.2 GPa. (b) A schematic of the principle of Brillouin oscillation. The incident probe pulse can be reflected by both the Al and the traveling acoustic wave which is launched by the pump beam. The two reflected probe beams can interfere with each other, resulting in oscillations in V_{in} signals as shown in (c). The acoustic wave moves at the speed of sound of silicone oil v_s. (d) Brillouin frequency of silicone oil *vs.* pressure. Blue dots are our data collected on silicone oil. Black dots are data in Ref. [21]. The red line is the fitting of Brillouin frequency of silicone oil *vs.* pressure in Ref. [37]. We calibrated pressures using both the ruby fluorescence spectrum and the Brillouin frequency of silicone oil.

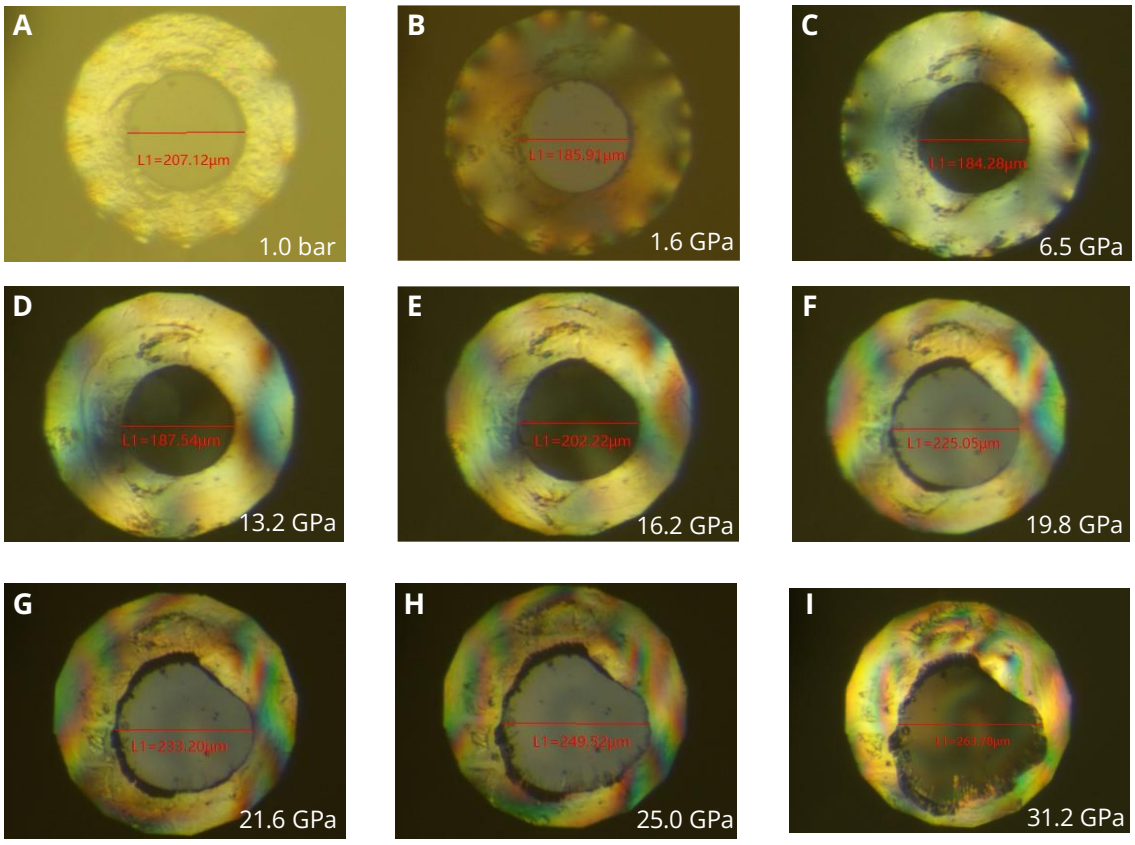

Figure 2.7. Images of the hole area in a diamond anvil cell with insufficient pre-indentation.

The pre-indentation is 65 μm. In this condition, the DAC hole expands significantly as pressure increases.

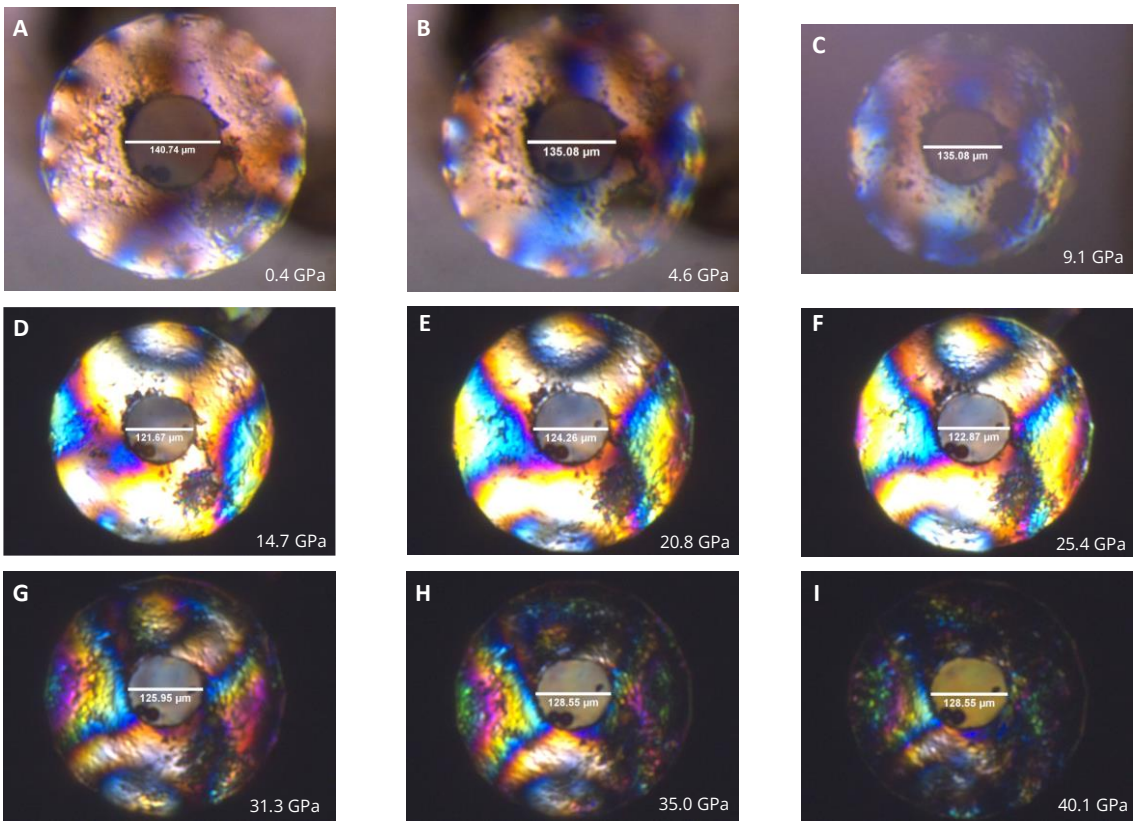

Figure 2.8. Images of the hole area with sufficient pre-indentation.

The pre-indentation is 35 µm. In this condition, the DAC hole remains constant at high pressure.

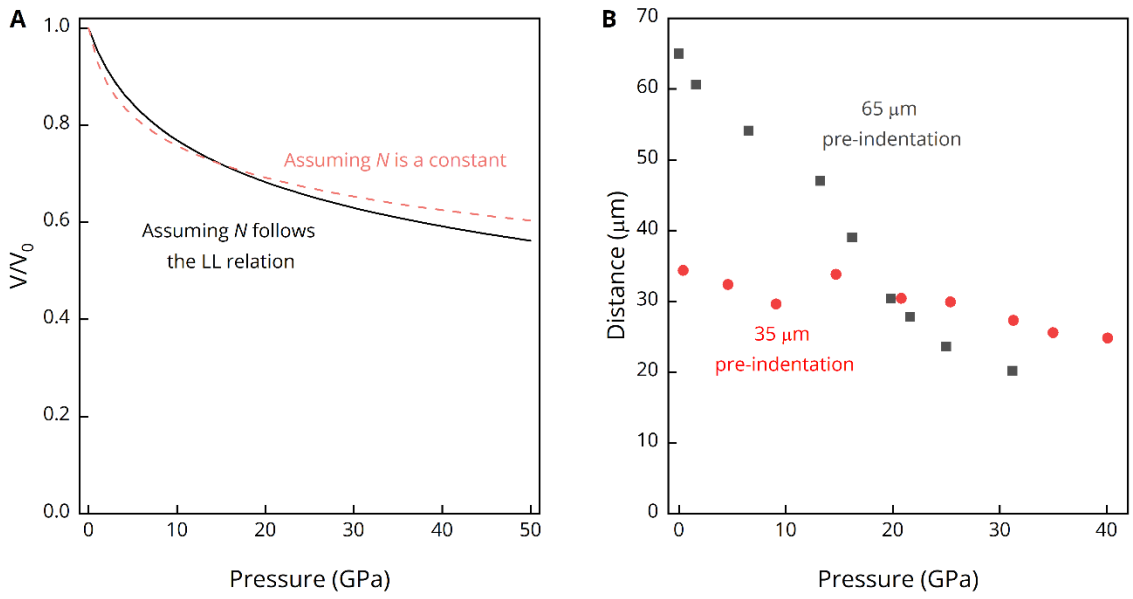

Figure 2.9. Consideration of the sample chamber volume in diamond anvil cells with silicone oil as the pressure medium.

(A) Equation of states of silicone oil derived from its Brillouin frequencies at high pressure. The solid line is the derived EOS assuming the refractive index *N* of silicone oil follows the LL relation. The dashed line assumes *N* is a constant under pressure. (B) The estimated distance between two diamond anvils in the cases of 65 μm pre-indentation (Figure 2.7) and 35 μm pre-indentation (Figure 2.8). The area *vs.* pressure data are from Figure 2.7 and 2.8.

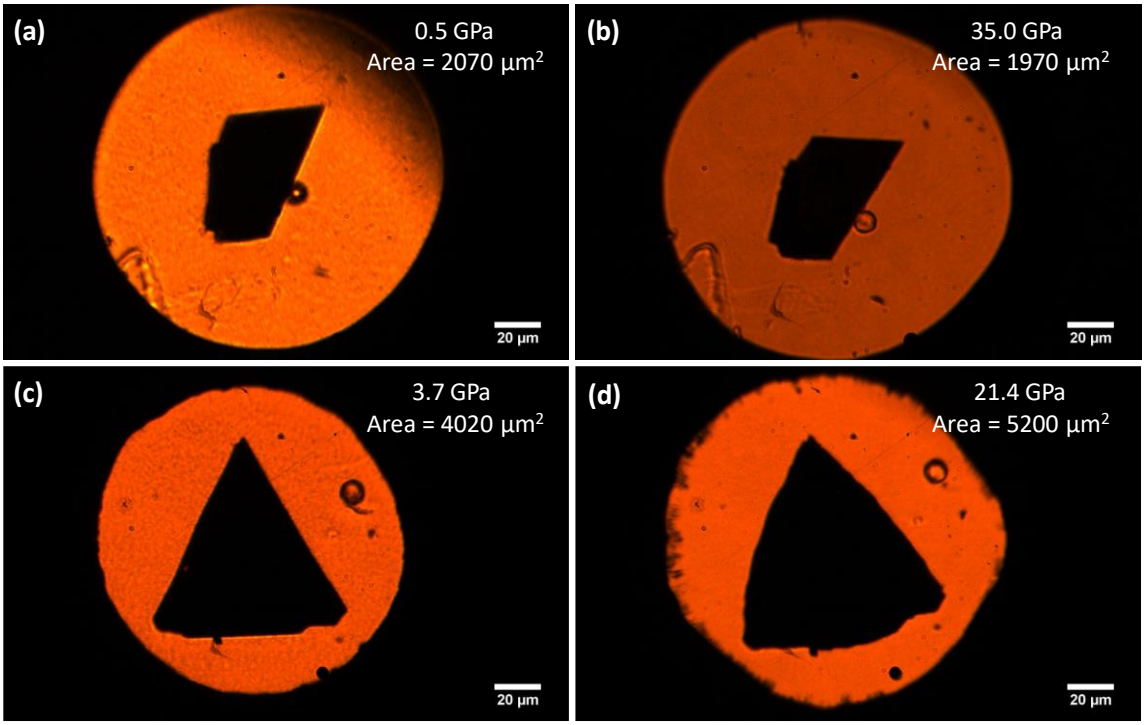

Figure 2.10. Illustration of the occurrence of plastic deformation in samples inside a DAC.

(a) and (b) show a sample that did not experience significant plastic deformation upon compression. The pre-indentation thickness of the gasket is ~30 μm and the sample thickness is ~7 μm. (c) and (d) show a sample that exhibits significant plastic deformation upon compression. The pre-indentation thickness of the gasket is ~65 μm and the sample thickness is ~20 μm. In my measurements, the data is discarded when the hole area and/or sample area increases.

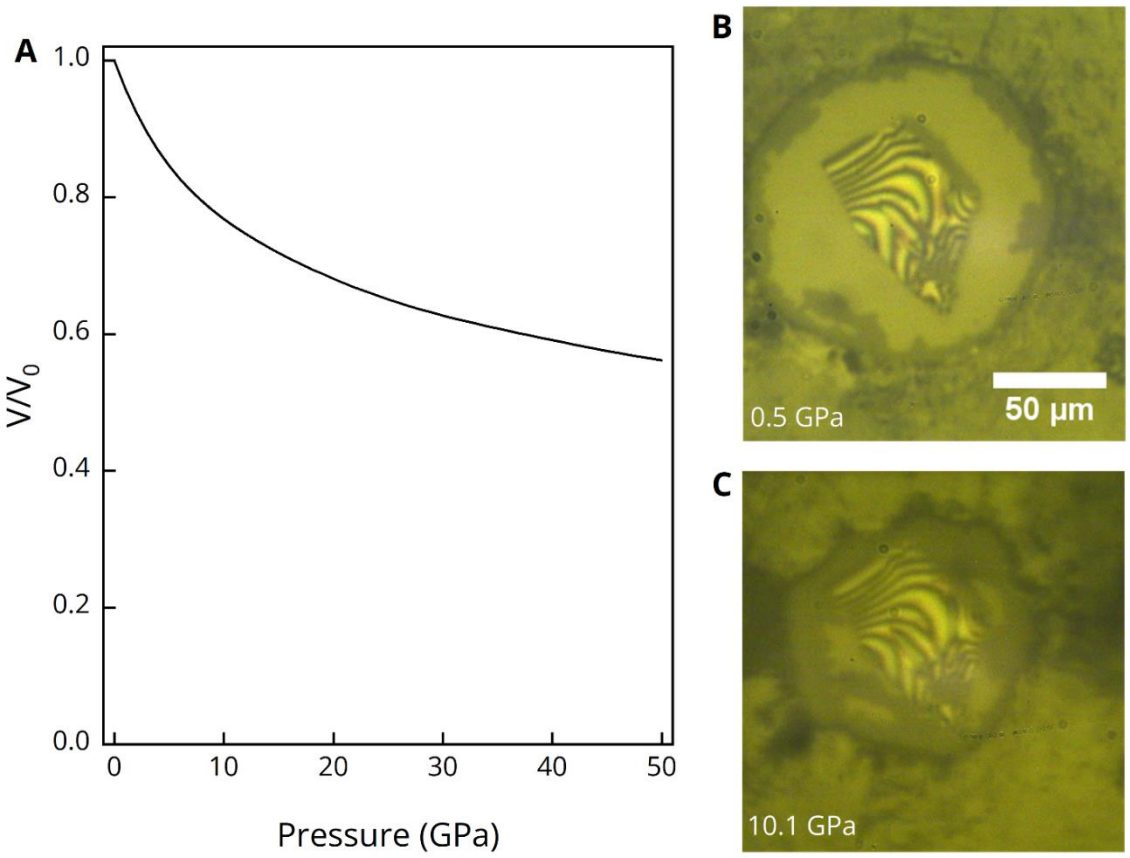

Figure 2.11. Change in area of the DAC hole at high pressure with Ne pressure medium. (A) Equation of states of Ne from Ref. [38]. (B) and (C) are images of a WSe_2 sample loaded in a diamond anvil cell with Ne as the pressure medium at 0.5 and 10.1 GPa, respectively. The pre-indentation is ~30 μm. In contrast to Figure 2.8, the hole shrinks significantly as pressure increases when using gaseous medium.

Table 2.1 Pressure maximum for different culet diameters of diamond anvils suggested by Almax easyLab.

Culet diameter (μm)	Pressure maximum (GPa)
800	≈ 20
700	≈ 30
500	≈ 40
400	≈ 60
300	≈ 80
200	≈ 100
150	≈ 150

2.4 Some notes for high-pressure TDTR

In this section, I discuss some of the concerns and experiences encountered during high-pressure TDTR experiments.

Spot size measurements in DACs.

One concern was whether the spot size conversion factor we calibrated in the air remains consistent as the laser passes through diamond anvils, ensuring the reliability of the spot size measured inside a DAC. We use the beam offset method to measure the laser spot size [39,40]. The pump beam displacement on the sample is $\Delta d = f_{obj}\Delta\theta$, where f_{obj} is the focal length of the objective lens, and $\Delta\theta$ is the angle change of the incident laser beam at the back-focal plane of the objective lens. We tune $\Delta\theta$ by tuning a mirror by actuators in horizontal (Δx) and vertical (Δy) directions [41]. $\Delta\theta_x = X_c\Delta x$ and $\Delta\theta_y = Y_c\Delta y$, where X_c and Y_c are conversion factors. On one hand, diamond has a high index of refraction ($N = 2.4$) at 783 nm laser wavelength, which may have a lensing effect on laser beams. On the other hand, the size of the diamond anvil is small (~2 mm), so the lensing effect of diamond anvils should be small. To make sure the X_c and Y_c calibrated in the air are the same, I measured the distance between two parallel lines in the air *vs.* through a diamond anvil, and got consistent values, see Figure 2.12. Therefore, X_c and Y_c remain the same as the ones calibrated in the air, and the spot size measured in a DAC is reliable.

Selection of transducers for high-pressure TDTR.

Another concern in high-pressure TDTR is the choice of transducer. Aluminum is a good transducer for ambient conditions and temperature-dependent TDTR measurements. However, the reflectance signal collected on Al drops significantly at high pressure due to the decrease of its thermoreflectance (dR/dT) [14,42]. This makes Al not an ideal transducer for high-pressure

TDTR. To find a better transducer, I did TDTR on samples coated with Ta, Pt, and Au at high pressure (Figure 2.13). All of these metals displayed relatively constant V_{in} signals at high pressure compared to Al. However, each has specific constraints. Ta requires high-temperature deposition (> 700 K) to obtain the α-phase [43], which has higher thermoreflectance than the β-phase Ta that results from room temperature deposition [44]. Ta may not be suitable for samples that cannot tolerate high temperatures. Au has a very low absorption (0.026) at 783 nm laser wavelength [45], and the observed reflectance signal is too small to measure, especially for high-thermal-conductivity materials whose V_{out} signals are small. Pt is stiffer than most semiconductors [32,46,47]. When Pt is coated on samples that are more compressible than Pt, it appears to buckle at high pressure, see Figure 2.14A. This is likely due to the fact BAs shrinks faster than Pt upon compression [32,47], and the Pt thin film cannot adhere well to the BAs substrate. As a result, at 2.6 GPa, the Pt film buckles, and the laser beam is distorted by the buckled transducer (Figure 2.14A). In comparison, when Pt is coated on samples that are less compressible, *e.g.*, diamond, the issue mentioned above will not happen, see Figure 2.14B.

The choice of transducer not only needs to consider the strength of the reflectance signal, but also to account for the match between the metal transducer and the substrate. For reflectance signal, we need to consider the product of absorption $(1 - R)$ and thermoreflectance (dR/dT) of the transducer. To match the transducer and the substrate, we need to choose a transducer that has a similar or smaller bulk modulus compared to the substrate. I emphasize that "match" means the transducer is not stiffer than the substrate. As long as the transducer is softer than the substrate, it should work. As mentioned above, if the substrate shrinks faster than the transducer at high pressure, the transducer will buckle upon compression. Since what we care about is the volume change under pressure, it is equivalent to consider the bulk modulus which is related to the first derivative of EOS. Figure 2.15A shows the $(1 - R) \times |dR/dT|$ *vs.* bulk modulus for different

metal transducers, and it can be used to find appropriate transducers for high-pressure TDTR. Most nonmetallic materials have an equation of state similar to Ta (Figure 2.15B), so V, Nb, Ni, Au, and Pd are good candidates for most nonmetallic materials in terms of EOS. Al is softer than most nonmetallic materials. Therefore, although its thermoreflectance is small at high pressure, Al is still a relatively good candidate for most nonmetallic materials since it will not buckle.

V and Nb are ideal transducers in terms of mechanical and optical properties. However, the measured thermal conductivity of silicon control samples coated with a single layer V or Nb is only around 90 W m^{-1} K^{-1}. This value is significantly lower than the accepted thermal conductivity of Si, which is approximately 140 W m^{-1} K^{-1}. The problem may stem from the low quality of the sputtered V (or Nb) thin films, evident from the high resistance (4.4 ohm for a 43.5 nm V thin film) measured by the four-point probe method. To solve this problem, I attempted to make a V/Al bilayer transducer, and tested it on Si, see Figure 2.16 and Table 2.2. The sample geometry comprises a 40 nm V layer, 30 – 50 nm Al layer, and Si substrate. I made three V/Al/Si bilayer samples with $h_V : h_{Al}$ ratio being 40:30, 40:40, and 40:50. The fitted thermal conductivity of Si for the three samples is 130 – 135 W m^{-1} K^{-1}. I summarize properties of interest of the bilayer samples in Table 2.2. The ambient longitudinal speed of sound of Al and V are 6.42 and 6 nm/ps, respectively. The ambient volumetric heat capacity of Al and V are 2.42 and 2.99 J cm^{-3} K^{-1}, respectively. The addition of an Al seed layer doubled the V_{in} compared to a single-layer V film, and, most importantly, led to a more reasonable fitted thermal conductivity of Si.

To test the performance of V/Al bilayer transducer at high pressure, I prepared a 40 nm V/50 nm Al/BAs sample and performed TDTR up to 30 GPa. The V_{in} signal increased upon compression and remained high up to 30 GPa, see Figure 2.13. At ambient conditions, the fitted thermal conductivity of BAs is ~ 1200 W m^{-1} K^{-1} from the V/Al/BAs sample, consistent with the value I

obtained from Al/BAs samples. Both the V/Al/BAs sample and Al/BAs sample are from the same BAs large piece.

Does pressure medium introduce artifacts in TDTR signals?

Another concern is whether the dn/dT of pressure medium introduces artifacts in the data. Since the pressure medium is in contact with the transducer surface, the reflected probe beam might be affected by its dn/dT. To investigate the impact of the pressure medium's dn/dT on experimental signals, I did two TDTR scans on a diamond sample coated with an 80-nm Ta film on its top surface, with silicone oil as the pressure medium (Figure 2.17). In one scan, the pump and probe beams were incident from the side of the silicone oil. In the other scan, the beams were incident from the side of the diamond substrate. The ratio signals at $t > 300$ ps of the two scans look the same. This indicates that the dn/dT of the silicone oil does not introduce artifacts in the fitted thermal conductivity. Additionally, I repeated the same measurements on an Al/diamond sample at 18 GPa (Figure 2.18). Another evidence is that our measurements on Al/MgO with laser incident from silicone oil agree with previous measurements [48] with laser incident from MgO (Figure 2.19).

Correct procedures to achieve 50 GPa.

TDTR requires an optically smooth surface. However, preparing samples for measurement in a DAC involves many procedures that can affect surface quality. For example, we need sample thickness to be as thin as ~10 μm, and mechanically polish the sample to accomplish this. Initially, I coated the sample with transducer, polished the coated sample to ~10 μm, and then broke it into small pieces. However, this procedure usually leads to an unsmooth surface. In response, I attempted an alternative approach: I first polished the substrate, broke it into small pieces, selected pieces with smooth and clean surface, and then coated them with a transducer.

This revised method yielded a cleaner surface. Note that once the sample size is smaller than $100 \times 100 \times 20$ μm^3, it can securely adhere to flat surfaces like glass slides and Si wafers through electrostatic forces. Consequently, when sputtering transducers to these small samples, adhesive is unnecessary. I conducted tests to confirm that these small samples remain in place even during procedures like plasma etching and sputtering at 850˚C.

Reaching 25 GPa in DAC-assisted TDTR is easy but obtaining 50 GPa is hard. This is why most high pressure thermal conductivity studies only go up to ~25 GPa [6]. Based on my experience, achieving a pressure of 50 GPa requires the following cautions:

1) The size of the diamond anvils should be $\leq$ 300 μm.
2) The pre-indentation should be less than 35 μm.
3) It is better if the sample thickness is less than 10 μm. 15 μm might work.
4) The lateral size of sample should be less than half of the DAC hole diameter.
5) For DACs with 300 μm culets, the highest pressure is 55 GPa. Exceeding 55 GPa may break the diamond anvils.

Meeting these requirements is a prerequisite for reaching 50 GPa, although it does not guarantee success. For example, if the sample contains dislocations, it may fracture under high pressure as dislocations propagate. Operating a DAC is akin to performing surgery: the more you practice, the greater your chances of success. Loading your first sample into the chamber is often the most challenging step. However, once you've accomplished it, your subsequent attempts tend to improve.

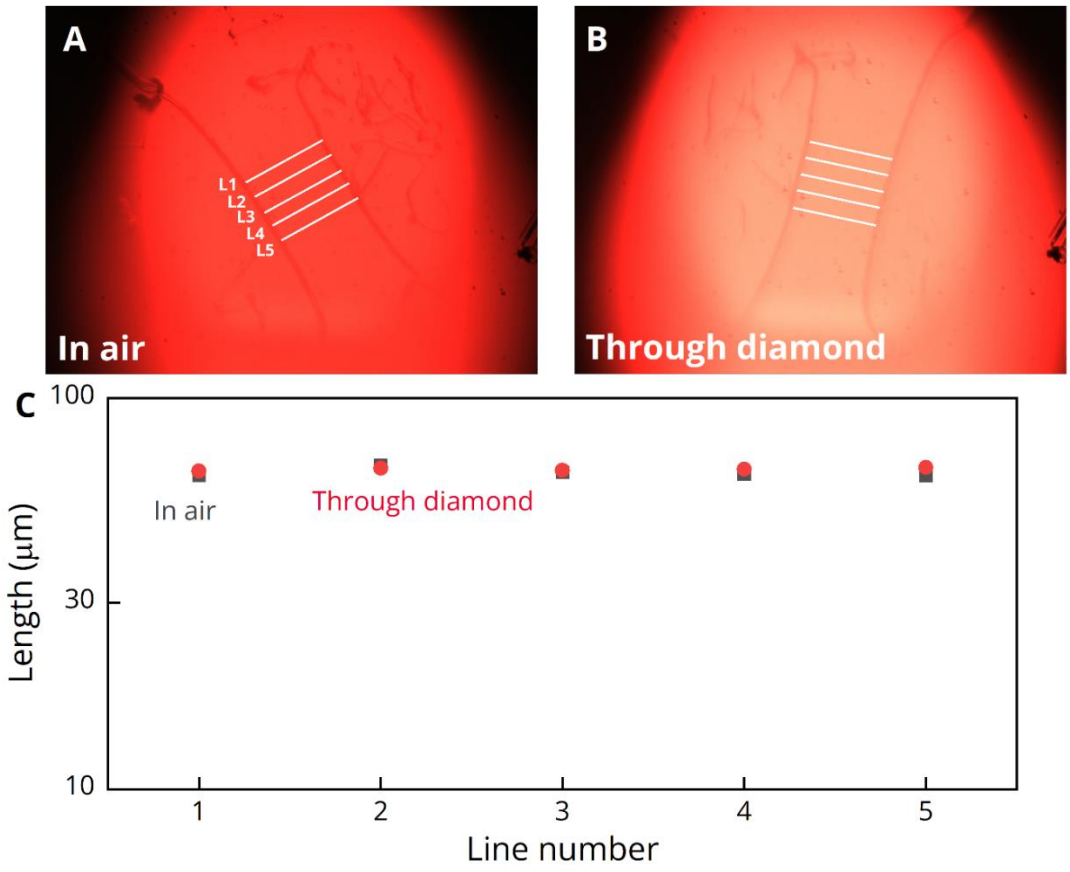

Figure 2.12. Laser beam spot-size measurements in a diamond anvil cell.

(A) An optical image of two scratches on a diamond surface taken in air. (B) An optical image of two scratches on a diamond surface with light going through the diamond. (C) Measured lengths of the 5 lines drawn in (A) and (B). The consistent results suggest that the conversion factor for measuring laser spot size is not affected by diamond anvils.

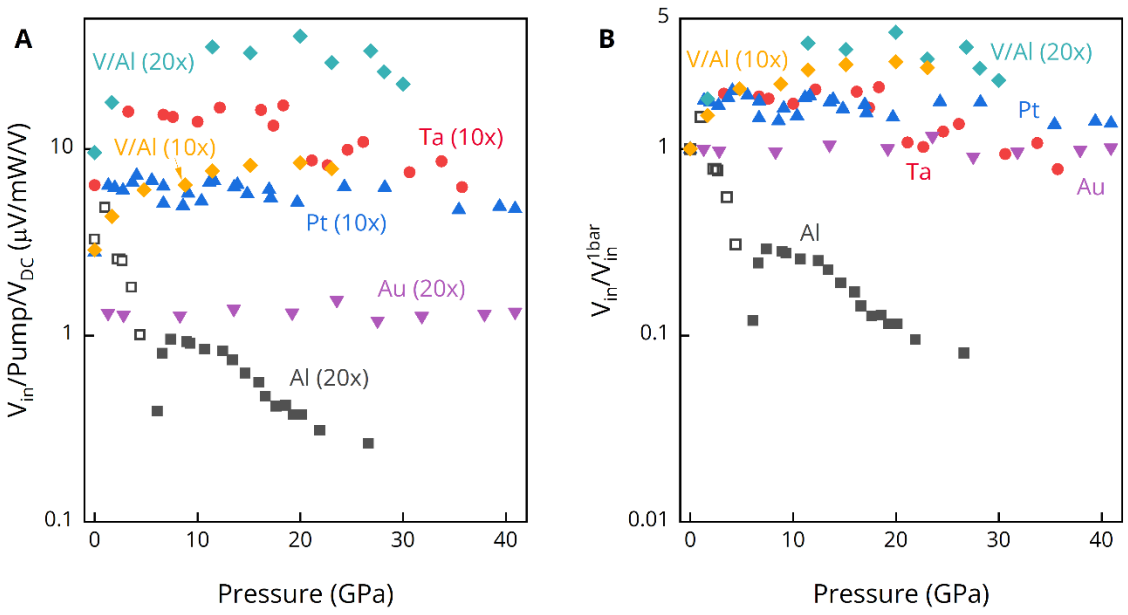

Figure 2.13. Variations of in-phase signal versus pressure for five different transducers.

(A) The in-phase raw data is normalized by pump power and the voltage on the photodiode detector. Al (gray squares), Au (purple triangles), and V/Al (green diamonds) were measured with a 20× objective lens (spot size ≈ 5 μm). Pt (blue triangles), Ta (red dots), and V/Al (yellow diamonds) were measured with a 10× objective lens (spot size ≈ 10 μm). (B) The relative in-phase signal variation compared to the ambient-condition V_{in}. Open and filled markers are used to distinguish that Al changes the sign in the V_{in} signal at ~ 6 GPa. Data of Al, Au, Pt, Ta, and V/Al were collected on an Al/BAs, Au/GaN, Pt/diamond, Ta/$SrTiO_3$, and V/Al/BAs sample, respectively. The two sets of V/Al data were obtained on the same sample with different spot sizes.

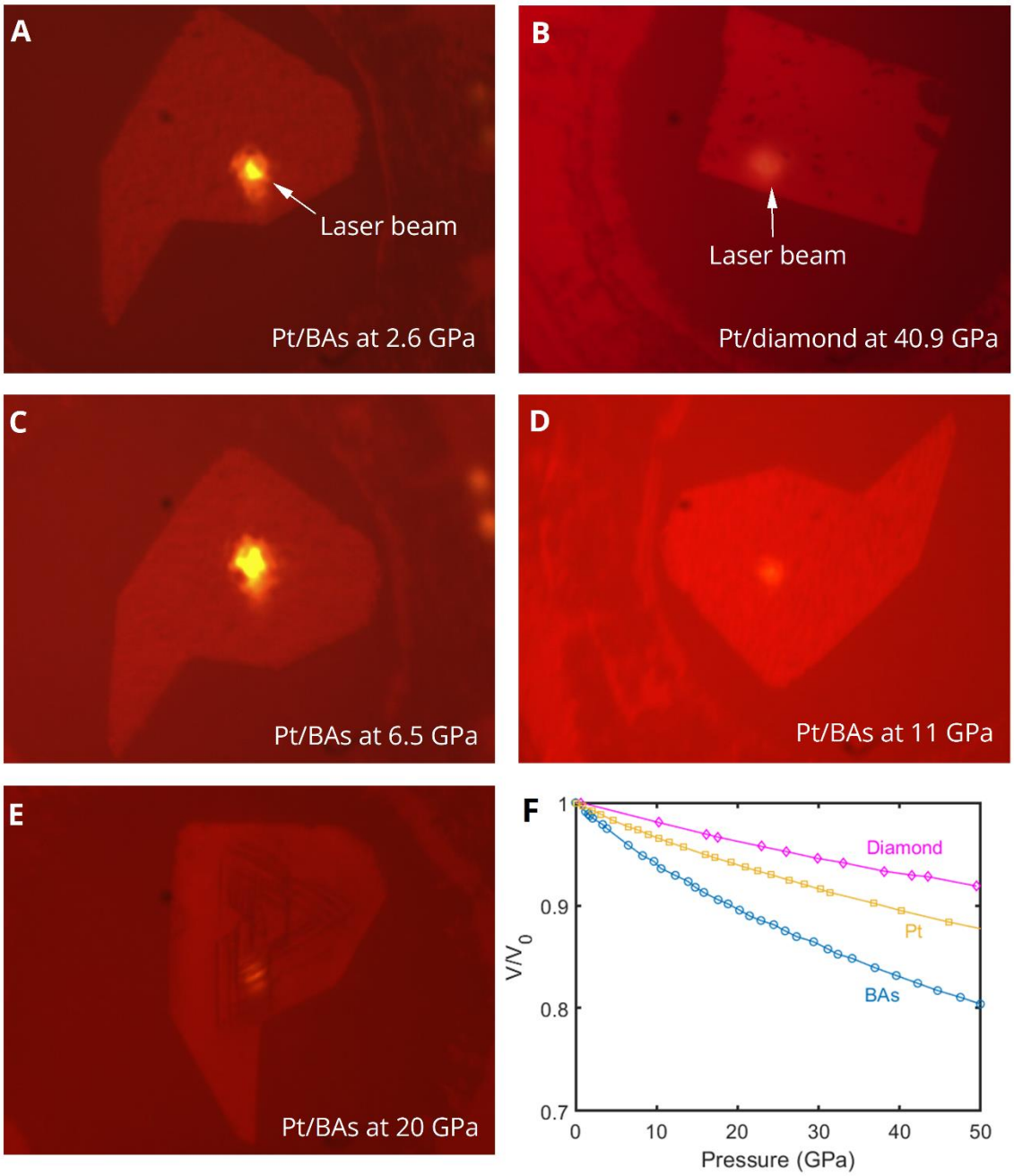

Figure 2.14. Illustration of the issue of incompatibility between transducer and substrate.

(A) A Pt/BAs sample at 2.6 GPa in a DAC. The laser beam appears distorted due to the buckling of Pt. (B) A Pt/diamond sample at 40.9 GPa. (C) – (E) show the images of Pt/BAs at 6.5, 11, and 20 GPa. (F) EOS of diamond, Pt, and BAs. The Pt/BAs surface looks better as pressure increases. The reason may be that the modulus mismatch between Pt and BAs becomes smaller as pressure increases, as shown by the gradient of their EOS.

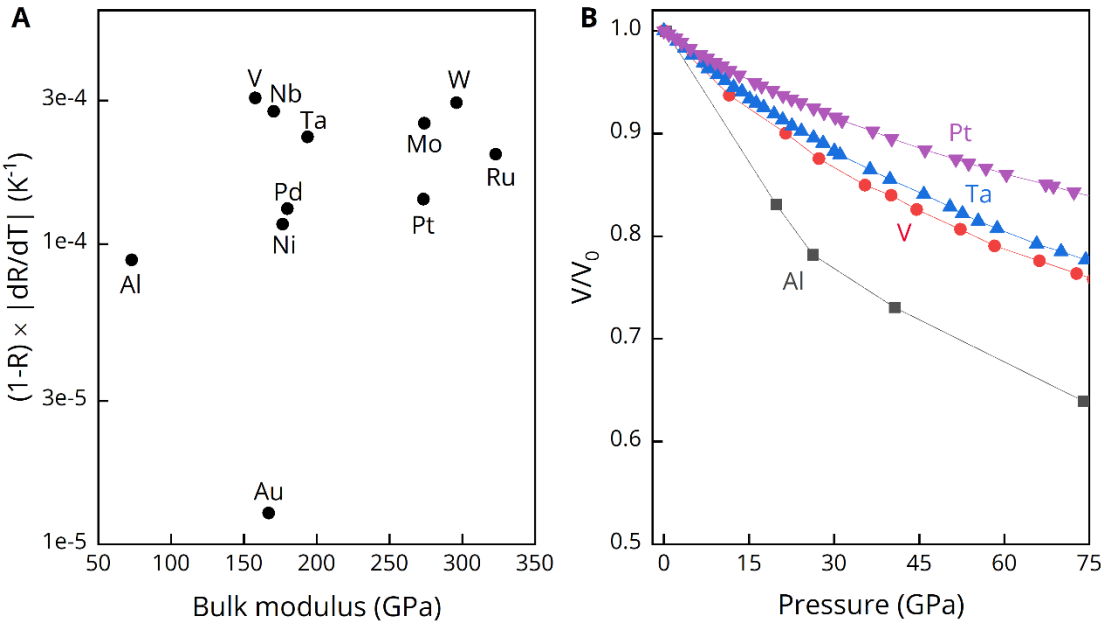

Figure 2.15. A summary of the mechanical and thermo-optic properties of various transducers.

(A) The product of absorption and thermoreflectance versus bulk modulus at ambient conditions for metal transducers. (B) Equations of states of Al, V, Ta, and Pt. Thermoreflectance and absorption data are from Ref. [45]. Bulk modulus data and EOS are from Ref. [16,17,25,32,49–53].

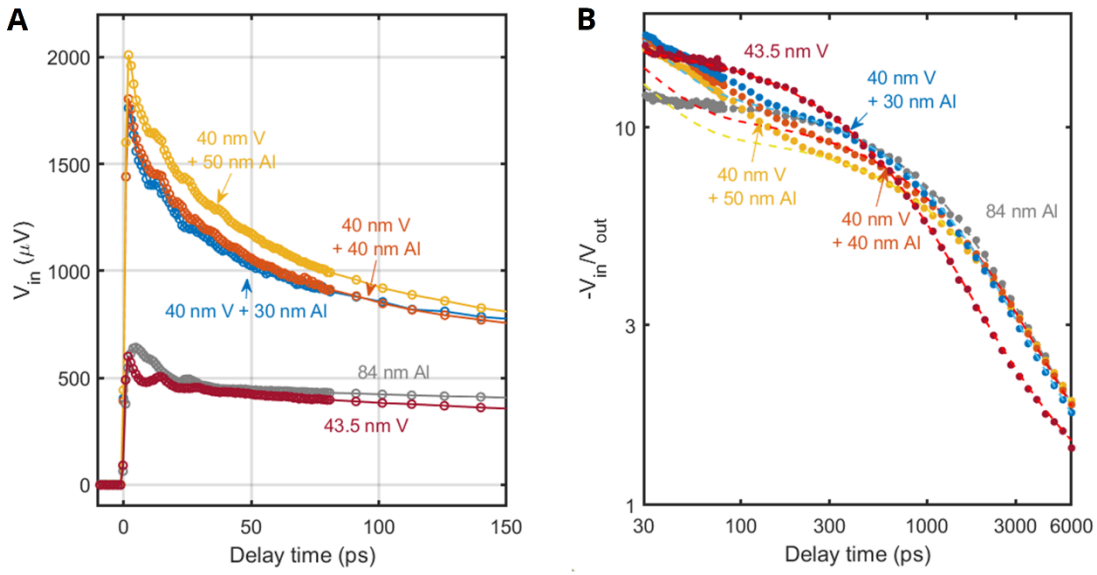

Figure 2.16. TDTR on Si samples coated with V/Al bilayer transducers.

(A) V_{in} versus delay time for Si samples coated with V/Al bilayer transducers. I used a Si sample coated with 84 nm Al and one coated with 43.5 nm V as control samples. (B) $-V_{in}/V_{out}$ versus delay time for the samples. Dashed lines are fittings of heat diffusion to the TDTR data of corresponding color. The fitted thermal conductivity and interface conductance are shown in Table 2.2. All the samples are measured with 21 mW pump power, 4.7 mW probe power, and 10.3 μm spot size.

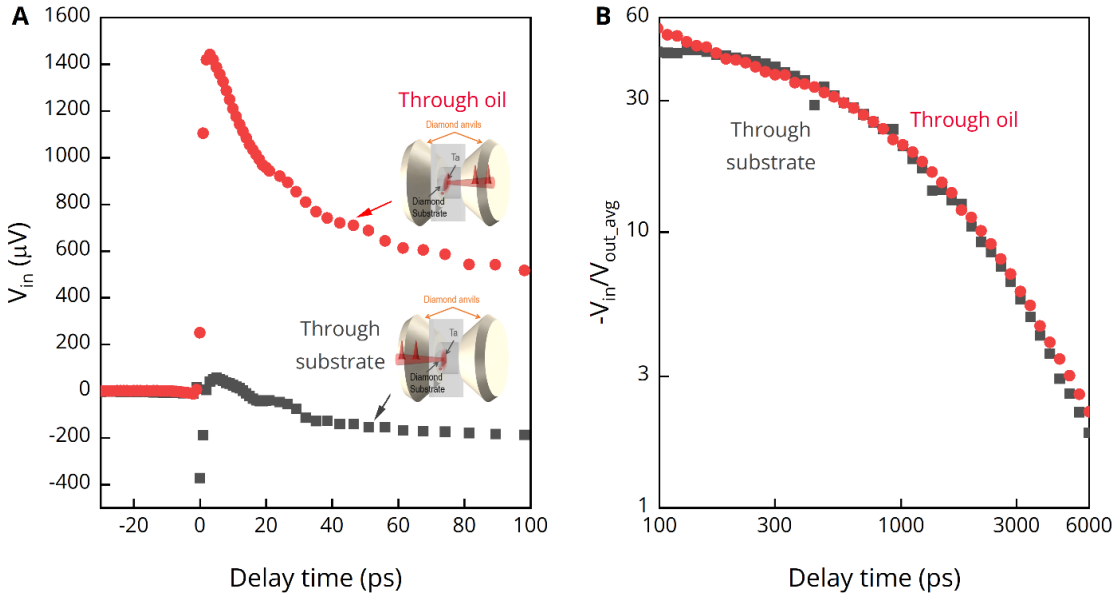

Figure 2.17. High-pressure TDTR data on a Ta/diamond sample with laser incident from the pressure medium versus from the substrate.

The data were collected on a diamond sample coated with an 80-nm Ta thin film on top at 31 GPa, with silicone oil as the pressure medium. (A) and (B) show the V_{in} and $-V_{in}/V_{out\_avg}$ signals of the two scans, respectively. V_{out_avg} is the average out-of-phase signal at negative delay time. The pump and probe power for these two scans are 31 mW and 11 mW, respectively. The laser spot size is ~ 10.5 μm.

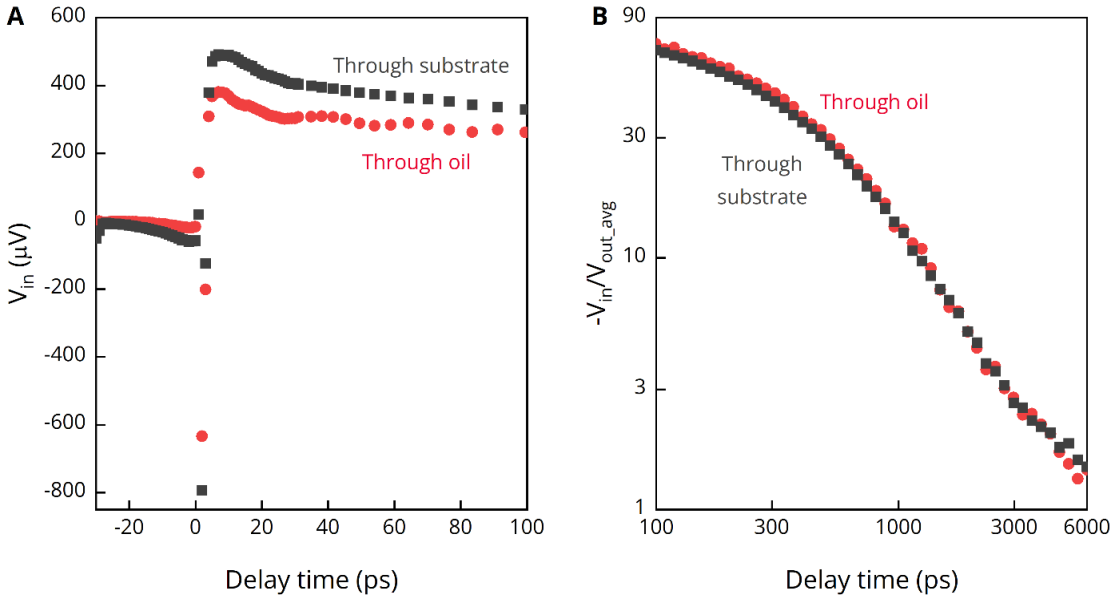

Figure 2.18. High-pressure TDTR data on an Al/diamond sample with laser incident from pressure medium versus from substrate.

The data were collected on a diamond sample coated with an 80-nm Al thin film on top at 18 GPa, with silicone oil as the pressure medium. (A) and (B) show the V_{in} and $-V_{in}/V_{out\_avg}$ signals of the two scans, respectively. V_{out_avg} is the average out-of-phase signal at negative delay time. The pump and probe power for these two scans are 30 mW and 7 mW, respectively. The laser spot size is ~10.5 μm. Figure 2.17 and 2.18 indicate the thermo-optic coefficient of pressure medium does not introduce artifacts in the TDTR signals.

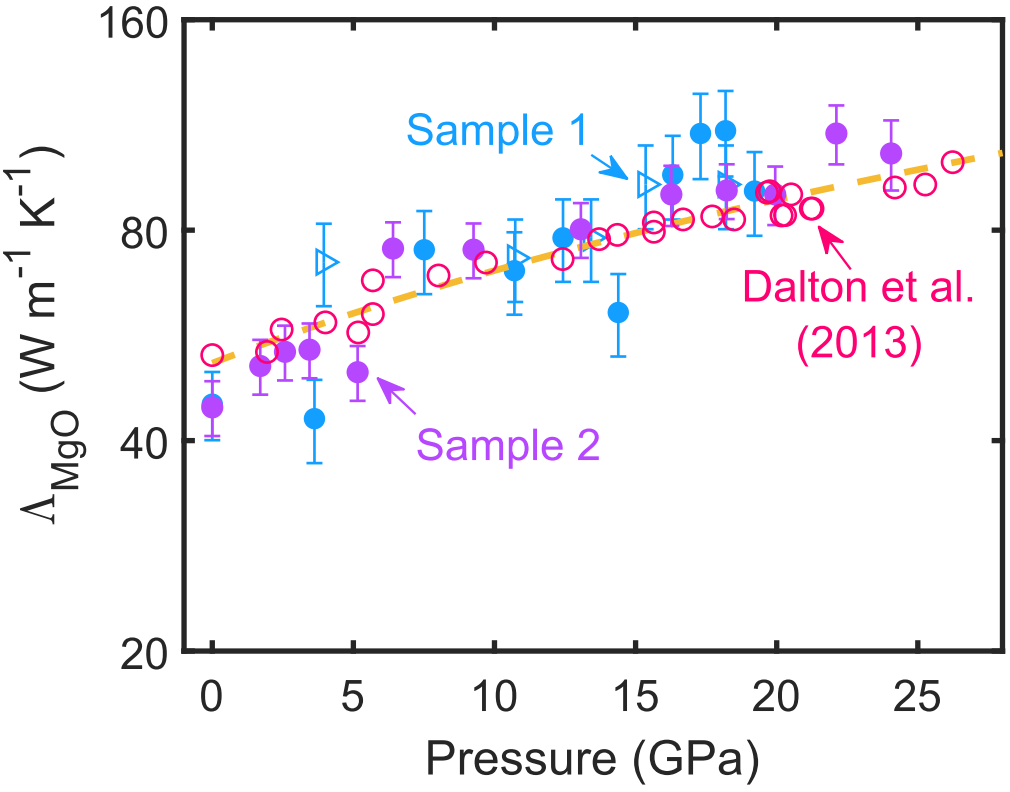

Figure 2.19. Thermal conductivity of MgO versus pressure.

We measured two Al/MgO samples (sample 1 and sample 2) with laser incident from the side of pressure medium. Our data are shown as blue and purple markers. In comparison, Dalton *et al.* [48] measured Al/MgO from the side of MgO. Our data are consistent with their data, indicating that the thermo-optic coefficient of pressure medium does not introduce artifacts in the TDTR signals.

Table 2.2. Properties of V/Al bilayer transducers.

Properties of interests include the thickness of vanadium (h_V), the thickness of Al (h_{Al}), the thermal conductivity of the whole transducer (Λ_{metal}), best-fit thermal conductivity of Si (Λ_{Si}), best-fit of interface conductance between transducer and Si substrate (G).

Sample	h_V (nm)	h_{Al} (nm)	Λ_{metal} (W m^{-1} K^{-1})	Fitted Λ_{Si} (W m^{-1} K^{-1})	Fitted G (W m^{-2} K^{-1})
Al/Si	0	84	170	145	150
40V/30Al/Si	40	30	60	130	170
40V/40Al/Si	40	40	90	135	160
40V/50Al/Si	40	50	110	135	160
V/Si	43.5	0	13	93	270

Chapter 3 Spin-Phonon Interactions Induced Anomalous Thermal Conductivity in NiO

Chapter 3 was published in "Spin-Phonon Interactions Induced Anomalous Thermal Conductivity in Nickel (II) Oxide." Qiyang Sun, Songrui Hou, Bin Wei, Yaokun Su, Victor Ortiz, Bo Sun, Jiao Y. Y. Lin, Hillary Smith, Sergey Danilkin, Douglas L. Abernathy, Richard Wilson, and Chen Li, *Materials Today Physics* 35: 101094 (2023).

3.1 Introduction

Thermal transports in magnetic insulators are predominantly governed by lattice dynamics, spin dynamics, and mutual interactions between them. Phonons and magnons are quantized energy carriers that correspond to lattice and spin degrees of freedom. Their contributions to thermal conductivity vary in different systems. Phonons usually carry most of the heat in magnetic insulators. Magnons also affect the thermal transport of magnetic insulators through two mechanisms. First, in some insulators, the amount of heat carried by magnons is comparable to that of phonons at low temperatures [54–58]. Second, spin-phonon interactions affect phonon energies and mean free paths, thus the transport of phonons [59,60]. Although thermal conductivity governed by phonon-phonon scattering can be understood by the theory of lattice anharmonicity [61], the effects of magnon and spin-phonon interactions are less well understood [62]. The majority of existing work focused on tuning thermal conductivity by an external magnetic field at low temperatures, where thermal transport is not dominated by phonons. It was observed that with increasing external magnetic field, the magnon-phonon interaction is weakened, and the thermal conductivity is enhanced in ferromagnetic, ferrimagnetic

and magnetic frustrated materials [63–65]. These observations suggest that spin-phonon interactions suppress thermal transport. However, the thermal conductivity in antiferromagnetic materials has a much weaker field dependence [59], thus the effects from spin-phonon interactions are not extensively explored. There is great potential in engineering thermal transport through such interactions.

Antiferromagnetic (AFM) insulators exhibit characteristics of low damping and robustness against external magnetic perturbations, which make them promising candidate materials for quantum computing devices [66], ultrafast spintronics [67–70], memory devices [71], and spin-caloritronic applications [72,73]. Colinear AFM insulator nickel (II) oxide (NiO) is a prominent candidate for next-generation spintronic and spin-caloritronic applications operating at room temperature because it has high spin transport efficiency [74–77] and high Néel temperature (T_N = 523 K) [78–80], and its magnetic order can be manipulated by ultrafast photoexcitation [81]. Importantly, spin-induced dynamic symmetry breaking and the mutual spin-phonon driving effect have recently been reported in NiO, suggesting the presence of strong spin-phonon interactions [82]. The observed strong spin-phonon interactions may significantly affect phonon transport and motivates the current work.

While there are extensive experimental and theoretical studies on thermal transport in single crystal NiO [83–88], there are no conclusive experimental thermal conductivity data or atomistic models for magnon and phonon transport in the context of spin-phonon interactions. The most cited experimental work was done by F. B. Lewis et al [85]. Although the thermal conductivity was reported to increase with temperature in the

paramagnetic (PM) phase, suggesting strong spin-phonon interactions, the measurement was not conclusive because of possible radiational heat loss [85]. The increase of thermal conductivity in the PM phase is contrary to later measurements done by M. Massot et al [87], who measured the thermal conductivity only in the vicinity of T_N. Moreover, characterizing the magnon and phonon dynamics is pivotal for investigating the effect of spin-phonon interactions. Previous Raman experiments only focused on the temperature dependence of the phonon energy at the zone center [89]. The lack of accurate measurements of thermal conductivity in a wide temperature range, characterizations of temperature-dependent magnon and phonon dynamics off zone centers, and atomistic models for magnon and phonon transport hindered further investigations of thermal transports in this important material. The present work sheds light on these points.

In the current work, we performed inelastic neutron scattering (INS) experiments to characterize magnon and phonon dynamics, time-domain thermoreflectance (TDTR) measurements to measure temperature-dependent thermal conductivity, and atomistic simulations to investigate phonon and magnon transport in the context of spin-phonon interactions in NiO. INS measurements of magnon lifetimes indicate that the magnon thermal conductivity is negligible at all temperatures. TDTR measurements reveal that the thermal conductivity of NiO decreases from ~55 $W/(m \cdot K)$ at 200 K to ~13 $W/(m \cdot K)$ at 500 K. First principles calculations show that this temperature dependence is greater than can be explained with phonon-phonon and phonon-defect scattering (from 53 to 20 $W/(m \cdot K)$ in the same temperature range). INS measurements of temperature-induced phonon energy softening cannot also explain the observed temperature dependence of thermal conductivity. We attribute the difference to spin-phonon interactions.

3.2 Methods

Inelastic Neutron Scattering Experiments.

Time-of-flight INS measurements were performed on single-crystal NiO with Wide Angular-Range Chopper Spectrometer (ARCS) at the Spallation Neutron Source at Oak Ridge National Laboratory. Incident energy of 150 meV was used for measurements under 10, 300, 540 and 640 K. The sample was loaded with Al foil and placed in a low-background electrical resistance vacuum furnace with (H,H,0) plane horizontal. Data reduction was performed with MANTID [90]. The INS data were normalized by the proton current on the target and corrected for detector efficiency using a vanadium scan. Since no detectable difference can be found in binning experimental data (10, 300 K) with distorted rhombohedral or FCC lattice coordinates, the slight structure distortion of the AFM phase was neglected, and the FCC crystal structure was used for data analysis. The data was sliced along high symmetry **Q**-directions in reciprocal space to produce two-dimensional energy-momentum views of dispersions.

Time-of-flight INS measurements were also performed on polycrystalline NiO. The sample was loaded in an Al sample can and mounted in a low-background electrical resistance vacuum furnace. The two-dimensional dynamic structure factors $S(|\mathbf{Q}|, E)$ were obtained at T = 50, 280, 450, 540 and 640 K using an incident energy of 50 and 150 meV. INS measurements on an empty Al can were performed at the same temperatures and neutron incident energy. The measured intensity, as the INS background induced by the sample holder, was subtracted from the polycrystalline data. The data have been corrected by multiphonon scattering and thermal occupation using *Getdos*.

Triple-axis INS measurements were performed on the same single-crystal with triple-axis spectrometer TAIPAN at OPAL reactor at ANSTO to map phonon dispersion near the zone

center. Constant **Q** scans near zone centers at (1,1,1), (0,2,2) and (0,0,2), and constant energy scans at 10, 15, and 20 meV along [1,1,1] were performed at 300, 450, and 650 K.

Time-domain Thermoreflectance Measurements.

We performed TDTR measurements on two single-crystal NiO samples between 125 and 675 K. TDTR is a well-established pump probe technique for the characterization of thermal properties [91]. Details of our TDTR setup can be found in Ref. [41]. We mounted the samples in a heater stage (Microptik MHCS600) for temperatures above 300 K and in a cryostat (Janis ST-300MS) below 300 K. We pumped the sample chamber down to ~10^{-5} torr during the experiments. We coated the NiO samples with an ~80 nm Al film. The Al film serves as both a heat absorber and a thermometer. In TDTR measurements, a train of 783-nm-wavelength laser pulses emitted from a mode-locked Ti:sapphire oscillator is split into a pump beam and a probe beam. The pump beam heats the sample at a modulation frequency of 10.7 MHz. The probe beam monitors the temperature decay at the sample surface via temperature-induced changes in the reflectance of the Al film. The reflected probe beam from the Al film is collected by a silicon photodiode detector. A lock-in amplifier reads the microvolt change in voltage output by the detector due to changes in reflected probe beam intensity. The amplifier outputs the in-phase signal V_{in} and the out-of-phase signal V_{out} at the 10.7 MHz modulation frequency. The size of the laser spot in $1/e^2$ radius w_0 = 6.5 μm and is measured by the beam offset method [39]. We controlled the steady-state temperature rise in NiO to be less than 5 K considering its phase transition at 523 K. The steady-state temperature increase in the TDTR measurements is [91]

$$\Delta T_s = \frac{P_i(1-R)}{2\sqrt{\pi}w_0\kappa}, \qquad (3.1)$$

where P_i is the incident laser power, R is the optical reflectivity of Al, and κ is the thermal conductivity of NiO. We make sure $\Delta T_s < 5$ K by controlling the incident pump and probe power.

We analyzed the collected ratio, $-V_{in} / V_{out}$, using a heat diffusion model to extract the thermal conductivity of NiO [91]. The model needs several input parameters, such as laser spot size, modulation frequency, and thermal properties of each layer. We measured the thickness of the Al film by picosecond acoustics [36]. We used experimental results from literature for the heat capacity of Al and NiO at different temperatures [85,92,93]. For the heat capacity of NiO above 630 K, there is no experimental data. Thus, we extrapolate the experimental results in Ref. [85].

INS data folding.

Data folding was used to increase the counting statistics and remove the neutron scattering form factor in the dynamic structure factors $S(\mathbf{Q}, E)$. Data folding was done by summing up the $S(\mathbf{Q}, E)$ data from over 100 BZs into an irreducible wedge in the first Brillouin zone. The offsets of the $\boldsymbol{q}$ grids were corrected by fitting the measured Bragg diffractions. This folding technique has been used in a previous study [94] and has been demonstrated to be reliable.

3.3 Results and Discussion

Time-of-flight INS measurements were performed on single-crystal NiO with ARCS spectrometer at the Spallation Neutron Source. The four-dimensional dynamic structure factors, $S(\mathbf{Q},E)$, were mapped at 10, 300, 540 and 640 K and folded into an irreducible wedge in one Brillouin zone. In Figure 3.1, the folded $S(\mathbf{Q},E)$ shows phonon and magnon dispersions. The spectral intensity of the magnons is weaker than that of the phonons. In Figure 3.1(c), the

measured phonon dispersion shown in the folded S(**Q**,E) is consistent with previous measurements at 300 K [95]. The S(**Q**,E) calculated by the coherent lattice INS at 10 K shows excellent agreement with the measurements (Fig1 a, b). Our DFT calculation predicts the longitudinal optic mode energy of 71.2 meV at the zone center (Γ), matching well with our measurement and previous Raman measurement at 300 K [89]. Two branches of nondispersive INS intensities around 23 and 35 meV overlay with low-lying optical modes (Figure 3.1(b) and (c)). These intensities arise from incoherent INS by nickel atoms, which have a non-trivial incoherent scattering cross section of 5.2 barn. This is confirmed by the coherent one-phonon scattering dynamic structure factor simulation in Figure 3.1(a). Similar incoherent scattering intensities have been observed in CoO [96]. Our INS measurements provide detailed characterizations of magnon and phonon properties and shed light on the calculation of thermal conductivity, as discussed below.

The total thermal conductivity (κ) in NiO can be represented as $\kappa = \kappa_m + \kappa_p$, where κ_m and κ_p are the thermal conductivity by magnon and phonon transports, respectively. In this system, the intrinsic linewidth broadenings of magnons were much smaller than the magnon energy. Magnons would be well defined and can be treated as propagating quasiparticles. In this case, the kinetic theory of thermal transport can be applied to calculate the magnon thermal conductivity [97]. The thermal conductivity along [1,0,0] can be calculated with

$$\kappa_m = \sum_q c_q v_q^2 \tau_q, \qquad (3.2)$$

where c_q, v_q, τ_q are the mode volumetric specific heat (energy density per unit volume), projected group velocity along the [1,0,0] direction and the mode relaxation time of magnon at the grid point q, respectively. The $c_q$takes the form,

$$c_q = \frac{1}{NV}\frac{\partial}{\partial T}\left(\frac{\omega_q}{exp\left(\frac{\omega_q}{k_b T}\right)-1}\right), \qquad (3.3)$$

where N is the total number of grid points in the reciprocal space; V is the volume of the unit cell; ω_q is magnon frequency at grid point q, k_b is the Boltzmann constant and T is the temperature. ω_q, c_q, v_q are obtained from the calculated magnon dispersions, which show great agreement with experimental data at 10 K (Figure 3.9).

The magnon thermal conductivity was obtained based on the lifetime calculated from the magnon linewidth. The magnon linewidths were obtained by fitting experimental and calculated (see SI note 2) one-dimensional dynamic structure factor S(E) slices at $\mathbf{Q}_1$ = (0.5,0.5,3) and $\mathbf{Q}_2$ = (1.75,1.75,1.75). The experimental data were fitted with a convolution of the resolution and the intrinsic lifetime broadening. The resolution function is Gaussian and its linewidth, Γ_G, includes contributions from the instrument energy and **Q** resolution. A Lorentzian function with its half-width half-maximum (HWHM), Γ_L, is used for the intrinsic lifetime broadening. For 10 K, the fitted Γ_L are 1.9$\pm$0.5 and 1.7$\pm$0.8 meV and magnon intrinsic lifetime, $\tau = \frac{1}{2\Gamma_L}$, are 172 and 191 fs at $\mathbf{Q}_1$ and $\mathbf{Q}_2$, respectively. The results on magnon lifetimes are comparable with previous measurements on ultrathin ferromagnetic films using spin-polarized high-resolution electron energy loss spectroscopy [98]. As suggested by Wu et al. [97], magnon lifetimes τ_q scale with ω_q^{-1} in the presence of spin-phonon interactions, hence, τ_q can be approximated by $\tau_q = \tau_0\omega_0/\omega_q$, in which τ_0 and ω_0 are the magnon energy and lifetime at the top of the dispersion. Although NiO has two magnon eigenmodes, they degenerate in a wide span of reciprocal space. The degeneracy is broken only in the vicinity of the magnetic zone center with magnon gaps of 4.3 and 0.6 meV [99,100]. In this case, the effect of the magnon gap on magnon transport was not considered. With specific heat, the projected group velocity and the lifetime obtained at 10 K, κ_m along [1,0,0] direction is calculated to be 0.2, 0.9, 1.3 $W/(m \cdot K)$ at 100, 300, 500 K respectively, as shown in Figure 3.3(d). It should be noted that the temperature dependences of magnon τ_q and

ω_q are not considered in the present calculation and the κ_m should be treated as an upper limit because both τ_q and ω_q decrease with temperature (Figure 3.2). At 300 K, the magnon intrinsic linewidth Γ_L are 5.7±1.0 and 6.4±0.8 meV and magnon intrinsic lifetime, are 58 and 51 fs at $\mathbf{Q}_1$ and $\mathbf{Q}_2$, respectively (Figure 3.2(a) and (b)). At 300 K, the calculated magnon thermal conductivity is around 0.3 $W/(m \cdot K)$ and much less than the upper limit. We estimated the κ_m between 10 to 500 K using temperature-dependent magnon energies and lifetimes, which are obtained from linear fittings of the experimental data at 10 and 300 K. As shown in Figure 3.3(d), the estimated κ_m first increases from 10 to 320 K and gradually decrease above 320 K.

The phonon thermal conductivity (κ_p) was calculated based on 3-phonon scattering with the single mode relaxation time (SMRT) approximation [101]. Phonon-isotope scattering due to the mass variance of isotope distributions was also considered. Phonon-defect scattering due to point defects was estimated by fitting TDTR data below 200 K. The calculated κ_p using SMRT approximation and direct solution of the linearized Boltzmann transport equation (LBTE) shows little difference (Figure 3.4). It should be mentioned that other calculational results of κ_p obtained by direct solution of LBTE with considered phonon-phonon and phonon-isotope scattering have recently been reported [88]. The reported κ_p is around 25 $W/(m \cdot K)$ at 300 K, much lower than our calculation (natural with defect, 31 $W/(m \cdot K)$) and our measurement (30 $W/(m \cdot K)$) shown in Figure 3.3(d). The difference may arise from the different exchange-correlation functionals that were used (LDA in the present work, hybrid-PBE in Ref. [88]) and the difference in phonon dispersion (~7% in the total energy scale). Above 200 K, the calculated κ_p follows T^{-1} (Figure 3.3(d)), which is typical for nonmetallic materials in high-temperature regimes due to phonon-phonon interactions [1].

The calculated thermal conductivity of the phonons is much larger than that of the magnons in the AFM phase (Figure 3.3(d)). The total thermal conductivity is determined mainly by phonon transport. The huge difference between κ_p and κ_m mainly results from the difference in cumulative specific heat, where the specific heat of magnons is about two orders of magnitude lower than that of phonons at 100 K (Figure 3.3(b)). Near and above T_N, magnon lifetimes are expected to decrease drastically due to the loss of long-range spin order, and the thermal conductivity by magnon is also expected to be small.

TDTR measurements were performed on two NiO single crystals labelled NiO (I) and NiO (II). TDTR is a transient method for thermal transport measurements whose experimental signals are proportional to thermal effusivity ($\sqrt{\kappa C}$). The NiO (I) crystal has a flat thermal effusivity below 200 K. Above 200 K, the thermal effusivity decreases with temperature, and a small dip was observed at 523 K. Using values from the literature for the heat capacity versus temperature of NiO [85,93] (Figure 3.5), we calculated the thermal conductivity versus temperature from the experimentally measured thermal effusivities.

The thermal conductivity of NiO (I) in the AFM phase depends strongly on temperature between 200-450 K. κ decreases from 55 $W/(m \cdot K)$ at 200 K to 17 $W/(m \cdot K)$ at 450 K. This corresponds to a temperature dependence of $T^{-1.5}$ (Figure 3.3(c)). At temperatures greater than 550 K in the PM phase, the temperature dependence of the thermal conductivity is weaker. The thermal conductivity decreases with T^{-1} above 550 K. The NiO (II) crystal has lower thermal conductivity with weaker temperature dependence (Figure 3.10) because of a higher defect concentration than NiO (I). κ of NiO (I) in Figure 3.3(c) is more representative of the intrinsic transport properties of NiO.

We now compare our results to prior measurements of κ of NiO. Our data show a trend similar to previous results measured by Zhuze et al. using a pulse technique [84], see Figure 3.3(c). Both measurements show an overall decreasing thermal conductivity with temperature, with a dip around T_N. Although our data are consistent with the results by Lewis et al. [85] below 200 K, the measured thermal conductivity is lower and shows a stronger temperature dependence from 200 to 450 K (Figure 3.3(c)). The discrepancy may be related to radiation heat loss in the steady-state longitudinal method used [85,102], see Figure 3.6. Errors in thermal conductivity caused by heat loss from radiation are known to follow the T^3 dependence [102]. We calculate the difference between our measurements and the steady-state results ($\Delta\kappa$) at 200-500 K and find it to be proportional to T^3 (Figure 3.6).

In Figure 3.3(d), we compare our experimental and theoretical predictions for thermal conductivity. While the calculated κ_p (natural with defect) and the measured κ are in good agreement for T < 300 K, they diverge for T above room temperature. Experimental κ decreases more rapidly with T than theory can explain. The discrepancy between theory and experiment increases as T increases from 300 to T_N = 523 K. Then, at temperatures above T_N, the difference between experimental and theoretical κ stays roughly constant at ~ 25 %. In addition to disagreeing with our theoretical predictions for NiO, we note that a $T^{-1.5}$ dependence for κ is different from other non-magnetic insulators with face-center-cubic crystal structure and similar phonon properties. For example, crystals such as MgO have a κ that is proportional to T^{-1} (Figure 3.7) in the same temperature range. Therefore, we conclude that simple phonon-phonon scattering, or phonon-isotope and phonon-defect scattering, cannot explain the observed temperature dependence of NiO at 200 - 450 K (Figure 3.3(d)). We conclude that there is another temperature-dependent scattering term that affects transport at temperatures above 300 K.

In kinetic theory, temperature effects on phonon transport can be reflected in two parts: changes in phonon energy and lifetime. On one hand, the shift in phonon energy affects thermal capacity (unless the temperature is well above Debye temperature) and group velocity, and thus thermal conductivity. From our INS measurements on polycrystalline NiO, the measured phonon energies monotonically decrease with temperature for both TA and LA modes (Figure 3.11(a) and (b)), and for optical modes (Figure 3.12). The softening of acoustic phonon energy with temperature was also observed via INS measurements on single crystal NiO, as shown in Figure 3.11(c) – (e). With the assumption of isotropic and uniform softening of the phonon modes on heating, the phonon energy for the specific phonon mode i at temperature T can be approximated by $\omega_i(T) = \omega_{0i}(1 - \eta T)$, where ω_{0i} is the phonon energy at 0 K, η is a positive coefficient representing softening of the acoustic phonon mode i and is obtained from linear fittings $\omega = \omega_0(1 - \eta T)$ on the measured phonon energy (Figure 3.11(a) and (b)). The obtained η_{TA} and η_{LA} are 5.6×10^{-5} and $4.5 \times 10^{-5}\ K^{-1}\ meV^{-1}$, respectively. In the long wavelength limit, the group velocity for mode i can be expressed as $v_i = v_{0i}(1 - \eta T)$. The effect of phonon softening on mode thermal conductivity can be shown by

$$\zeta_i(T) = \frac{c_i(T)v_i(T)^2}{(c_i(T)v_i(T)^2)|_{\eta=0}}, \qquad (3.4)$$

$$c_i(T) = \frac{1}{V}\frac{\partial}{\partial T}\frac{\omega_{0i}(1-\eta T)}{exp(\frac{\omega_{0i}(1-\eta T)}{k_b T})-1}. \qquad (3.5)$$

Assuming that the phonon lifetime does not change, the thermal conductivity with temperature-induced acoustic phonon energy shifts was calculated as

$$\kappa_p'(T) = \sum_{qj} \kappa_{p,qj}\, \zeta_{qj}(\eta, T) = \sum_{qj} c_{p,qj} v_{p,qj}^2|_{\eta=0}\, \zeta_{qj}(\eta, T)\tau_{p,qj}, \qquad (3.6)$$

in which $\kappa_{p,qj}$ represents the calculated mode thermal conductivity for specific phonon mode at point q for branch j, and the softening coefficient η was set to be η_{TA} for all acoustic phonon modes. The group velocities (Figure 3.1) and lifetimes (Figure 3.13) of the acoustic phonon modes are much larger than those of the optical modes, and the acoustic phonon modes contribute more than 90% of the total thermal conductivity at 300-700 K (Figure 3.13). In this case, the κ_p' can be approximated by considering only acoustic phonons. As shown in Figure 3.3(d), the κ_p' is not sufficient to explain the $T^{-1.5}$ temperature dependence, although it was underestimated due to the exclusion of optical phonon transport, the approximation of group velocities in long wavelength limit, and the use of a large softening coefficient η for all acoustic modes.

In our discussion above, we have ruled out phonon-isotope scattering, phonon-defect scattering, and phonon softening as explanations for the κ vs. T dependence of NiO. We now turn our attention to spin-phonon interactions that affect phonon lifetime. In magnetic insulators, magnon-phonon scattering (MPS) can also affect phonon transport. According to Matthiessen's rules, the scattering rate for the specific phonon mode i is expressed by

$$\tau_{p,i}^{-1} = \tau_{pp,i}^{-1} + \tau_{pi,i}^{-1} + \tau_{pd,i}^{-1} + \tau_{mp,i}^{-1}, \qquad (3.7)$$

where $\tau_{pp,i}^{-1}$, $\tau_{pi,i}^{-1}$, $\tau_{pd,i}^{-1}$, $\tau_{mp,i}^{-1}$ correspond to the scattering rate for phonon-phonon, phonon-isotope, phonon-defect, and magnon-phonon scattering processes.

Spin-phonon interactions will have two effects on thermal transport. First, MPS ($\tau_{mp,i}^{-1}$) will reduce the phonon lifetimes. The single-mode acoustic phonon scattering rate can be expressed by $\tau_{mp,i}^{-1} = nv_s\sigma$, where n is the density of scatters, v_s is the speed of sound, σ is the scattering cross section [65]. In this simplified MPS model, the temperature dependences of σ can be described by $\sigma = \pi(\lambda(T)/2)^2$ [65] where $\lambda(T)$ is the magnetic correlation length. We

approximate the correlation length from the HWHM ($\Theta_{me}(T)$) of magnetic elastic Bragg peak (Figure 3.14(a)) by $\lambda(T) = 1/\Theta_{me}(T)$. Noting that the $\lambda(T)$ is underestimated due to the instrument resolution in **Q** (~ 0.04 Å). For phonons scattered by magnon mode, $n = \int n_{BE}(E,T) g_m(E) dE$, where n_{BE} is Bose-Einstein statistics, E is magnon energy and $g_m(E)$ is the magnon density of state. With a fixed v_s, the normalized single phonon scattering rates $\tau_{mp,i}^{-1}(T)/\tau_{mp,i}^{-1}(450\ K)$ first increases slowly then dramatically from 0 to 450 K (Figure 3.14(b)). The $\tau_{mp,i}^{-1}$ at 200 K is only 8% of the $\tau_{mp,i}^{-1}$ at 450 K, hence, the magnon-phonon scattering is less important at low temperatures. At 200-450 K, $\tau_{mp,i}^{-1}$ is of a higher order of T and can lead to the observed strong temperature dependence of thermal conductivity. We note that fully quantifying the contribution of MPS to thermal conductivity requires a detailed calculation of the phase space and interaction strength (collision matrix) of MPS. This is beyond the scope of the current work.

Near T_N (450-550 K), the kink in the heat capacity is a measure of the entropy in the lattice and spin system due to the phase transition. Because the measured thermal effusivity shows no kink there, the increase in heat capacity (caused by an increase in disorder through the phase transition) is compensated by a corresponding decrease in thermal conductivity. This suggests that the average phonon lifetime is inversely proportional to the disorder in the spin system. The dip in thermal conductivity is attributed to critical magnetic fluctuation-phonon scattering [67].

The measured thermal conductivity shows a weaker temperature dependence of T^{-1} above T_N. It has been shown that the slight structural distortion from magnetostriction hardly affects the thermal conductivity by phonon transport in NiO [88]. The measured κ is still lower than the calculated κ_p (natural isotope with defects) at 550-700 K, suggesting that the effects from spin-phonon interactions may still be significant above T_N. This is expected because paramagnons (Figure 3.9) and phonon eigenvector renormalizations [82] are observed in this temperature

range. As a result, the effects from magnon-phonon scattering and spin-induced dynamic symmetry breaking do not vanish. Although there is no long-range spin order in this state, a short-range spin order exists and may give rise to the spin-phonon interaction. Suppression of thermal conductivity by spin-phonon interactions was also found previously in other materials in the PM state [63,103].

Generally, one would expect the melting of antiferromagnetic order to do one of two things to magnon-phonon scattering rates above the T_N. Either, magnon-phonon scattering rates would saturate, i.e., stop increasing with temperature because the entropy in the spin system has been maximized. Or, magnon-phonon scattering would vanish due to the lack of antiferromagnetic order. If the magnon-phonon scattering rates saturate, i.e., $\tau_{mp,i}^{-1}$ became temperature independent above T_N, then the above expression for thermal conductivity predicts a T^{-n} dependence with $n < 1$, like is observed in insulating crystals with significant crystalline disorder. Alternatively, if magnon-phonon scattering vanishes due to the lack of spin order, then the thermal conductivity should recover. These seem to contradict the observed temperature dependence. In the present case, we observed the existence of paramagnon above T_N below 640 K (Figure 3.9). This indicates that magnetic entropy is not yet maximized in this temperature range, and strong short-range spin correlations give rise to coherent paramagnons. The paramagnon-phonon scattering may contribute to the suppression of thermal conductivity above T_N.

Another possible mechanism for the observed temperature dependence above T_N is that changes in the antiferromagnetic order lead to changes in phonon-phonon scattering rates. This could occur for several reasons. One possibility is spin-disorder effects

bonding [104], which could lead to an increase in anharmonicity. To explore the effect of spin order on phonon anharmonicity, we calculated the phonon properties with ferromagnetic (FM) spin order to understand the effects of magnetic order. The obtained phonon mode Grüneisen parameters (Figure 3.15) as well as temperature-dependent mode energies (Figure 3.10) show only minor changes compared with those in the AFM state. However, we note that the temperature dependence of the INS measured phonon frequencies is higher near the T_N than what our calculations for NiO in the AFM or FM state predict. Thus, the spin-phonon interaction on the phonon thermal conductivity can be indirect: melting of the spin order causes changes in phonon anharmonicity, which leads to larger phonon-phonon scattering rates in the PM vs. AFM phase.

The TA, LA, TO, LO decrease in energy of 3%, 3%, 5%, 4% from 50 to 640 K, respectively (Figure 3.11(a) and (b) & Figure 3.12(c) and (d)). We calculated the 3-phonon scattering phase space at 0 and 640 K and found that the phonon-phonon scattering phase space changes little (see Figure 3.16). Therefore, temperature-dependent DFT such as molecular dynamics calculations shall not change the results significantly.

3.4 Conclusions

In summary, by performing INS and TDTR thermal conductivity measurements and atomistic thermal conductivity calculations, spin-phonon interactions are identified as the origin of strong temperature dependence of thermal conductivity in the AFM phase. Using the extrapolated magnon lifetime from INS measurements, the magnon thermal conductivity is estimated to be more than one order of magnitude smaller than its phonon counterpart in the temperature range

studied. In the AFM phase, the measured thermal conductivity at 200 ~ 450 K shows a strong temperature dependence of $T^{-1.5}$. We ruled out phonon-isotope scattering, phonon-defect scattering, and phonon softening as the source of the anomalous temperature dependence. The stronger temperature dependence is attributed to magnon-phonon scattering and spin-induced dynamic symmetry breaking. Our results provide a detailed study of thermal transport in this important material, highlighting the pivotal role of spin-phonon interactions in lattice thermal transport. Similar interactions and their effects may play significant roles in thermal transport in other materials where spin and lattice degrees of freedom are strongly coupled. The results shed light on controlling thermal transport through spin-phonon interactions and engineering functional antiferromagnetic spintronics materials through these interactions.

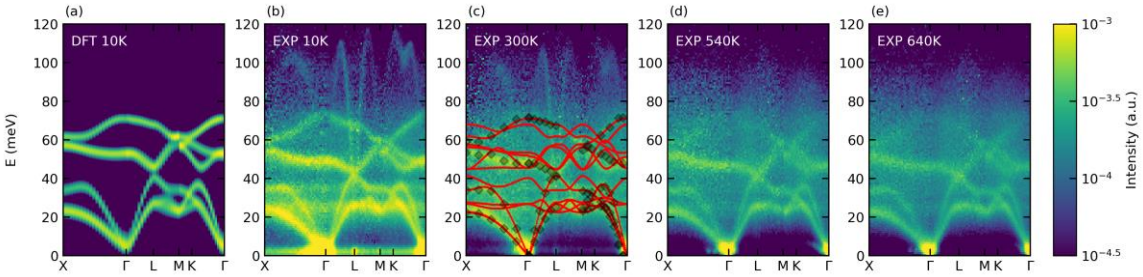

Figure 3.1. Folded spectrums of the experimental and calculated INS dynamic structure factor $S(Q,E)$.

Data folding was done by integrating the intensity of INS over 100 slices, which have data coverages greater than 70%, into an irreducible wedge. (a) Folded coherent one-phonon scattering $S(Q,E)$ simulation at 10 K with the same Q integration configurations as experimental ones. (b-e) Experimental $S(Q,E)$ at 10, 300, 540 and 640 K. Previous phonon dispersion measurements at 300 K [57] and calculated phonon dispersions are plotted in (c) as black dots and red curves, respectively. Thermal occupation corrections were applied to both the calculated and experimental data.

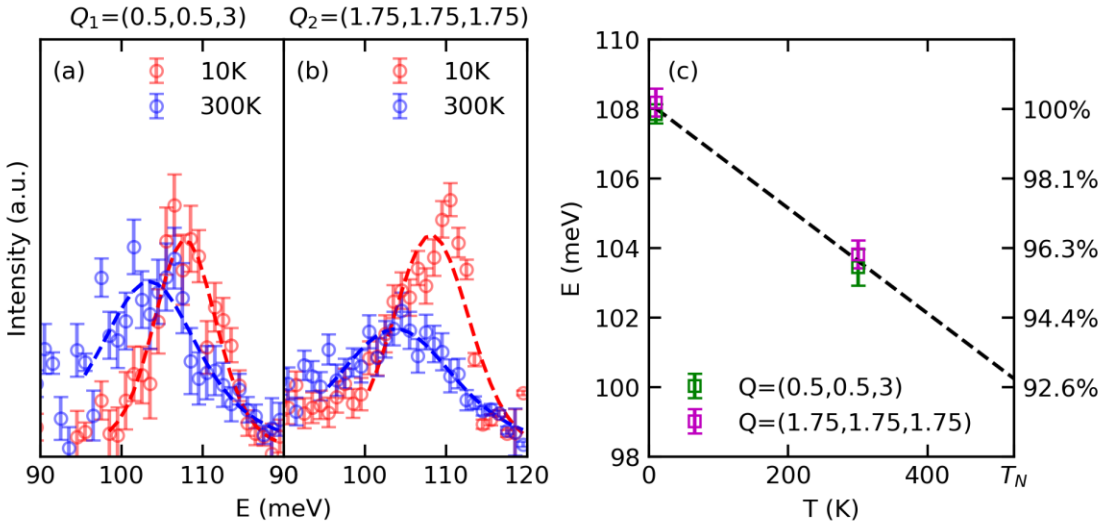

Figure 3.2. Temperature dependence of magnon energy at Q_1 = (0.5,0.5,3) and Q_2 = (1.75,1.75,1.75).

(a) and (b) are fittings of the experimental data at Q_1 and Q_2 with a Q integration range of ± 0.1 (*r.l.u.*). Red and blue circles are experimental data at 10, 300 K, respectively. Error bars denote statistical errors. Dashed lines are the fitting results (see text) by the Voigt function with fixed Gaussian linewidth obtained from the fitting magnon $S(Q, E)$ calculation at 10, 300 K, respectively. The energy of the magnon decreases with temperature. The green and purple squares are centers of the fitted peaks at Q_1 and Q_2, and the error bars denote the fitting errors.

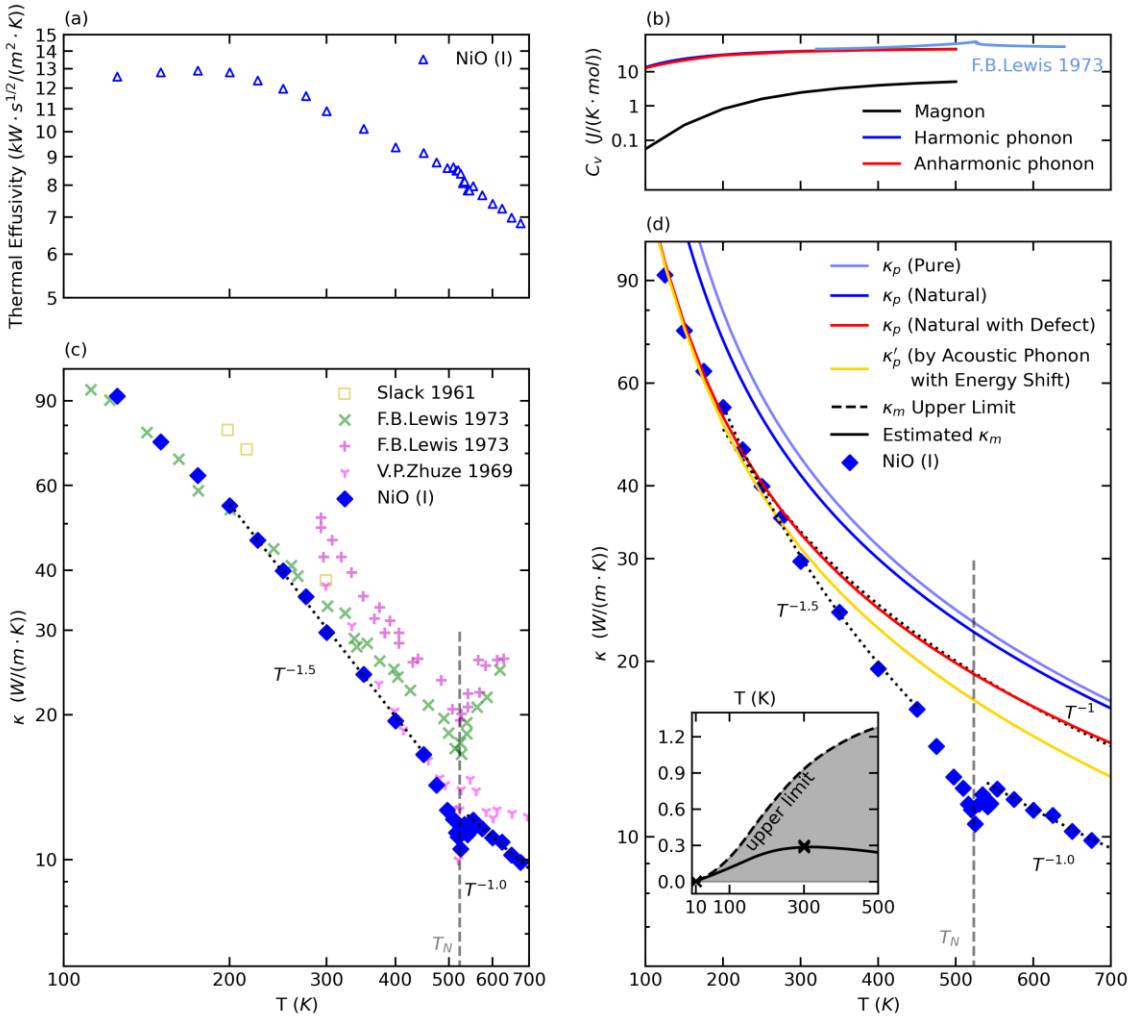

Figure 3.3. Temperature-dependent experimental and calculated thermal properties of NiO.

(a)Thermal effusivity of NiO (I) measured by TDTR. (b) Calculated specific heat of magnons and phonons. The blue (red) curves indicate the calculated specific heat of the harmonic (anharmonic) phonons. The calculated specific heat agrees well with previously measured data around 400 K [85]. The black curve indicates the calculated specific heat of the magnon. (c,d) Experimental and calculated thermal conductivity. The blue squares show the thermal conductivity results for NiO (I) from the TDTR measurement. In panel (c), purple, green, yellow and pink labels show previous thermal conductivity measurements on NiO [83–85]. In panel (d), solid lines of different colors represent calculations considering different scattering processes. We fit our experimental data by power functions as indicated by the black dotted lines. In the inset, the black dashed curve indicates the calculated upper limit of κ_m and the solid curve shows the estimated κ_m from temperature-dependent magnon energies and lifetimes. The black cross labels indicate κ_m calculated at 10 K and 300 K.

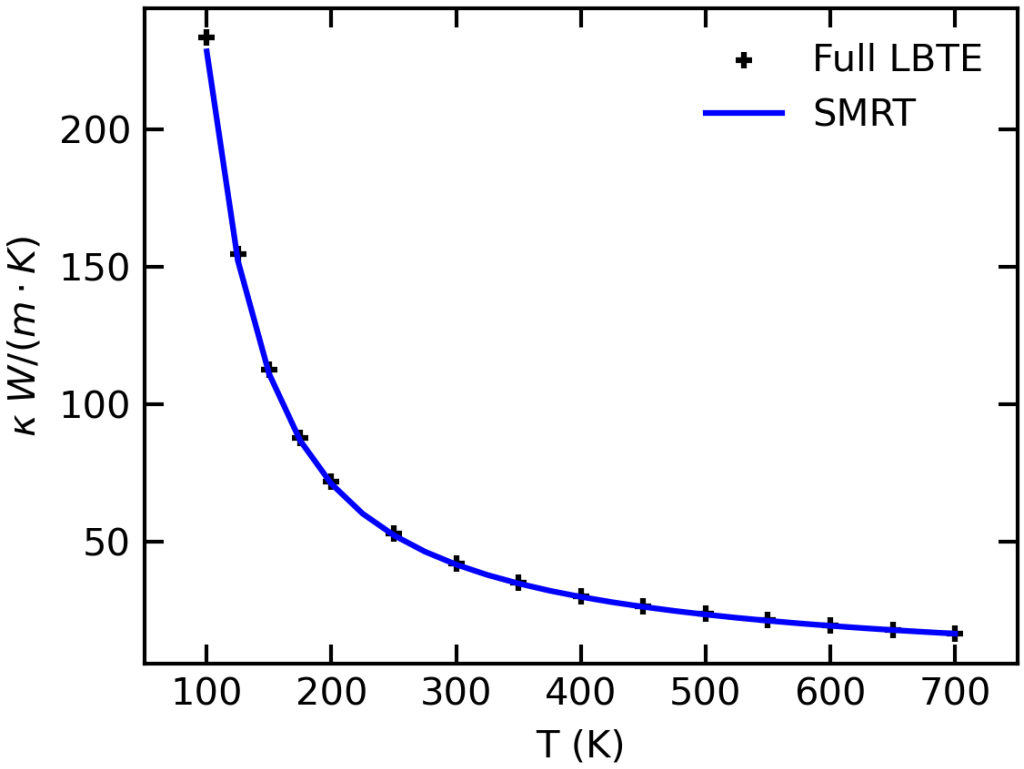

Figure 3.4. Comparison of the calculated phonon thermal conductivity κ_p (natural) using the direct solution of LBTE (black label) and the SMRT approximation (blue curve) (performed by Qiyang Sun).

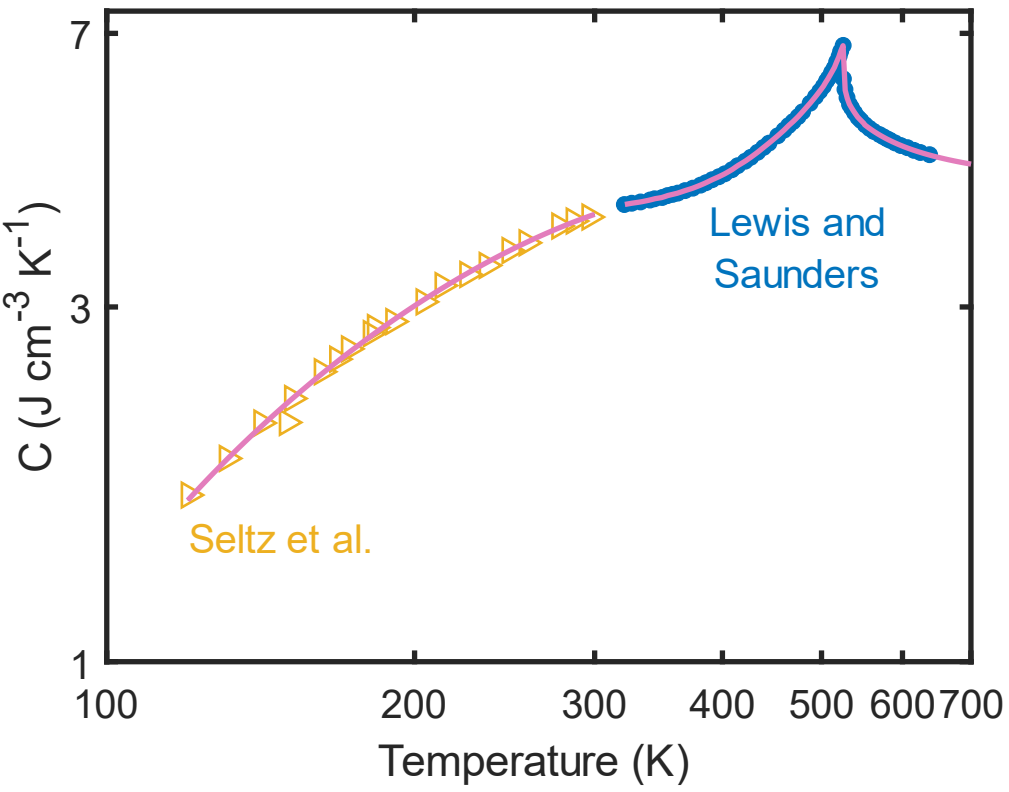

Figure 3.5. Heat capacity of NiO. Labels indicate previous measurements, and curves show the extrapolations.

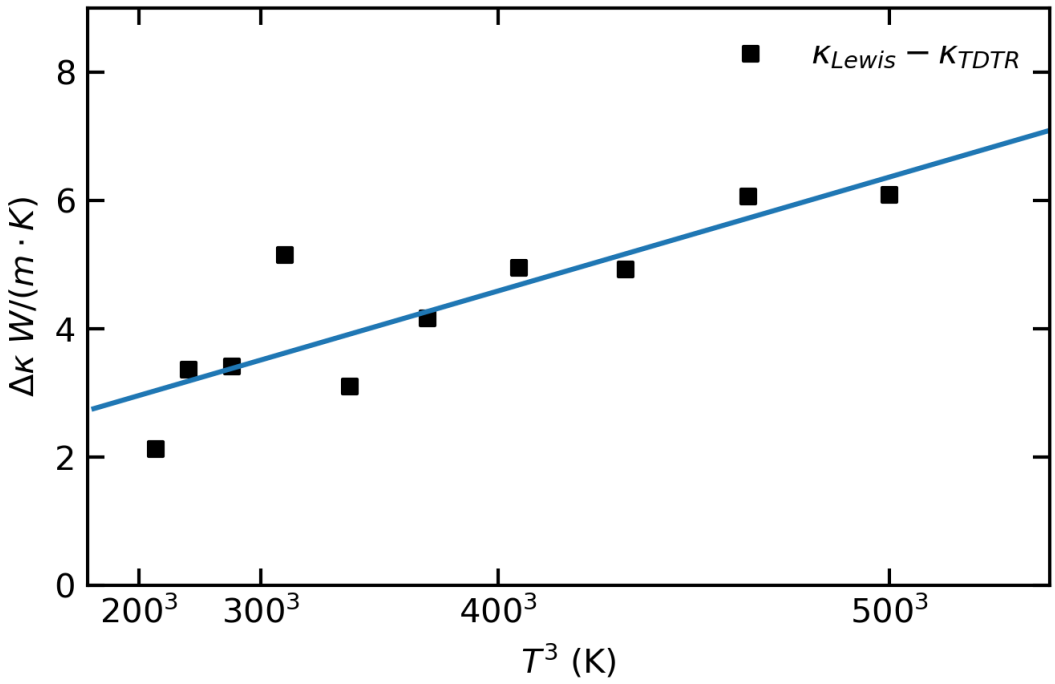

Figure 3.6. The difference between our measurements and the steady-state results [85] ($\Delta\kappa$) at 200-500 K.

Black dots show the difference between NiO (I) and one set of data measured by Lewis. Blue line shows the T^3 relation fitting.

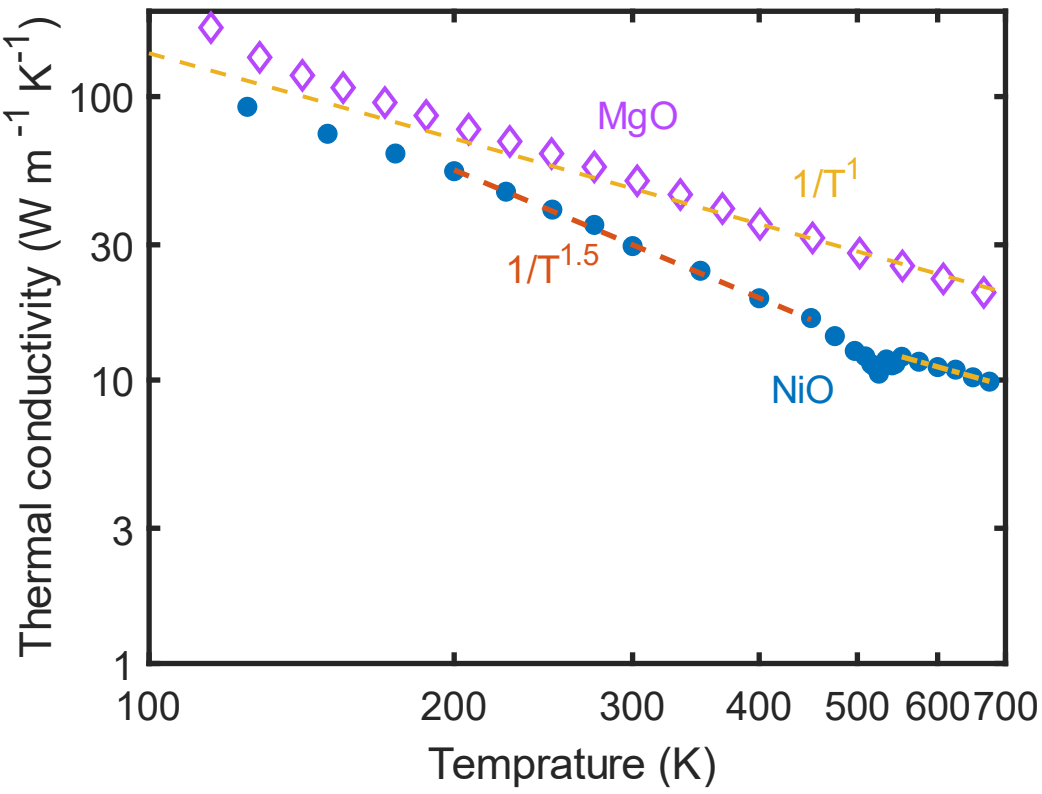

Figure 3.7. Thermal conductivity comparison between MgO and NiO.

The MgO (purple diamonds) data is from Ref. [105]. The yellow and orange lines represent the $1/T$ and $1/T^{1.5}$ dependences, respectively.

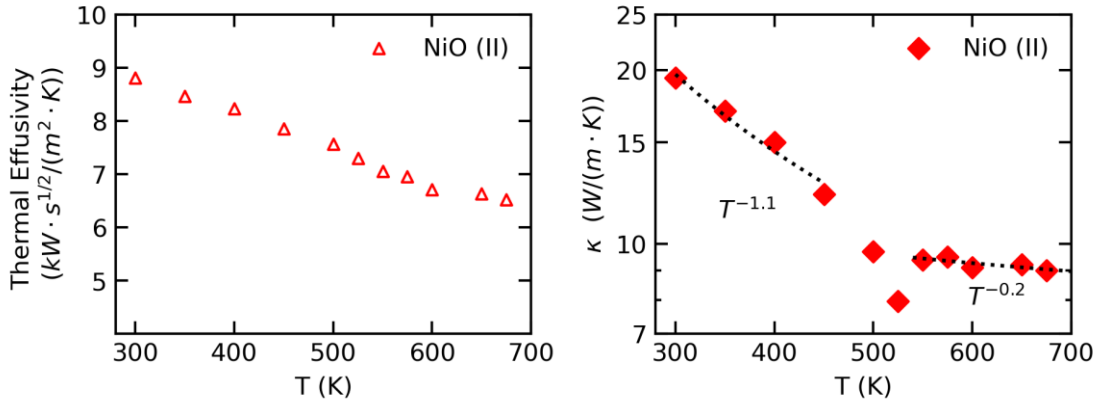

Figure 3.8. Thermal effusivity (a) and conductivity (b) of a NiO sample with lower ambient thermal conductivity.

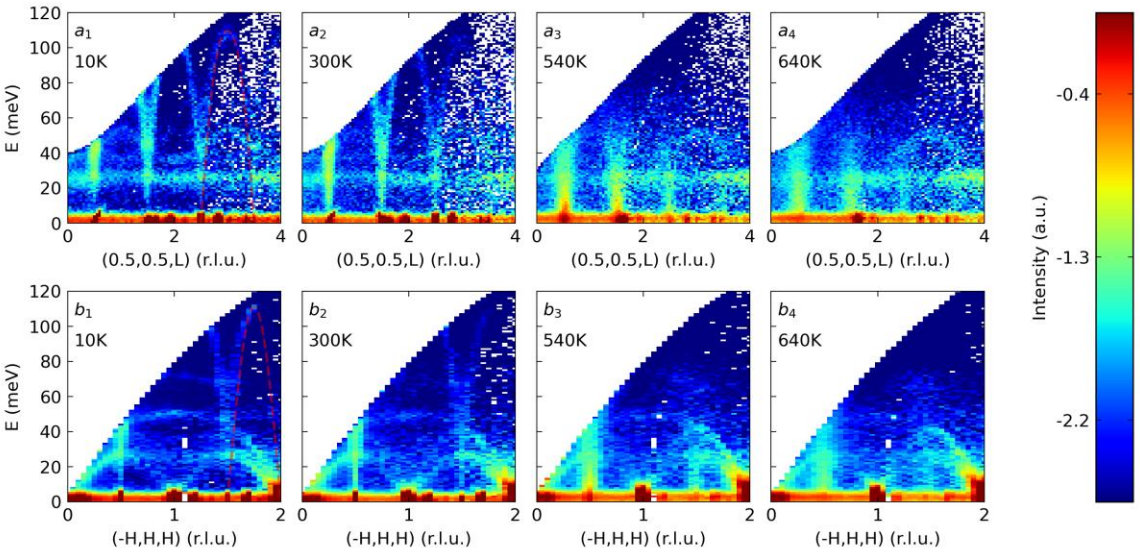

Figure 3.9. Measured INS dynamic structure factor $S(Q, E)$ at 10, 300, 540, and 650 K in small Q region for [0,0,1] (a_{1-4}) and [-1,1,1] (b_{1-4}).

Measured $S(Q, E)$ is integrated over ± 0.1 ($r.l.u$) along the perpendicular axes and plotted on the logarithmic color scale. The calculated magnon dispersions are overplotted with the measured $S(Q, E)$ at 10 K in red dashed lines.

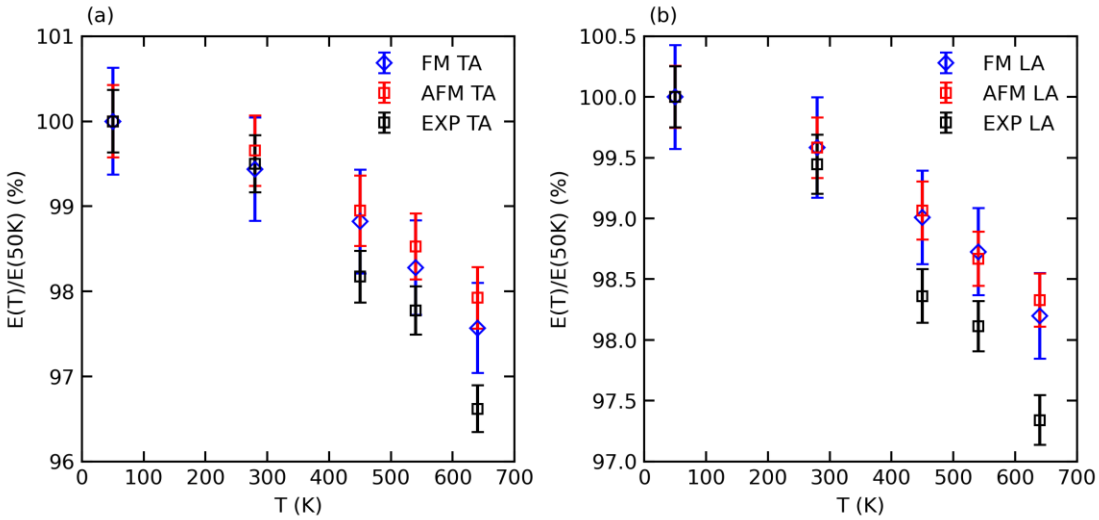

Figure 3.10. Normalized phonon energies with FM (blue) and AFM (red) spin order for TA (a) and LA (b) phonons at 50, 280, 450, 540 and 640 K.

The phonon energies are obtained from Lorentzian fitting of the calculated temperature dependent phonon density-of-state (see text). The results are compared with the measured phonon energies by INS (black). Error bars indicate fitting errors.

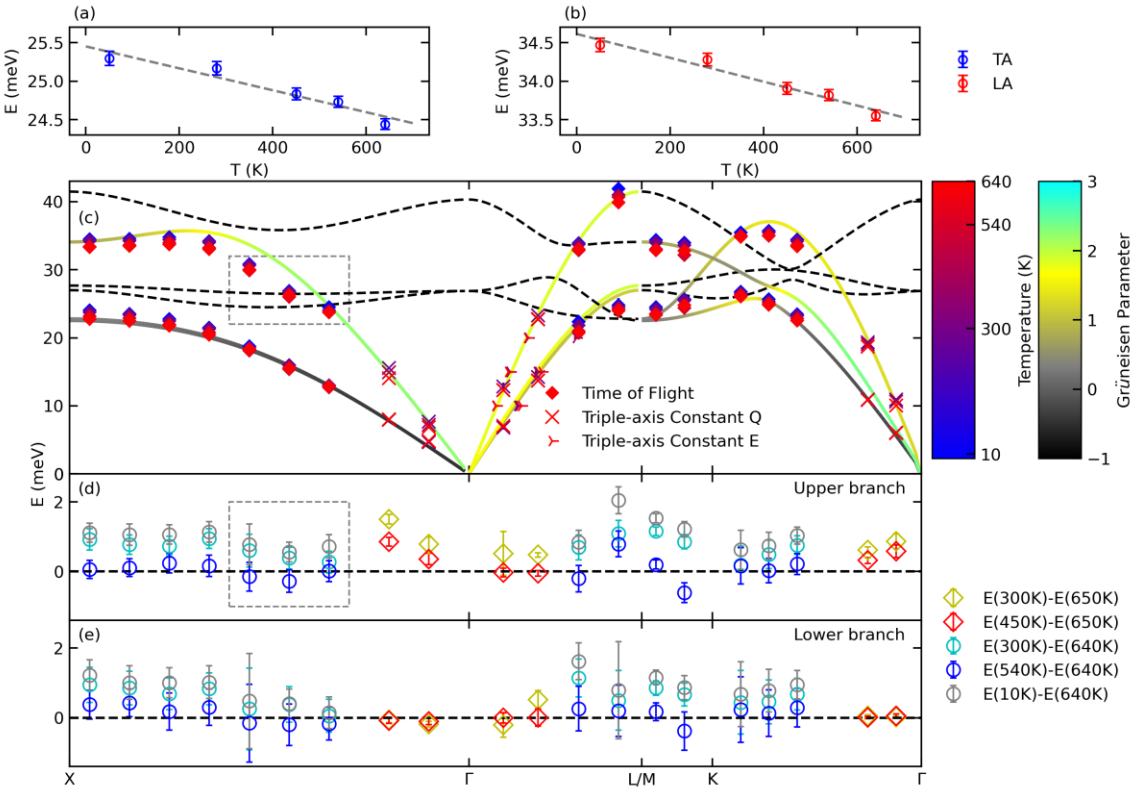

Figure 3.11. Temperature-dependent phonon energy variations from INS experiments.

(a,b) Phonon energies from the phonon density of state INS measurements with incident neutron energy of 50 meV at 50, 280, 450, 540 and 640 K. The experimental data have been corrected for multiphonon scattering and thermal occupation. There are two distinct peaks around 25 and 34 meV, corresponding to the (a) TA and (b) LA phonon modes. (c) Measured and calculated phonon energies for LA and TA modes along high-symmetry directions. Squares and cross markers represent phonon energies from the time-of-flight (measured at 10, 300, 540 and 640 K) and triple-axis (measured at 300, 450 and 650 K) INS measurements, and the corresponding colors denote temperatures. The q-resolved mode Grüneisen parameters are calculated based on quasi-harmonic approximation and indicated by the colored lines. Zone-folding modes that cannot be seen from INS experiments are shown in dashed lines. The fitting errors are smaller than the marker size. (d,e) Difference of the phonon energy from low to high temperature of the upper branch (d) and the lower branch (e). All phonon energies were extracted from Lorentzian fittings of the measured data, and error bars indicate fitting errors. The incoherent INS scattering signals around 26 meV can cause slightly biased phonon energies, as denoted by grey boxes.

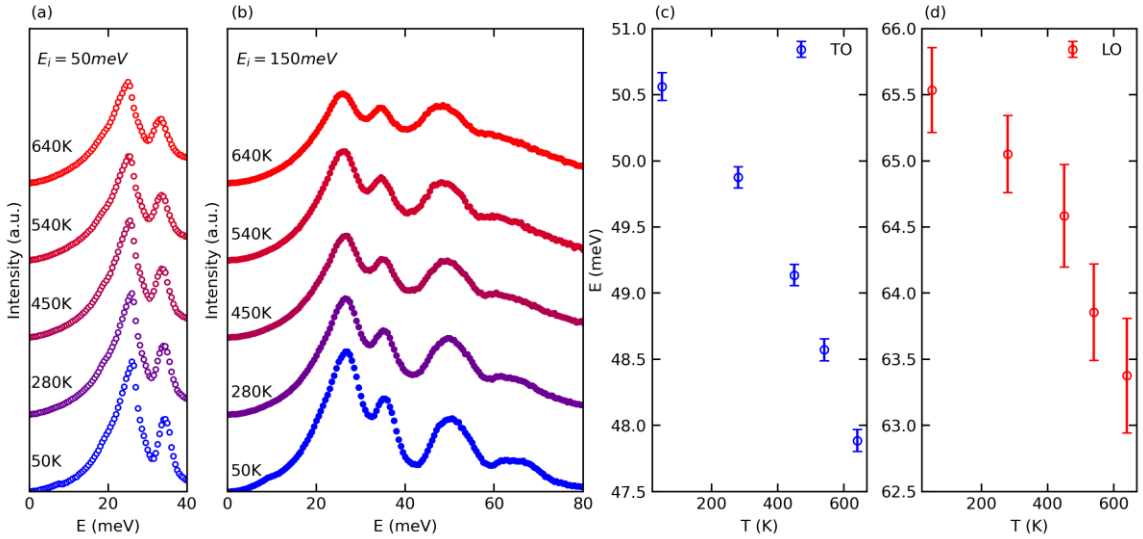

Figure 3.12. Temperature-dependent neutron-weighted phonon density of states and temperature-dependent optical phonon energies.

(a, b) Neutron-weighted phonon density of state measured with an incident have of E = 50 meV (empty circles) and E = 150 meV (dots) at 50, 280, 450, 540, and 640 K. Experimental data has been corrected for multiphonon scattering and thermal occupation. (c, d) TO, LO phonon energies are extracted from Lorentzian fitting of the measured data, and error bars indicate fitting errors.

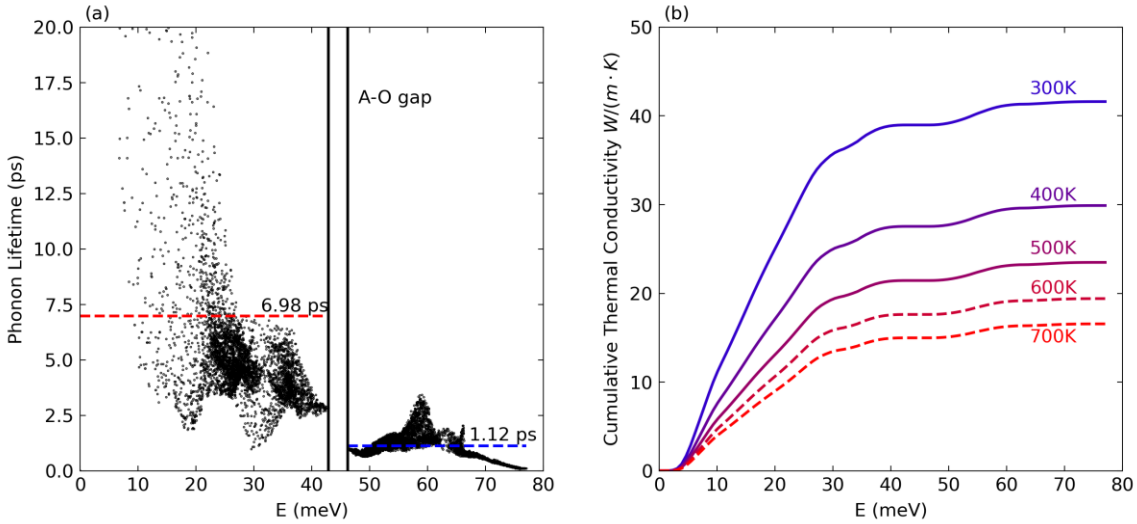

Figure 3.13. Phonon lifetime and cumulative thermal conductivity calculated by first-principles calculations (performed by Qiyang Sun).

(a) Calculated phonon lifetimes of NiO at 300K at a $20 \times 20 \times 20$ q-mesh. Average phonon lifetimes for acoustic (optical) phonons are denoted by red (blue) dashed lines. The black lines represent the acoustic-optic (A-O) gap. (b) Cumulative thermal conductivity of the phonon system at various temperatures. The thermal conductivity is dominated by acoustic phonon modes below 30 meV at all temperatures.

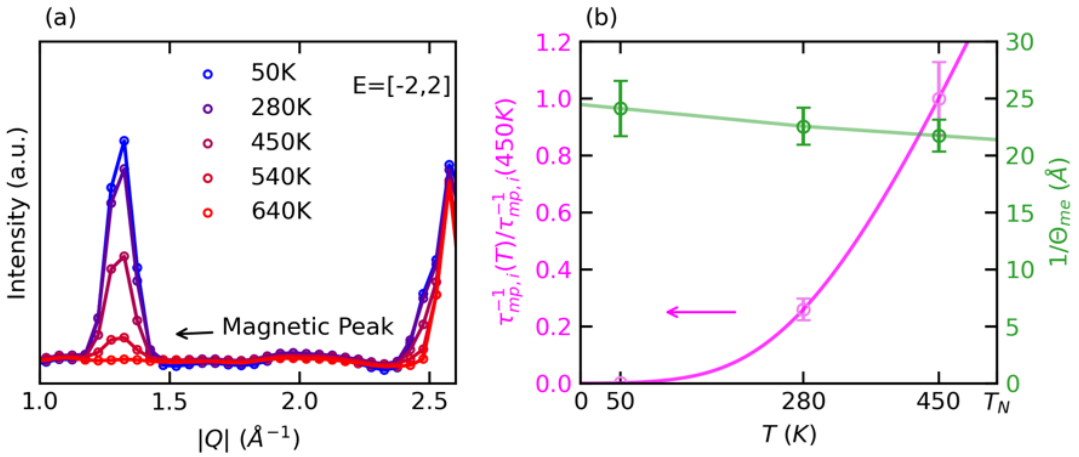

Figure 3.14. Sketch of the phonon scattering rate in the MPS process.

(a) One-dimensional S(|Q|) by INS powder measurements at 50 – 640 K with energy integration of ± 2 meV. The elastic magnetic peaks show around 1.3 Å^{-1} and their intensities weaken on heating significantly, whereas elastic lattice peaks retain the same. (b) The inverse of the HWHM of the magnetic elastic Bragg peak $1/\Theta_{me}(T)$ (green labels) and normalized phonon scattering rate $\tau_i^{-1}(T)/\tau_i^{-1}(450\ K)$ (purple labels). Colored lines are guides for the eye.

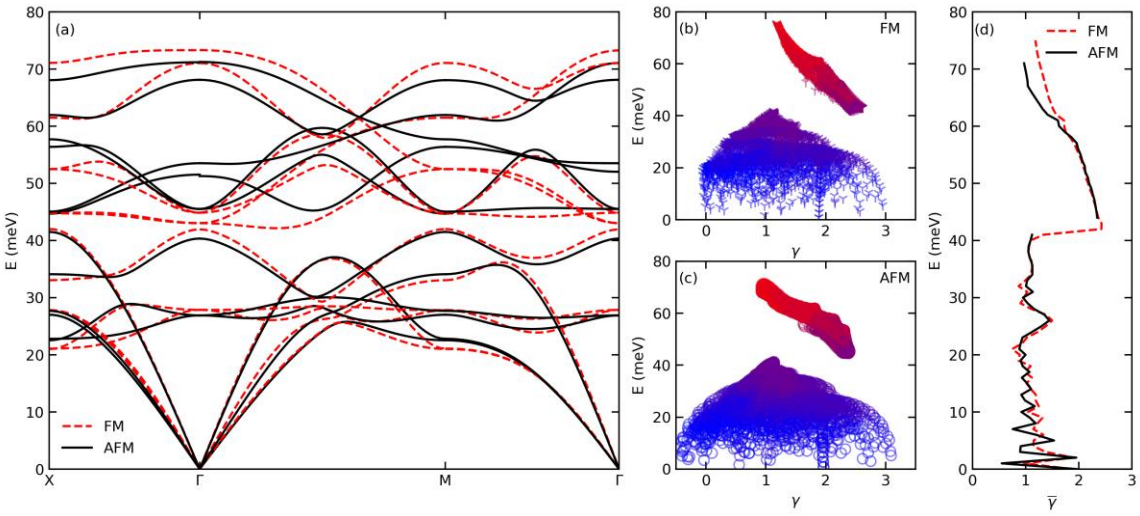

Figure 3.15. Comparison between calculated phonon properties with ferromagnetic (FM) and antiferromagnetic (AFM) spin order (calculated by Qiyang Sun).

(a) Phonon dispersion with FM (red) and AFM (black) spin order. (b,c) Phonon mode Grüneisen parameter (γ) with FM (b) and AFM (c) spin order. The colors denote different phonon branches. (d) Energy-dependent averaged γ with FM (red) and AFM (black) spin order.

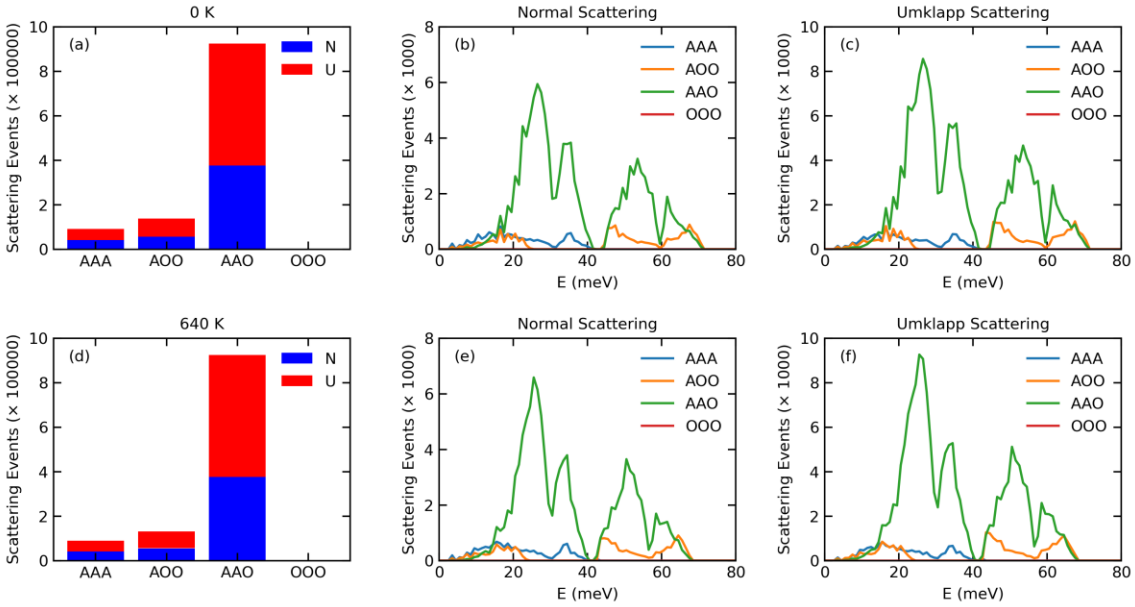

Figure 3.16. Three-phonon scattering phase space at 0 and 640 K (performed by Qiyang Sun).

(a, d) Bar plots of scattering phase space categorized by AAA, AOO, AAO, OOO in normal and Umklapp processes at 0 (a) and 640 (d) K. (b, e) Energy-dependent scattering events of normal scattering. (c, f) Energy-dependent scattering events of Umklapp scattering.

Chapter 4 Ultrahigh Thermal Conductivity and Unexpected Strong Temperature Dependence of Cubic Boron Arsenide

4.1 Introduction

Cubic boron arsenide (c-BAs, for simplicity, BAs is used throughout the paper) is of interest for next generation electronics due to its combined high thermal conductivity (> 1000 W m^{-1} K^{-1}) and high carrier mobility (> 1400 cm^2 V^{-1} s^{-1}) [7,106–112]. BAs's exceptional transport properties were first predicted by first-principles calculations that considered the effect of its special phonon dispersion on scattering [7,108,111]. The difference in atomic mass between B and As leads to a large acoustic-optical (*a*-*o*) phonon frequency gap. This large gap, together with bunching of acoustic phonon branches, leads to weak phonon-phonon scattering. Weak polarity and high frequency of optical phonons suppress polar scattering of charge carriers [113]. As a result, both heat carriers (acoustic phonons) and charge carriers (electrons and holes) have long mean free paths.

First-principles calculations predict a room temperature Λ of 1240 to 1440 W m^{-1} K^{-1} for ^{nat}BAs [108,111], and 1380 to 1720 W m^{-1} K^{-1} for isotopically pure BAs [114,115]. These predictions are in reasonable agreement with prior experimental observations of Λ between 1000 and 1300 W m^{-1} K^{-1} for natural BAs [109,110], between 1160 and 1260 W m^{-1} K^{-1} for isotopically enriched BAs [108,115,116]. However, theoretical predictions assume minimal defects. Recent studies suggest defect levels in BAs crystals are not negligible. Chen *et al.* used secondary ion mass spectroscopy and electron probe microanalysis to study impurities in BAs crystals [117]. The crystals were prepared in the same way as those studied in Ref. [108] and possessed room-temperature Λ ≈ 900 W m^{-1} K^{-1}. They observed a Si impurity level of 0.047 at%. BAs crystals are

often reported to have peaks in their photoluminescence spectra near 1.5 eV [118,119]. Originally, these peaks were interpreted to imply a band gap of 1.5 eV in BAs [120,121]. However, recent studies have constrained the band gap of BAs to be between 1.8 and 2 eV [118,119,122–125], and credit photoluminescence peaks at 1.5 eV to group IV impurities [119].

Temperature-dependent measurements can help identify the impact of defects on thermal transport. In insulating materials, Λ *vs.* T hinges on the temperature (T) dependence of phonon scattering rates. Phonon-defect scattering rates stay constant with temperature [126,127], while phonon-phonon scattering rates are temperature sensitive [111]. So, Λ is expected to vary less with temperature if defect concentrations are appreciable. Reports for Λ *vs.* T between 300 and 600 K in BAs varies between $1/T^{1.3}$ and $1/T^2$ [108–110]. Samples with higher defect concentrations are expected to exhibit lower ambient thermal conductivity and weaker temperature dependence due to phonon-defect scattering. However, prior experimental results from different groups on BAs samples with $\Lambda > 1000$ W m^{-1} K^{-1} do not follow this trend. First-principles calculations predict $\Lambda \propto 1 / T^{1.6}$ between 300 and 600 K for ^{nat}BAs [108,111]. For isotopically pure BAs, its temperature dependence is predicted to fall between $\Lambda \propto 1/T^{1.7}$ and $1/T^{1.8}$ [114,115,128].

In this study, we investigated about fifty BAs samples synthesized by our collaborators. We performed time-domain thermoreflectance measurements on five selected BAs samples with different ambient thermal conductivity varying from 700 to 1500 W m^{-1} K^{-1} in the temperature range between 300 and 600 K. We observed a $\Lambda \propto 1/T^2$ relationship on the 1500 W m^{-1} K^{-1} sample, a stronger temperature dependence than prior experimental results and theoretical predictions. We performed Raman and Brillouin scattering between 300 and 600 K to study the

temperature-induced phonon dispersion changes of BAs. Additionally, we characterized the defect level of our BAs samples using pump/probe transient reflectivity microscopy (TRM) with incident photon energy of 1.58 eV which is about 0.26 eV below the band gap of BAs. We observed that samples with higher thermal conductivity exhibit lower TRM signal.

4.2 Materials and Methods

To study the temperature dependent thermal conductivity of BAs, we synthesized a variety of BAs crystals by chemical vapor transport [108,129]. All source ingredients involved in the synthesis process were purchased from Alfa Aesar with high purity (metal basis). To synthesize BAs crystals, source boron (B, 99.9999%), arsenic (As, 99.99999%), and transport agent iodine (I_2, 99.9985%) were sealed in a fused quartz tube under vacuum (10^{-4} Torr). The boron source is >98% ^{11}B. A piece of quartz fiber or GaAs wafer was also placed and fixed to the other end of the tube as nucleation sites for crystal growth. Then the sealed quartz tube was placed into a two-zone horizontal tube furnace for crystal growth, with high temperature for source side and low temperature for growth side. The high-temperature zone of the furnace was heated up to 895 ℃ while the low-temperature zone was heated up to 790 ℃. After crystal growth, the furnace cooled down naturally to room temperature.

We coated our samples with 80-nm Al films using magnetron sputtering for time-domain thermoreflectance (TDTR) and beam offset measurements. Before sputtering Al, we cleaned the as-grown BAs surface with ethanol, followed by Ar plasma etching in vacuum at room temperature. We used 25 W radio-frequency (RF) power (149 V and 168 mA) in plasma etching, and the area of the sample holder is ~60 cm^2. The sample stage was not heated during etching or

Al deposition. For forced Brillouin scattering measurements, we coated a 5-nm Pt thin film on BAs.

After TDTR measurements, we etched off the Al films using aluminum etchant type A (Transene Inc.) and rinsed BAs samples with de-ionized water and ethanol. Then we performed pump/probe measurements on bare BAs samples (transient reflectivity microscopy measurements).

Control samples for pump/probe transient reflectivity microscopy measurements are commercially available. GaP and GaAs single crystals are purchased from MTI corporation. GaN is from Sumitomo Electric Industries Ltd. Single crystal Si is from University Wafer.

Time-domain thermoreflectance is a well-established pump/probe technique for characterizing the thermal properties of materials [130]. In our TDTR measurements, we used a 783 nm laser wavelength, with pump beam modulated at 10.7 MHz. We used laser spot size of ~15 μm in $1/e^2$ radius. Further elaboration on the principles underlying TDTR can be found in Ref. [130].

Our analysis of the $-V_{in}\ /\ V_{out}$ versus delay time involved fitting the data to a heat diffusion model, yielding the thermal effusivity ($\sqrt{\Lambda C}$, with Λ and C being thermal conductivity and heat capacity, respectively) of BAs. The beam offset method [39,40] measures the in-plane heat diffusion on the transducer surface. We fit the full width at half maximum (FWHM) of the V_{out} signal with a heat diffusion model to determine the thermal diffusivity (Λ/C) of BAs. Utilizing known literature data on the heat capacity of BAs (Figure 4.10A), we derived thermal conductivity values via TDTR and beam offset measurements.

In our experimental setup for TDTR and beam offset measurements at temperatures exceeding 300 K, we maintained a vacuum chamber with a pressure consistently below 1×10^{-3} Torr. Simultaneously, we continuously monitored temperature levels of the heater stage using a

thermocouple. The measured samples are attached to the stage (close to the thermocouple) using carbon paste. Additional specifics regarding our pump/probe system can be found in Ref. [41].

In the heat diffusion model, the thermal conductivity of BAs and the interface conductance between Al and BAs are two essential yet unidentified parameters. For other parameters that the model relies on and is sensitive to, we either directly measured them or obtained them from available literature sources. Specifically, we assessed the thickness of the Al film through picosecond acoustics [36]. We employed the speed of sound of Al of 6.42 nm/ps [131] to interpret the picosecond acoustic echoes, and added a 3-nm oxidation layer on top. We measured the electrical resistivity of the Al film by a four-point probe method and calculated its thermal conductivity according to the Wiedemann-Franz law. We measured the laser spot size by the beam offset method. We also measured the spot-size using the camera integrated into our setup, together with an SEM ruler to convert pixel width to microns. Beam-offset measurements and camera measurements gave the same spot-size to within 5%. We acquired the heat capacity of Al and BAs from Ref. [92] and Ref. [132], respectively.

We measured the Raman and photoluminescence (PL) spectrum of BAs using our home-built setup. The excitation laser has a 532 nm wavelength, the numerical aperture (NA) of the objective lens is 0.28, and the focused laser spot size is ~ 6 μm ($1/e^2$ radius). We used a monochromator (Acton SpetraPro-2500i) to collect the scattered light. We placed a long-pass edge filter (Semrock LP03-532RE-25) in front of the spectrometer to filter out background noise. For Raman measurements at high temperatures, we used the same heat stage and conditions as high-temperature TDTR measurements.

Brillouin – Mandelstam spectroscopy (BMS) studies were carried out utilizing a 532 nm laser (*p*-polarized) excitation wavelength at an angle of incidence of 30 degree in the conventional

backscattering setup. Solid-state diode-pumped continues-wave laser (Spectra Physics) was used as the light source. A lens with a NA of 0.34 was employed to concentrate the laser beam on the sample. The same lens was used to capture the scattered light, which was then sent to a spectrometer and a high-contrast, high-resolution 3 + 3 pass tandem Fabry-Perot interferometer (TFP-1, JRS Optical Instruments, Switzerland). The TFP's mirror spacing was changed to 0.9 mm for measurements of bulk acoustic phonons.

The group velocity of transverse and longitudinal acoustic phonon modes can be calculated according to $v = f\lambda/2N$ in which f, λ, and N are the spectral position of the peaks in the Brillouin spectrum, laser excitation wavelength, and refractive index of the material at the laser excitation, respectively. We take the data for the index of refraction N of 3.25 at 532 nm laser wavelength from Ref. [133]. The BMS results on nine BAs samples are shown in Table 4.2. We note that the obtained results are not along the surface normal, *i.e.*, the [111] direction. In a back-scattering BMS setup, the speed of sound is measured in the direction parallel to the wavevector of the refracted beam. For an angle of incidence of 30 degrees, the angle of refraction is ~8 degrees. Along the [111] direction, the TA phonon branches are degenerate. But the 8-degree deviation breaks this degeneracy.

We performed forced Brillouin scattering measurements using our TDTR setup [41] on a BAs sample coated with 5 nm Pt. The incident laser beams were perpendicular to the sample surface. When the pump beam heats the Pt surface, it launches a strain wave into the BAs. The strain wave front moves at the longitudinal sound velocity of BAs. Both the strain wave and the transducer can reflect the subsequent probe beam. These two reflected probe beams interfere with each other and cause Brillouin oscillations in the in-phase voltage signal V_{in} [36]. The Brillouin frequency is

$$f = 2Nv_l / \lambda, \qquad (4.1)$$

where N is the index of refraction of BAs, v_l is the longitudinal sound velocity of BAs, and λ is the laser wavelength which is 783 nm. We use the measured Brillouin frequencies of BAs as a measure of the longitudinal speed of sound in these materials. The index of refraction of BAs is 3.15 at 783 nm laser wavelength [133]. We obtained the ambient longitudinal sound velocity of 8100 m/s for BAs along [111] direction, which is consistent but a bit lower than our BMS result. The 8100 m/s value is in reasonable agreement with prior reports [132,134]. For Brillouin measurements at high temperatures, we used the same heat stage and conditions as high-temperature TDTR measurements.

We performed transient reflectivity microscopy (TRM) using our pump/probe system [41]. For most TRM measurements, the laser wavelength is fixed at 783 nm. For the wavelength-dependent TRM, the laser wavelength was tuned from 690 to 980 nm. The pump modulation frequency was 10.7 MHz, and the incident pump power was 20 mW. We used either 7.5 μm or 15 μm $1/e^2$ laser radius. We observed the V_{in} signal was linearly proportional to laser power density. Therefore, for measurements with 7.5 μm laser radius, we normalized the V_{in} signal by dividing it by 4. The observed V_{in} signal is normalized by the power of pump beam and the voltage on the photodiode detector.

For wavelength-dependent TRM measurements, we use a Pt thin film as the control sample to calibrate the wavelength-dependent factors originated from optics. The collected signal is

$$\Delta R = \frac{dR}{dT}\Delta T \propto C(\lambda) \cdot \frac{dR}{dT}(\lambda) \cdot [1 - R(\lambda)] \cdot P_{pump}(\lambda) \cdot V_{DC}(\lambda). \qquad (4.2)$$

Here, dR/dT is the thermoreflectance, ΔT is the temperature rise due to the heating of pump beam, R is the reflectance, P_{pump} is the pump power, and V_{DC} is the voltage on the photodiode

detector. $C(\lambda)$ is a wavelength-dependent factor related to optics in our pump-probe system. For example, the transmission of objective lens and the modulation envelope of electro-optic modulator are wavelength dependent. To calibrate $C(\lambda)$, we performed TRM on a Pt thin film as a function of wavelength. We measured P_{pump} and V_{DC} at every wavelength, and obtained wavelength dependent $(1-R)$ and dR/dT of Pt from Ref. [14]. We used this calibrated $C(\lambda)$ for wavelength-dependent TRM on BAs samples.

We collected thermal conductivity and transient reflectivity microscopy maps with ~15 μm laser spot size and 10.7 MHz modulation frequency. The mapping process employed a step size of 10 μm. For the thermal conductivity map, we chose the delay time to be ~300 ps at which the interface conductance has zero sensitivity. To mitigate artifacts in V_{out} associated with phase jitters in the lock-in amplifier at positive delay time, we conducted two separate mappings at positive and negative delay times, respectively. In our analysis of the thermal conductivity map, we analyzed $-V_{in}(t>0)\,/\,V_{out}(t<0)$ instead of directly analyzing $-V_{in}\,/\,V_{out}$.

4.3 Results and Discussion

We characterized our BAs samples using X-ray diffraction (XRD), Raman scattering, photoluminescence (PL), and Brillouin scattering (Figs. S1-S4). The XRD results were consistent with a (111) growth facet. Most of our samples exhibited a Raman peak at 700 cm^{-1} (corresponding to an optical phonon frequency of 21 THz), consistent with nearly isotopically pure ^{11}BAs [135]. A few samples we studied were grown from a boron source of isotopically pure ^{10}B and they had a Raman peak at 729 cm^{-1} (22 THz), consistent with previously reported spectra of ^{10}BAs [115,135]. In most samples, we observed PL spectra centered near 1.75 eV. But some

samples exhibited additional PL peaks centered at lower energies. Our PL results were consistent with the spectra observed in prior studies [106,107,118,119].

Li *et al.* [110] observed a relationship between thermal conductivity and the integration of the Raman intensity from 1050 to 1150 cm^{-1} in BAs. We analyzed our Raman spectra following their procedure and observed a similar trend, see Figure 4.2B. To analyze the background of the Raman spectra, we subtract the spectra of BAs by the dark background of the monochromator, *i.e.*, the signal collected at the same collection time without any incident light.

We conducted Brillouin-Mandelstam spectroscopy [136] on nine BAs samples, a technique used to measure low-frequency acoustic phonons. A 532 nm laser beam was shined on the BAs sample at an incident angle of 30 degrees. We measured the backscattered light that was inelastically scattered by acoustic phonon modes. We observed three peaks in the Brillouin spectra associated with two transverse acoustic (TA) and one longitudinal acoustic (LA) phonons at 58.8, 62.1, and 101.6 GHz, respectively. These frequencies correspond to TA and LA sound velocities of 4800, 5080, and 8320 m/s along the direction of the refracted laser beam, which is ~8° from the [111] direction. Our Brillouin scattering results are consistent with prior experimental results of 4978 and 8513 m/s for the transverse and longitudinal acoustic phonons along [111] direction, respectively, obtained using picosecond interferometry [134].

Time-domain thermoreflectance (TDTR) measurements reveal the ambient thermal conductivity (Λ_{300K}) of synthesized crystals are as high as 1500 W m^{-1} K^{-1} (sample BAs-1500), higher than previous experimental observations [108–110]. As part of this study, we measured the thermal conductivity of more than fifty BAs crystals. Among these, four crystals had thermal conductivity above 1400 W m^{-1} K^{-1}. TDTR data for one of the high-thermal-conductivity crystals is shown in Figure 4.5A. TDTR data for the other three are shown in Figure 4.6. In TDTR experiments, the

$-V_{in}/V_{out}$ signal describes the thermal response of the sample to optical heating. We fit the TDTR signals with a heat diffusion model to extract the thermal conductivity of BAs [91]. The temperature-dependent parameters in the heat diffusion model are shown in Figure 4.10A. We noticed that different etching times yield different interface conductance between Al and BAs (Figure 4.10B). The interface conductance increased from 130 to 180 MW m^{-1} K^{-1} when we extended the plasma etching time from 90 to 120 s.

We observe that BAs crystals with Λ_{300K} =1500 W m^{-1} K^{-1} exhibit $\Lambda \propto 1 / T^2$ between 300 and 600 K (Figure 4.5B). This is a stronger temperature dependence than being predicted by first-principles calculations [108,111,114,115,128], and stronger than prior experimental results of BAs [109,110]. We corroborated the observed $1/T^2$ dependence by performing separate beam-offset TDTR measurements [40] of the in-plane thermal conductivity versus temperature on the sample in Figure 4.5B. Additionally, we measured another BAs sample with $\Lambda_{300K} = 1500$ W m^{-1} K^{-1} and observed the same temperature dependence, see Figure 4.8.

Based on sensitivity analyses (Figure 4.11), we estimate a 10% and 15% uncertainty for TDTR and beam offset, respectively. Sensitivity to parameters is quantified as follows:

$$S_\alpha = \frac{\partial\, ln(-V_{in}/V_{0ut})}{\partial\, ln\, \alpha}, \qquad (4.3)$$

where α represents parameters of interest in the heat diffusion model. We estimate a 3% uncertainty for the heat capacitance (hC) of the Al transducer, a 5% uncertainty in laser spot size (w_0), and a 3% uncertainty in heat capacity of BAs. Our TDTR data fitting was performed within the 100-6000 ps delay time range, during which the model exhibits low sensitivity to the thermal conductivity of the Al film. The error bar of beam offset measurements is larger than that of TDTR due to the high sensitivity of laser spot size in beam offset analysis. The sensitivity of laser

spot size is nearly twice of the sensitivity of the in-plane thermal conductivity of BAs, implying that a 5% uncertainty in laser spot size propagates a 10% uncertainty in the in-plain Λ of BAs.

In beam offset measurements, the sensitivity of Λ_{BAs} is maximized when the laser spot size closely matches the heat diffusion length [137]. The heat diffusion length is $d = \sqrt{\Lambda / \pi C f}$, where f represents the pump modulation frequency. To enhance the sensitivity of Λ_{BAs}, we deliberately chose laser spot sizes and modulation frequencies that align with the heat diffusion length in our beam offset measurements, as detailed in Table 4.1.

Surface roughness can possibly affect TDTR and beam offset measurements due to unwanted modulation of diffuse scattering by thermoelastic effect [138,139]. To confirm our BAs samples with high thermal conductivity have smooth surfaces, we performed atomic force microscopy (AFM) on an area of 10×10 μm^2 of a BAs sample with Λ_{300K} of 1500 W m^{-1} K^{-1} (Figure 4.12A). The measured root-mean-square (RMS) roughness is 1.8 nm which is smooth enough for TDTR measurements. Picosecond acoustic echoes in TDTR measurements can deliver some indirect information of interface roughness between Al and substrates [140]. Substrates with smooth surfaces yield sharp and narrow acoustic echoes in V_{in} signals. Sometimes, acoustics from rough surfaces yield wider acoustic echoes, which is an indicator that surface roughness is too high. We compared the acoustic echo from the Al/BAs sample with echoes from commercially available Si and diamond wafers coated with Al (Figure 4.12B). We observed that the acoustic echoes from the BAs sample have similar widths as echoes from Si and diamond wafers. For most BAs samples, we did not perform AFM measurements. Instead, we checked all picosecond acoustic peaks for broadening, and confirmed that the specular reflectance of all samples was within 5% of the expected value for an Al coated surface.

To investigate the mean-free-path distribution of heat-carrying phonons in BAs, we conducted TDTR measurements as a function of laser spot size [141–143]. When the laser spot size is small, the in-plane heat current carried by phonons with long mean free path is less than what Fourier's law predicts [141]. This results in spot-size dependent apparent thermal conductivity (Λ_A), where we define Λ_A as the Λ that yields the best fit of the heat diffusion model to the experimental data. We measured Λ_A of the BAs-1500 sample at temperatures of 300, 450, and 600 K (Figure 4.5C). At 300 K, a spot-size reduction from 15 to 1.7 μm led to a ~20% reduction in Λ_A. A similar suppression of Λ_A was observed in silicon and diamond [141–143]. The 20% drop we observed is much smaller than prior reports for Λ_A versus spot size in BAs [109,110]. A weak dependence of Λ_A on spot size for BAs is in qualitative agreement with first-principles calculations [108], and consistent with Peierls-Boltzmann transport equation simulations of non-diffusive heat transfer in TDTR measurements of BAs [144]. First-principles calculations predict 80% of the heat is carried by phonons with mean free paths between 0.3 and 1.5 μm. At 450 and 600 K, laser spot size does not affect Λ_A. This suggests that for $T \geq 450$ K, the mean free paths of all heat-carrying phonons are less than 1.7 μm. To avoid mean-free-path effects in the rest of our experiments, we used a $1/e^2$ laser radius greater than 10 μm.

To further explore the temperature-dependent thermal conductivity of BAs, we selected four other BAs samples and measured their Λ *vs. T*. These samples had Λ_{300K} of 1350, 1200, 1000, and 700 W m^{-1} K^{-1}. We also measured a type IIa diamond crystal from Element Six as a control sample. We fit the measured data of Λ *vs.* T by $\Lambda \propto 1/T^{\alpha}$ to obtain the temperature exponent α. We plot α *vs.* Λ_{300K} for the selected BAs samples (Figure 4.13B). The temperature exponent of diamond is 1.2, in good agreement with prior reports [109,111]. As Λ_{300K} decreases, the temperature dependence weakens. As described above, this is expected. Phonon-defect scattering rates are proportional to the concentration of defects. The higher the defect concentration, the

lower the ambient thermal conductivity. Since defect concentrations are independent of temperature, phonon-defect scattering lowers α.

The temperature dependence of Λ we observe for BAs is unusually large. At high temperatures, the temperature dependence of Λ is primarily determined by the type of scattering processes that limit mean free paths of heat carrying phonons. In most high purity single crystals, three-phonon scattering is the dominant process, resulting in $\Lambda \propto 1/T$ ($\alpha = 1$) [111,128]. A higher temperature exponent can indicate higher-order phonon scattering processes [128]. Three-phonon-scattering rates increase linearly with temperature, while four-phonon-scattering rates increase quadratically with temperature [111].

In the limit where four-phonon scattering processes dominate, α is expected to be equal to 2 [111]. Some materials exhibit $\alpha > 1$, but it is rare for α being close to 2. For instance, BP and InP have temperature exponents of 1.4 [145] and 1.5 [146], respectively. BP and InP are III-V semiconductors with an *a-o* gap due to the large mass ratio between constituent atoms [7,128]. A large *a-o* gap limits the phase space of three-phonon scattering, which can increase the importance of four-phonon scattering processes. BP, InP, and BAs are examples of this trend. (Notably, GaN does not follow this trend, despite a large *a-o* gap.) The relationship between α and mass ratio for III-V compounds with zincblende structure is summarized in Figure 4.15.

In BAs, four-phonon-scattering processes are expected to be important, but not dominant [111,114,128]. For ^{nat}BAs, theory predicts $\alpha \approx 1.6$ [108,111]. For isotopically pure BAs, theoretical predictions for α lie between 1.7 and 1.8 [114,115,128]. The small disagreement in theory *vs.* experiment for α could originate from several factors. The ratio of four-phonon to three-phonon scattering rates in BAs could be higher than predictions [114,115,128]. Although first-principles calculations do not use fitting parameters, their accuracy is affected by a variety of

factors [147,148]. Jain and McGaughey found the choice of exchange-correlation function can change the predicted thermal conductivity of Si by ~30% [147]. Zhou *et al*. report that fourth-order force constants are extremely sensitive to the energy surface roughness of the exchange correlation functionals [148]. Another possibility for why the experimental α is higher than theoretical predictions is that higher-order processes than four-phonon scattering affect Λ in BAs.

Another possible explanation for why α in BAs is higher than theoretical predictions is temperature-induced changes of the phonon dispersion. Three- and four-phonon scattering rates in BAs are sensitive to the *a-o* gap and the bunching of acoustic modes [7,23,149,150]. To investigate this hypothesis, we conducted temperature-dependent Brillouin and Raman scattering experiments to assess how phonon frequencies evolve with increasing temperature, see Figure 4.16 and 4.17. Our Brillouin scattering measurements revealed that the longitudinal acoustic phonon frequencies near the zone center change by less than 1% upon heating from 300 to 600 K. Raman scattering measurements indicated that the optical phonon frequency at zone center experiences a 1% decrease. Therefore, it is unlikely that temperature-induced changes to the phonon dispersion can explain why Λ is proportional to $1/T^2$. We note that neither Raman nor Brillouin scattering measures the zone-edge acoustic phonons that are most responsible for heat transfer in BAs. So, our experiments do not definitively exclude temperature-induced changes in phonon dispersion as an important effect.

To characterize defects in our samples, we performed pump/probe transient reflectivity microscopy (TRM) on bare BAs samples with incident photon energy of 1.58 eV (Figure 4.18). In these experiments, we irradiated the BAs surface with a pump beam. We measured the intensity of a reflected probe beam as a function of pump/probe delay time. The laser energy is ~ 0.26 eV less than the 1.84 eV band gap of BAs [118,125]. Therefore, in the absence of impurities,

we expect negligible absorption and no pump-induced change in the reflectance of BAs. In the presence of impurities that form defect states in the band gap, we expect measurable TRM signal. The effect of an impurity on absorption will depend on the energy level of the defect state. If the defect state's energy is near the conduction or valence band edges (ionization energy $\leq 3k_BT \approx$ 75 meV), the impurity affects absorption by introducing free carriers, see Figure 4.18A. Alternatively, defects that form states far from the conduction or valence band edges will allow optical transitions to/from the defect state, see Figure 4.18B. For impurities with moderate ionization energies, *e.g.*, 100-300 meV, we expect both these absorption mechanisms will matter.

We observed non-zero TRM signals in most BAs samples (Figure 4.18C). We performed TRM measurements at ≥ 10 spots on each sample. Most measurements were performed with a pump fluence of 0.7 J/m^2 and probe power of 2 mW. A few measurements were conducted with different pump fluences and probe powers. For these measurements, to facilitate comparisons in Figure 4.18, we scaled the signals by a factor to account for the difference in pump fluence and probe power. Each marker in Figure 4.18C represents the average value of all measured spots, while error bars represent the standard deviation. We observed a correlation between $\Lambda_{300\mathrm{K}}$ and TRM signals (Figure 4.18C). Additionally, we performed wavelength-dependent pump/probe TRM measurements (Figure 4.18E) on BAs-1500 as well as two BAs samples whose $\Lambda_{300\mathrm{K}}$ are 1000 (BAs-1000) and 400 W m^{-1} K^{-1} (BAs-400), respectively. For this measurement, we fixed our laser beam on a region that had a small TRM signal, *i.e.*, a region with a low density of defects. We observed an increasing TRM signal as photon energy approaches the band gap of BAs. As a set of control experiments, we also performed TRM measurements with a laser energy of 1.58 eV on crystals with different band gaps: Si (1.12 eV) [151], GaAs (1.42 eV) [152], GaP (2.26 eV) [153], and GaN (3.39 eV) [154]. The carrier densities of the GaP and GaN samples are $(4\sim6) \times 10^{16}$ cm^{-3} and $\sim 1 \times 10^{18}$ cm^{-3}, respectively. As expected, TRM signals are large for

crystals with band gaps less than 1.58 eV, and negligibly small for crystals with band gaps greater than 1.58 eV, see Figure 4.18F.

To explore sample homogeneity, we mapped how TDTR and TRM signals change with position for two of the crystals: BAs-1500 and BAs-1000 (Figure 4.19). We note that the TRM and TDTR maps are not well correlated: the TRM maps display bright spots that are not visible on the TDTR maps. Moreover, we observed nearly zero TRM signals on a BAs sample (Figure 4.21) with $\Lambda_{300K} \approx 800$ W m^{-1} K^{-1}. We interpret these observations to mean that point defects within the sample can affect the absorption/emission spectrum while having little impact on thermal conductivity, and vice-versa. As we explain below, this explanation aligns with prior theoretical modeling of how point defects affect optical and thermal properties [119,155].

Prior studies show the presence of impurities such as C, Si, O, and I in BAs crystals [108,117,119,156]. Theoretical calculations [157] predict that the substitutional defects formed by O on As sites (O_{As}) lead to defect states in the middle of the band gap. Alternatively, C and Si impurities on As sites (C_{As} and Si_{As}) are predicted to be shallow acceptors with ionization energies of 0.081 and 0.07 eV, respectively [157]. So, C_{As} and Si_{As} are expected to affect absorption by introducing free-holes. C and Si impurities on B sites (C_B and C_{Si}) are predicted to be donors with ionization energies of 0.28 and 0.14 eV, respectively [157]. Therefore, C_B and Si_B are expected to affect absorption in one of the two ways mentioned above. Ionized C_B and Si_B impurities introduce free electrons, while C_B and Si_B that are not ionized will allow optical transitions from defect states into the conduction band.

All these types of impurities are also expected to have different effects on the thermal conductivity of BAs. Chen *et al.* [117] predict that reducing BAs's thermal conductivity by 10% requires a concentration of $\approx 3\times10^{18}$ cm^{-3} neutral C_B defects, $\approx 10^{18}$ cm^{-3} Si_{As} or C_{As} defects, and

3×10^{17} cm^{-3} O_{As} defects. So, in short, while impurities affect both thermal transport and below-band-gap optical absorption, we do not expect a perfect correlation between these physical properties.

Based on the TRM results, BAs samples with Λ_{300K} of 1500 W m^{-1} K^{-1} are not free of defects. This indicates that the intrinsic thermal conductivity could be larger than 1500 W m^{-1} K^{-1}, and the intrinsic temperature dependence between 300 and 600 K of BAs may be stronger than $1/T^2$. Existing first-principles calculations cannot explain the coexistence of Λ_{300K} > 1500 W m^{-1} K^{-1} and $\alpha > 2$. First principles calculations predict Λ_{300K} of 3100 W m^{-1} K^{-1} and $\alpha = 1$ if only considering three-phonon scattering [149]. In the limit of only four-phonon scattering happens in BAs, Λ_{300K} is 15330 W m^{-1} K^{-1} and $\alpha = 2$ [111,149]. Simply adding phonon-defect scattering in the calculations can reproduce Λ_{300K} > 1500 W m^{-1} K^{-1} but will result in $\alpha < 2$. One possible explanation for $\alpha > 2$ is that higher-order processes than four-phonon scattering affect Λ in BAs. However, simply adding higher-order processes to prior first-principles calculations will further reduce the phonon lifetimes, and subsequently result in lower ambient thermal conductivity. Therefore, the current ultrahigh thermal conductivity at room temperature and its strong T dependence ($\alpha = 2$) is unexpected.

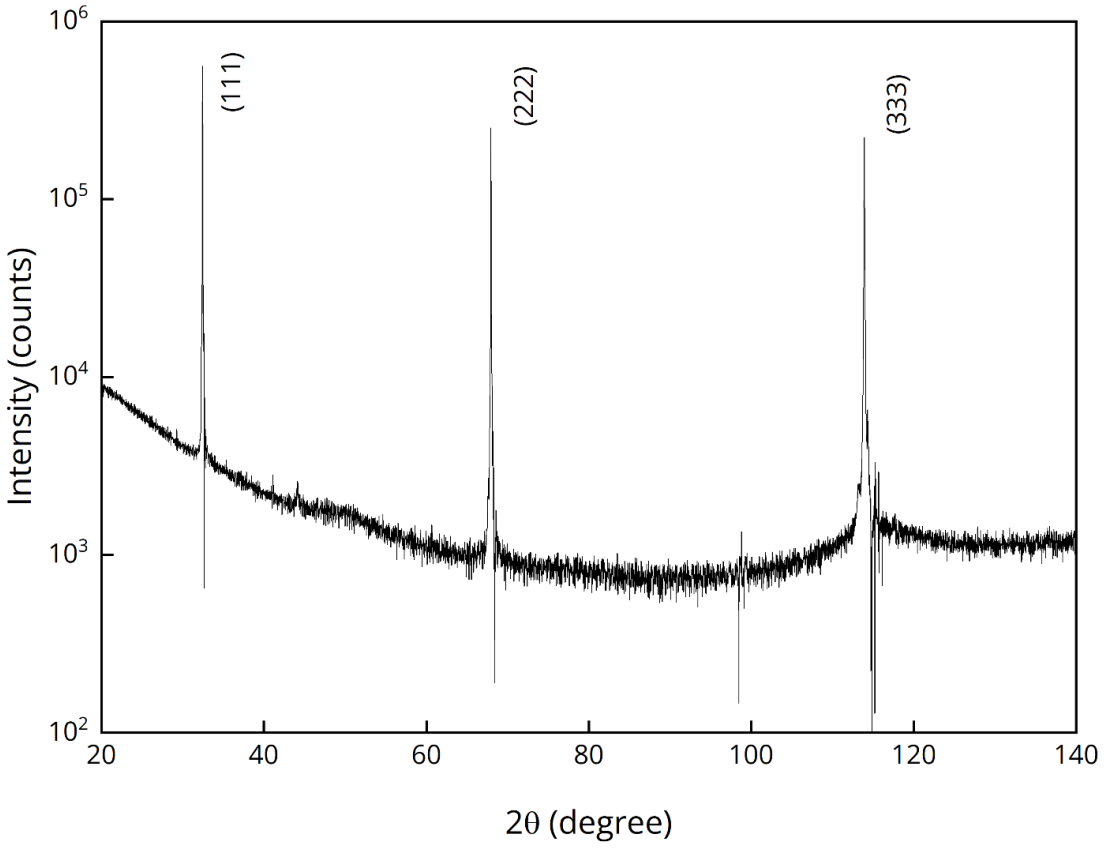

Figure 4.1. X-ray diffraction measurement on a BAs sample with room-temperature thermal conductivity of 1500 W m^{-1} K^{-1} (measured by Fengjiao Pan).

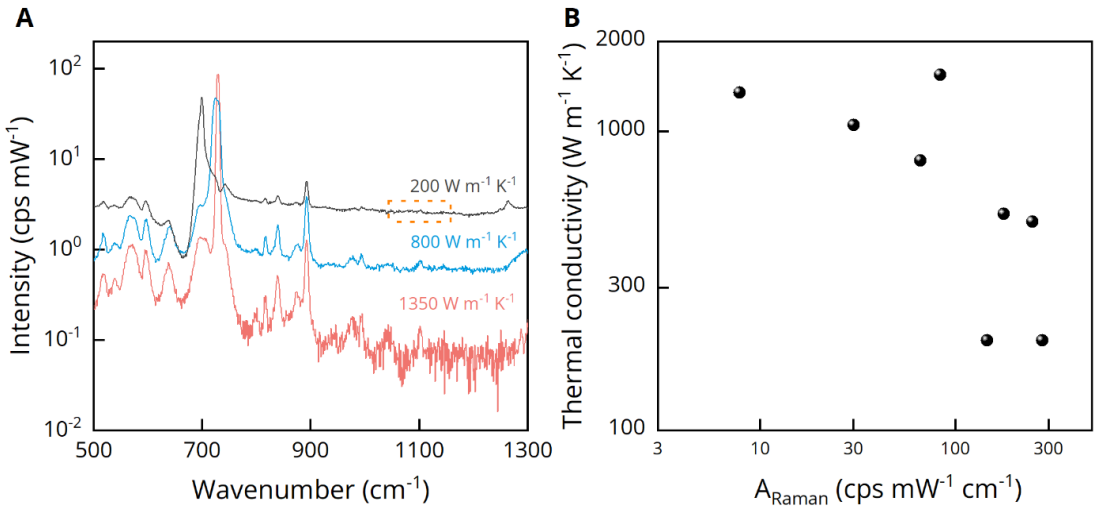

Figure 4.2. Raman scattering of BAs crystals.

(A) Raman spectra of three BAs samples of different thermal conductivity. The 200 W m^{-1} K^{-1} sample is an 11BAs, and the 800 and 1350 W m^{-1} K^{-1} ones are ^{10}BAs samples. The orange rectangle denotes the wavenumber range from 1050 to 1150 cm^{-1} in which the intensity integration is performed. (B) Thermal conductivity versus the intensity integration of selected BAs samples. The excitation laser has a 532 nm wavelength, the incident laser power is 15 mW, the collection time is 50 s, and the numerical aperture (NA) of the objective lens is 0.28. The focused laser spot size is ~ 6 μm ($1/e^2$ radius).

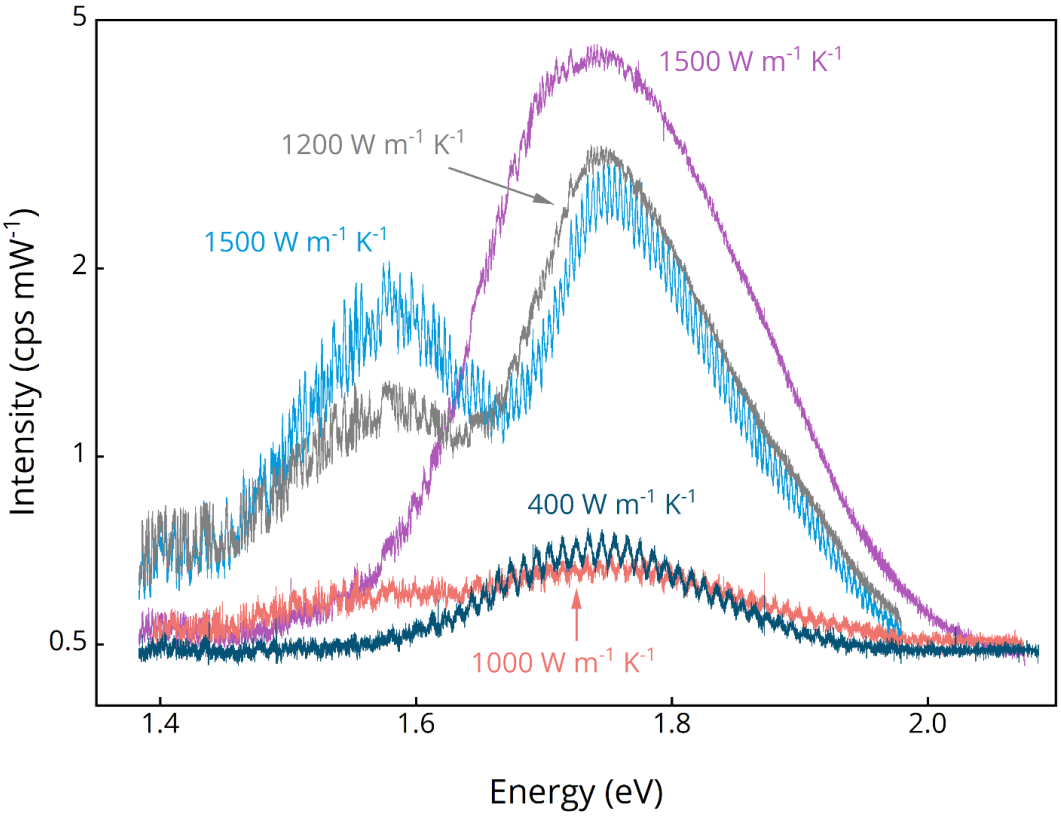

Figure 4.3. Photoluminescence measurements of five BAs samples with different thermal conductivities.

The excitation laser has a 532 nm wavelength, the incident laser power is 20 mW, the collection time is 30 s, and the NA of the objective lens is 0.28. The focused laser spot size is ~ 6 μm ($1/e^2$ radius).

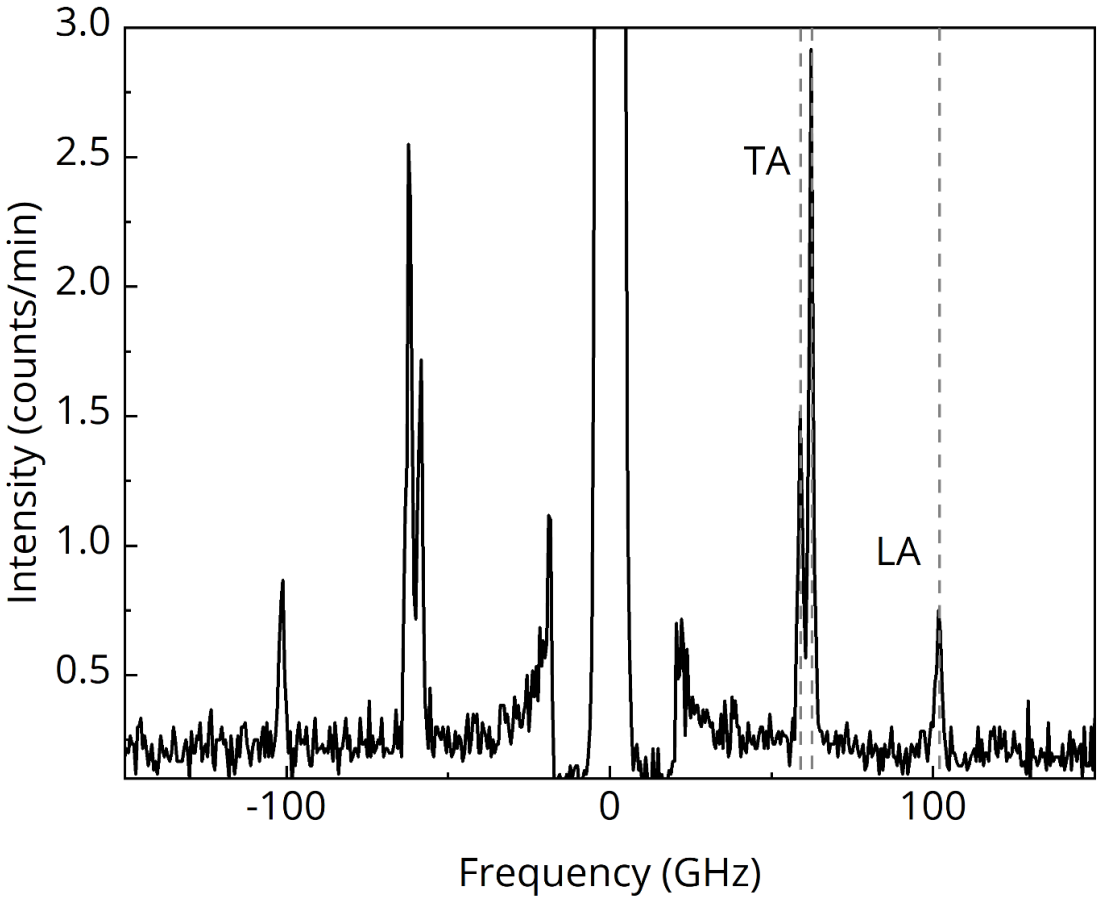

Figure 4.4. Brillouin light scattering spectrum of a BAs sample in the backscattering geometry (measured by Zahra Ebrahim Nataj).

The angle between incident laser beam and surface normal ([111]) is 30°. The peaks labeled as LA and TA correspond to the longitudinal acoustic and the transverse acoustic bulk phonons. The dashed lines are guides to the acoustic phonon frequency of these peaks. The excitation wavelength is 532 nm. The incident laser beam is *p*-polarized. The index of refraction of BAs is 3.25 [133]. In the [111] direction, we expect the transverse branches to degenerate. The splitting of the transverse peaks indicates a small misalignment of the measurement axis relative to the [111] direction. The calculated refraction angle for the 30-degree incidence is 8 degrees. Therefore, we are measuring the sound velocity along a direction which is 8 degrees away from [111].

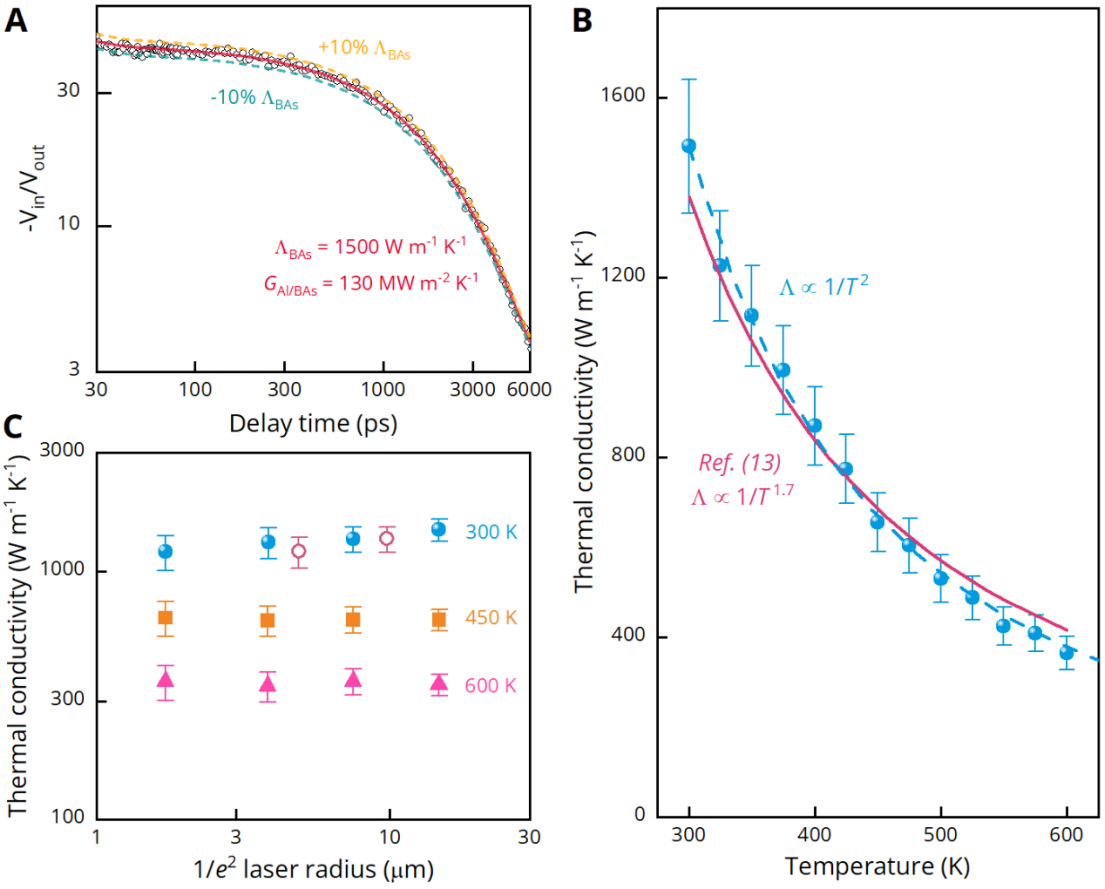

Figure 4.5. Thermal conductivity of BAs measured by TDTR.

(A) Time domain thermoreflectance data with thermal model best-fit (red line) for a high purity BAs crystal with $\Lambda \approx 1500$ W m^{-1} K^{-1}. (B) BAs thermal conductivity versus temperature (markers), along with theoretical predictions for isotopically pure BAs [115]. (C) Apparent thermal conductivity of BAs versus laser spot size ($1/e^2$ radius) at 300, 450, and 600 K. (Filled and open markers denote measurements performed at UCR and UIUC, respectively.)

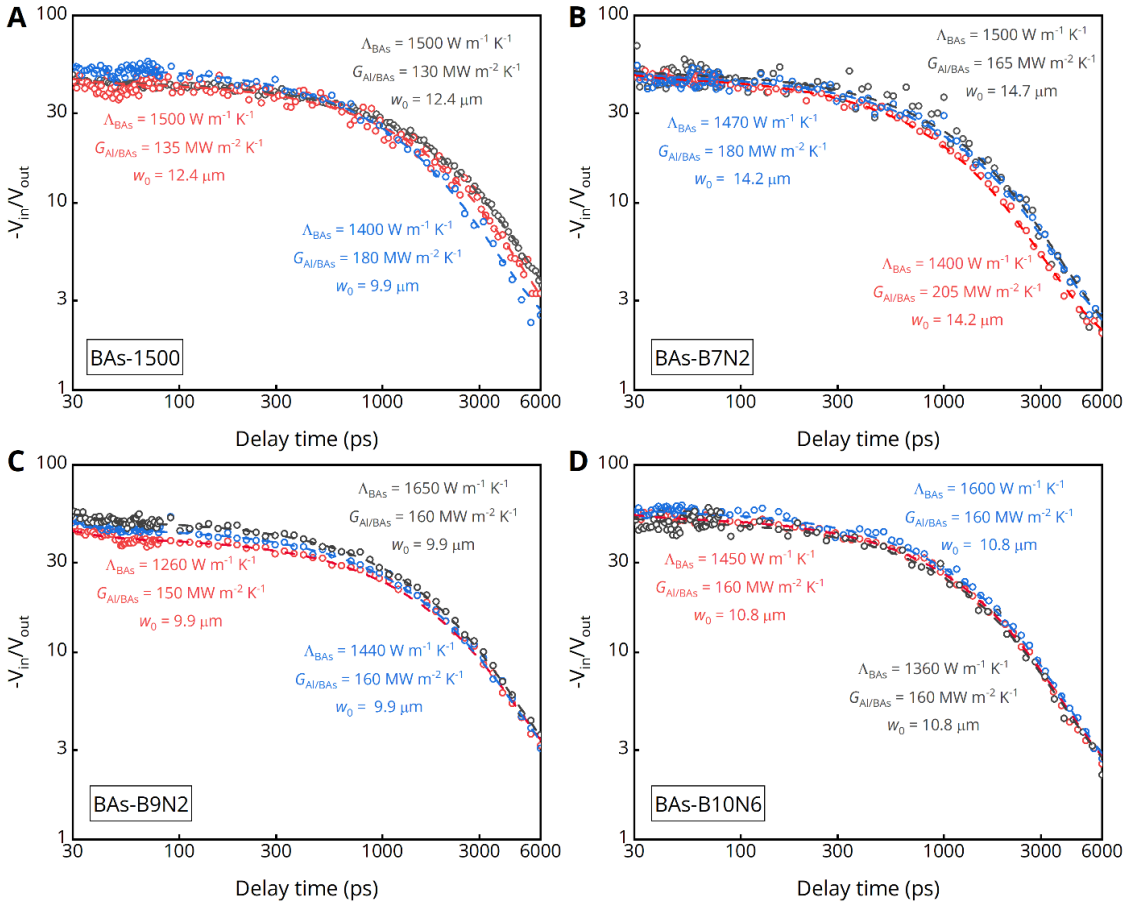

Figure 4.6. TDTR scans on four distinct high-thermal-conductivity BAs samples at different measurement spots, along with fittings of the heat diffusion model.

Each panel in the figure showcases TDTR scans performed on a specific sample. Different colored circles represent data collected from distinct spots on each sample. Dashed lines in corresponding colors depict fittings of the heat diffusion model. Alongside the data, the fitted thermal conductivity, interface conductance, and measured laser spot size for each scan are labeled. Note that we examined the impact of plasma-etching time on interface conductance for BAs-1500 and BAs-B7N2. As a result, different scans on these two samples exhibit varying interface conductance. Additionally, measurements on BAs-1500 and BAs-B7N2 were not conducted on the same day, leading to differences in laser spot sizes. Three TDTR scans on BAs-B9N2 were conducted on the same day, and the same applies to BAs-B10N6. We emphasize that these four samples have spots with thermal conductivity higher than 1500 W m^{-1} K^{-1} and spots lower than 1500 W m^{-1} K^{-1}, although we report their thermal conductivity of 1500 W m^{-1} K^{-1}. Statistically, 1500 W m^{-1} K^{-1} is the most common value we observe on these four samples.

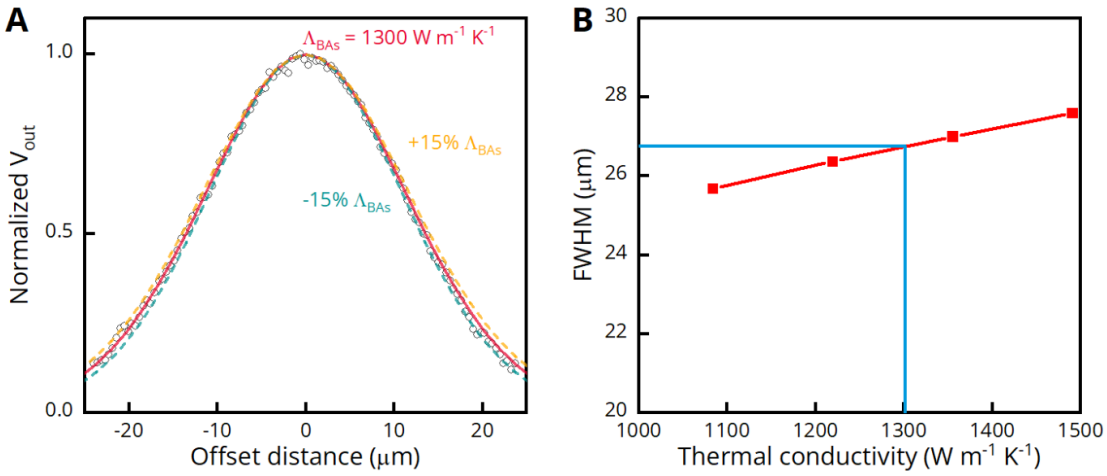

Figure 4.7. Data analysis of beam offset measurements.

(A) A beam offset scan (circles) along with the best fit (red line). Predictions for 15% larger and smaller thermal conductivity of BAs are shown as yellow and green dashed lines, respectively. The vertical axis is the normalized out-of-phase signal, V_{out} / $V_{0ut}(max)$. The horizontal axis represents the offset distance between pump and probe beams. (B) The full width at half maximum (FWHM) versus thermal conductivity predicted from the heat diffusion model.

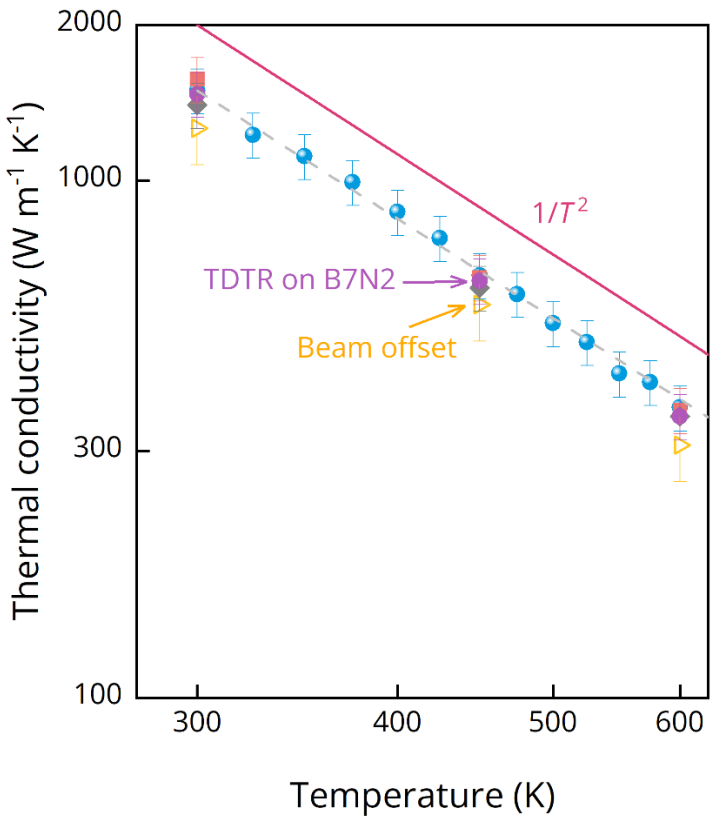

Figure 4.8. Test of reproducibility of the temperature dependent thermal conductivity of the BAs-1500 sample.

We reproduced TDTR measurements on the BAs-1500 sample twice at different dates, shown as gray and pink symbols. Yellow triangles are thermal conductivity of the BAs-1500 sample measured using beam offset measurements. Additionally, we measured another BAs crystal (purple diamonds) whose ambient thermal conductivity is also 1500 W m^{-1} K^{-1}, labelled as B7N2.

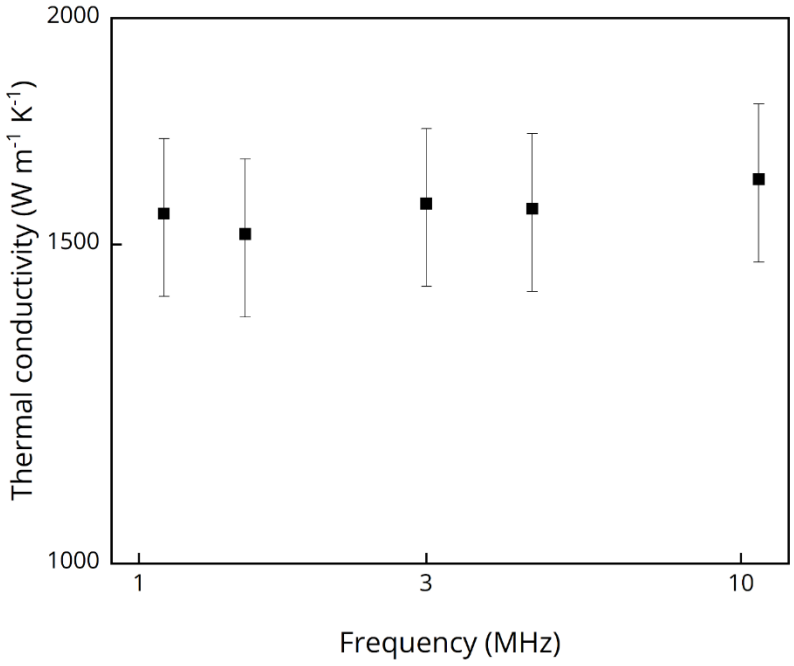

Figure 4.9. Thermal conductivity versus pump modulation frequency in TDTR measurements.

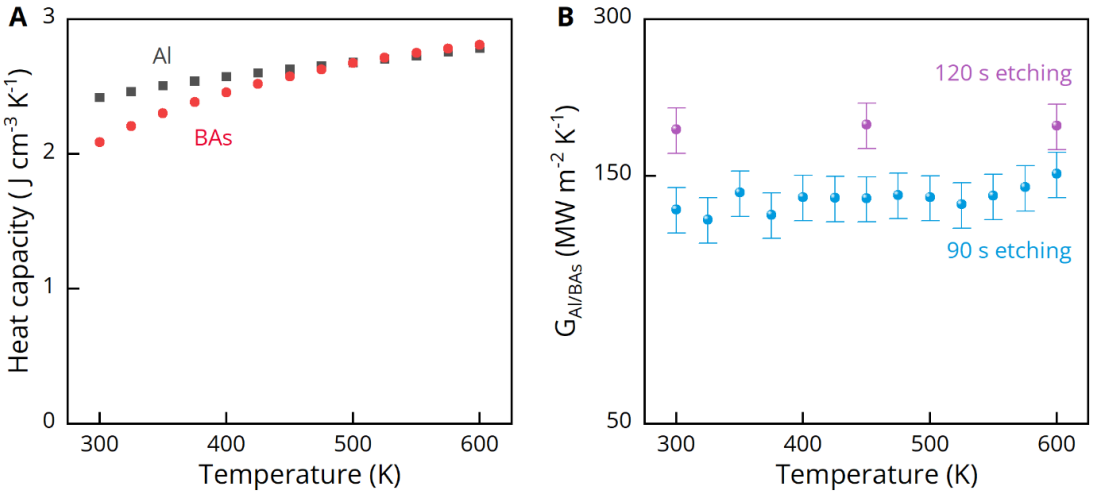

Figure 4.10. Temperature dependent parameters in the heat diffusion model.

(A) Heat capacity of Al (gray squares) and BAs (red dots) versus temperature from Ref. [92] and [132]. (B) Interface conductance between Al and BAs versus temperature derived from TDTR measurements.

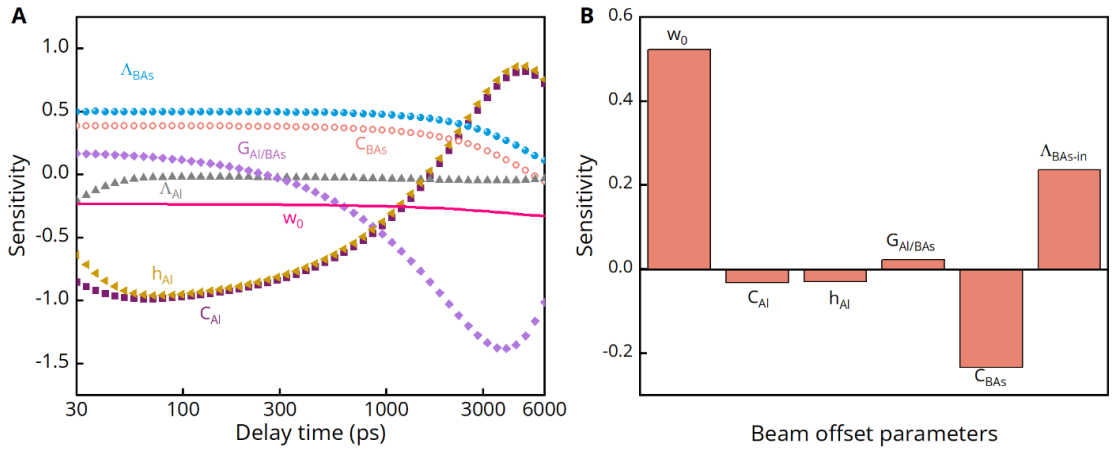

Figure 4.11. Sensitivity analyses of TDTR and beam offset measurements.

(A) Sensitivity analysis of TDTR. Parameters of interest include thermal conductivity (Λ) of Al and BAs, heat capacity (C) of Al and BAs, thickness (h) of the Al film, interface conductance (G) between Al and BAs, and $1/e^2$ laser radius (w_0). (B) Sensitivity analysis of beam offset measurements. The sensitivity of the cross-plane thermal conductivity of BAs is close to zero. Λ_{BAs-in} denotes the in-plane thermal conductivity of BAs.

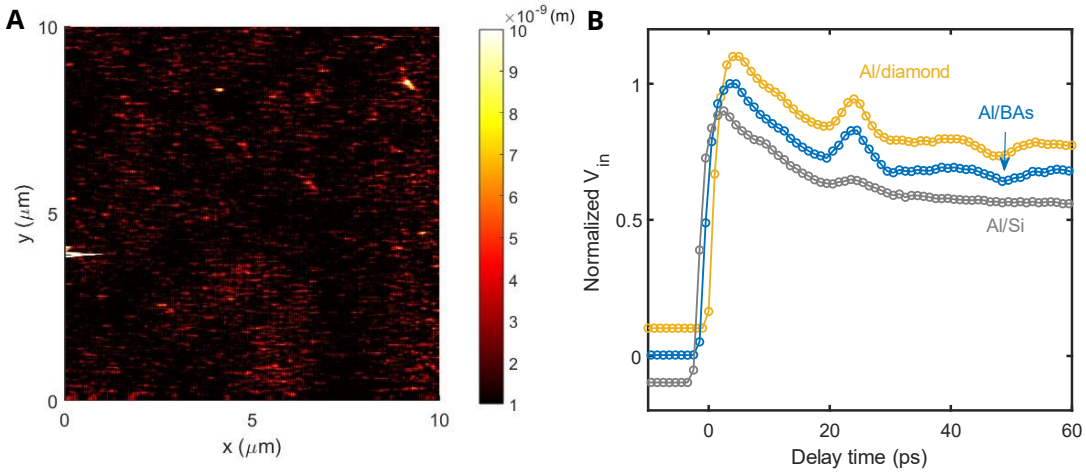

Figure 4.12. Roughness characterization of a BAs sample with thermal conductivity of 1500 W m^{-1} K^{-1}.

(A) Atomic force microscopy on the BAs sample. The root-mean-square roughness of the measured area is 1.8 nm. (B) Comparison of the acoustic echoes between Al/BAs, Al/Si, and Al/diamond samples. Roughness can sometimes cause broadening of the acoustic echoes. So, we monitor the echo width in all TDTR measurements. The V_{in} signal is normalized by its maximum value and shifted for clarity.

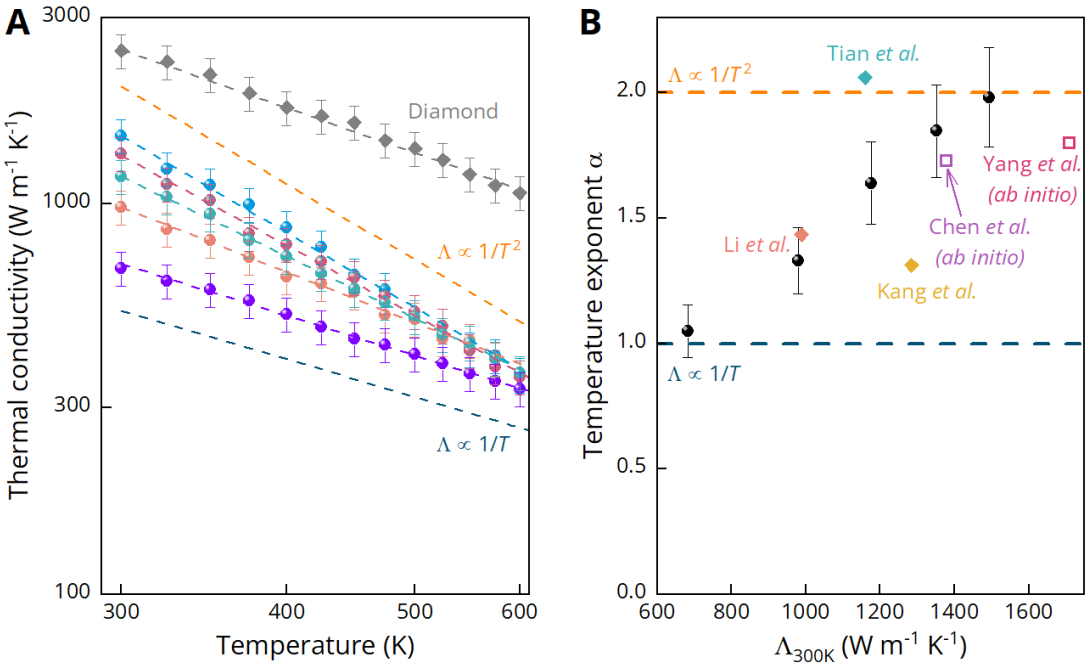

Figure 4.13. Temperature-dependent thermal conductivity of five selected BAs samples.

(A) Thermal conductivity of five selected BAs crystals and a type IIA diamond measured using TDTR. (B) The relationship between the temperature exponent and the room-temperature thermal conductivity of the five BAs crystals shown in (A). Diamond and square markers are prior experimental results and theoretical predictions (isotopically pure BAs).

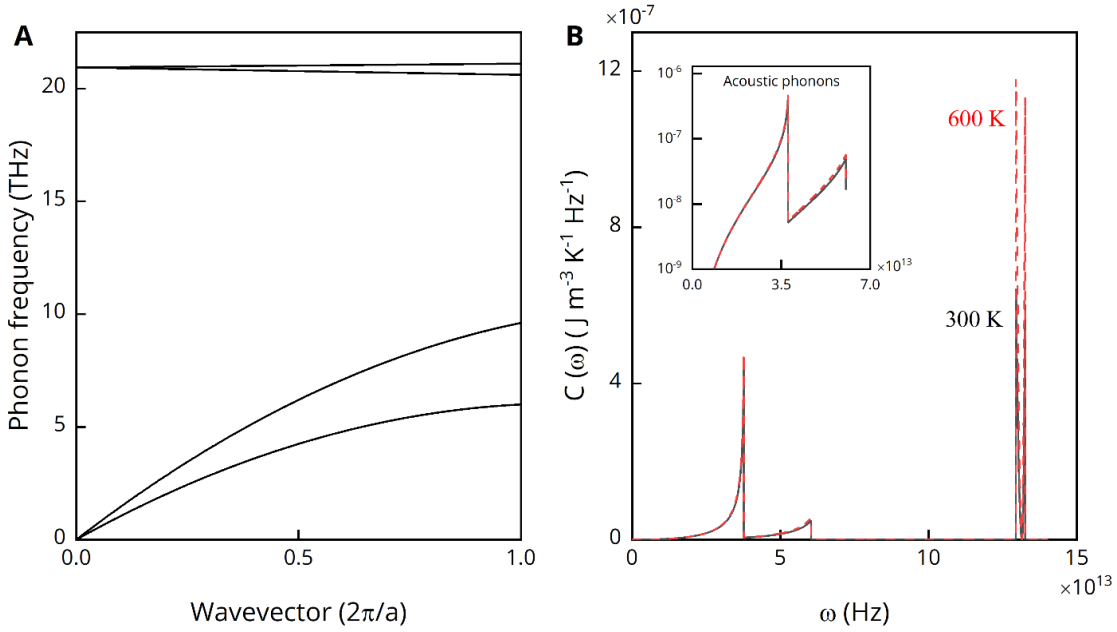

Figure 4.14. Spectral heat capacity of BAs at 300 and 600 K calculated from an approximate isotropic phonon dispersion.

(A) Approximate isotropic phonon dispersion of BAs. The phonon dispersion is constructed based on the experimental results in Ref. [158]. (B) Spectral heat capacity at 300 and 600 K calculated from the phonon dispersion in (A). The inset shows a highlight of heat-carrying acoustic phonons.

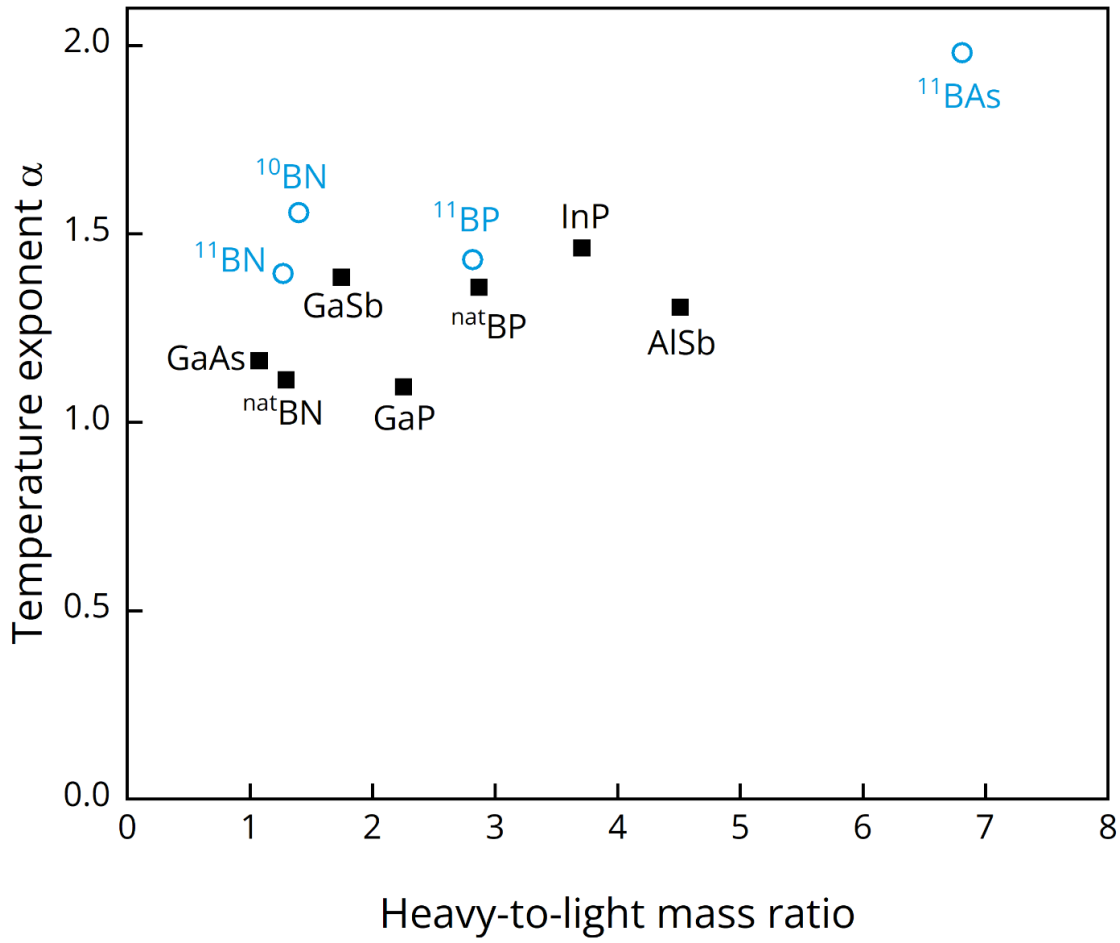

Figure 4.15. Temperature exponent versus heavy-to-light mass ratio for III-V semiconductors.

The temperature exponent is obtained by fitting the thermal conductivity versus temperature experimental data at 300-600 K using $\Lambda \propto 1/T^{\alpha}$. GaAs [159], ^{nat}BN [109], GaSb [160], GaP [160], ^{nat}BP [161], InP [146], and AlSb [160] are compounds synthesized using natural isotope concentrations (black squares). ^{11}BN [115], ^{10}BN [115], ^{11}BP [161], and ^{11}BAs are isotopically pure samples (blue circles). All the included samples have a zincblende crystal structure.

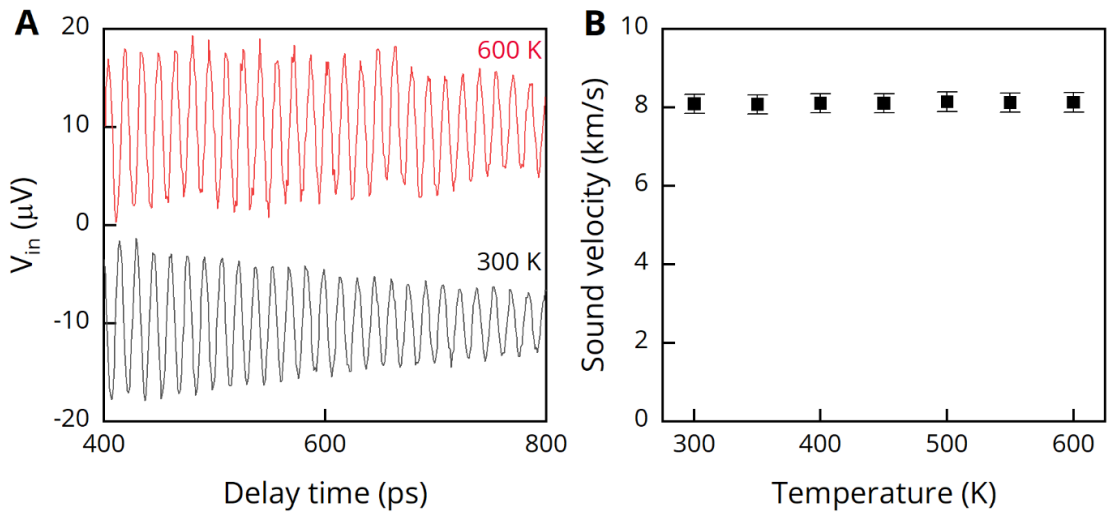

Figure 4.16. Forced Brillouin scattering on BAs between 300 and 600 K.

(A) Brillouin oscillation of BAs at 300 and 600 K. The laser power is 25 mW, excitation wavelength is 783 nm, and the focused laser spot size is ~ 10 μm in $1/e^2$ radius. Our BAs samples show spatial variations in absorption, as indicated by TRM mappings (Figure 4.19). The two scans were not measured at the same spot, so the absorptions are different. (B) The longitudinal sound velocity along [111] direction of BAs versus temperature derived from the Brillouin frequency. The observed Brillouin frequency is 65.2 GHz, consistent with prior report which is 65.2 GHz with 778 nm excitation wavelength [134,162]. The error bars are derived from the FWHM of the Brillouin spectrum (fast Fourier transform of panel A).

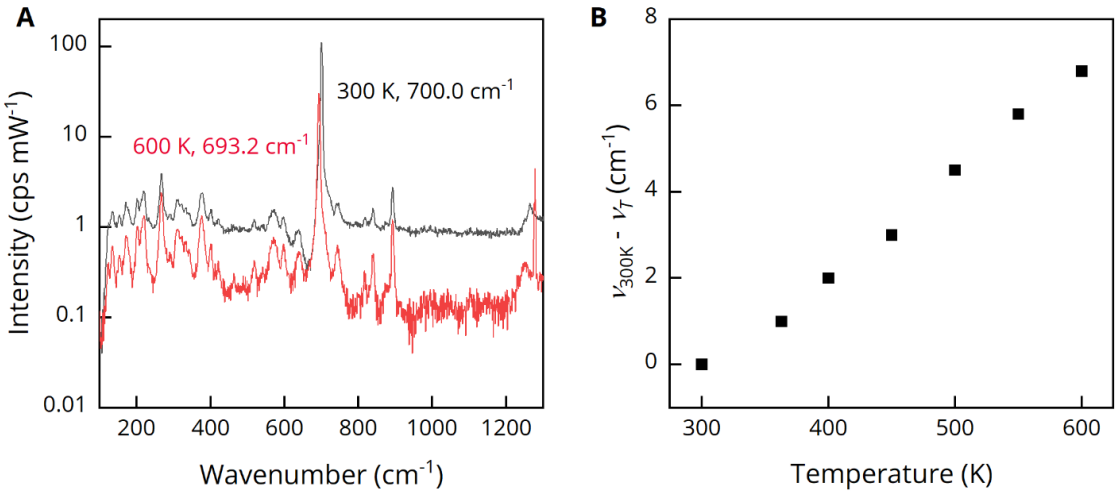

Figure 4.17. Raman scattering on BAs between 300 and 600 K.

(A) Raman spectra of BAs at 300 and 600 K. (B) Wavenumber change of the Raman peak relative to the 300 K value versus temperature. The excitation laser has a 532 nm wavelength, the incident laser power is 8 mW, the collection time is 20s, and the NA of the objective lens is 0.28. The focused laser spot size is ~ 6 μm ($1/e^2$ radius). Ref. [115] predicts that there is no frequency change for the zone-center optical phonon between 300 and 1000 K by first-principles calculations. Ref. [163] claims a volumetric thermal expansion coefficient of ~1.2×10^{-5} K^{-1}, and a Grüneisen parameter of 1 for the zone-center transverse optical phonon mode in BAs. The calculated phonon softening is ~0.4%, smaller than our Raman scattering measurements.

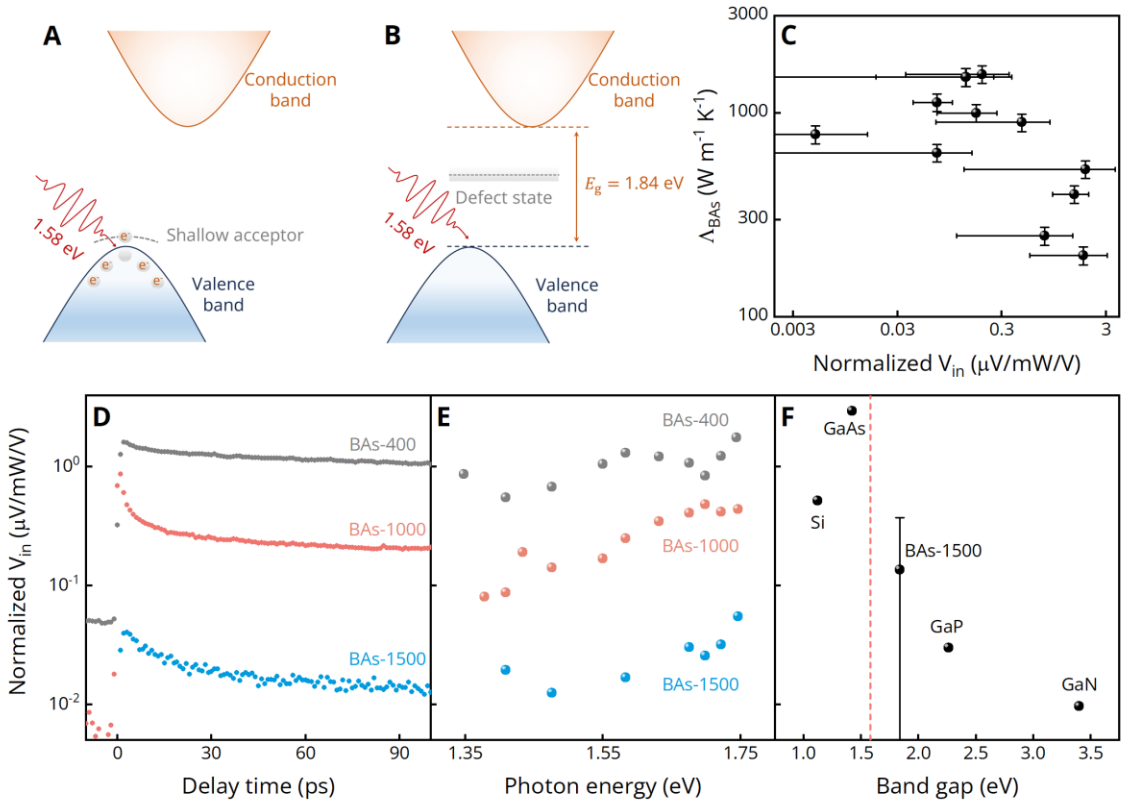

Figure 4.18. Relationship between transient reflectivity microscopy signal and thermal conductivity of BAs.

Free carriers from shallow donors/acceptors, and deeper defect states in the band gap lead to optical absorption and non-zero transient reflectivity signal at photon energies below the band gap. (A) and (B) are schematics showing the impact of a shallow acceptor and a deep defect state on absorption of energies below the band gap, respectively. (C) Thermal conductivity of BAs crystals versus TRM signals obtained from bare BAs samples with 1.58 eV incident photons. The normalized V_{in} is the in-phase voltage measured by lock-in amplifier, normalized by the pump laser power and voltage on the photodiode detector. (D) Raw data obtained from the transient reflectivity microscopy with 1.58 eV incident photons. (E) Transient reflectivity microscopy signals on three bare BAs samples as a function of excitation photon energy. (F) Transient reflectivity microscopy signals for bare Si, GaAs, BAs, GaP, and GaN single crystals. The vertical dashed line indicates laser energy.

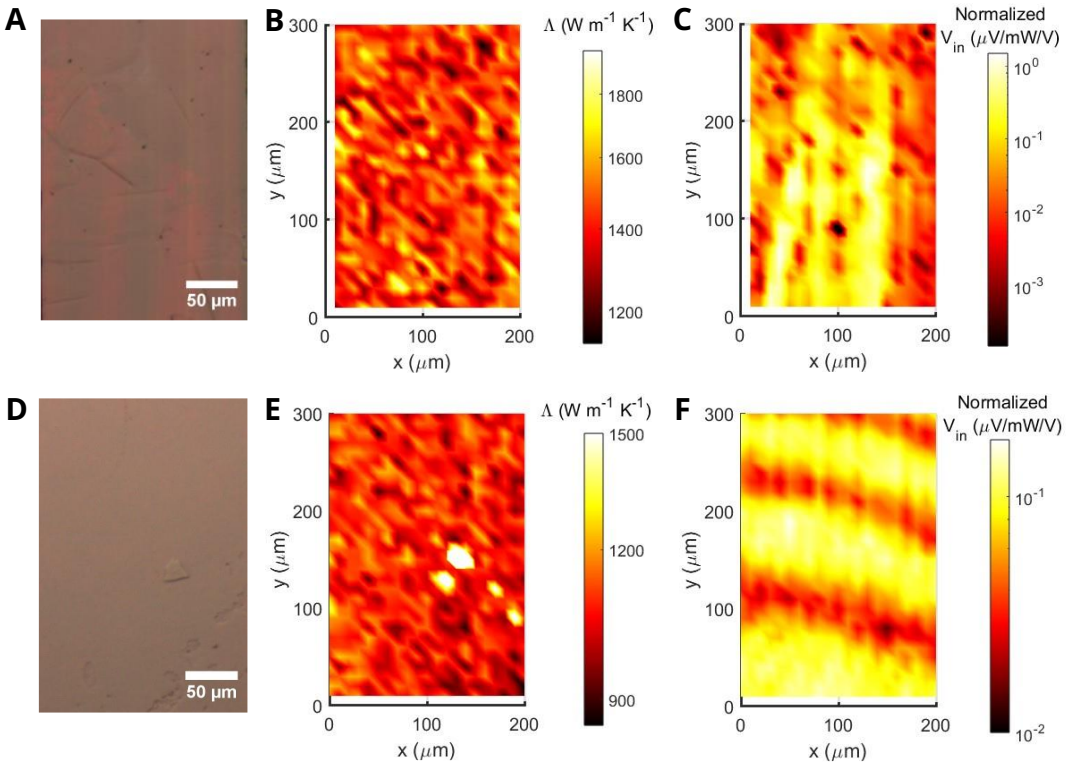

Figure 4.19. Thermal conductivity and TRM maps on BAs crystals.

(A) and (D) are optical images of two BAs samples whose ambient thermal conductivity are 1500 and 1000 W m^{-1} K^{-1}, respectively. (B) and (E) are corresponding thermal conductivity maps. (C) and (F) are reflectance maps on the two bare BAs samples correspondingly.

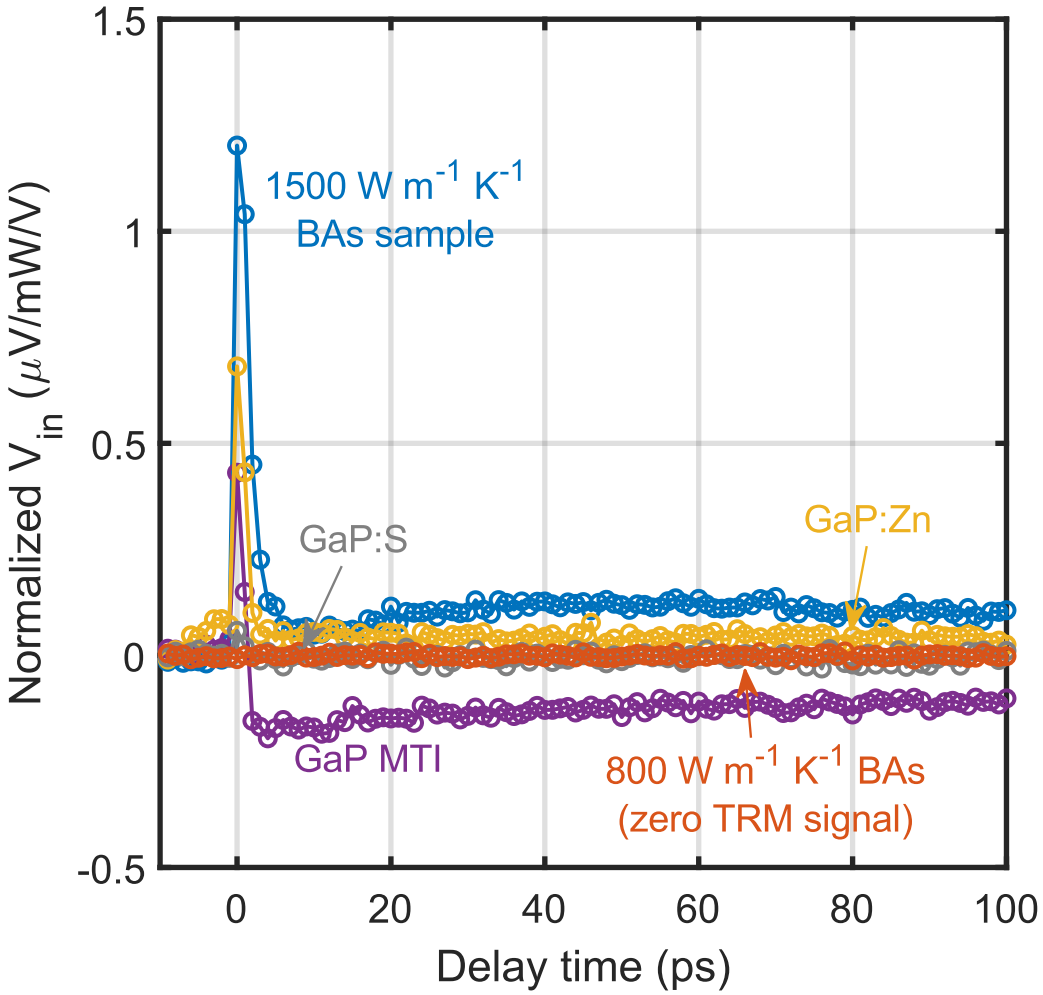

Figure 4.20. Pump/probe transient reflectivity microscopy measurements on BAs and GaP samples

V_{in} is the in-phase voltage measured by the lock-in amplifier and is proportional to the pump-induced reflectivity change. The carrier concentrations for the Zn-doped and S-doped GaP are 1.15×10^{18} and 1.9×10^{18} cm^{-3}, respectively (provided by the vendor). We observed zero-TRM signals on a BAs sample with ambient thermal conductivity of 800 W m^{-1} K^{-1} (orange circles). The incident laser wavelength is 783 nm.

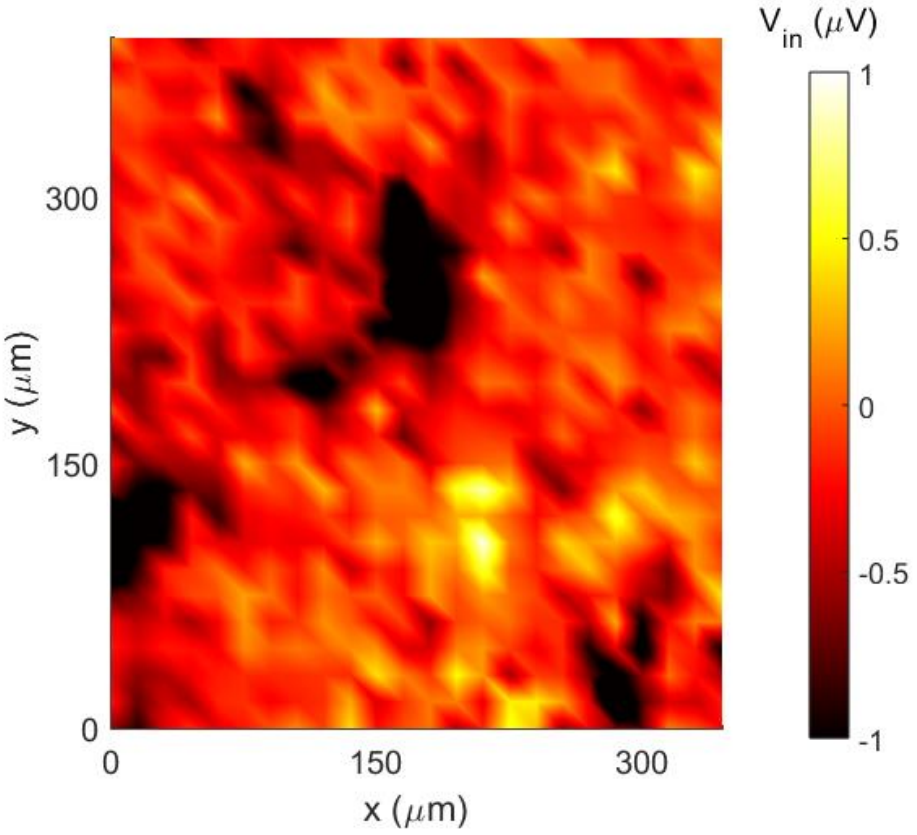

Figure 4.21. TRM map on the 800 W m^{-1} K^{-1} BAs sample. Most spots on the sample show nearly zero TRM signals.

Table 4.1. Parameters in beam offset measurements.

We selected appropriate laser spot size (w_0) and pump modulation frequency (f) to make w_0 match the heat diffusion length (d) at given temperatures.

Temperature (K)	w_0 (μm)	f (MHz)	C_{BAs} (J cm^{-3} K^{-1})	Λ_{BAs} (W m^{-1} K^{-1})	d (μm)
300	9.9	1.9	2.09	1500	11
450	5.0	3.2	2.58	650	5.0
600	5.0	1.8	2.81	365	4.8

Table 4.2. Brillouin – Mandelstam spectroscopy results on nine BAs samples.

The ambient thermal conductivity (Λ_{300K}) is measured by time-domain thermoreflectance. The frequencies of low-wavevector transverse (TA) and longitudinal acoustic (LA) phonons are measured by BMS.

Sample number	Λ_{300K} (W m^{-1} K^{-1})	TA frequency (GHz)	LA frequency (GHz)
1	390	62.71	102.27
2	300	62.65	101.89
3	670	62.22	101.76
4	320	62.29	101.24
5	300	62.23	101.77
6	1000	62.31	102.61
7	720	62.22	101.76
8	1180	63.09	103.34
9	250	62.03	101.63

Chapter 5 Vibrational Properties and Thermal Conductivity of Perovskites under Pressure

Chapter 5 was published in "Response of Vibrational Properties and Thermal Conductivity of Perovskites to Pressure." Songrui Hou, Richard B. Wilson, Chen Li, *Materials Today Physics* 32: 101010 (2023).

5.1 Introduction

Perovskite oxides are an important class of functional materials because small modifications in crystal structure can cause dramatic changes in properties [164,165]. $SrTiO_3$ is a 'model' system for this kind of structure/property relationship due to its quantum paraelectric ground state, as well as its cubic-tetragonal phase transition at 105 K. As a result, the relationship between temperature, vibrational dynamics, and thermal transport in perovskites such as $SrTiO_3$ has been explored for more than half a century [166–170]. However, the question of how pressure-induced changes in vibrational dynamics affect Λ has received much less attention [171]. In many ways, pressure is a more effective experimental knob for changing vibrational dynamics than temperature. Phonons are quanta of lattice vibration and the main heat carriers in nonmetallic crystals [11]. The thermal conductivity from phonons is

$$\Lambda = \int_0^{\omega_m} \frac{1}{3} c(\omega) \cdot v(\omega)^2 \cdot \tau(\omega)\, d\omega, \qquad (5.1)$$

where $c(\omega)$ is the heat capacity per phonon of frequency ω, $v(\omega)$ is the phonon group velocity, and $\tau(\omega)$ is the phonon lifetime. All three parameters depend on the vibrational dynamics. Temperature is only effective in tuning the frequency of some low-energy transverse optic

phonons in perovskites [172,173]. Pressure will affect the frequency of nearly all phonon modes. By measuring both vibrational dynamics and thermal conductivity under pressure, we can determine how pressure-induced changes in vibrational dynamics affect thermal transport.

In this work, we measured the $\Lambda(P)$ of $SrTiO_3$ and $KTaO_3$ up to 28 GPa by time-domain thermoreflectance (TDTR) with a diamond anvil cell (DAC). We also performed Raman and stimulated Brillouin scattering measurements of vibrational properties vs. pressure.

$SrTiO_3$ and $KTaO_3$ were chosen for our study due to their similarities and differences. Both materials have similar crystal and vibrational structures. $SrTiO_3$ and $KTaO_3$ have a cubic structure under ambient conditions (space group: $Pm\bar{3}m$). Both crystals have soft TO phonon modes near Γ point in the Brillouin zone [173,174]. By soft modes, we mean that the frequencies of these modes decrease upon cooling. $SrTiO_3$ and $KTaO_3$ have different phase diagrams, allowing us to examine the effect of phase transition on vibrational and thermal properties. $SrTiO_3$ experiences a cubic-tetragonal phase transition upon cooling (~105 K at atmospheric pressure) or pressurization (~9.6 GPa at room temperature) [175]. $KTaO_3$ does not undergo a similar phase transition. As a result, $\Lambda(T)$ of $KTaO_3$ has a nearly $1/T$ dependence above 100 K, while $SrTiO_3$ does not [166]. Other reasons we chose to study $SrTiO_3$ include that it is considered a model system for soft-phonon related phase transition phenomena [176] and that its phase transition upon compression is well documented and understood [175,177,178].

We observe that $\Lambda(P)$ of both $SrTiO_3$ and $KTaO_3$ increase linearly upon compression. Between 0 and 20 GPa, Λ of $SrTiO_3$ doubles. Across the same pressure range, Λ of $KTaO_3$ triples. Raman and Brillouin scattering suggest that $SrTiO_3$ experiences a phase transition at ~9.1 GPa. $KTaO_3$ does not change phase in the studied range of 0 to 30 GPa. The Raman modes of $SrTiO_3$ and $KTaO_3$ show similar stiffening under pressure. We compare the pressure-dependent thermal

conductivity of $SrTiO_3$ and $KTaO_3$ with materials of similar crystal structure. The comparison shows that $SrTiO_3$ has a typical pressure dependence, while $KTaO_3$ has a stronger-than-typical pressure dependence. Significant changes in thermal conductivity imply significant changes in one, or all, of the following vibrational properties: (i) number of phonons, (ii) phonon group velocity, and (iii) phonon lifetime. Raman and Brillouin scattering measurements rule out (i) and (ii) as likely causes of the pressure-dependent thermal conductivity. Alternatively, measurements of the Brillouin frequency in $KTaO_3$ and $SrTiO_3$ suggest significant changes in phonon anharmonicity upon compression. Furthermore, the change is more than a factor of 2 larger in $KTaO_3$ than in $SrTiO_3$. Therefore, we conclude $d\Lambda/dP$ of $SrTiO_3$ and $KTaO_3$ are consequences of pressure-induced changes in phonon anharmonicity.

5.2 Materials and Methods

Sample Preparation

The $SrTiO_3$ and $KTaO_3$ are from MTI Corporation. To prepare samples for diamond anvil cell measurements, we polished the samples down to thicknesses of 7 ± 2 μm. We used an optical microscope to estimate the final thickness after polishing. Then we used a needle to break the crystals into small pieces. We selected pieces with lateral dimensions of ~50-80 μm. We deposited an ~80-nm-thick Al or Ta film on the selected pieces. The metal film serves as an optical transducer for TDTR and stimulated Brillouin scattering experiments. Al is a good transducer for TDTR experiments conducted under ambient conditions. However, Al's thermoreflectance at 783 nm is a strong function of pressure and is small above 20 GPa [44]. Our motivation to carry out additional experiments with an α-Ta transducer is to verify that the observed trends are not related to the small thermoreflectance of Al in certain pressure ranges.

The thermoreflectance of α-Ta is large at high pressures [44]. We deposited Ta at 800 °C to obtain α-phase Ta [43], which has higher thermoreflectance than the β-phase Ta that results from room temperature deposition [44]. For Raman scattering measurements, we prepared samples that were not coated with a metal film.

We loaded the samples into DACs with a culet size of 300 μm. All measurements were made on the (100) surface of the samples. We loaded ruby spheres alongside the samples. The fluorescence spectrum of the Ruby was used as a pressure gauge. We used silicone oil (polydimethylsiloxane) as the pressure medium for most measurements. We used Ne as the pressure medium in one set of Brillouin scattering measurements on $SrTiO_3$ (yellow circles in Figure 5.4(b)).

Raman Scattering

We measured the Raman spectrum of $SrTiO_3$ and $KTaO_3$ from 100 to 1200 cm^{-1}. We first measure the ambient Raman spectrum in the air. At high pressure, we collect the spectrum inside a DAC with silicone oil as the pressure medium. To exclude the Raman signals of the pressure medium, we also measured the Raman spectrum of the pressure medium along with our samples as the pressure changes. The exciting laser has a 532-nm wavelength. We used a monochromator (Acton SpetraPro-2500i) to collect the scattered light. We placed a long-pass edge filter (Semrock LP03-532RE-25) in front of the spectrometer to filter out background noise.

TDTR and Stimulated Brillouin Scattering Measurements

The schematics of stimulated Brillouin scattering and TDTR measurements are shown in Figures 5.1(b) and 5.1(c). We performed TDTR measurements of the thermal conductivities of $SrTiO_3$ and $KTaO_3$ at pressures between 0 and 28 GPa. TDTR is a well-established pump probe technique for thermal property characterization [179]. Details of our TDTR setup can be found in

Ref. [180]. The pressure is calibrated using the pressure-dependent shift of the R1 line in the ruby fluorescence spectrum [181].

We also performed stimulated Brillouin scattering measurements using our TDTR setup. For Brillouin measurements of the perovskite crystals, the laser beams impinged through the substrate side of the sample. The beams went through pressure media, samples ($SrTiO_3$ or $KTaO_3$), and then hit the transducer surface. At all pressures that we studied, $SrTiO_3$ and $KTaO_3$ are insulators with band gaps larger than 3 eV [182,183], so they are transparent to laser beams. For Brillouin measurements of the silicone oil, the laser beams impinged on the transducer side of the sample. The beams went through the silicone oil and then were reflected from the transducer. In both sets of measurements, the laser beams were perpendicular to the sample. When the pump beam heats the transducer surface (Al or Ta in our experiments), it launches a strain wave into the perovskite substrates or silicone oil. The strain wave front moves at the longitudinal speed of sound of the samples. Both the strain wave and the transducer can reflect the subsequent probe beam. These two reflected probe beams interfere with each other and cause Brillouin oscillations in the in-phase voltage signal V_{in} [36]. We use the measured Brillouin frequencies of $SrTiO_3$ and $KTaO_3$ as a measure of the longitudinal speed of sound in these materials. We use the Brillouin frequency of silicone oil as an additional measure of pressure [24] to complement our ruby fluorescence measurements.

We use a bidirectional heat diffusion model to analyze the collected TDTR data [15]. The bidirectional model accounts for heat flow from the transducer to both the substrate and silicone oil. The thermal conductivity, heat capacity, and thickness of each layer are the input parameters in the heat diffusion model. Therefore, we must estimate how these parameters evolve with pressure to interpret our TDTR data. We describe how we account for the pressure dependence of all parameters in the following.

Before loading the sample into the diamond anvil cell (DAC), we measured the thickness of the transducers using picosecond acoustics [36]. At high pressures, we assume that the substrates ($SrTiO_3$ and $KTaO_3$) shrink equally in every direction, since both substrates are cubic crystals (space group: $Pm\bar{3}m$). Although $SrTiO_3$ experiences a cubic-tetragonal phase transition at ~9.6 GPa, the tetragonal distortion is small [175]. If the volume of the substrate at pressure P is V_P, and the in-plane area is S_P, then $S_P = S_0 \cdot (V_P / V_0)^{\frac{2}{3}}$. Here, V_0 and S_0 are the volume and area of the substrate at 0 GPa. We assume that the in-plane area of the transducer is equal to S_p. Then the thickness of the transducer at pressure P will be $h_P \approx V_P^{td}/S_P$. Here, V_P^{td} is the transducer volume at pressure P based on its equation of state (EOS) [184,185].

To estimate the pressure dependence of the heat capacities of Al and Ta, we follow Ref. [24], and use a Debye model. For silicone oil, we use published pressure-dependent heat capacities and thermal conductivities [186]. We use first-principles theory predictions for the pressure-dependent heat capacities of $SrTiO_3$ and $KTaO_3$ [187,188]. The first-principles predictions extend only to 20 GPa. Therefore, to interpret the data at pressures above 20 GPa, we extrapolate. We show the pressure-dependent thermal parameters in Figure 5.7.

We measured the electric resistance of Al and Ta films by a four-point probe method, and then calculated their thermal conductivities by the Wiedemann-Franz law. The measured thermal conductivities were 170 and 37 W m^{-1} K^{-1} for Al and Ta, respectively. We fitted the $-V_{in}/V_{out}$ data after 100 ps for Al-coated samples and after 300 ps for Ta-coated samples. The TDTR signal is not sensitive to the thermal conductivity of the transducer at delay times greater than 100 ps. Therefore, we do not need to account for the changes of Λ_{Al} and Λ_{Ta} with pressure.

To explore whether spot size matters in high-pressure TDTR measurements, we used two different spot sizes when measuring $KTaO_3$, R = 6.8 and 3.3 μm, where R is the $1/e^2$ radius of the

laser beam. We measured the laser spot size with a beam-offset method at every pressure when using the 3.3 μm laser beam considering its sensitivity in our heat diffusion model [189]. For $SrTiO_3$ measurements, the laser spot size was ~6.8 μm.

We use the sensitivity analysis to determine the uncertainty of the derived values of Λ. The sensitivity parameter (S) quantifies relative changes of $-V_{in} / V_{out}$ induced by variation of the input parameter α in the heat diffusion model:

$$S = \frac{\partial\, ln(-V_{in}/V_{out})}{\partial\, ln\, \alpha}, \qquad (5.2)$$

Two sensitivity analyses at different pressures for $SrTiO_3$ are included in Figure 5.9. Typically, we have a ~5% uncertainty in $h_{td}C_{td}$ [190], ~5% in the spot size R, ~3% for C_{sub}. We also estimate an uncertainty of ~5% in the thermal effusivity of silicone oil, $\sqrt{\Lambda_{oil}C_{oil}}$, and ~5% uncertainty in the Al/$SrTiO_3$ interface conductance. These yield a total uncertainty in the derived values for Λ of ~13%. We expect the uncertainties of these parameters to increase under pressure.

Among the parameters of interest, h_{td} is generally considered the most important, as it is difficult to measure at high pressure and has high sensitivity [35,42]. We used silicone oil (polydimethylsiloxane) as the pressure medium for most measurements because its low thermal conductivity helps improve the sensitivity of the TDTR measurements to the thermal conductivity of the perovskites, see Figure 5.7(c) and 5.9. However, when using silicone oil as the pressure medium, the picosecond acoustic echo of the transducer will be buried in the Brillouin oscillation signal from the silicone oil. We cannot easily obtain the transducer thickness by reading the acoustic echo in the TDTR measurements, as we usually do under ambient conditions.

One way to make the acoustic echo visible under pressure is to replace silicone oil with gaseous medium such as Ne, see Figure 5.8. We performed picosecond acoustic measurements on an

Al/$SrTiO_3$ sample with Ne as pressure medium. When the pump beam hits the Al surface, it will launch an acoustic wave that travels through the Al film. When reaching the Al/$SrTiO_3$ interface, part of the acoustic wave will be reflected, and propagate back to the Al surface. Therefore, the echo indicates the time interval (t) for the acoustic wave to travel back and forth in the Al film, $t = 2h_{Al} / v_L$, where v_L is the longitudinal speed of sound of Al. By assuming $v_L \propto \sqrt{K / \rho}$, we can calculate pressure dependent v_L using the equation of states of Al [184], and then calculate the thickness of Al. Here, K is the isothermal bulk modulus defined as $K = -dP / d\ln V$. Figure 5.8(b) shows the comparison between our picosecond acoustic measurements and the calculated Al thickness (Figure 5.7(a)) under pressure. Our measurements and calculations agree well with each other, suggesting that our method for calculating the transducer thickness is accurate.

We cannot use Ne as a pressure medium for thermal conductivity measurements. The thermal conductivity of the gaseous medium is comparable to that of $SrTiO_3$ and $KTaO_3$ at high pressure [20]. If we use Ne in high-pressure TDTR measurements, the sensitivity of the thermal conductivity of Ne will be as large as Λ of $SrTiO_3$ and $KTaO_3$. Without accurate knowledge of the thermal conductivity of Ne and the interface conductance between Ne and Al, we cannot extract the thermal conductivity of substrates from the TDTR data. Therefore, we only report the Brillouin frequency data from the Ne/Al/$SrTiO_3$ sample.

5.3 Results

$SrTiO_3$ has a cubic phase (space group: $Pm\bar{3}m$) below 9.1 GPa. The cubic symmetry of $SrTiO_3$ forbids first-order Raman scattering. However, $SrTiO_3$ has two broad bands (210 to 440 cm^{-1}, 550 to 780 cm^{-1}) that are attributable to second-order Raman scattering [175,191]. The two broad bands blue shift upon compression. At room temperature and above 9.1 GPa, $SrTiO_3$ transforms

into a tetragonal phase (space group: *I*4/*mcm*). In this phase, several phonon modes are Raman active [175]. At pressures above 9.1 GPa, we observe two peaks form near 162 and 466 cm^{-1}, see Figure 5.2(a). These two peaks are first-order Raman peaks with $E_g + B_{1g}$ symmetry and indicate the cubic-tetragonal phase transition.

$KTaO_3$ has cubic symmetry (space group: $Pm\bar{3}m$), so all the features in the Raman spectra are second order [192]. As the pressure increases, all peaks shift to higher wavenumbers, and, unlike $SrTiO_3$, we do not observe any new Raman peak form at higher pressures (Figure 5.2(b)). This is consistent with our expectation that $KTaO_3$ does not undergo a phase transition in the studied pressure range.

The Raman shifts *vs.* pressure for selected Raman peaks are shown in Figure 5.4(a). The Raman shifts reflect increases in the frequency of the phonons responsible for Raman scattering. Therefore, these measurements provide a measure of the stiffening of vibrational dynamics with pressure. We excluded Raman peaks of the pressure medium (silicone oil, polydimethylsiloxane. Its pressure-dependent Raman spectra are shown in Figure 5.3(a)). We followed Ref. [175] and labeled the selected $SrTiO_3$ peaks B2, B3, C2, C3 (these labels are arbitrary). For $KTaO_3$, we labeled the selected peaks as K1, K2, K3. We only tracked the B2 peak of $SrTiO_3$ up to 9.1 GPa due to degradation of its signal quality. The K1 peak of $KTaO_3$ drops below the transition width of our edge filter below 5.5 GPa. The frequencies of the selected peaks increase mostly linearly upon compression. The pressure dependence of each Raman mode is shown in Figure 5.4(a). We observe that the shifts of the Raman peaks of $SrTiO_3$ and $KTaO_3$ have a similar pressure dependence. At 13 GPa, all selected peaks increase by ~15%. Our pressure-dependent Raman results for $SrTiO_3$ are mostly consistent with the results reported in Ref. [175], as shown by the comparison in Figure 5.5. The main difference is that our C3 Raman mode shows a larger pressure dependence than the results in Ref. [175].

The Brillouin frequency of $SrTiO_3$ shows a decrease within 2 GPa around the phase transition (~9 GPa in Figure 5.4(b)). This anomaly is consistent with previous reports for the elastic constants of $SrTiO_3$ vs. pressure [178]. The observed transition pressure is also consistent with our Raman results in Figure 5.2(a) and 5.4(a). For $KTaO_3$, we observe a monotonically increasing Brillouin frequency. The Brillouin frequency is

$$f = 2Nv_l / \lambda, \qquad (5.3)$$

Where N is the index of refraction of the sample, v_l is the longitudinal speed of sound of the sample, and λ is the excitation wavelength (783 nm in our experiments).

We observe linearly increasing thermal conductivity as the pressure increases in both $SrTiO_3$ and $KTaO_3$ (Figure 5.6). We obtain similar thermal conductivity results with different transducers and laser spot sizes. The gradient, $d\Lambda/dP$, is ~0.61 W m^{-1} K^{-1} GPa^{-1} for $SrTiO_3$ in the cubic phase and ~0.37 W m^{-1} K^{-1} GPa^{-1} for $SrTiO_3$ in the tetragonal phase. The thermal conductivity of an $SrTiO_3$ sample (red dots in Figure 5.6) is ~20% lower than the other three. A possible explanation is that the polishing procedure necessary to prepare samples for DAC measurements caused minor plastic deformation in that sample near its surface. Two sets of our $SrTiO_3$ data (blue and gray dots in Figure 5.6(a)) show a ~10% decrease between 8 and 13 GPa. When the transducer is switched to Ta (magenta markers), the decrease is reduced to ~5%. In the red-dot dataset, there is no decrease at all. The small change in thermal conductivity that we observed in some data sets near the phase transition may be related to the drop in group velocity at the phase transition (Figure 5.4(b)). We note that the 5-10% changes we observe are comparable to the overall jitter in our thermal conductivity results. Therefore, if there is a change in thermal conductivity induced by the phase transition, the magnitude of the change is smaller than what we can reliably resolve by TDTR in a DAC. Recent work on $SrTiO_3$ reports that their sample has a sharp drop of -25% at

phase transition (~6 GPa) [193]. Their data also show a change in slope at phase transition (~0.54 and ~0.34 W m^{-1} K^{-1} GPa^{-1} for cubic and tetragonal $SrTiO_3$, respectively). Their slope values are ~10% lower than our results. $d\Lambda/dP$ = 1.2 W m^{-1} K^{-1} GPa^{-1} for $KTaO_3$. The relative change at 20 GPa, $\Lambda(20\ GPa)/\Lambda(1\ bar)$, is ~200% for $SrTiO_3$, and ~300% for $KTaO_3$. The data of the pressure-dependent interface conductance between transducers and substrates are shown in Figure 5.10(a).

5.4 Discussion

Our results in Figures 5.4 and 5.6 show that both the vibrational dynamics and thermal conductivity have strong pressure dependencies. And, notably, Λ of $SrTiO_3$ does not have an abrupt change at phase transition. Now we focus on understanding these observations.

Why does the phase transition at 9.1 GPa not cause a more significant change in $SrTiO_3$'s thermal conductivity? Phase transitions sometimes cause abrupt changes in thermal conductivity. For example, $\Lambda(P)$ of NaCl drop by 60% at the phase transition pressure of 30 GPa [194]. However, unlike the first-order phase transition in NaCl, the cubic-tetragonal phase transition in $SrTiO_3$ is a second-order displacive phase transition [195]. $SrTiO_3$'s transition is related to the rotation of TiO_6 octahedral, which is continuous and gradual. The tetragonal distortion is small below 30 GPa (c/a = 1.01 at 30 GPa) [175]. No abrupt change in $\Lambda(T)$ of $SrTiO_3$ at ambient pressure is observed at the phase transition temperature of 105 K [166,167]. Therefore, it is not surprising that we did not observe clear evidence of a significant drop in $\Lambda(P)$ of $SrTiO_3$ at 9.1 GPa.

Now we evaluate the magnitude of $d\Lambda/dP$ we observe for $SrTiO_3$ and $KTaO_3$. To do this, in Figure 5.11(c) we compare the increase in relative thermal conductivity of different materials at

20 GPa, $\Lambda(20\ GPa)/\Lambda(1\ bar)$. Most of the materials that we include for comparison are oxides and have a cubic crystal structure. All materials in Figure 5.11(c) show a monotonically increasing thermal conductivity under compression. $SrTiO_3$ has a pressure dependence of Λ similar to most materials, while $KTaO_3$ has a stronger pressure dependence than other materials.

Pressure-induced changes in thermal conductivity are caused by changes in heat capacity per mode, phonon group velocity, and phonon lifetime (see Eq. (4.1)). To explore why $SrTiO_3$ and $KTaO_3$ have different pressure dependence in $\Lambda(P)$, we evaluate changes of these three parameters. To do this, we consider predictions of the Leibfried-Schlömann equation (LS) for the heat capacity, the phonon group velocity, and the phonon lifetime change with pressure. Then, we consider what our Raman and Brillouin scattering measurements vs. pressure imply for the pressure dependence of phonon heat capacity, phonon group velocity, and phonon lifetime. Finally, we consider the predictions of previous theoretical studies that utilized first-principles methods to calculate vibrational dynamics [168,169].

The LS equation is commonly used to explain observed trends for $\Lambda(P)$ in nonmetallic crystals such as NaCl [194] and MgO [196]. The LS equation approximates c, v, and τ in Eq. (4.1) using properties that can be extracted from the volume-pressure equation of states (V-P EOS) [10]. The volumetric heat capacity is assumed to be $C \propto 1/V$. The group velocity v is parameterized as $v = \sqrt{K_T/\rho} \propto \delta\theta$. Phonon mean free path is set to be $l \propto \delta\ /\ T\alpha\gamma$ [11]. Here, K_T is the isothermal bulk modulus defined as $K_T = -dP\ /\ d\ ln\ V$, and α is the volumetric thermal expansion coefficient which can be calculated by $\alpha = C\gamma\ /\ K_T$. Plugging these approximations into Eq. (5.1) yields

$$\Lambda = \frac{B\bar{M}\delta\theta^3}{T\gamma 2}. \qquad (5.4)$$

Here B is a constant, $\overline{M}$ is the average mass of an atom in the crystal, δ^3 is the average volume occupied by one atom in the crystal, θ is the Debye temperature, T is temperature, and γ is the Grüneisen parameter. δ, θ, and γ are all pressure dependent. To calculate Λ vs. P using Eq. (5.4), we follow the procedures in Ref. [10] to extract these parameters from the *V-P* EOS. The evolution of δ, θ, γ with pressure depends on the first, second, and third derivatives of the *V-P* EOS. We adopt the third-order Birch-Murnaghan equation of states (B-M EOS) in Ref. [175] to calculate the pressure dependent δ, θ, and γ. Cubic and tetragonal B-M EOS produce different fittings for $SrTiO_3$ (see Figure 5.11(a)). Due to the lack of experimental EOS for $KTaO_3$, we assume that $KTaO_3$ follows the cubic B-M EOS of $SrTiO_3$. This assumption is reasonable because of their similar crystal structure. The results of the first-principles calculations [188] support this assumption (see Figure 5.11(b)).

The LS equation agrees reasonably well with our experimental $\Lambda(P)$ of $KTaO_3$ and $SrTiO_3$. Note that we choose different values for the constant B in Eq. (5.4) for our predictions in Figure 5.11(a) for cubic and tetragonal $SrTiO_3$. For cubic $SrTiO_3$, we set B to make Eq. (5.4) agree with Λ under ambient conditions. For tetragonal $SrTiO_3$, we set B to be in agreement with Λ at 10 GPa, the lowest pressure that we observe $SrTiO_3$ to be in the tetragonal phase. Therefore, the difference in the LS equation curves for cubic vs. tetragonal $SrTiO_3$ at 10 GPa is not a prediction of the LS equation. Instead, the abrupt drop in the LS equation curves at 10 GPa reflects the fact that the LS equation predicts a higher $d\Lambda/dP$ (0.73 W m^{-1} K^{-1} GPa^{-1}) for cubic $SrTiO_3$ than what we experimentally observe.

The LS equation predicts that most of the change in the thermal conductivity of $SrTiO_3$ and $KTaO_3$ upon compression to 20 GPa is due to changes in the lifetimes of phonons. According to their *V-P* EOS, upon compression to 20 GPa, V decreases by 9% for $SrTiO_3$ and $KTaO_3$ at 20

GPa (Figure 5.11(b)). One of the standard methods to calculate the Debye temperature is from elastic constants [197], $\theta \propto \sqrt{\delta K_T}$, which can be calculated from the first derivative of *V-P* EOS. Analyzing the *V-P* EOS of $SrTiO_3$ and $KTaO_3$ in Ref. [175], we find θ increases by 20% for $SrTiO_3$ and 30% for $KTaO_3$. The LS equation uses the "Slater γ", which is defined as $\gamma = \frac{1}{2}\frac{dK_T}{dP} - \frac{1}{6}$ [12]. By calculating the second derivative of *V-P* EOS, we find that Slater γ decreases by 10% for $SrTiO_3$ and 13% for $KTaO_3$. Therefore, for $SrTiO_3$, the LS equation credits 10%, 15%, and 60% of the increase in Λ to changes in heat capacity, group velocity, and phonon mean free path, respectively. For $KTaO_3$, the numbers are 10%, 25%, 100% accordingly. We note that while the first and second derivatives of the EOS are straightforward to extract from experimental data, the third derivatives are not. Therefore, some skepticism is warranted for the LS equation prediction for $d\Lambda/dP$.

We now turn our attention to what our scattering measurements in Figure 5.4 imply for the heat capacity per phonon mode in Eq. (5.1). The heat capacity per mode is

$$c(q) = D(q)\hbar\omega_q \frac{\partial n(\omega_q)}{\partial T}. \qquad (5.5)$$

Here, q is phonon wavevector, $D(q)$ is the density of states with wavevector q, and n is the Bose-Einstein distribution. The primary way that pressure affects $c(q)$ is through mode stiffening. Upon compression to 20 GPa, the Raman frequencies of $SrTiO_3$ and $KTaO_3$ increase by up to ~20%, see Figure 5.4(a). First-principles calculations for $SrTiO_3$ predict that, at room temperature, heat is carried primarily by phonons with ω_q between 0 and 15 THz [198]. For modes with ω_q = 5, 10, and 15 THz at 0 GPa, a ~20% increase in ω_q upon compression to 20 GPa will lead to a decrease in $\hbar\omega_q\frac{\partial n}{\partial T}$ by 2, 7, and 11%, respectively. So, our experimental data on the vibrational dynamics suggest changes in $c(q)$ will be small, in agreement with the LS-

equation prediction described above. The first-principles calculations predict that the total heat capacity of $SrTiO_3$ and that of $KTaO_3$ are nearly constant up to 20 GPa [187,188] (see Figure 5.7(d)).

Now, we consider the effect of pressure on group velocity. Our Brillouin frequency data allow us to calculate the group velocity of low-energy longitudinal acoustic (LA) phonons along the [100] direction. To calculate v_l, we need to estimate the index of refraction *N* under pressure. To our knowledge, there is no experimental data of *N* of $SrTiO_3$ and $KTaO_3$ under pressure. First-principles calculations suggest that *N* has nearly negligible pressure dependence. The *N* of $KTaO_3$ decreases by 4% at 40 GPa [199]. The *N* of $SrTiO_3$ decreases by 3% at 60 GPa [182]. Therefore, since the effect of pressure is small, for simplicity we assume $dN/dP \approx 0$. Then the longitudinal group velocity increases by ~10% for $SrTiO_3$ and ~20% for $KTaO_3$ at 20 GPa (Figure 5.4(b) and Eq. (5.3)). This compares favorably with the LS-equation estimates described above of a 15% and 25% increase in group velocity for $SrTiO_3$ and $KTaO_3$, respectively. Therefore, we conclude that while velocity changes are larger than heat capacity changes, their effects are still minor. Pressure-induced changes in phonon velocity cannot explain the factor of 2 and 3 increase we see in Λ of $SrTiO_3$ and $KTaO_3$ upon compression to 20 GPa.

We now turn our attention to what information our Brillouin measurements have regarding phonon lifetimes. One way to estimate phonon lifetime changes is to consider the mode Grüneisen parameter γ of the phonons. γ is defined as the relative change in the frequency (ν) of a phonon due to a relative change in volume (V),

$$\gamma = -\frac{d\,ln\,\nu}{d\,ln\,V}. \qquad (5.6)$$

We fit $\nu(P)$ by a line using the nearest three data points at a given pressure, use the Birch-Murnaghan EOS to convert $\nu(P)$ to $\nu(V)$, and calculate γ by Eq. (5.6). The γ for $SrTiO_3$ drops by

50% at 20 GPa (2.25 at 0 GPa and 1.09 at 20 GPa). And the γ for $KTaO_3$ drops by 80% at 20 GPa (3.62 to 0.65). The Grüneisen parameter is a measure of phonon anharmonicity, and, in general, phonon lifetimes decrease with increasing anharmonicity. Therefore, our Brillouin data provide evidence that pressure-induced changes in phonon lifetime are significant in both $SrTiO_3$ and $KTaO_3$, and that the changes are larger in $KTaO_3$. Based on predictions and our experimental data, we conclude that pressure-induced changes in Λ are mainly driven by changes in the phonon lifetime. This explains the greater pressure dependence we observe for Λ of $KTaO_3$ than $SrTiO_3$, see Figure 5.6.

Why do phonon lifetimes and phonon anharmonicity change more with pressure in $KTaO_3$ than in $SrTiO_3$? It is known that $KTaO_3$ is close to a ferroelectric phase transition under ambient conditions, while $SrTiO_3$ is relatively stable [168,169,200]. First-principles calculations show that displacements of Ta and O atoms in $KTaO_3$ occur in non-parabolic potential wells, indicating large anharmonicity [200]. The calculations suggest that volume contraction will make potential wells parabolic and the crystal lattice stable. In addition, first-principles calculations suggest that the phonon frequencies of the low-lying TO modes near Γ point in $KTaO_3$ are more sensitive to pressure than those of $SrTiO_3$. For the low-lying TO modes in $KTaO_3$, a 1% volume expansion can decrease their frequencies by 60% [168]. The corresponding Grüneisen parameter is ~50. For $SrTiO_3$, a 6% volume expansion decreases the frequencies of low-lying TO modes by only 30% [169]. The corresponding γ is only ~5. For $KTaO_3$ under ambient conditions, the low-lying optic phonon branch has a frequency similar to that of the longitudinal acoustic phonon branch near Γ point [168]. This feature can produce a large phase space for phonon-phonon scattering since the selection rules (conservation of energy and momentum) can be easily satisfied [128]. Pressurization drives the low-lying TO branch away from the LA branch in frequency. The

increase of the frequency gap makes satisfying selection rules harder and can therefore be expected to decrease the phonon-phonon scattering phase space of $KTaO_3$.

5.5 Conclusions

We measured the $\Lambda(P)$ of $SrTiO_3$ and $KTaO_3$ up to 28 GPa by time-domain thermoreflectance with diamond anvil cells. We observe the $\Lambda(P)$ of $KTaO_3$ has an unusually large pressure dependence, while $SrTiO_3$ has a typical pressure dependence. By correlating the thermal conductivity and scattering measurements, we show that the different pressure dependence in $\Lambda(P)$ is caused by differences in how the phonon lifetimes evolve with pressure. Furthermore, we show that most of the observed change in Λ is caused by changes in phonon lifetime. We find that the predictions of the LS equation for the thermal conductivity and vibrational properties agree fairly well with our observations. Our observation that modest changes in phonon frequencies of ~10-20% cause significant changes in Λ and average phonon lifetimes of 200-300% has important implications for a variety of fields. Understanding the relationship between vibrational spectra and thermal conductivity is an active area of research in the heat transfer community [128,150], with the ultimate goal of identifying materials with high thermal conductivities for thermal management applications [8]. Our findings are also relevant to the science of thermoelectric materials. Many perovskites are promising thermoelectric materials [201,202], and understanding the relationship between vibrational properties, phonon lifetimes, and thermal conductivity is important for engineering materials with low thermal conductivity [203]. Finally, our finding that changes in phonon lifetime dominate $d\Lambda/dP$ is relevant to ongoing efforts in the geophysics community to understand the thermal balance and history of the Earth [6]. Many minerals in the Earth mantle have a perovskite crystal structure,

e.g., bridgmanite, and knowledge of how pressure and temperature affect thermal conductivity is crucial to modelling heat flux at the core-mantle boundary [6].

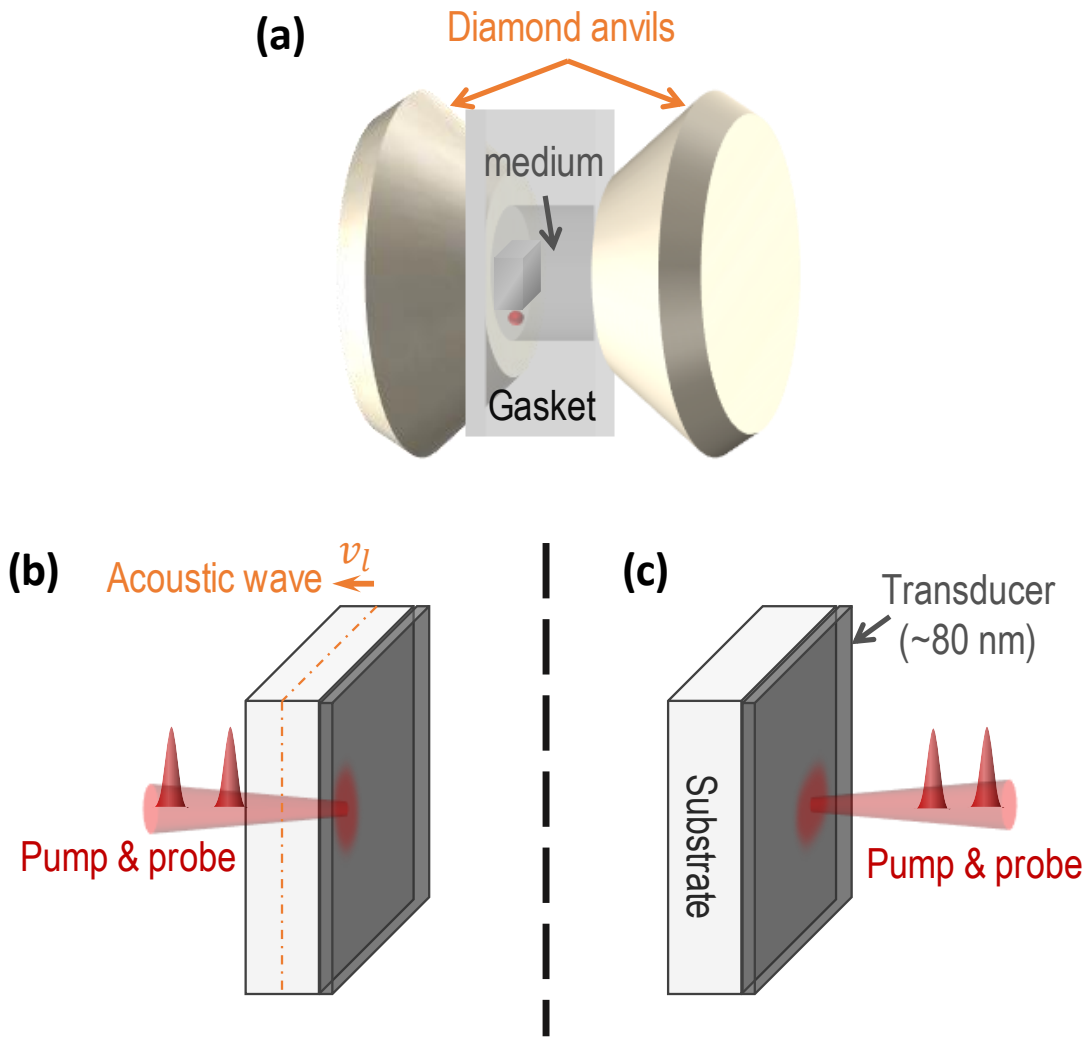

Figure 5.1. Schematics of the diamond anvil cell (DAC) assembly and experimental geometries.

(a) The samples along with the ruby spheres are loaded into the DAC chamber. (b) For stimulated Brillouin scattering measurements, the pump and probe beams impinge on the substrate side of the sample. (c) For TDTR measurements, the pump and probe beams impinge on the transducer side of the sample.

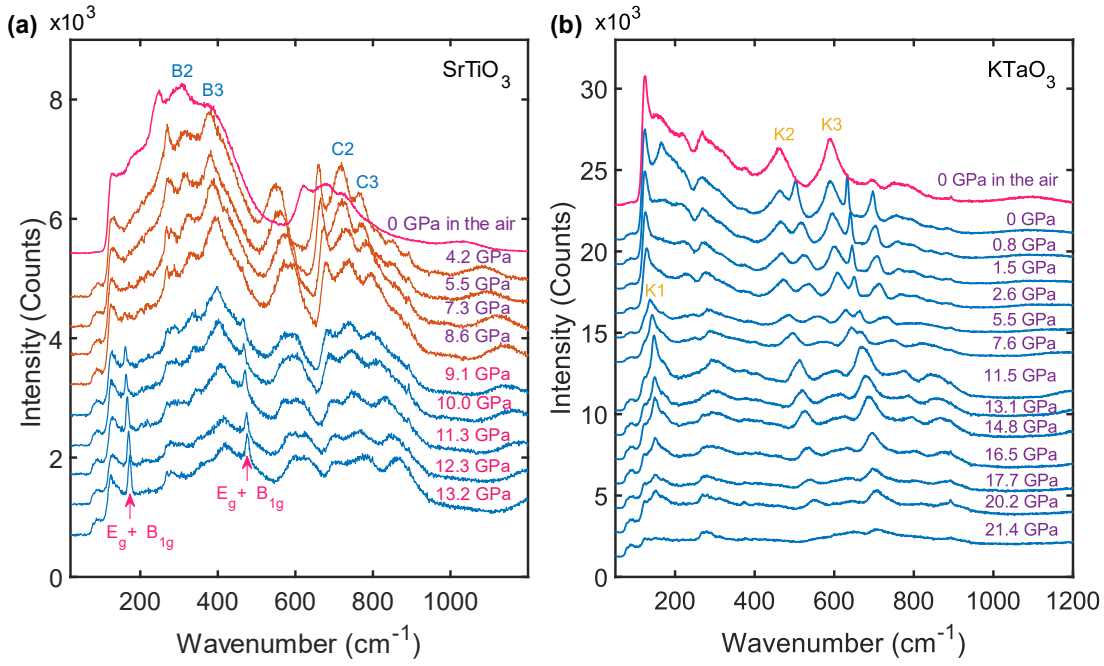

Figure 5.2. Raman spectra of $SrTiO_3$ and $KTaO_3$ under pressure.

In panel (a), the peak near 600 cm^{-1} is a Raman peak from silicone oil. The $SrTiO_3$ Raman peak near 700 cm^{-1} overlaps with a silicone oil peak. In panel (b), peaks around 170 cm^{-1}, 500 cm^{-1}, 630 cm^{-1}, and 700 cm^{-1} are Raman peaks from silicone oil. The $KTaO_3$ Raman peak near 260 cm^{-1} overlaps with a silicone oil peak. A detailed comparison between the $KTaO_3$ spectrum with and without silicone oil can be found in Figure 5.3(b).

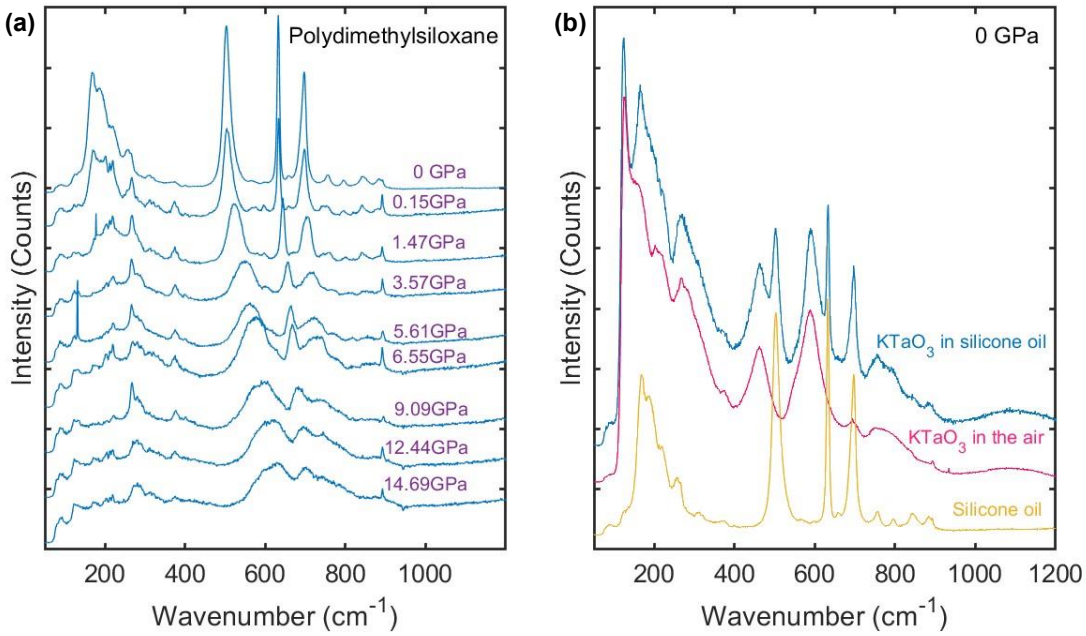

Figure 5.3. Raman spectra of silicone oil at high pressure.

(a) Raman spectrum of silicone oil (polydimethylsiloxane) under pressure. (b) Raman spectrum of $KTaO_3$ at 0 GPa. We include this figure to show the way we exclude the Raman peaks of silicone oil.

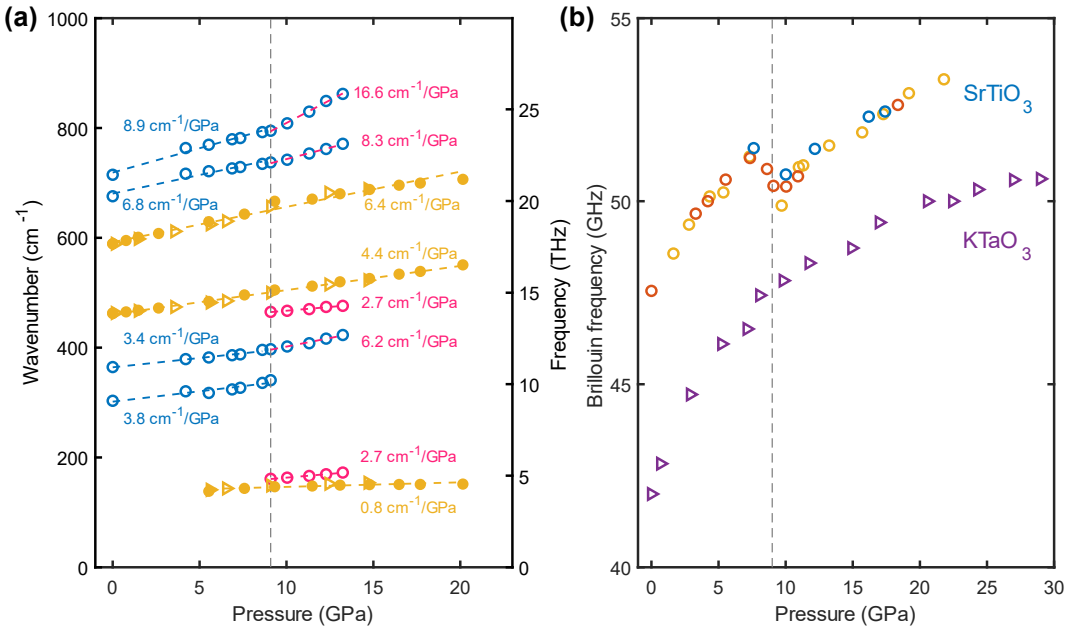

Figure 5.4. Scattering data vs. pressure for $SrTiO_3$ and $KTaO_3$.

(a) Frequencies of selected Raman peaks vs. pressure. Circles and triangles are data collected during pressure increase and pressure decrease, respectively. Dashed lines are linear fittings to the data. Each fitting is labelled with its slope. For $SrTiO_3$, the slope is determined separately for cubic vs. tetragonal phases. (b) Brillouin frequency vs. pressure in the [100] direction. The circles are data collected on $SrTiO_3$. Different colors represent different pieces of $SrTiO_3$. The triangles are $KTaO_3$. The vertical dashed line in (a) and (b) show the phase transition pressure of $SrTiO_3$.

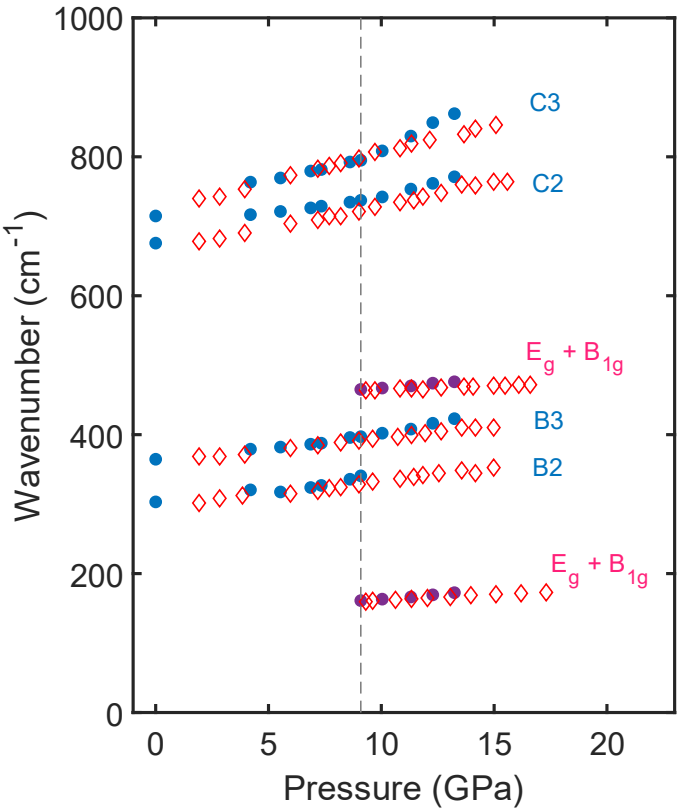

Figure 5.5. Comparison between our $SrTiO_3$ Raman peak shifts and literature results.

Dots are our data. Diamonds are literature data. We follow the nomenclature in Ref. [175] for $SrTiO_3$ Raman peaks. The vertical dashed line indicates the phase transition pressure. The difference in C3 may be related to the different pressure medium that we use.

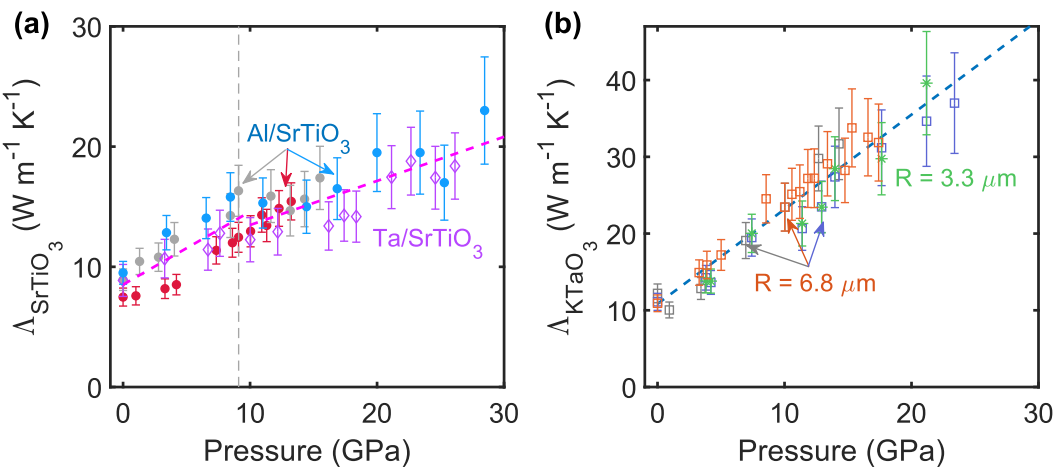

Figure 5.6. Thermal conductivity of $SrTiO_3$ and $KTaO_3$ under pressure measured by TDTR.

(a) We measure the $\Lambda(P)$ of $SrTiO_3$ with two different optical transducers: Al and Ta. Three datasets are measured with Al (blue, red, and gray), and one with Ta (purple). (b) We measure the $\Lambda(P)$ of $KTaO_3$ with two different spot sizes (6.8 and 3.3 μm). Three datasets are measured using 6.8 μm laser spot size (orange, blue, gray), and one is 3.3 μm (green). The error bars here denote our estimate of ~13-20% uncertainty that arises from uncertainty in the input parameters for the heat diffusion model that we use to analyze time-domain thermoreflectance data. The dashed lines are linear fittings to the data. The vertical dashed line shows the phase transition pressure of $SrTiO_3$.

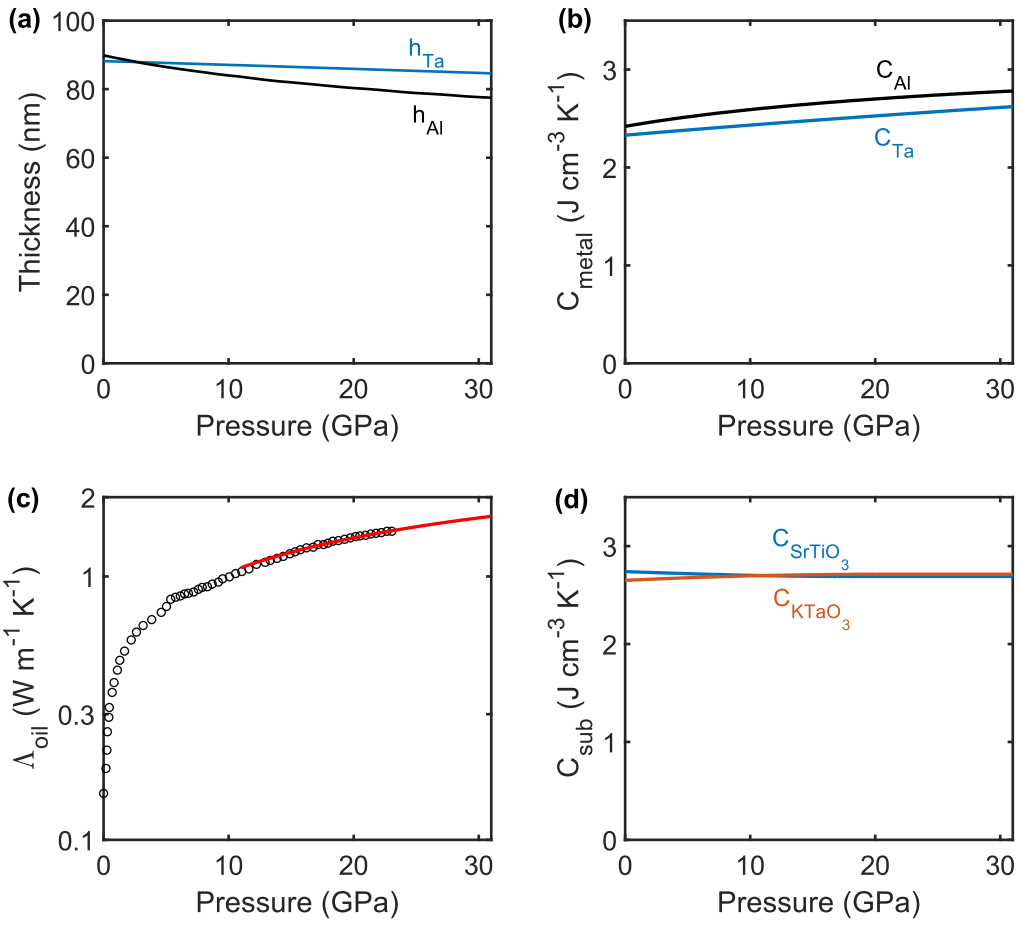

Figure 5.7. Pressure-dependent parameters in the heat diffusion model.

(a) Calculated pressure-dependent thickness of transducers. (b) Pressure-dependent heat capacities of transducers calculated by the Debye model. (c) Thermal conductivity of silicone oil under pressure. Data below 23 GPa are from Ref. [12]. Data beyond 23 GPa are extrapolations of the literature data. (d) Heat capacities of $SrTiO_3$ and $KTaO_3$ under pressure from Ref. [187] and [188].

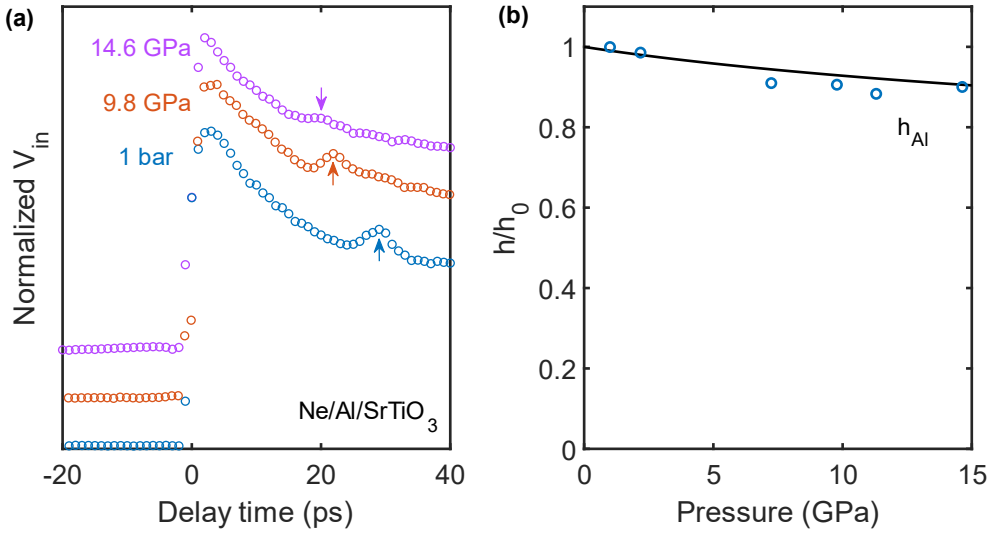

Figure 5.8. Comparison between picosecond acoustic measurements and the calculation of Al thickness.

(a) Normalized V_{in} vs. delay time signals under pressure collected on an Al/$SrTiO_3$ sample in a DAC with Ne as the pressure medium. The arrows denote the picosecond acoustic echo peaks. The three data sets are shifted for clarity. (b) The Al thickness under pressure normalized by the thickness at atmospheric pressure. The black line is the calculated thickness mentioned in Figure 5.7(a). The blue circles are experimental data interpreted from panel (a).

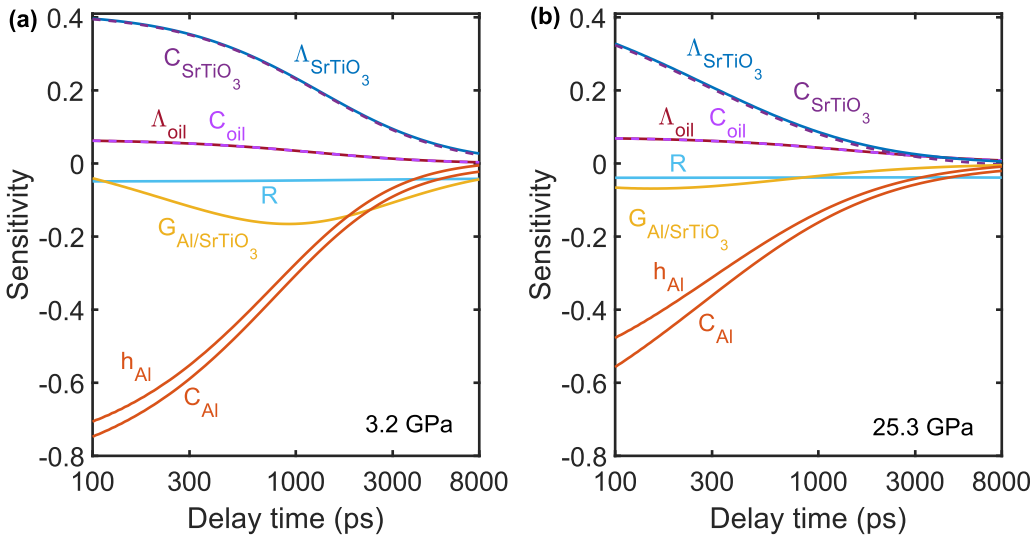

Figure 5.9. Sensitivity analyses of Al/$SrTiO_3$ at 3.2 GPa and 25.3 GPa.

Parameters to consider include thermal conductivity (Λ) and heat capacity (C) of $SrTiO_3$, thermal conductivity and heat capacity of silicone oil, spot size R, Al/$SrTiO_3$ interface conductance G, the thickness (h) and heat capacity of Al. The sensitivity of the interface conductance decreases as pressure increases.

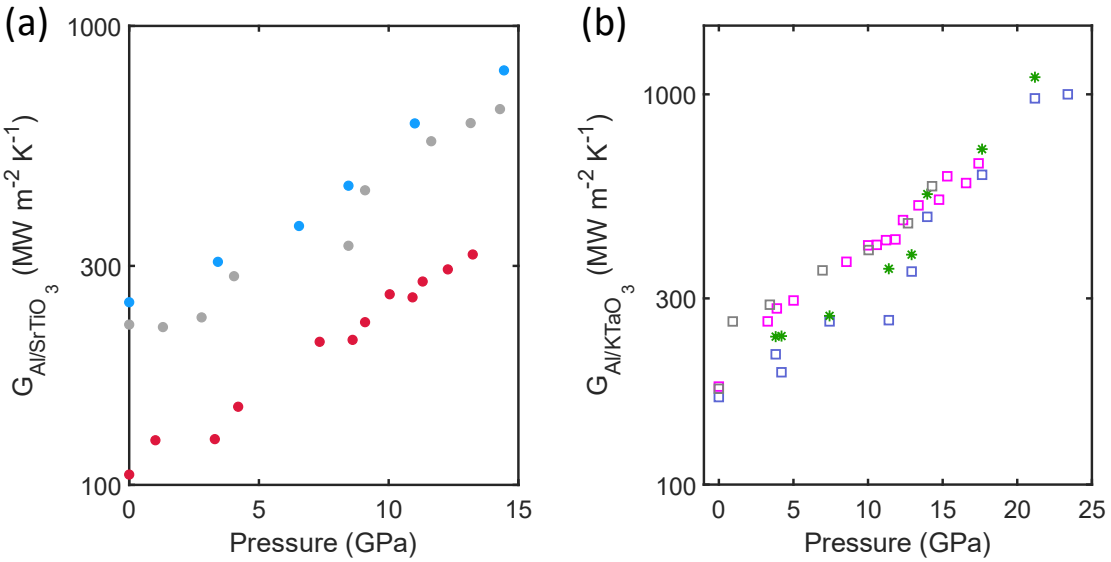

Figure 5.10. Interface thermal conductance between $Al/SrTiO_3$ and $Al/KTaO_3$.

(a) We lost the sensitivity of G of $Al/SrTiO_3$ above 15 GPa (see Figure 5.9) and fixed it to be 800 MW m^{-2} K^{-1} in the heat diffusion model. The red dots have lower values of *G* than the other two samples. We speculate that it is because the polishing procedure during sample preparation induced strain at the sample surface. Different colors represent different samples.

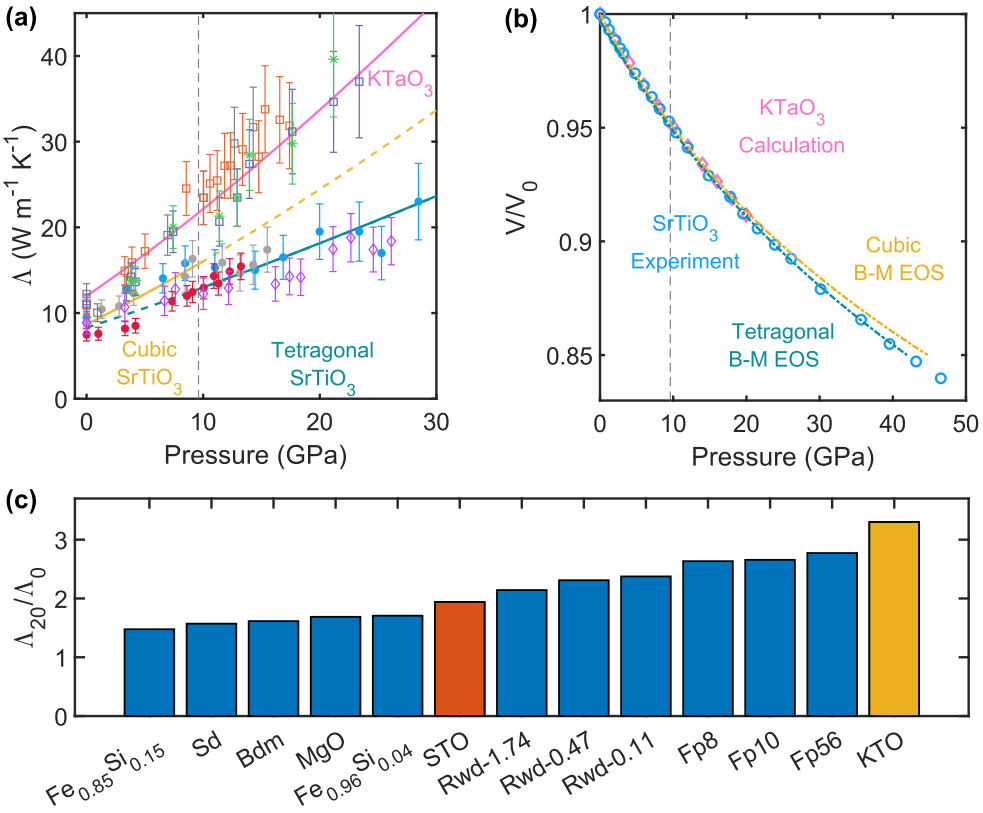

Figure 5.11. Comparison between our experimental results and the LS predictions for $SrTiO_3$ and $KTaO_3$.

(a) Predictions of the LS equation (solid lines) in comparison to measured thermal conductivity of $SrTiO_3$ and $KTaO_3$ (markers). The solid pink line is the prediction of the LS equation for $KTaO_3$. The yellow and green lines are the LS predictions using cubic and tetragonal B-M EOS for $SrTiO_3$, respectively. (b) Equations of states of $SrTiO_3$ and $KTaO_3$. V / V_0 is the unit cell volume relative to the ambient volume V_0. The blue circles are the experimental data of $SrTiO_3$ from Ref. [175]. The yellow and green dash-dot lines are B-M EOS fittings to the experimental data, also from Ref. [175]. Pink diamonds are calculated EOS of $KTaO_3$ from Ref. [188]. The vertical dashed line represents the cubic-tetragonal phase transition in $SrTiO_3$. (c) The ratio between thermal conductivity at 20 GPa and atmospheric pressure for various materials. Materials for comparison include Fe-Si alloys [28], MgO [196], ferropericlase (Fp) [205], bridgmanite (Bdm) [29], ringwoodite (Rwd) [206], siderite (Sd) [207], $SrTiO_3$ (STO) and $KTaO_3$ (KTO).

Chapter 6 Thermal Conductivity of BAs under Pressure

Chapter 6 was published in "Thermal conductivity of BAs under pressure." Songrui Hou, Bo Sun, Fei Tian, Qingan Cai, Youming Xu, Shanmin Wang, Xi Chen, Zhifeng Ren, Chen Li, and Richard B. Wilson. *Advanced Electronic Materials*, 2200017 (2022).

6.1 Introduction

High-thermal-conductivity materials are desirable for thermal management applications. Power electronic devices operate at power densities higher than 100 W/cm^2, roughly three orders of magnitude larger than the irradiance of the Sun [208,209]. Discovery and integration of high thermal conductivity materials into electronics offer a route for increasing performance. Discovery of such materials requires a detailed understanding of material properties that lead to high thermal conductivity. However, despite more than a half century of study, a complete microscopic understanding does not exist for why some materials have high thermal conductivity, while other similar materials do not. Our study aims to help fill this fundamental gap by experimentally testing the relationship between BAs's phonon dispersion and phonon scattering rates.

In the 1970s, Slack came up with four rules for finding nonmetallic crystals with high thermal conductivity. These rules are: i) low average atomic mass, ii) strong interatomic bonding, iii) simple crystal structure, and iv) low anharmonicity [210]. Given their simplicity, the apparent accuracy of Slack's rules has been something of a long-standing puzzle. Theoretical models for phonon-phonon scattering rates have long predicted that, because phonon scattering processes must conserve energy and crystal momentum, phonon dispersion can have a strong effect on

phonon scattering rates [211,212]. Certain features in the phonon dispersion can make it difficult for a three-phonon scattering processes to satisfy selection rules [211,212]. It is well known that crystals with similar crystal structures and average atomic mass can have distinct differences in phonon dispersion [213]. But Slack's rules imply that differences in phonon dispersion between such crystals will have little effect on thermal transport.

In the past ten years, a number of theoretical and experimental studies have started to unravel this puzzle and correct Slack's rules [214–223]. In 2013, Lindsay *et al.* used first principles calculations based on density functional theory (DFT) and the Peierls-Boltzmann equation (PBE) to study the effects of atypical phonon dispersion on thermal transport [214–216]. Their first-principles based work predict that phonon dispersion relations have a strong effect on scattering rates via selection rules [214–216]. For example, first principles theory predicts that crystals with special phonon dispersion properties like BAs will have a thermal conductivity higher than the value Slack's rules predict [215,224]. BAs's phonon dispersion is special for two reasons. First, BAs has a large frequency gap between acoustic and optic phonons. This gap should eliminate the phase space for three-phonon scattering between acoustic and optic phonons [215,225]. Second, the acoustic phonon branches of BAs are unusually close together [225]. This acoustic bunching effect is predicted to result in a small phase space for three-phonon scattering processes of acoustic phonons [215,226].

Several recent experimental studies have verified first principles predictions that BAs has an anomalously large thermal conductivity [219–221]. BAs has a thermal conductivity between 1000 and 1300 W m^{-1} K^{-1}, see Figure 6.1. Despite similar average atomic mass, bonding, and crystal structure, BAs has a thermal conductivity ~7× larger than silicon.

The good agreement between experiment and first-principles theory for the thermal conductivity of BAs, and a number of other high thermal conductivity materials [216,219–223], provides compelling indirect evidence that a strong relationship exists between phonon dispersion properties and thermal conductivity. However, so far, there are no experimental studies that directly test the hypothesis that acoustic bunching leads to higher thermal conductivity. Testing of this hypothesis requires systematically tuning a material's phonon dispersion relation and observing the subsequent changes in thermal conductivity.

The pressure dependence of BAs's thermal conductivity offers a way to experimentally explore the relationship between phonon dispersion, phonon scattering selection rules, and thermal transport. Thermal conductivity is a weighted average of phonon lifetimes. Therefore, measurements of thermal conductivity vs. pressure provide some indirect information about how phonon lifetimes depend on pressure. First principles calculations show that pressure stiffens longitudinal acoustic phonons, thereby increasing the energy difference between longitudinal and transverse acoustic phonons [217,218]. In other words, compression of BAs reduces acoustic bunching, see Figure 6.1(a), and makes BAs's dispersion relation more like a typical crystal, *e.g.*, Si. Furthermore, pressure dependent measurements of BAs's thermal conductivity also offer the opportunity to study how phonon dispersion affects four-phonon scattering processes. Four phonon scattering processes are believed to play an important role in BAs [219–221,224]. Four phonon scattering rates are believed to depend on phonon dispersion properties such as the frequency gap between acoustic and optic modes [216,217].

The aim of our experimental study is to investigate phonon scattering mechanisms in BAs using high pressure. We perform time-domain thermoreflectance (TDTR) measurements of BAs in a diamond anvil cell (DAC) (Figure 6.2). TDTR is a well-established tool for measuring thermal conductivity [179]. Diamond anvil cells can generate pressures on the scale of GPa. We include

detailed descriptions of our experiments in Methods. We report the thermal conductivity as a function of pressure, $\Lambda(P)$, for three BAs samples with different ambient thermal conductivities. The apparent thermal conductivities of our three samples derived from TDTR measurements at ambient conditions are ~1100, 600 and 350 W m^{-1} K^{-1}. We also measure the thermal conductivity of two MgO single crystals as control experiments. The thermal conductivities of all three BAs samples depend weakly on pressure between 0 and 30 GPa. To confirm the pressure-independent thermal conductivity of high-thermal-conductivity BAs crystals, we repeated measurements on four other BAs samples with thermal conductivity of ~1000 W m^{-1} K^{-1} and got similar results. Alternatively, for MgO, we observe a monotonically increasing thermal conductivity with increasing pressure.

The weak pressure dependence of $\Lambda(P)$ for BAs implies that phonon scattering rates have a weak pressure dependence. We credit the weak pressure dependence of phonon scattering rates to how pressure affects three-phonon vs. four-phonon scattering rates. Decreases in acoustic bunching increase three phonon scattering rates. An increase in the frequency gap between acoustic and optic phonons decreases four-phonon scattering rates. The net effect leads to phonon scattering rates to be pressure independent.

6.2 Methods

Materials synthesis

Single crystal BAs (space group: $F\bar{4}3m$) samples are grown by chemical vapor transport (CVT). The reactants are pure boron bulk particles and arsenic lumps. We employ small amount of iodine powder as the transport agent. B and As with a B:As ratio of 1:1.2 along with some iodine were sealed in a fused vacuum quartz tube. The quartz tube was placed in a horizontal two-zone tube

furnace with high-temperature zone held at ~890 °C and low-temperature zone held at ~800 °C. Further details about the synthesis can be found in Refs. [227,228].

We used various boron sources in the synthesis processes. Sample A (~1100 W m^{-1} K^{-1}) is grown with ^{10}B isotopes, Sample B (~600 W m^{-1} K^{-1}) and Sample C (~350 W m^{-1} K^{-1}) are grown with ^{11}B isotopes. Samples made of different boron source have different characteristic Raman peaks [135,228].

Detailed defect characterizations, such as transmission electron microscopy (TEM), scanning electron microscopy (SEM), energy-dispersive X-ray spectroscopy (EDX), time-of-flight secondary ion mass spectrometry (TOF-SIMS) etc., can be found in Refs. [219,229,230]. Samples measured in this study were synthesized at the same time with the samples characterized in the mentioned works. TEM shows low dislocation density in high thermal conductivity BAs samples [219]. TEM also shows the presence of mirror twin boundaries. Hall effect measurements indicate our BAs samples are *p*-type conductive with hole concentrations between 10^{17} and 10^{20} cm^{-3} [229,231]. Impurities such as Si and C are attributed to be the origin of the *p*-type conductivity. Our previous electron probe microanalysis (EPMA) measurements demonstrate Si impurities of ~0.05 at. % (with a 0.003 at. % detection limit) are present in our BAs samples [229]. Theoretical calculations suggest an impurity concentration of 3.6×10^{19} cm^{-3} for a 500 W m^{-1} K^{-1} BAs sample [229].

Sample preparation

We prepared three pieces of BAs for DAC experiments. Two of them (1100 and 600 W m^{-1} K^{-1}) were first polished down to 7 ± 2 μm. The final thickness was measured with an optical microscope. Then, we deposited a ~ 80-nm-thick Al film on the sample. The other sample (350 W m^{-1} K^{-1}) was first coated with an ~90-nm-thick Al film, then being polished from the uncoated

side down to 7 ± 2 μm. We loaded the samples with 50-80 μm in lateral dimensions into a DAC with a culet size of 300 μm. We loaded ruby spheres alongside the samples as pressure indicators. We used silicone oil (Polydimethylsiloxane, CAS No. 63148-62-9 from ACROS ORGANICS) as the pressure medium for all measurements.

We used 250 μm thick stainless-steel gaskets and pre-indented them in our DAC to a thickness between 30 to 60 μm. Then we drilled holes with a diameter of ~170 μm at the center of the indentations by a laser drill system or an electro-discharge machine. The holes serve as containers for the samples, ruby spheres, and pressure medium.

Time-domain thermoreflectance (TDTR) in diamond anvil cells

We measured the thermal conductivity of BAs at ambient and high pressures by TDTR. TDTR is a well-established pump-probe technique. In TDTR measurements, a train of 783-nm-wavelength laser pulses emitted from a mode-locked Ti:sapphire oscillator is split into a pump beam and a probe beam. The pump beam heats the sample at a modulation frequency of ~10 MHz. The probe beam monitors the temperature decay at the sample surface via temperature induced changes in reflectance. The reflected probe beam from the sample surface is collected by a silicon photodiode detector. A lock-in amplifier reads the micro-volt change in voltage output by the detector due to changes in reflected probe beam intensity. The amplifier outputs the in-phase signal V_{in} and out-of-phase signal V_{out} at the ~10 MHz pump modulation frequency. TDTR measurements on the high-purity BAs sample were carried out at the University of California Riverside. Further details of our setup can be found in Ref. [180]. TDTR measurements on the other two samples (Sample B and C) were performed at Tsinghua Shenzhen International Graduate School.

Figure 6.2(a) shows a schematic of the TDTR measurement in a DAC. The pump and probe beams go through the diamond anvil and silicone oil, and reach the sample surface. Figure 6.2(b) shows a photo of a BAs sample (Sample B) loaded inside a DAC. The pressure of the system is calibrated using the pressure dependent shift of the R1 line in the ruby fluorescence spectrum [181]. We also use the Brillouin frequency of silicone oil as a second measure of pressure [24]. Figure 6.2(c) shows a Brillouin oscillation that we observe in our experimental TDTR signals. When the pump beam heats the Al surface, it launches a strain wave into the silicone oil medium. The strain wave front moves at the speed of sound of silicone oil. Both the strain wave and Al can reflect the subsequent probe beam. These two reflected probe beams interfere with each other and cause Brillouin oscillations in the V_{in} signal [36].

We used the beam-offset method to measure the laser spot size [232]. The $1/e^2$ radii were 4.5 μm and 5.1 μm for the measurements on Sample B and C (600 and 350 W m^{-1} K^{-1}), respectively. For the high-purity sample, we measured the spot size at every pressure, and the $1/e^2$ radii were all around 7 μm.

Prior studies of BAs crystals report a Λ variation of ~10-15% across the crystal surface [221]. We also observed Λ variation on a BAs sample, see Figure 6.1(b) for the thermal conductivity map. To deal with this concern, we performed TDTR scans at 4-5 locations on the samples at each pressure. However, our results show the variation is only 5-10% at most pressures for all three samples. The thermal conductivity values we report for three samples are the average from the measured spots.

As a control experiment, we measured the pressure dependent thermal conductivity of two MgO samples. The pressure dependence of MgO's thermal conductivity is well studied experimentally [196] and theoretically [217,233]. We prepared the first MgO sample (blue

symbols in Figure 6.6) following similar procedures as Sample C (coat with Al first, then polish to reduce thickness). For the second MgO sample (purple dots in Figure 6.6), we followed similar procedures as Sample A and B (polish first, then coat with Al). Then we performed TDTR measurements at pressures between 0 and 25 GPa. The $1/e^2$ beam radii for measurements of MgO were ~3 and 7 μm for the first and second MgO sample, respectively.

Data analysis of TDTR under pressure

We use a bidirectional heat diffusion model to analyze the collected TDTR data [179]. The bidirectional model accounts for heat flow from the Al transducer into both the BAs and silicone oil. The thermal conductivity, heat capacity and thickness of each layer are the input parameters in the heat diffusion model. Therefore, we must estimate how these parameters evolve with pressure to interpret our TDTR data. Below, we describe how we account for the pressure dependence of all parameters.

Prior to loading the sample into the DAC, we measure the Al film thickness by picosecond acoustics [36]. At high pressures, we assume BAs shrinks equally in every direction since BAs is a cubic crystal [234]. If the volume of BAs at pressure P is V_P, and the in-plane area is S_P, then $S_P = S_0 \cdot (V_P \,/\, V_0)^{\frac{2}{3}}$. Here, V_0 and S_0 are volume and area of BAs at 0 GPa. We assume the in-plane area of Al is equal to S_p. Then the thickness of Al at pressure P will be $h_P \approx V_P^{Al}/S_P$. Here, V_P^{Al} is the Al volume at pressure P based on Al's equation of state [235].

To estimate the pressure dependence of Al's heat capacity, we follow Ref. [24], and use a Debye model. For silicone oil, we use previously reported pressure dependent heat capacities and thermal conductivities [186].

To model the pressure dependence of BAs's heat capacity, we use a simple isotropic model for the phonon dispersion. We assume $\omega = v_s k - Ak^2$. Here ω is the phonon frequency, v_s is the longitudinal or transverse speed, k is the wavevector magnitude, and *A* is a constant. The value of *A* is determined by the phonon frequency at the Brillouin zone boundary. We set the values of v_s and *A* to mimic first principle calculations for phonon dispersion relations vs. pressure [217,236]. Figure 6.1(a) shows the constructed phonon dispersion relations at 0 and 30 GPa. From the phonon dispersion, we calculate the heat capacities.

We calculate the heat capacity of BAs using [237]

$$C = \sum_j \int d\omega k_B D_j(\omega) \frac{x^2 e^x}{(e^x-1)^2}, x = \hbar\omega / k_B T. \qquad (6.1)$$

Here k_B is the Boltzmann constant, *j* denotes polarizations of phonon branches, ω is the phonon frequency, D_p is the phonon density of states (DOS) calculated from dispersion relations we constructed, *T* is the temperature.

The changes of dispersion under pressures are based on DFT results [217,236]. For transverse phonon branches, we assume they do not change under pressure. For the longitudinal phonon branch, we increase its speed of sound v_s and maximum frequency ω_m based on DFT results [217,236]. For optic phonons, we set the frequencies at zone center and zone boundary under pressures based on DFT results [217].

Finally, to interpret the pressure dependent TDTR measurements of MgO, we use the heat-capacity data reported in Ref. [196].

Thermal conductivity map

We measured the thermal conductivity map of a BAs single crystal. Our high-purity BAs sample for DAC measurements is cut from this BAs single crystal. We collected the map by a 7-μm laser beam in radius, with step size being 14 μm.

Optical artifacts in DAC-assisted TDTR measurements

TDTR is a well-established technique for thermal conductivity measurements and produces robust results provided experimental signals are due to temperature changes on the sample, and not related to other effects. There are situations where this assumption breaks down. For example, acoustic artifacts [238] and roughness [239] have been observed to cause systematic errors in TDTR experiments. In DAC-assisted TDTR measurements, we have observed that optical artifacts can introduce systematic errors in our analysis. Our experience suggests these optical artifacts are caused by diffuse scattering from defects on the sample surface that make the optical quality poor. Or they can be caused by interference effects between the diamond surfaces and Al coated BAs sample. A clear indicator that there are optical artifacts affecting our measurement is a TDTR signal strength that depends on position. Therefore, in all the data we report in this study, we took care to exclude data from samples whose TDTR signal was not reproducible across the sample's surface.

As an example of the effects we sometimes see, and that we use spatial mapping to identify, we present two TDTR scans vs. position of two samples in Figure 6.11. In Figure 6.11(a), we show a $-V_{in}/V_{out}$ map for a sample with a clean surface loaded inside a DAC. The $-V_{in}/V_{out}$ is homogenous across the sample, and the TDTR data shows no signs of artifacts. Alternatively, Figure 6.11(b) shows an abnormal $-V_{in}/V_{out}$ map. The interference pattern clearly indicates there are optical artifacts unrelated to temperature affecting our signals. When observing significant variance in TDTR signals with position, we discard that sample's data set, and reload

the DAC with a new sample. We believe the specific fringe-like pattern seen in Figure 6.11(b) was caused by interference effects between the diamond anvil surface and Al film. Diamond has an index of refraction of 2.417. According to Fresnel's law, there is 7% laser reflection at diamond/silicone-oil interface. The diamond/silicone-oil interface is only 10-30 μm away from the sample surface, which is a distance comparable to the beam's depth of focus. Surfaces with severe plastic deformation, or optically damaged surfaces also lead to large TDTR signal variance with position, and were discarded to avoid optical artifacts affecting our results.

Relaxation time approximation model

To better understand the atypical pressure dependence of BAs's Λ, we use a relaxation time approximation (RTA) model to analyze our experimental results. The RTA model examines how pressure induced changes in phonon group velocities, phonon number density, phonon-phonon scattering, and defect scattering affect Λ *vs.* P.

In the relaxation time approximation (RTA) model, we assume optic phonons carry no heat because of their low group velocity, small occupation factor, and short lifetimes. Then, the thermal conductivity is

$$\Lambda = \sum_j \int_0^{\omega_m} \frac{1}{3} C_j(\omega) v_j(\omega) l_j(\omega)\, d\omega. \qquad (6.2)$$

Here j labels polarizations, $v_j(\omega)$ is the group velocity of polarization j at phonon frequency ω, $C_j(\omega)$ is the integrand in eq. (1), and

$$l_j(\omega) = v_j(\omega)\tau(\omega). \qquad (6.3)$$

Here τ is the total phonon relaxation time for all processes. And

$$\tau(\omega)^{-1} = \tau_{pp}(\omega)^{-1} + \tau_m(\omega)^{-1}. \qquad (6.4)$$

Here $\tau_{pp}(\omega)^{-1}$ is the intrinsic phonon scattering rate of BAs. We assume $\tau_{pp}(\omega)^{-1} = Af(\omega)$, where A is a pressure dependent scattering amplitude and $f(\omega)$ is a function chosen so to mimic the frequency dependence of τ_{pp}^{-1} predicted by DFT [217]. $\tau_m(\omega)^{-1}$ is the mass-disorder scattering rate, which is [240]

$$\tau_m(\omega)^{-1} = \frac{\pi V}{6}\Gamma\omega^2 D(\omega). \qquad (6.5)$$

Here V is the volume per atom, Γ is the scattering strength and $D(\omega)$ is the density of states per atom.

Here are two notes for $\tau^m(\omega)^{-1}$: 1) In principle, Γ can be calculated by the atomic mass of different component. However, we set its value so Eq. (6.2) predicts thermal conductivity of 480 and 350 W m^{-1} K^{-1} at 0 GPa for sample B and C, respectively. We also assume Γ is independent of pressure. Then, the pressure dependence for mass-disorder scattering depends only on $V \cdot D(\omega)$. For mass-disorder scattering rate in Eq. (6.5), we use DFT predictions for $D(\omega)$ from Ref. [241]. Figure 6.9 shows the phonon-phonon scattering rates and mass-disorder scattering rates we use in our RTA model for Sample B at 0 GPa.

Here are our simulation steps. First, we set A to make the thermal conductivity of BAs without defects be ~ 1300 W m^{-1} K^{-1} at 0 GPa. Second, adjust Γ to generate a thermal conductivity of 480 W m^{-1} K^{-1}. Finally, calculate the pressure dependent thermal conductivity of Sample B by assuming a pressure independent A. We set the pressure dependence of phonon group velocities and density of states to mimic DFT predictions [217,241,242].

Our RTA analysis suggests the weak pressure dependence of Λ on P is because total phonon-phonon scattering rates are pressure independent. Therefore, we conclude that our experiments

are consistent with DFT predictions for how acoustic bunching, three-phonon scattering, and four-phonon scattering govern Λ *vs.* P in BAs [217].

6.3 Results

The focus of our study is on a high-purity BAs single crystal with thermal conductivity ranging 1000-1300 W m^{-1} K^{-1}. We show a thermal conductivity map of this triangular BAs single crystal in Figure 6.1(b). After collecting the map, we broke the crystal into small pieces and processed one of them for diamond anvil cell (DAC) measurements (Sample A).

The thermal conductivity of BAs is known to be sensitive to even small concentrations of defects [229,243,244]. Therefore, to explore how defects affect the pressure dependent thermal conductivity of BAs, we also studied two other crystals with lower ambient thermal conductivities (Samples B and C). The ambient thermal conductivities of these samples are ~600 and 350 W m^{-1} K^{-1}.

We observe that high-purity BAs has a constant thermal conductivity of ~1000 W m^{-1} K^{-1} between 0 and 30 GPa, see Figure 6.3. This is the main result of our study. We also observe that BAs crystals with low concentrations of defects (Samples B and C) have a pressure independent thermal conductivity.

TDTR is a well-established method whose uncertainty depends on input parameters in the heat diffusion model [245–247]. In our measurements, the uncertainty mostly comes from the thickness of Al (h_{Al}), heat capacity of Al (C_{Al}), laser spot size (ω_0), and heat capacity of BAs (C_{BAs}). Typically, we have a ~5% uncertainty in $h_{Al}C_{Al}$ [190], ~5% uncertainty in spot size ω_0.

We also estimate an uncertainty of ~3% uncertainty for C_{BAs}. These yield a total uncertainty in the derived values for Λ_{BAs} of ~15%. The error bars in Figure 6.3 indicate the uncertainty in Λ_{BAs}.

As described in Methods, we performed multiple TDTR measurements at various locations on the BAs samples at each pressure. The thermal conductivity reported in Figure 6.3 is the average value from all measurements for a given sample and pressure. The purpose of measuring multiple spots is to avoid optical artifacts and guarantee the reproducibility of our measurements. As expected for a high-quality homogenous crystal, the variance in thermal conductivity at different sample locations is small at most pressures.

The apparent thermal conductivity we derive from TDTR measurements of the BAs crystals depends on the size of the laser beam we use in our experiments, see Figure 6.8. The apparent dependence of the thermal conductivity on laser spot size is an artifact caused by the breakdown of the heat-diffusion equation [248,249]. As a result of this spot-size effect, the pressure dependent thermal conductivity values reported in Figure 6.3 are ~20% lower than the intrinsic value. Our primary interest is the pressure dependence of thermal conductivity. Because the spot-size artifact should not depend on pressure [250], this small deviation does not affect our conclusions. The apparent dependence of BAs's thermal conductivity on laser spot size is an artifact caused by the breakdown of the heat-diffusion equation [248,249]. Our observations for how the TDTR derived apparent thermal conductivity of BAs depends on laser spot size are consistent with prior TDTR studies of BAs [221]. Ideally, we would avoid the spot-size artifact by measuring the thermal conductivity of BAs only with large spot sizes, *e.g.*, 25 μm in radius. However, we are unable to do so because the DAC requires small samples. The lateral scales of our samples are of tens of microns as mentioned in Methods. Additionally, upon compression, samples undergo some plastic deformations that cause warped regions on the surface we must avoid. Avoiding such regions is more difficult with a large-area beam. A third issue with larger

laser spot sizes is they also involve a larger depth of focus. Typically, the depth of focus of a 5× objective lens is 14 μm. The sample-diamond distance in a DAC is 10-30 μm. This can lead to interference between sample-reflected beam and diamond-reflected beam, see Figure 6.11. To compromise these problems, we used a spot size of 7 μm in $1/e^2$ radius.

In Ref. [250], a "generalized Fourier's law" is employed to account for the spot-size artifact in TDTR measurements. Their calculations predict the reduction of BAs thermal conductivity in Al/BAs geometry depends on the interface conductance between Al and BAs ($G_{Al/BAs}$). Their generalized Fourier's law predicts that the Λ reduction will be small when the pump beam diameter is 14 μm. Their calculations predict the spot-size artifact in a TDTR experiment is ~ 6% when $G_{Al/BAs}$ = 115 MW m^{-2} K^{-1} and ~ 4% when $G_{Al/BAs}$ = 253 MW m^{-2} K^{-1}. Our Al/BAs interface conductance data are included in Figure 6.13 - 6.15.

The weak pressure dependence we observe for all three BAs crystals is in stark contrast with our observations for MgO, see Figure 6.6. For MgO, we observe a factor of two increase in the thermal conductivity upon compression to 20 GPa. Our results for MgO agree with prior reports [196].

6.4 Discussion

In the absence of contextualizing information, the dramatic difference in $\Lambda(P)$ for BAs vs. MgO (Figure 6.3 *vs.* Figure 6.6) is quite surprising. The bulk modulus of BAs is 142 GPa, while MgO is 160 GPa [251,252]. Both materials have a relatively small atomic mass per unit cell and simple unit cells. BAs has a zin-blende crystal structure ($F\bar{4}3m$) and MgO has a halite structure

($Fm\bar{3}m$). The Grüneisen parameter of BAs and MgO are both expected to experience a ~10% decrease between 0 and 20 GPa [242,253].

To understand what the difference in $\Lambda(P)$ for BAs *vs.* MgO implies, it is useful to consider the microscopic origins for a material's thermal conductivity. The thermal conductivity of a material is determined by group velocities, number density, and relaxation times of phonons. Therefore, the pressure dependent thermal conductivity is determined by the pressure dependence of these three vibrational properties. The Leibfried-Schlömann (LS) equation is a simple model for quantifying how these three vibrational properties govern Λ. A number of prior experimental studies show the LS equation often has predictive power in explaining $\Lambda(P)$ [10,22,196]. The LS equation predicts

$$\Lambda = \frac{B\bar{M}\delta\theta^3}{T\gamma 2}. \qquad (6.6)$$

Here B is a constant, $\bar{M}$ is the average mass of an atom in the crystal, δ^3 is the average volume occupied by one atom in the crystal, θ is the Debye temperature, T is temperature, and γ is the Grüneisen parameter. We take the pressure dependence of these quantities for BAs from Refs. [234,242]. Not surprisingly, given BAs's special phonon dispersion relation, the LS equation drastically overestimates the $\Lambda(P)$ of BAs, see Figure 6.3(b). Nevertheless, the LS equation prediction serves as a useful benchmark for what $\Lambda(P)$ should look like if pressure-induced changes to the phonon dispersion do not dramatically alter the phase space for phonon-phonon scattering. We observe that the LS equation does a good job predicting $\Lambda(P)$ in MgO, see Figure 6.6.

We emphasize that a pressure independent thermal conductivity between 0 and 30 GPa is extremely unusual behavior for nonmetallic materials. Normally, thermal conductivity

monotonically increases with increasing pressure [210]. At high pressures, atomic bonds tend to stiffen, and phonon frequencies tend to increase, favoring a higher thermal conductivity. Furthermore, three-phonon scattering rates are governed by phonon anharmonicity. Anharmonicity typically decreases with increasing pressure, as evidenced by the fact that the Grüneisen parameter of most materials tend to decrease upon compression [254]. A reduction in anharmonicity also favors a larger thermal conductivity at a higher pressure. $MgSiO_3$'s thermal conductivity increases from 6 to 10 W m^{-1} K^{-1} upon compression to 20 GPa [255]. The thermal conductivity of various ferropericlase materials roughly doubles upon compression to 20 GPa [255]. Ice VII's thermal conductivity increases from 4 to 25 W m^{-1} K^{-1} between 2 and 22 GPa [10]. PMMA's thermal conductivity increases by a factor of 3 upon pressurization from 0 to ~10 GPa [256]. The thermal conductivity of muscovite mica, $KAl_2(Si_3Al)O_{10}(OH)_2$, increases by a factor of 10 between 0 and 20 GPa [22]. In a recent review article, Hofmeister reports the $d\Lambda/dP$ for 22 materials [257]. 21 out of 22 materials have positive derivatives that are larger than 3.5% per GPa. Materials whose thermal conductivity do not monotonically increase with pressure often involve a phase transition, *e.g.*, Si [26] or KCl [258]. BAs is not expected to undergo a phase transition below 100 GPa [234].

The unusual pressure independent thermal conductivity of BAs corroborates first-principles predictions that phonon lifetimes in BAs are governed by different processes than in other non-metallic materials. In most materials, three-phonon scattering among two acoustic and one optic mode (*aao*) or three acoustic modes (*aaa*) are the most important type of processes [216,218,259]. However, in BAs, selection rules forbid *aao* processes because the frequency of all optic phonons are more than twice that of the highest frequency of the acoustic mode. As a result, *aaa* and *aaoo* (four-phonon) processes are expected to have the strongest effect on the lifetime of heat-carrying phonons [217]. An *aaoo* process is a four-phonon scattering

process that involves two acoustic modes and two optic modes. To understand why BAs has a pressure independent thermal conductivity, we need to consider how *aaa* and *aaoo* processes are affected by pressure.

Upon compression, we expect scattering rates involving *aaa* processes to increase, and the scattering rates for *aaoo* processes to decrease. As mentioned in the introduction, upon compression, there are two major changes to the phonon dispersion of BAs. First, acoustic bunching decreases [217,218], see Figure 6.1(a). By this, we mean there is a larger difference in frequency between the different acoustic phonon branches. Second, the frequency of optic phonons increases [260].

A decrease in acoustic bunching should increase three-phonon scattering rates by increasing the phase space for *aaa* processes. To understand why, it's instructive to note that an acoustic phonon cannot decay into two acoustic phonons in the same branch [212,226]. This is because it is impossible for three acoustic phonons in the same branch to satisfy crystal momentum and energy selection rules unless the phonon dispersion relation is perfectly linear [212]. Therefore, in the limit that all three acoustic phonon branches were degenerate, the phase space for *aaa* processes would be zero. Of course, transverse, and longitudinal branches are not degenerate in BAs, so *aaa* processes are allowed. But the phase space for such process is more restricted when the frequencies of transverse and longitudinal acoustic branches get closer.

The increase in the frequency of optic phonons should decrease four-phonon scattering rates involving *aaoo* process. Four-phonon scattering rates involving two optic phonons will be proportional to $(1 + n_{o\prime})n_{o\prime\prime}$, where $n_{o\prime}$ and $n_{o\prime\prime}$ are the thermal occupation factors for the two optic modes. Thermal occupation of optic modes at room temperature will decrease upon compression because frequencies increase.

The above discussion provides a qualitative explanation for why BAs's thermal conductivity depends weakly on pressure. Three-phonon scattering rates increase. Four-phonon scattering rates decrease. These two effects offset each other, and as a result the thermal conductivity remains constant upon compression.

An important goal of our study is to experimentally quantify the relationship between acoustic bunching and three-phonon scattering rates. The weak pressure dependence of BAs thermal conductivity implies the total scattering rate for phonons also depends weakly on pressure. We use this fact to estimate how much three-phonon scattering rates change upon compression to 30 GPa. Raman scattering data and first principles calculation suggest the frequency of optic phonons of BAs increase from ~21 to 25 THz [217,260]. This will lead to a factor of two decrease in thermal occupation of optic modes. Since *aaoo* scattering rates are expected to be proportional to $(1 + n_o)n_o$, we expect the stiffening of optic mode frequencies to decrease *aaoo* scattering rates by a factor of 2. To make crude estimates for how much 3-phonon scattering rates change with pressure, we make two simplifying assumptions. We assume the thermal resistance from three- and four-phonon processes add in series. And, for simplicity, we assume three- and four-phonon scattering processes are of roughly equal importance at 0 GPa. This latter assumption is consistent with first-principles calculations, which predict a thermal conductivity roughly twice what is observed at ambient pressure when four-phonon processes are neglected [215,217,224]. With these assumptions, in order to compensate for a 2× fewer *aaoo* scattering events, *aaa* scattering needs to increase upon compression to 30 GPa by ~50%.

Despite the crudeness of the above analysis, it is in good agreement with first principles calculations. First principles calculations predict that in the absence of four-phonon scattering, Λ of BAs would decrease by 40% upon compression to 30 GPa at 300 K [217]. Additionally, first

principles calculations predict *aaoo* scattering rates at frequencies above 5 THz decrease from ~1 GHz to ~ 0.5 GHz [217].

In Ref. [217], Ravichandran and Broido theoretically studied how temperature and pressure tune the phonon scattering rates in BAs. At 300 K, their calculated thermal conductivity increases by 11% at ~18 GPa and then decreases. They performed calculations on both natural and isotopically pure BAs and claimed that isotope disorder would not affect the pressure dependence. Our measurements on Sample A (1100 W m^{-1} K^{-1}) are in excellent agreement with the their calculation results from 0 to 30 GPa at 300 K [217], as shown in Figure 6.3(b).

Measurements on the two lower-thermal-conductivity BAs samples allow us to evaluate the effect of phonon scattering from crystalline disorder on the $\Lambda(P)$ of BAs. The thermal conductivities of the less-ordered BAs crystals are 40 – 70% lower than the sample shown in Figure 6.1(b). In this work, we measured three samples with different defect concentrations to see how defects affect the pressure dependence of Λ_{BAs}. It is well known that even a minute concentration of point defects can hugely suppress BAs's thermal conductivity [229,243,244]. Previous studies suggest there could be many kinds of defects in BAs [229,243,244,260,261]. A boron or arsenic vacancy concentration of ~1.5×10^{19} cm^{-3} would be sufficient to explain the reduced Λ of our samples [243]. Similarly, As_B-B_{As} antisite pair concentration of ~1.5×10^{19} cm^{-3} [261], or carbon impurity concentrations of ~10^{20} cm^{-3} [229], would also explain Λ ~500 W m^{-1} K^{-1} of BAs. To quantitatively evaluate how point-defect disorder affects $\Lambda(P)$ of BAs, we construct a simple relaxation time approximation (RTA) model. The RTA model examines how pressure induced changes in phonon group velocities, phonon-phonon scattering, and defect scattering affect $\Lambda(P)$. The predictions of the RTA are shown in Figure 6.3(b) as the yellow line. By assuming a pressure independent phonon-phonon scattering rates in BAs, our RTA model agree well with $\Lambda(P)$ of two

lower-thermal-conductivity BAs samples. We attribute the pressure independent thermal conductivity of these two samples to pressure independent total phonon-phonon scattering rates.

In conclusion, we measured the pressure dependent thermal conductivity of three BAs samples between 0 and 30 GPa. In contrast to the typical behavior for nonmetallic materials, we observe the thermal conductivity of BAs to be independent of pressure. We attribute this unusual behavior to the pressure independent phonon-phonon scattering rates at $P < 30$ GPa. We believe the pressure independent scattering rates are caused by a competition between weakening of four-phonon scattering processes and strengthening of three-phonon scattering processes. Our experiments provide the first test of first-principles theories regarding the relationship between phonon dispersion, phonon selection rules, and three- and four-phonon scattering rates [216,217], and improve fundamental understanding of thermal transport in high-thermal-conductivity materials.

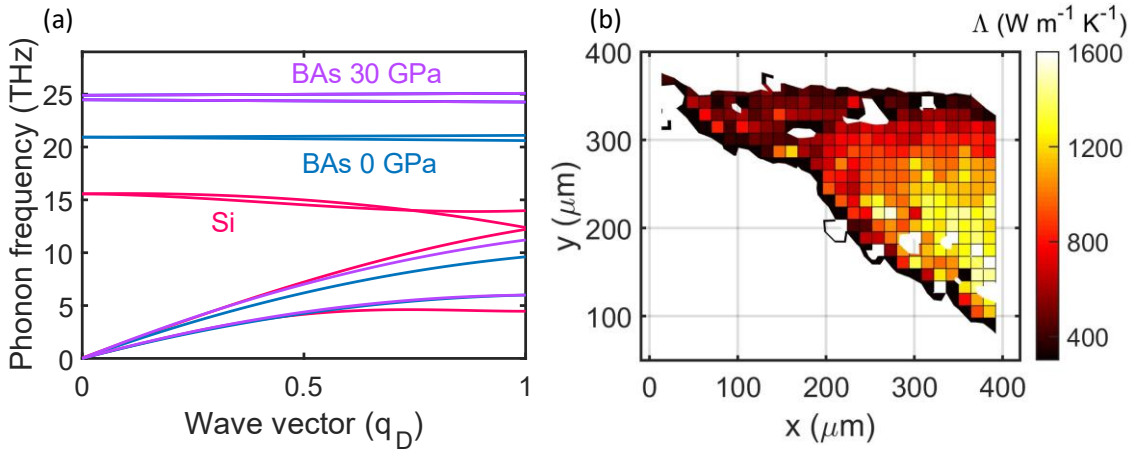

Figure 6.1. A schematic of pressure-induced changes in phonon dispersion of BAs.

(a) Approximate phonon dispersion relations of BAs at 0 and 30 GPa. q_D refers to the wave vector at the zone boundary. We construct isotropic dispersions of BAs by imitating the DFT calculation results of BAs in Ref. [217]. Stiffening of the longitudinal acoustic phonon branch with increasing pressure reduces acoustic bunching. The dispersion relations of Si at 0 GPa are included as red curves [262]. The large *a*-*o* gap and acoustic bunching are believed to lead to the high Λ of BAs. Increased pressure reduces the bunching of BAs's acoustic modes, leading to a dispersion relation more like Si. (b) Map of the thermal conductivity at 0 GPa of the triangular BAs crystal that is the focus of our study. The thermal conductivity in the interior of the crystal ranges between 1000 and 1300 W m^{-1} K^{-1}.

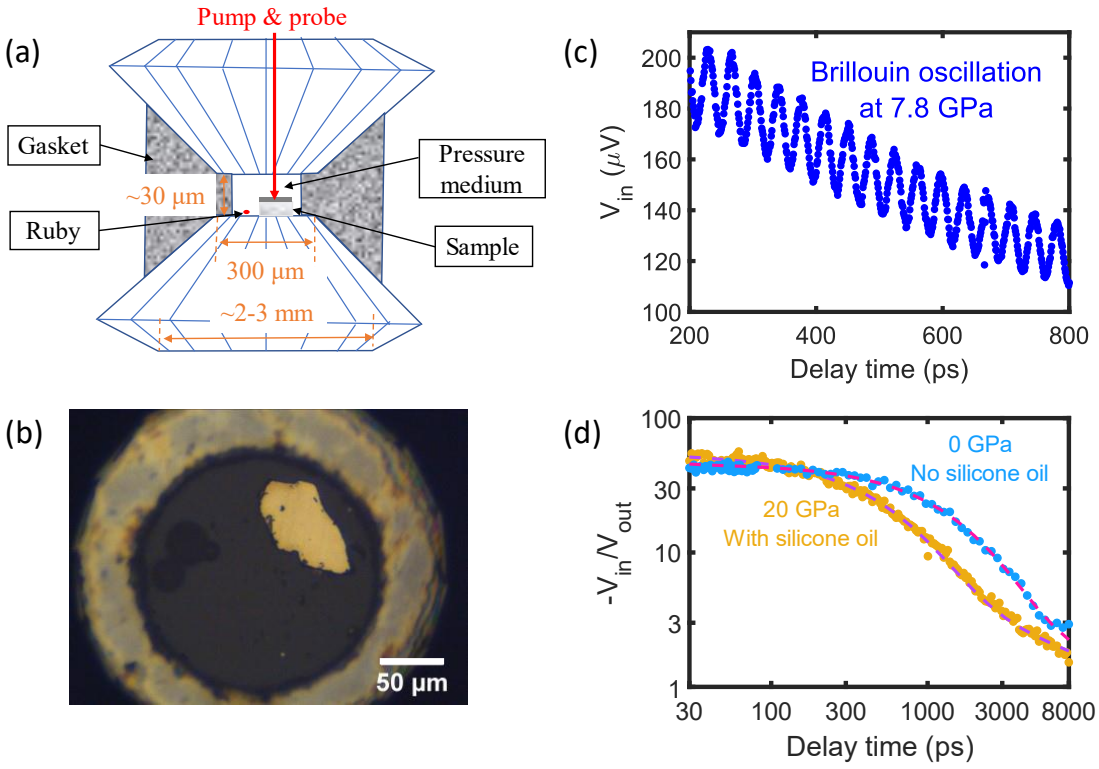

Figure 6.2. Schematics of DAC-assisted TDTR measruements on BAs.

(a) A schematic of the DAC-assisted TDTR measurement. The pump and probe beams transmit through the diamond and pressure medium, and are focused onto the sample surface. (b) Image of a BAs sample coated with Al inside a DAC. We load ruby spheres as pressure indicators. We use a stainless-steel gasket and silicone-oil pressure medium. (c) An example of Brillouin oscillations from the silicone oil in our experimental signal. The frequency of the Brillouin oscillation provides a sensitive measure of local pressure at the sample. (d) TDTR data collected on Sample A at 0 and 20 GPa. The dots and dash lines are the experimental results and the predictions by the heat diffusion model, respectively.

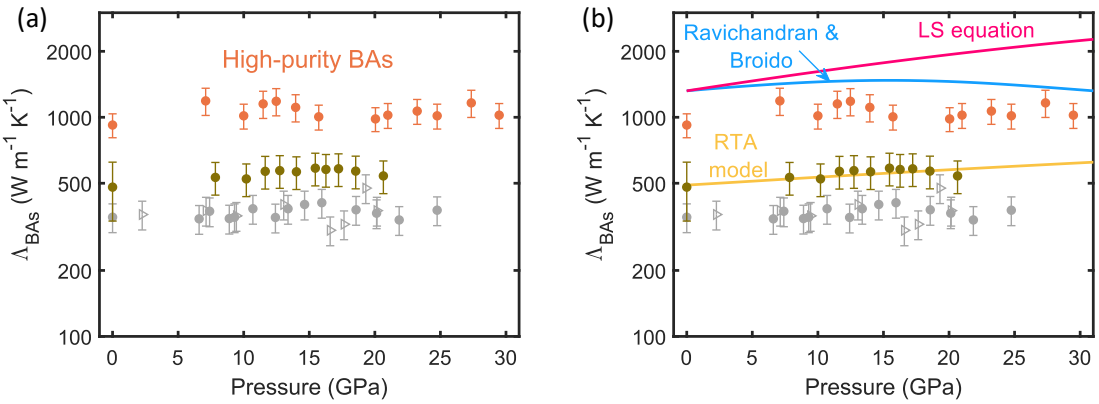

Figure 6.3. Thermal conductivity versus pressure for three BAs samples with different ambient thermal conductivity.

(a) Pressure dependent thermal conductivities of three BAs samples. Dots are compression data while triangles are decompression data. Different colors stand for different samples. (b) Model predictions for the thermal conductivity of BAs. The blue curve is the thermal transport calculation at 300 K from Ref. [217]. The red line represents the Leibfried-Schlömann equation prediction. To show the different trend predicted by first-principles thermal transport calculation and LS equation, we set the ambient Λ values equal. The yellow line is a relaxation time approximation model prediction. The RTA model considers the effects of phonon-phonon scattering and phonon-defect scattering.

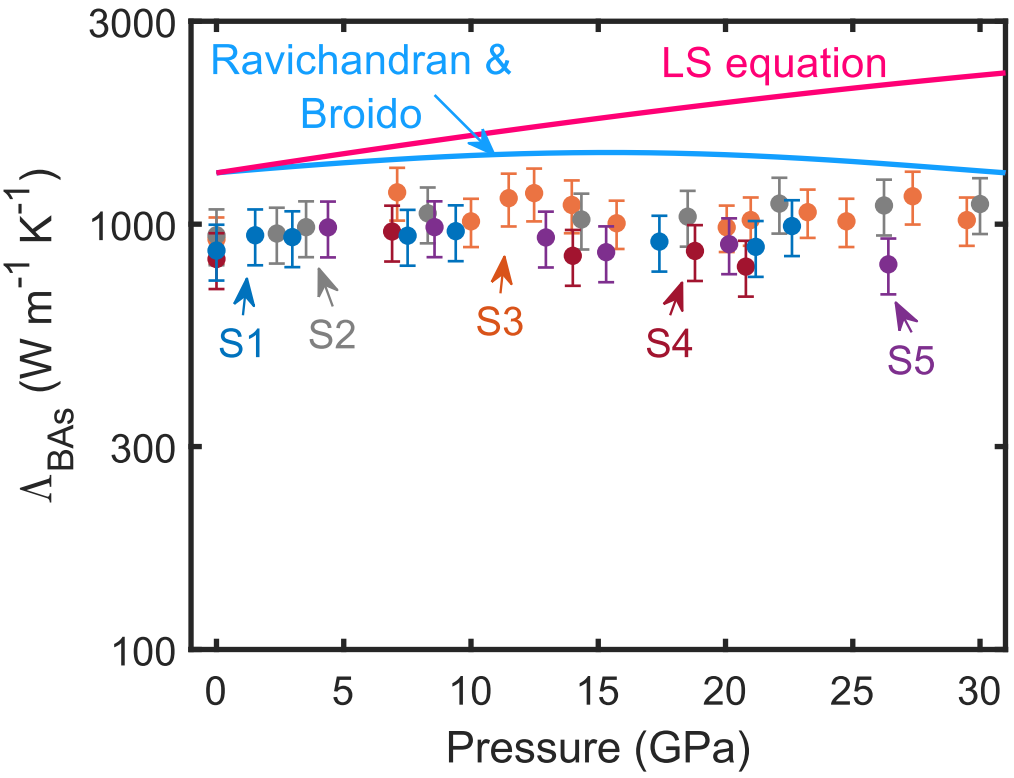

Figure 6.4. Pressure-dependent thermal conductivity of five BAs samples with ambient thermal conductivity of ~1000 W m^{-1} K^{-1}.

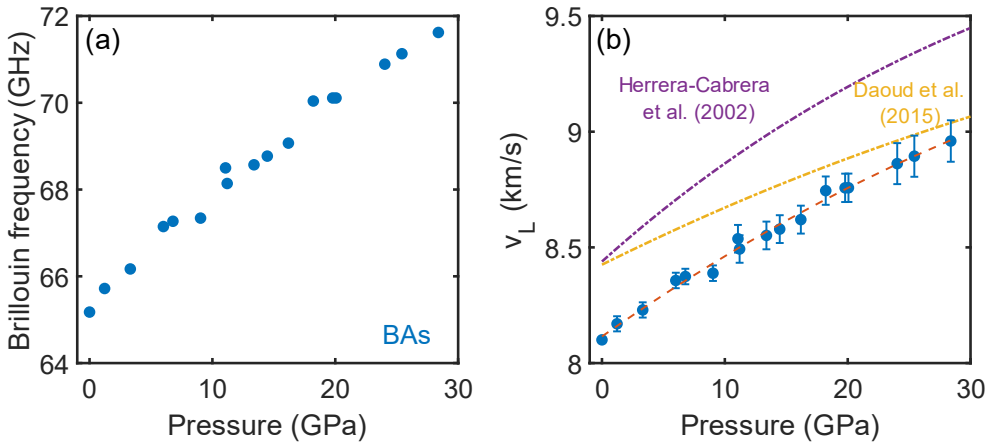

Figure 6.5. Pressure-dependent Brillouin scattering on BAs along the [111] direction.

(a) Relationship between Brillouin frequency and pressure, obtained from measurements on the high-purity BAs sample. (b) The group velocity of BAs as a function of pressure, calculated based on the measured Brillouin frequency. The purple and yellow dash-dot lines represent theoretical predictions [236], while the orange dash line provides a guide for our data.

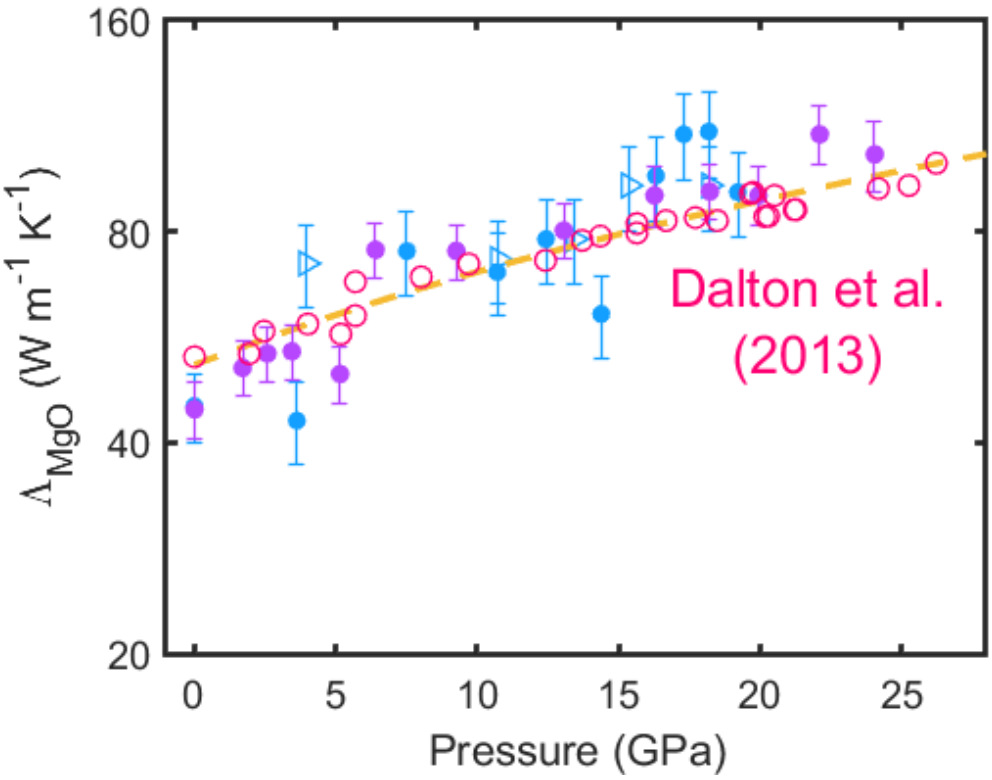

Figure 6.6. Thermal conductivity versus pressure of MgO.

We characterized two MgO samples as control measurements shown as the blue and purple symbols. Dots and triangles are compression and decompression data, respectively. Here we measured only a single location at each pressure. The error bars here represent the ~ 10% uncertainties in thermal conductivity that arise from uncertainties in thermal model parameters. Red circles and the orange dashed line are the published experimental data and prediction of the Leibfried-Schlömann equation, both from Ref. [196].

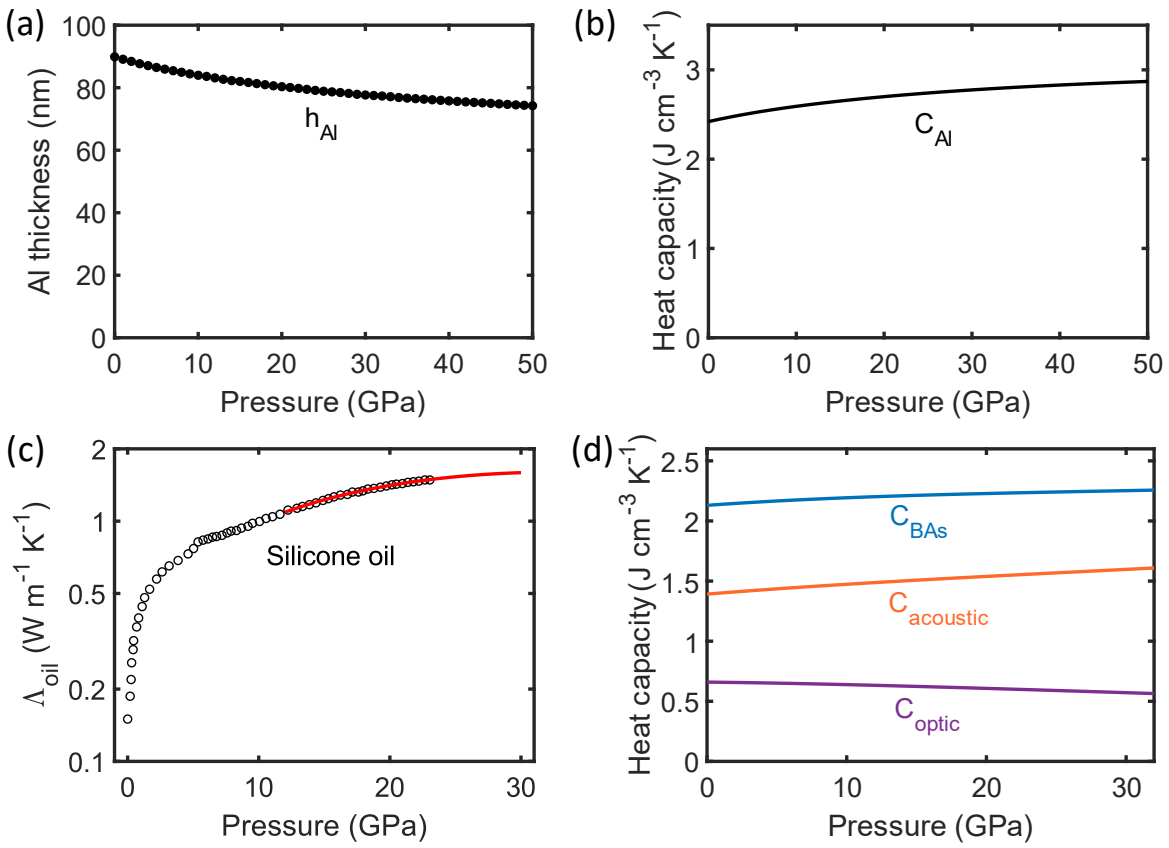

Figure 6.7. Pressure dependent properties of interests in the bidirectional heat diffusion model.

(a) Al thickness under pressures. The thickness h_{Al} is calculated based on the volume-pressure equation of state of Al and BAs [184,263]. (b) Pressure dependent heat capacity of Al calculated by the Debye model. We follow the assumptions in Ref. [264] and get the same results. (c) Pressure dependent thermal conductivity of silicone oil. Circles are the simulation in Ref. [204], the red line is an extrapolation of the simulation. (d) Pressure dependent heat capacity of BAs calculated from the constructed isotropic dispersion relations. We normalized C_{BAs} at 0 GPa to the value reported in Ref. [221].

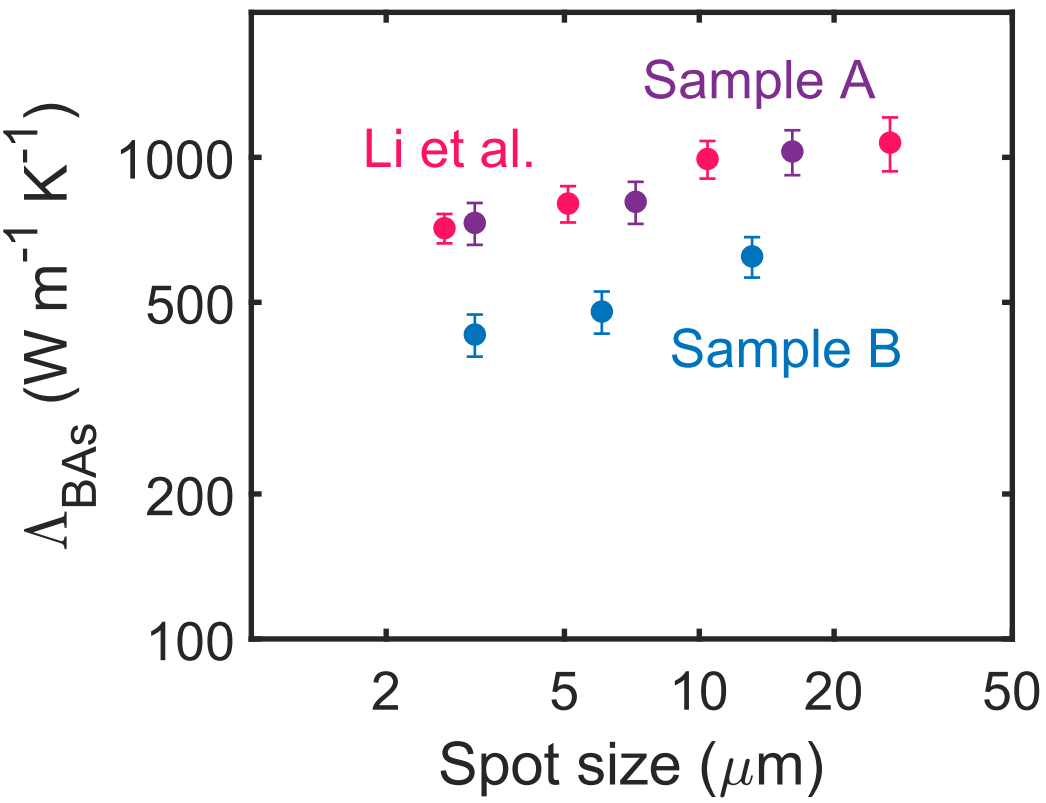

Figure 6.8. Spot-size dependent measurements of BAs Sample A and B.

Here the spot size is in $1/e^2$ radius. The measured thermal conductivity of BAs decreases when the spot size decreases. This phenomenon is also reported in Ref. [221] and Ref. [265]. We include the results from Ref. [221] as a comparison.

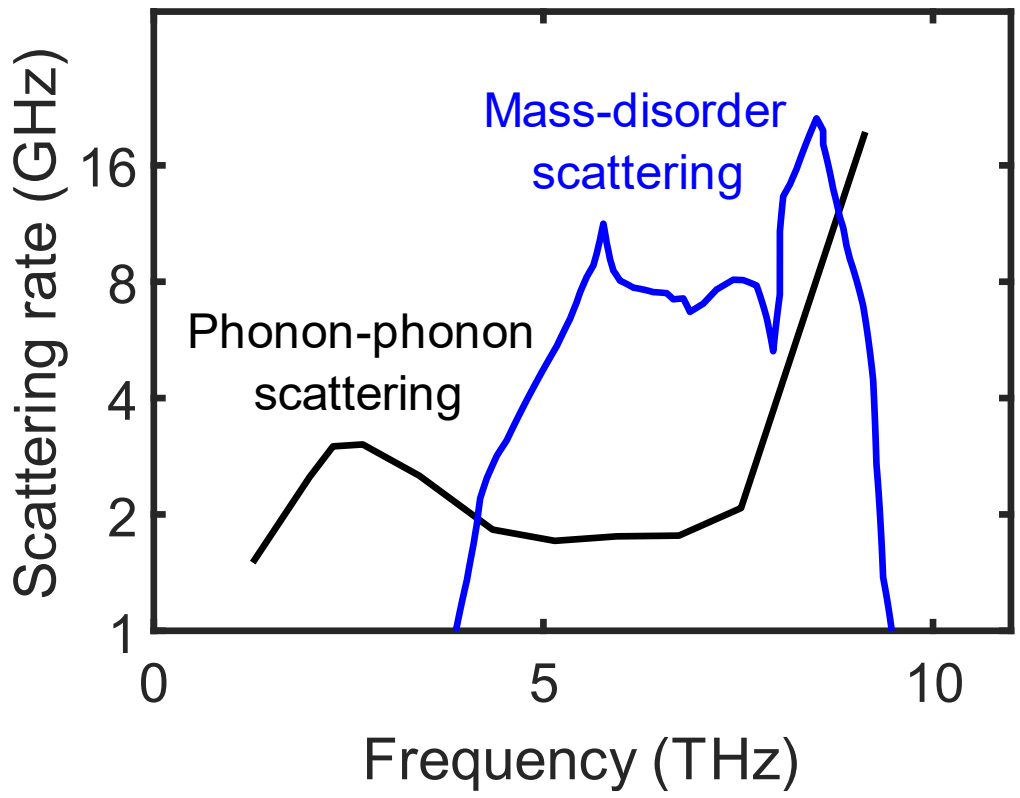

Figure 6.9. Constructed phonon-phonon scattering rates and mass-disorder scattering rates at 0 GPa.

We construct the phonon-phonon scattering rates to mimic the DFT results [217].

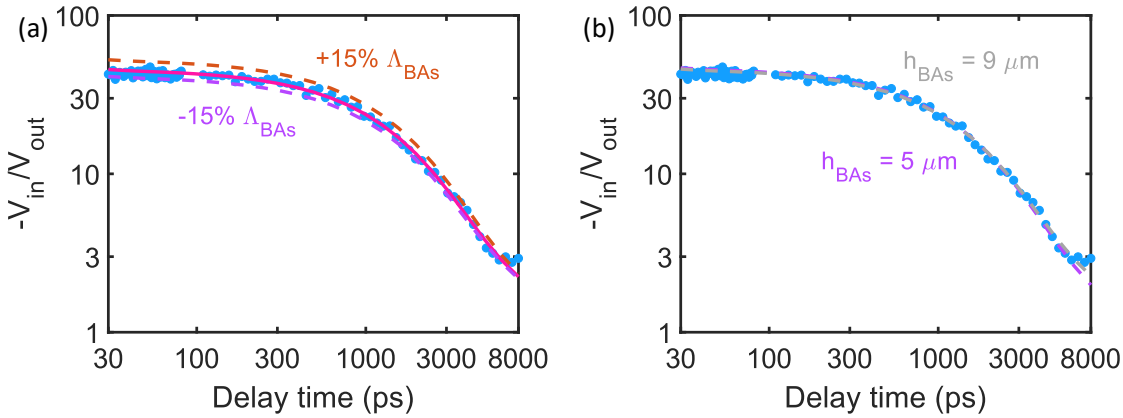

Figure 6.10. Examples demonstrating the sensitivities of Λ_{BAs} and the thickness of BAs sample.

Dots are TDTR ratio data (in-phase signal V_{in} divided by out-of-phase signal V_{out} from the lock-in amplifier) collected on the high-purity BAs sample at 0 GPa. The $1/e^2$ intensity radius of the laser spot is 7.1 μm. (a) An example to show the sensitivity of Λ_{BAs} in the heat diffusion model. The solid line is the best fitting for the ratio data. The two dash curves are model fittings by inputting 15% larger or smaller Λ_{BAs} in the heat diffusion model. (b) Comparison of TDTR data with thermal model predictions. We include thermal model predictions that assume a BAs thickness of 5 and 9 μm. TDTR is a surface sensitive technique, and measures transport properties only over the distance heat can diffuse in one modulation period of the pump heating. In our experiments, the thermal penetration depth in BAs is only 3.7 μm. As a result, the sample thickness is not an important parameter in our analysis.

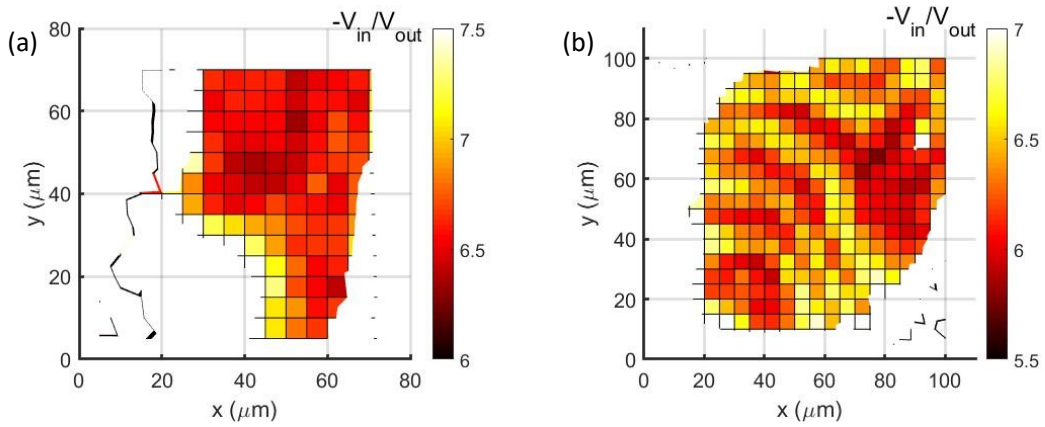

Figure 6.11. TDTR map of $-V_{in}/V_{out}$ on two single crystal samples measured in diamond anvil cells.

(a) and (b) are two pieces of samples from the same batch. (a) is homogenous while (b) shows fringe-like patterns. The patterns in (b) is caused by optical artifacts in DAC-assisted TDTR measurements. Please note the samples are not BAs. We use this figure to demonstrate potential optical artifacts in DAC-assisted TDTR measurements.

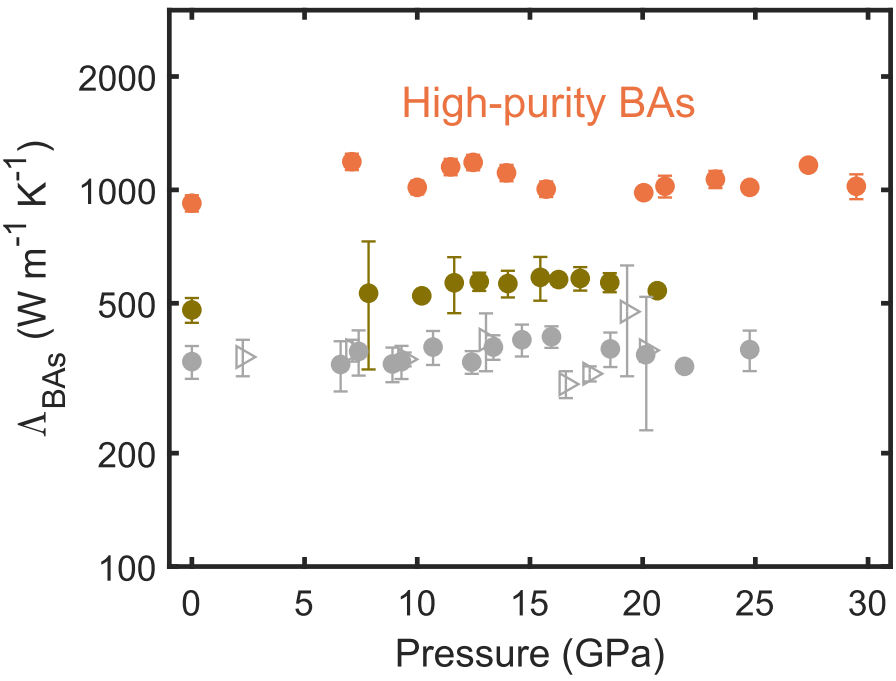

Figure 6.12. Thermal conductivity of BAs *vs.* pressure with error bars indicating variance among measured spots.

We measured multiple spots in each BAs samples to guarantee the reproducibility of our data. The symbols are averages of Λ_{BAs} at measured spots. Error bars are standard deviations.

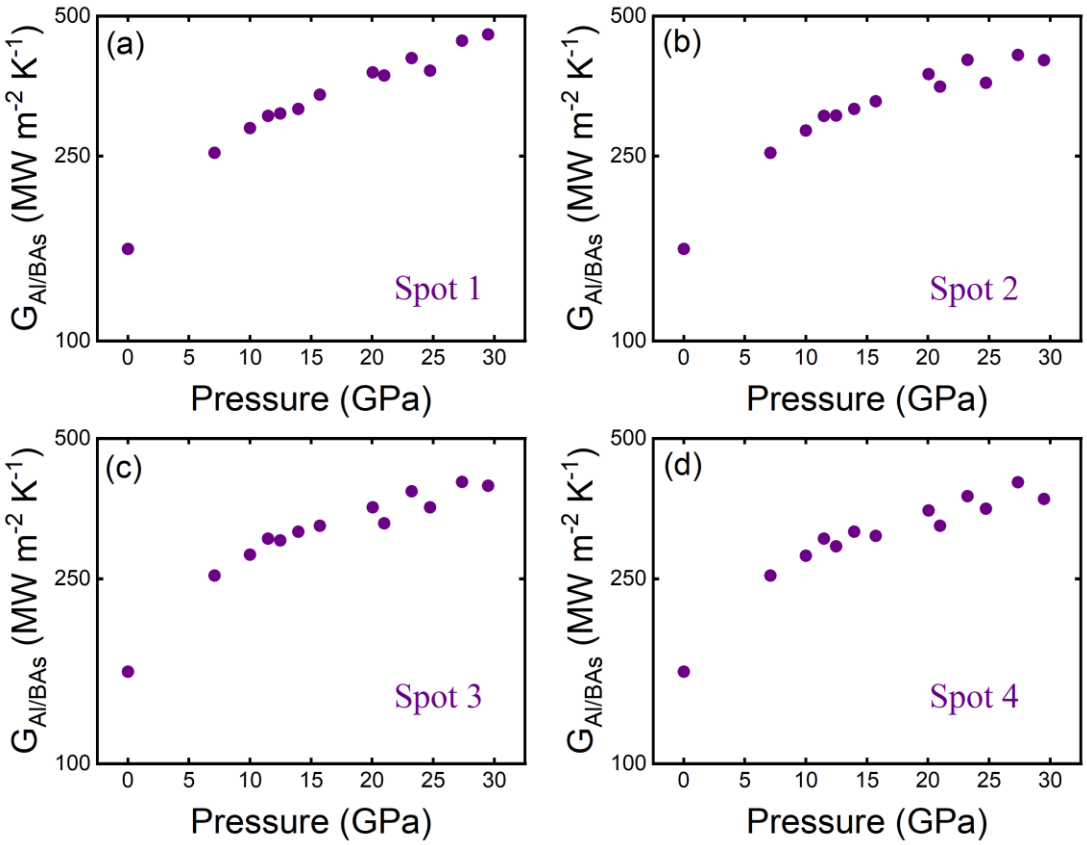

Figure 6.13. Pressure dependent interface conductance of the four spots on Sample A (1100 W m^{-1} K^{-1}). The interface is the one between Al and BAs.

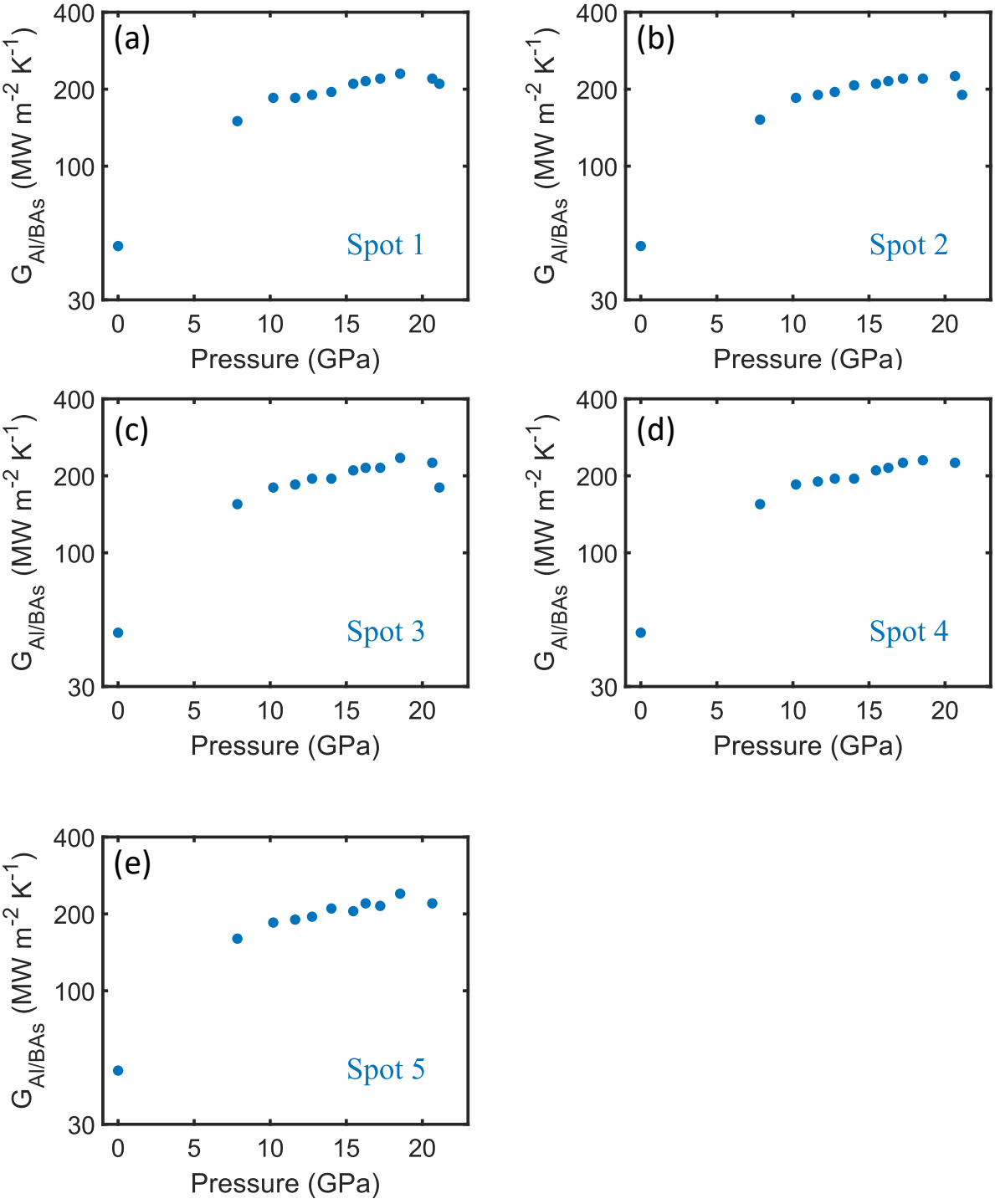

Figure 6.14. Pressure dependent interface conductance of the five spots on Sample B (600 W m^{-1} K^{-1}).

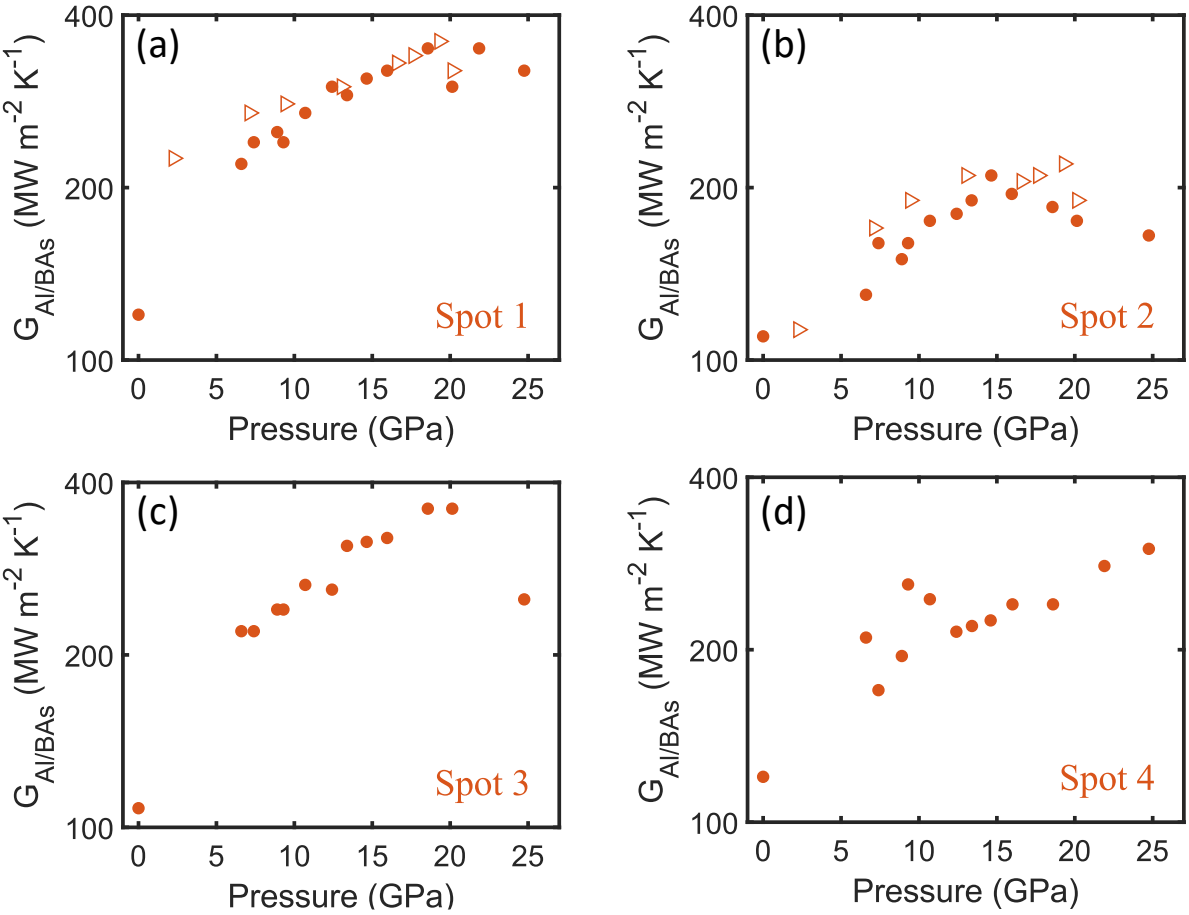

Figure 6.15. Pressure dependent interface conductance of the four spots on Sample C (350 W m^{-1} K^{-1}).

Chapter 7 Testing the Effect of Phonon-Frequency Gap on the Pressure Dependence of Thermal Conductivity in BAs, GaN, and Diamond

7.1 Introduction

Upon compression, most materials exhibit an increasing thermal conductivity in the absence of phase transition due to the stronger interatomic bonding [6]. Recently, we reported that cubic boron arsenide (BAs) demonstrates a pressure-independent thermal conductivity up to 30 GPa [23,150]. So far, BAs is the only material exhibiting a non-increasing thermal conductivity at high pressure without phase transition. The proposed mechanism behind the unusual pressure-independent thermal conductivity is that pressure induces opposing changes in the rate of three-phonon scattering vs. four-phonon scattering. Three-phonon scattering rates increase, while four-phonon scattering rates decrease as pressure increases [150,217]. Consequently, phonon lifetimes stay constant as pressure increases, leading to a pressure-independent thermal conductivity in BAs up to 30 GPa.

One of the unique features of the phonon dispersion of BAs is the large frequency gap between acoustic and optical phonons [158], see Figure 7.1(a). This gap nearly freezes out three-phonon scattering between acoustic and optical phonons, specifically, scattering processes involving two acoustic and one optical phonon. This is because even two acoustic phonons of highest frequency cannot combine into an optical phonon of minimum frequency. The small phase space of three-phonon scattering improves the importance of four-phonon scattering in BAs [111,128].

The large frequency gap in BAs originates from the large mass ratio between boron and arsenic atoms (m_{As}:m_B = 6.9). It has not been studied if other materials with large mass ratios between constituent atoms behave similarly as BAs at high pressure, for example, GaN. The mass ratio between Ga and N atoms is 5, and there is also a frequency gap in the phonon dispersion [266] of GaN (Figure 7.1(b)). It is not known whether the $\Lambda\ vs. P$ for GaN will behave more like BAs or most other materials.

Additionally, in our recent work, we discovered BAs single crystals with ambient thermal conductivity of 1500 W m^{-1} K^{-1}, ~ 20 - 30% higher than the samples used in prior high-pressure studies [23,150]. This suggests that the reported pressure dependence of BAs' thermal conductivity in previous studies is affected by phonon-defect scattering rates. Another goal of this study is to investigate the more intrinsic pressure dependence of the thermal conductivity of BAs. To do this, we measured the $\Lambda\ vs. P$ of the same BAs sample which we studied in Chapter 4 ("BAs-1500" in Chapter 4).

To investigate the impact of phonon-frequency gap on the pressure dependence of thermal conductivity, we measured the thermal conductivity of BAs, GaN, and diamond by performing time-domain thermoreflectance (TDTR) in a diamond anvil cell (DAC) up to 30 GPa, 20 GPa, and 55 GPa, respectively. As indicated by Figure 7.1, BAs has a large frequency gap, GaN has a medium one, and diamond has no frequency gap in the phonon dispersion. To acquire information of pressure-induced changes in phonon dispersion, we characterized BAs, GaN, and diamond using Raman scattering and Brillouin scattering at high pressure. We observed increasing thermal conductivity as pressure increases in all three materials. Although BAs and GaN demonstrated similar changes in Raman frequency and sound velocity at high pressure, the two materials display different pressure dependence of the thermal conductivity. Specifically, the relative increase of BAs was only half of the increase of GaN at 20 GPa. For diamond at 50 GPa,

we observe a 6% increase in the longitudinal sound velocity, 10% increase in zone-center optical phonon mode, and 40% increase in thermal conductivity.

7.2 Materials and Methods

Sample Preparation

We synthesized BAs crystals by chemical vapor transport [108,129]. Details about the growth of BAs can be found in Chapter 4. The diamond and GaN single crystals are from Applied Diamond. Inc and Sumitomo Electric Industries Ltd, respectively.

To prepare samples for diamond anvil cell measurements, we polished BAs and GaN samples down to a thickness of ~ 10 μm. We used an optical microscope to estimate the final thickness after polishing. The as-received diamond sample is ~8 μm thick and no need to polish. Then we broke samples and selected pieces with lateral dimensions of ~50-80 μm. We deposited an ~80-nm-thick transducer on the selected pieces for TDTR and forced Brillouin scattering experiments. We deposited some BAs samples with 80 nm Al, and one with 40 nm V/50 nm Al bilayer. Most of the BAs sample for high-pressure TDTR measurements is cut from the "BAs-1500" sample in Chapter 4. We also measured two BAs samples with ambient thermal conductivity of 900 W m^{-1} K^{-1} for reference. We performed TDTR on three GaN samples at high pressure, with Al, Ta, and TiN as the transducer, respectively. Details about the growth of TiN can be found in Ref. [267]. For diamond, the three samples were deposited with Al, Ta, and Pt, respectively. We deposited Ta at 800 °C to obtain α-phase Ta [43], which has higher thermoreflectance than the β-phase Ta that is deposited at room temperature [44]. For Raman scattering measurements, we prepared samples that were not coated with a metal film.

We loaded the samples into DACs with a culet size of 300 μm. Measurements of GaN, BAs, and diamond were made on the (0001), (111), and (100) surface, respectively. We loaded ruby spheres alongside the samples. The fluorescence spectrum of the Ruby was used as a pressure gauge [181]. We used silicone oil (polydimethylsiloxane) as the pressure medium. We used 250-μm-thick stainless-steel or Re as the gasket and pre-indented it to be ~ 30 μm thick.

Raman Scattering

We measured the Raman spectrum of GaN and BAs from 300 to 1000 cm^{-1}. We first measured the ambient Raman spectrum in the air. At high pressure, we collected the spectrum inside a DAC with silicone oil as the pressure medium. To exclude the Raman signals of the pressure medium, we also measured the Raman spectrum of the pressure medium along with our samples as the pressure changes. The excitation laser had a 532-nm wavelength. The spot size was 6 μm ($1/e^2$ radius). The laser power was 20 mW. We used a monochromator (Acton SpetraPro-2500i) to collect the scattered light. We placed a long-pass edge filter (Semrock LP03-532RE-25) in front of the spectrometer to filter out background noise.

TDTR and forced Brillouin Scattering Measurements

We performed TDTR measurements of the thermal conductivities of diamond, BAs, and GaN at high pressure. TDTR is a pump-probe technique to measure the thermal properties of materials [245]. We used a laser wavelength of 783 nm, a laser spot size of ~ 10 μm or 5 μm, and modulation frequency of 10.7 MHz. Details of our TDTR setup can be found in Ref. [180]. To avoid optical artifacts in DAC-assisted TDTR measurements [150,268], we measured three spots on each sample at every pressure. Every thermal conductivity data point reported in this study is the average of three measurements.

We performed forced Brillouin scattering measurements using our TDTR setup. For Brillouin measurements of GaN, BAs, and diamond, the laser beams impinged through the substrate side of the sample. The beams went through pressure media, samples, and then hit the transducer surface. For Brillouin measurements of the silicone oil, the laser beams incident on the transducer side of the sample. The beams went through the silicone oil and then were reflected from the transducer. In both sets of measurements, the laser beams were perpendicular to the sample. When the pump beam heats the transducer surface, it launches a strain wave into the substrate or silicone oil. The strain wave front moves at the longitudinal speed of sound of the sample. Both the strain wave and the transducer can reflect the subsequent probe beam. These two reflected probe beams interfere with each other and cause Brillouin oscillations in the in-phase voltage signal V_{in} [36]. We use the measured Brillouin frequencies of diamond, BAs, and GaN as a measure of the longitudinal speed of sound in these materials. We use the Brillouin frequency of silicone oil as an additional measure of pressure [24] to complement our ruby fluorescence measurements.

We use a bidirectional heat diffusion model to analyze the collected TDTR data [15]. The bidirectional model accounts for heat flow from the transducer to both the substrate and silicone oil. The thermal conductivity, heat capacity, and thickness of each layer are the input parameters in the heat diffusion model. Therefore, we must estimate how these parameters evolve with pressure to interpret our TDTR data. We describe how we account for the pressure dependence of all parameters in the following.

Before loading the sample into the diamond anvil cell (DAC), we measured the thickness of the Al, Ta, and V/Al transducers using picosecond acoustics [36]. Pt does not have acoustic echoes, so we obtain its thickness by fitting the TDTR data of a Si sample whose thermal conductivity is known. The Si sample is coated together with the diamond sample, so the Pt film on the Si crystal is the same thickness as the Pt film coating the diamond. At high pressures, we assume that

diamond and BAs shrink equally in every direction, since they have cubic structures (space group: $Fd\bar{3}m$ for diamond and $F\bar{4}3m$ for BAs). For GaN, we used its in-plane lattice constant a versus pressure to account for the area change considering its wurtzite structure(space group: $P6_3mc$) [269]. If the volume of the substrate at pressure P is V_P, and the in-plane area is S_P, then $S_P = S_0 \cdot (V_P \,/\, V_0)^{\frac{2}{3}}$ for diamond and BAs, and $S_P = S_0 \cdot (a_P^2 \,/\, a_0^2)$ for GaN. Here, V_0 and S_0 are the volume and area of the substrate at 0 GPa. We assume that the in-plane area of the transducer is equal to S_p. Then the thickness of the transducer at pressure P will be $h_P \approx V_P^{td}/S_P$. Here, V_P^{td} is the transducer volume at pressure P based on its equation of state (EOS) [184,185].

To estimate the pressure dependence of the heat capacities of Al, Pt, and Ta, we follow Ref. [24], and use a Debye model. For silicone oil, we use published pressure-dependent heat capacity and thermal conductivity [186]. We calculated the volumetric heat capacity of BAs in the same way as reported before [150]. We estimated the volumetric heat capacity of GaN and diamond based on the changes of their longitudinal sound velocity, Raman frequency, and unit cell volume. For example, at 50 GPa, diamond experiences a 6% increase in the longitudinal sound velocity, 10% increase in Raman frequency, and 10% decrease in unit cell volume. In comparison, at 20 GPa, BAs experiences a 7% increase in longitudinal sound velocity, 10% increase in Raman frequency, and 10% decrease in unit cell volume. The calculated volumetric heat capacity of BAs increases by 5% at 20 GPa, so the heat capacity of diamond should increase by 5% at 50 GPa considering the similar changes in phonon frequency and unit cell volume. We show the pressure-dependent thermal parameters in Figure 7.6.

We measured the electric resistance of Al, V/Al, Pt, and Ta films by a four-point probe method, and then calculated their thermal conductivities by the Wiedemann-Franz law. The measured thermal conductivities were 170, 110, 40, and 45 W m^{-1} K^{-1} for Al, V/Al, Pt, and Ta, respectively.

We fitted the $-V_{in}/V_{out}$ data after 100 ps for Al-coated samples and after 300 ps for Pt-coated V/Al-coated, and Ta-coated samples. The TDTR signal is not sensitive to the thermal conductivity of the transducer at delay times greater than 100 ps. Therefore, we do not need to account for the thermal conductivity changes of transducers with pressure.

We use the sensitivity analysis to determine the uncertainty of the derived values of Λ. The sensitivity parameter (S) quantifies relative changes of $-V_{in}\ /\ V_{out}$ induced by variation of the input parameter α in the heat diffusion model:

$$S = \frac{\partial\, ln(-V_{in}/V_{out})}{\partial\, ln\, \alpha}, \qquad (7.1)$$

Typically, we have a ~ 5% uncertainty in $h_{td}C_{td}$ [190], ~ 5% in the spot size R, ~ 3% for C_{sub}. We also estimate an uncertainty of ~ 5% in the thermal effusivity of silicone oil, $\sqrt{\Lambda_{oil}C_{oil}}$, and ~ 5% uncertainty in the interface conductance. These yield a total uncertainty in the derived values for Λ of ~ 12% for GaN, 20% for BAs, and 20% for diamond.

7.3 Results and discussion

We observed linearly increasing thermal conductivity versus pressure in diamond, BAs, and GaN (Figure 7.3). For a given substrate, we observed ~ 20% differences between different transducers. We obtained similar pressure dependence with different transducers on diamond and GaN, but different pressure dependence between Al/BAs and V/Al/BAs samples. We fitted all the data for each material by a linear function and obtained the gradient, $d\Lambda/dP$, which is ~ 14 W m^{-1} K^{-1} GPa^{-1} for diamond up to 55 GPa, ~ 30 W m^{-1} K^{-1} GPa^{-1} for Al/BAs up to 30 GPa, and ~ 5 W m^{-1} K^{-1} GPa^{-1} for GaN up to 20 GPa. For diamond, the increase at 55 GPa relative to the ambient thermal conductivity is ~ 40%. For BAs, the relative increase at 30 GPa is ~ 70% for Al-coated

samples. For GaN, the relative increase at 20 GPa is ~ 60%. For V/Al/BAs samples, thermal conductivity first increases, then decreases as pressure increases.

The bulk moduli of diamond, BAs, and GaN are dramatically different, which are 446 [30], 142 [251], and 237 GPa [269], respectively. Therefore, it is helpful to factor in the bulk modulus for pressure. Here we define an effective pressure $P_n = P/K_0$, where K_0 is the ambient bulk modulus of each material. Figure 7.5 shows a comparison of Λ vs. P_n for diamond, BAs, and GaN. Like the analysis above, the fitted $dln\Lambda/dP_n$ is 3.66 for diamond, 3.24 for Al/BAs, and 5.42 for GaN.

For measurements using Al as the transducer, the pressure only extends 30 GPa due to the thermoreflectance of Al decreases as pressure increases [42]. We only measured GaN to 20 GPa since we observed cracks on GaN at 20 GPa (see Figure 7.15). We only measured the V/Al/BAs sample up to 30 GPa for the same reason. The cracks may originate from the propagation of dislocations induced during polishing. The thermal conductivity results discussed above are collected on pieces cut from the BAs-1500 sample. As for the BAs sample with ambient thermal conductivity of 900 W m^{-1} K^{-1} (BAs-900), we observed a pressure-independent thermal conductivity below 30 GPa, consistent with our previous observations [150]. Between 30 and 50 GPa, we observed the thermal conductivity of BAs-900 decreases by 50%, see Figure 7.3(d). However, above 30 GPa, the surfaces of the two samples, Al/BAs-s3 and Al/BAs-s4 in Figure 7.3(d), became very rough which may affect TDTR measurements (Figure 7.14). As for the TiN/GaN sample, below 5 GPa, there were fringe-like patterns on the surface which may result from the mismatch between TiN and GaN as discussed in section 2.4 of Chapter 2. Above 5 GPa, the sample showed severe cracks on the surface which may be related to the isostructural phase transition of TiN near 6 GPa [270,271]. Images of the TiN/GaN sample are shown in Figure 7.13.

Considering the bad surface condition, data of TiN/GaN and data of Al/BAs-s3/s4 above 30 GPa are questionable.

To further understand the pressure dependence of thermal conductivity, we compare our experimental results with theoretical predictions. We first consider predictions of a phenomenological model, Leibfried-Schlömann (LS) equation, for diamond, BAs, and GaN, see Figure 7.4(a). The LS equation shows good agreement with our experimental $\Lambda(P)$ of GaN, acceptable agreement with diamond, and dramatic failure with BAs. Detailed analysis of the LS equation can be referred to our previous study [268].

We now compare our thermal conductivity results with first-principles calculations [149,272,273], see Figure 7.4(b). Our $\Lambda\ vs.\ P$ results of diamond agree well with first-principles calculations [272]. The calculation predicts that Λ of diamond will increase by 50% at 55 GPa, and we observed a 40% increase. For GaN, first-principles calculations predict an increasing-then-decreasing thermal conductivity as pressure increases. The turning pressure is 20 GPa. However, in the pressure range we studied, we only observed a linearly increasing thermal conductivity. As for the relative increase at 20 GPa, first-principles calculations predict a 50% increase, and we observe a 60% increase in GaN. The relative increases are comparable, although the calculation predicts an almost twice larger ambient thermal conductivity for GaN than our measurement. Note that the ambient thermal conductivity we observed on GaN is consistent with reported measurements [274]. For BAs, first-principles calculations predict a flat thermal conductivity between 0 and 30 GPa. We observed a monotonically increasing thermal conductivity on Al/BAs samples, and a pressure-independent thermal conductivity on the V/Al/BAs sample.

Both diamond and GaN show weak pressure dependence in their Brillouin frequency, while BAs shows stronger pressure dependence (Figure 7.8(a)). The error bars of Brillouin frequency are derived from the full width at half maximum (FWHM) of the Brillouin spectrum which is the fast Fourier transformation (FFT) of Figure 7.7. The Brillouin frequency is

$$f = 2Nv_l / \lambda, \qquad (7.2)$$

Where N is the index of refraction of the sample, v_l is the longitudinal speed of sound of the sample, and λ is the excitation wavelength (783 nm in our experiments). We obtained the pressure dependent N from Ref. [31,275,276]. The literature data only extends to a few GPa. We extrapolated their data at higher pressure. The error bars of sound velocity in Figure 7.8(b) originate from the fitting uncertainty of Brillouin frequency as mentioned above. We observed a linear increase in the sound velocities of diamond, BAs, and GaN. The gradient is 0.02 GHz/GPa, 0.03 GHz/GPa, and 0.03 GHz/GPa for diamond, BAs, and GaN, respectively. The relative increase at 20 GPa is 2%, 7%, and 7% for diamond, BAs, and GaN, respectively.

The Raman spectra of GaN and BAs are shown in Figure 7.9 and 7.11, respectively. We observed that the Raman spectrum of GaN experienced a dramatic base line shift at ~ 45 GPa (Figure 7.10). This is because GaN has a phase transition from wurtzite to rock salt structure at ~ 45 GPa [269,277]. For BAs, we observed one Raman peak at low pressure, and two Raman peaks at high pressure (Figure 7.11). At low pressure, transverse (TO) and longitudinal optical (LO) phonon degenerate at the Brillouin zone center in BAs, so there is only one Raman peak. At 7.5 GPa, TO and LO split, and two Raman peaks exhibit. This is consistent with previous measurements on BAs [23,157].

The Raman shifts vs. pressure for selected Raman peaks of GaN and BAs are shown in Figure 7.12. The Raman shifts reflect increases in the frequency of the phonons responsible for Raman

scattering. Therefore, these measurements provide a measure of the stiffening of vibrational dynamics with pressure. We excluded Raman peaks of the pressure medium (silicone oil, polydimethylsiloxane). We tracked three Raman peaks of GaN, labelled as A_1, E_1, and E_2 based on the symmetry. The A_1 and E_1 Raman modes correspond to two transverse optical phonon modes at the Brillouin zone center [277]. We tracked the TO and LO modes of BAs. The Raman frequency of diamond at high pressure from Ref. [30] is included in Figure 7.12 for comparison. All Raman frequency of the GaN, BAs, and diamond increases linearly as pressure increases. The three Raman frequencies of GaN and the two of BAs all exhibit a gradient of ~ 0.1 THz/GPa. The Raman frequency of diamond exhibits a gradient of 0.08 THz/GPa. The relative increase at 30 GPa is 6%, 15%, and 20% for diamond, BAs, and GaN, respectively. Our Raman results on GaN and BAs are consistent with previous experimental results [23,157,277]. Density functional theory calculations predict that the zone-center optical phonon modes stiffen by 30% for GaN at 45 GPa [273], and 20% for BAs at 32 GPa [149], consistent with our experimental results.

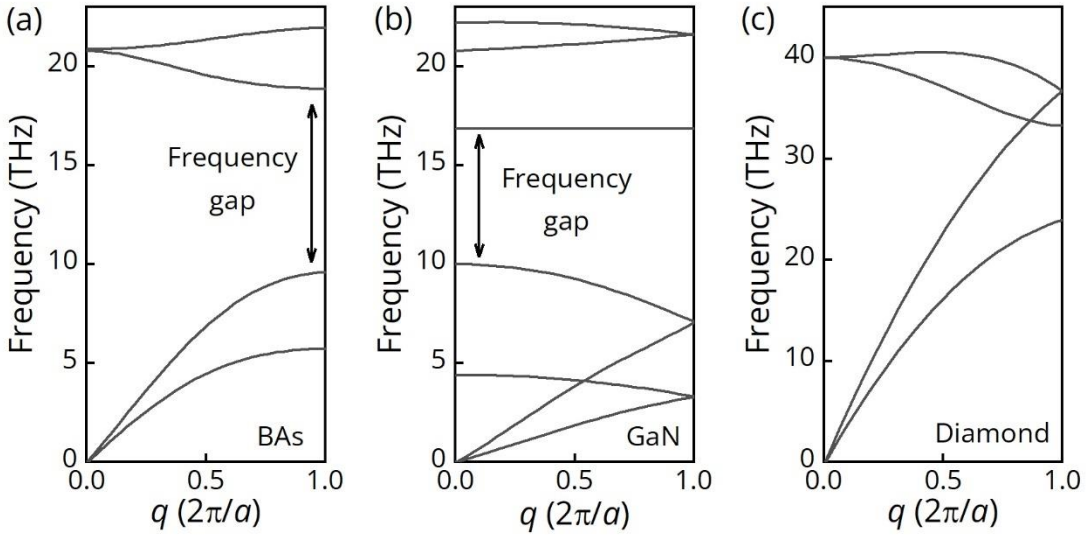

Figure 7.1. Schematics of phonon dispersion of BAs, GaN, and diamond.

The horizontal axis labels the wavevector in the unit of $2\pi/a$, where a is the lattice constant. The phonon dispersions of BAs, GaN, and diamond are constructed by taking reference of the first-principles-calculation results in Ref. [217,266,278].

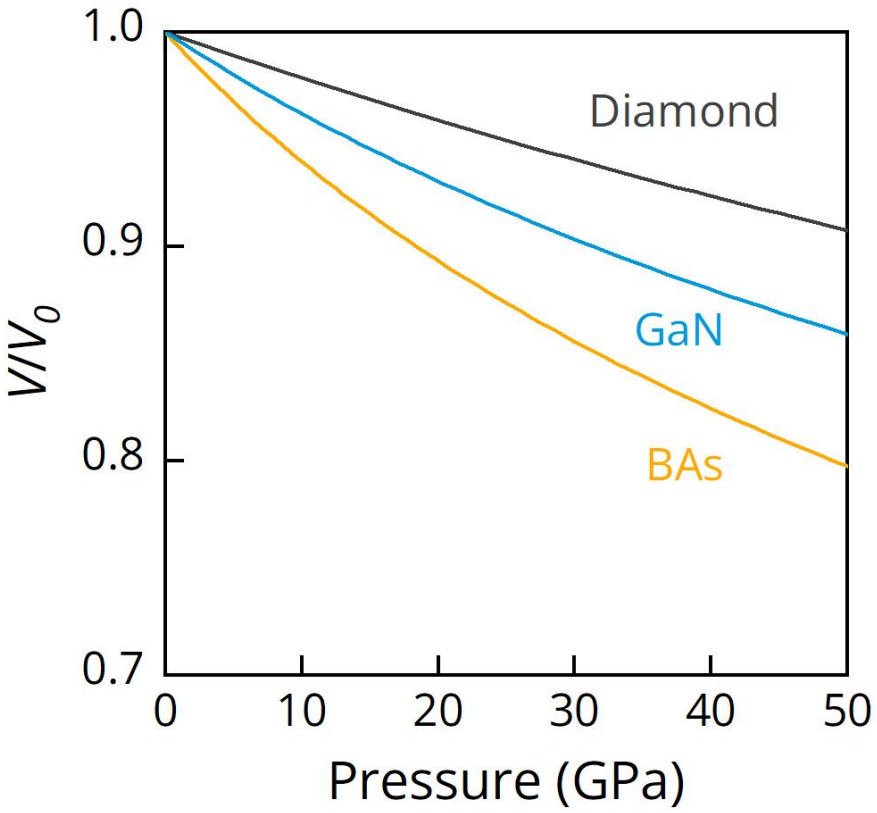

Figure 7.2. Volume-pressure equation of states of diamond, GaN, and BAs from Ref. [30,251,269]

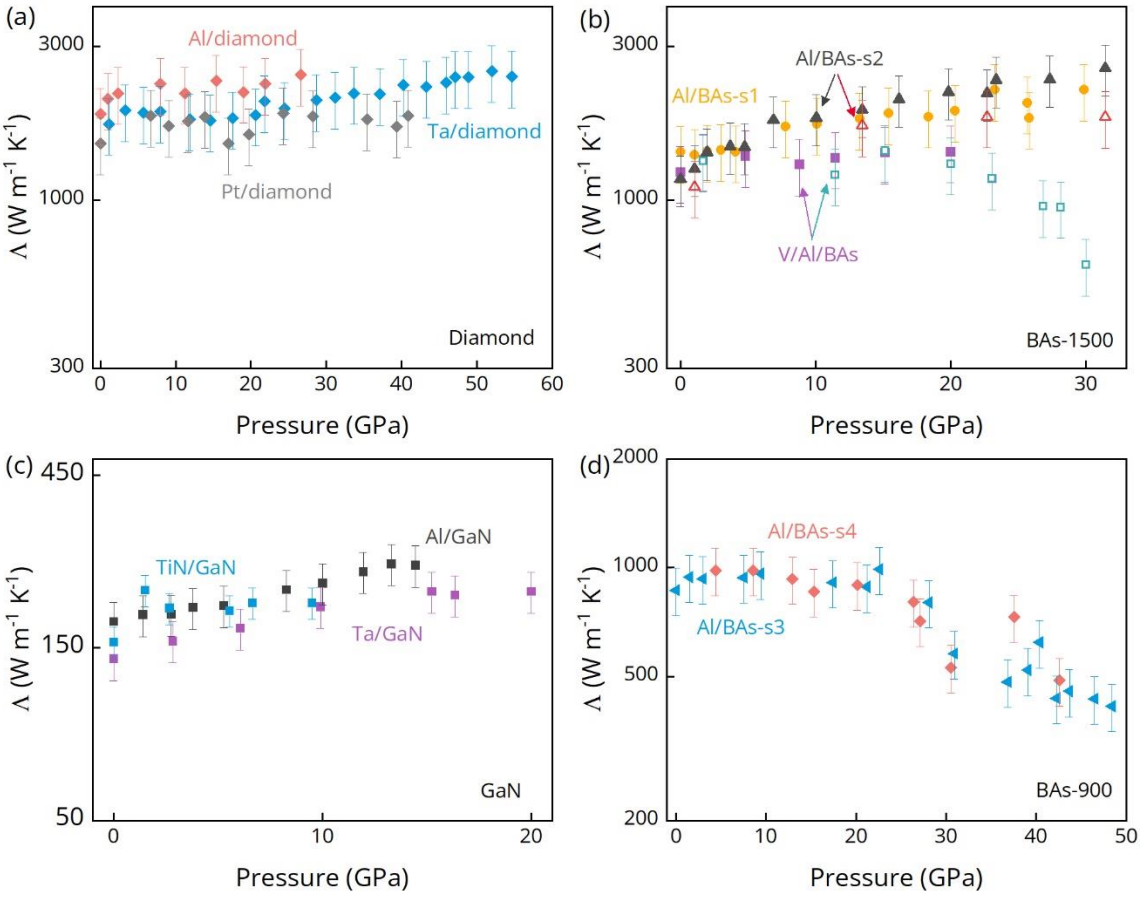

Figure 7.3. Thermal conductivity versus pressure for diamond, BAs, and GaN.

(a) We coated Al, Pt, and Ta on three diamond samples, respectively, and measured their thermal conductivity at high pressure, shown as diamond symbols of different colors. All measurements were done with a 10× objective lens (spot size ≈ 10 μm). (b) We coated Al on two BAs samples (circles and triangles), V/Al bilayer on one sample (squares) and performed TDTR at high pressure. Filled markers are measurements with a 10× objective lens (spot size ≈ 10 μm). Open markers were done with a 20× lens (spot size ≈ 5 μm). (c) Three GaN samples measured with Al (dark squares), Ta (purple squares), and TiN (blue squares) as the transducer, respectively. All measurements were done with a 10× objective lens (spot size ≈ 10 μm for Ta/GaN, ≈ 7 μm for Al/GaN and TiN/GaN). Note that the surface of TiN/GaN sample looked weird at high pressure, which makes the TiN/GaN data questionable, see Figure 7.13. (d) Thermal conductivity versus pressure collected from two pieces of BAs samples whose ambient thermal conductivity is ~ 900 W m^{-1} K^{-1}. Both measurements were performed with a 10× objective lens (spot size ≈ 7 μm). The data above 30 GPa are questionable because of the rough surfaces, see Figure 7.14.

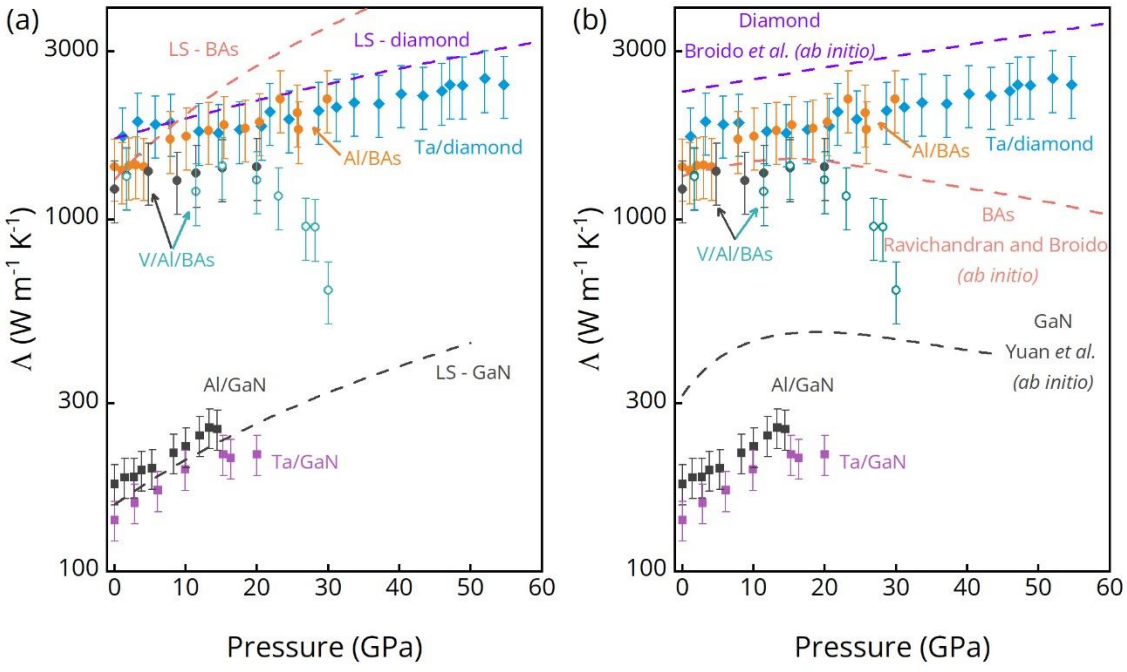

Figure 7.4. Comparison between experimental data and theoretical predictions for diamond, BAs, and GaN.

I only included selected data from Figure 7.3 for clarity. (a) Comparison between experimental results and the prediction of the Leibfried-Schlömann equation. Purple, pink, and gray dash lines are the predictions of Leibfried-Schlömann equation for diamond, BAs, and GaN, respectively. (b) Comparison between our data and predictions of first-principles calculations for diamond [272], BAs [217], and GaN [273]. Filled and open markers are measurements performed with a 10× and 20× objective lens, respectively.

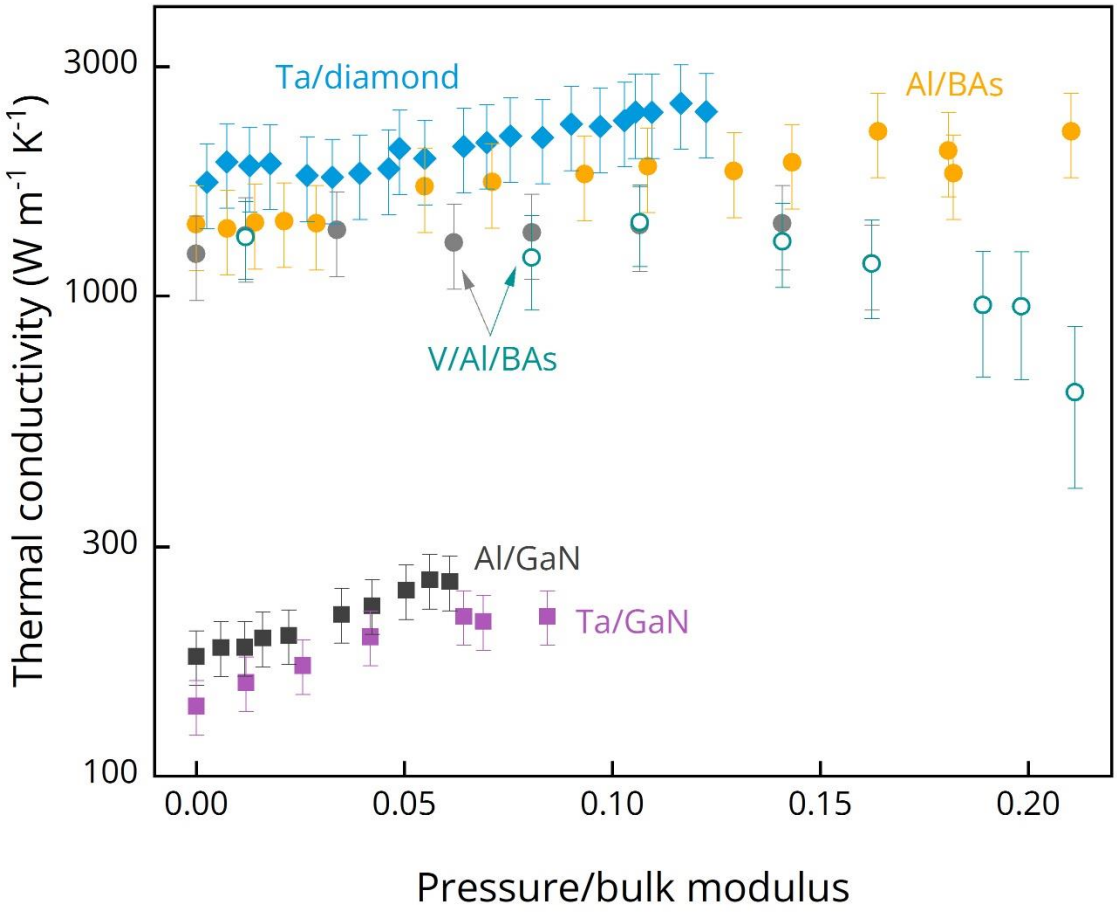

Figure 7.5. Thermal conductivity versus normalized pressure for diamond, BAs, and GaN.

Pressure is normalized by the ambient bulk modulus of each material. Filled and open markers are measurements performed with a 10× and 20× objective lens, respectively.

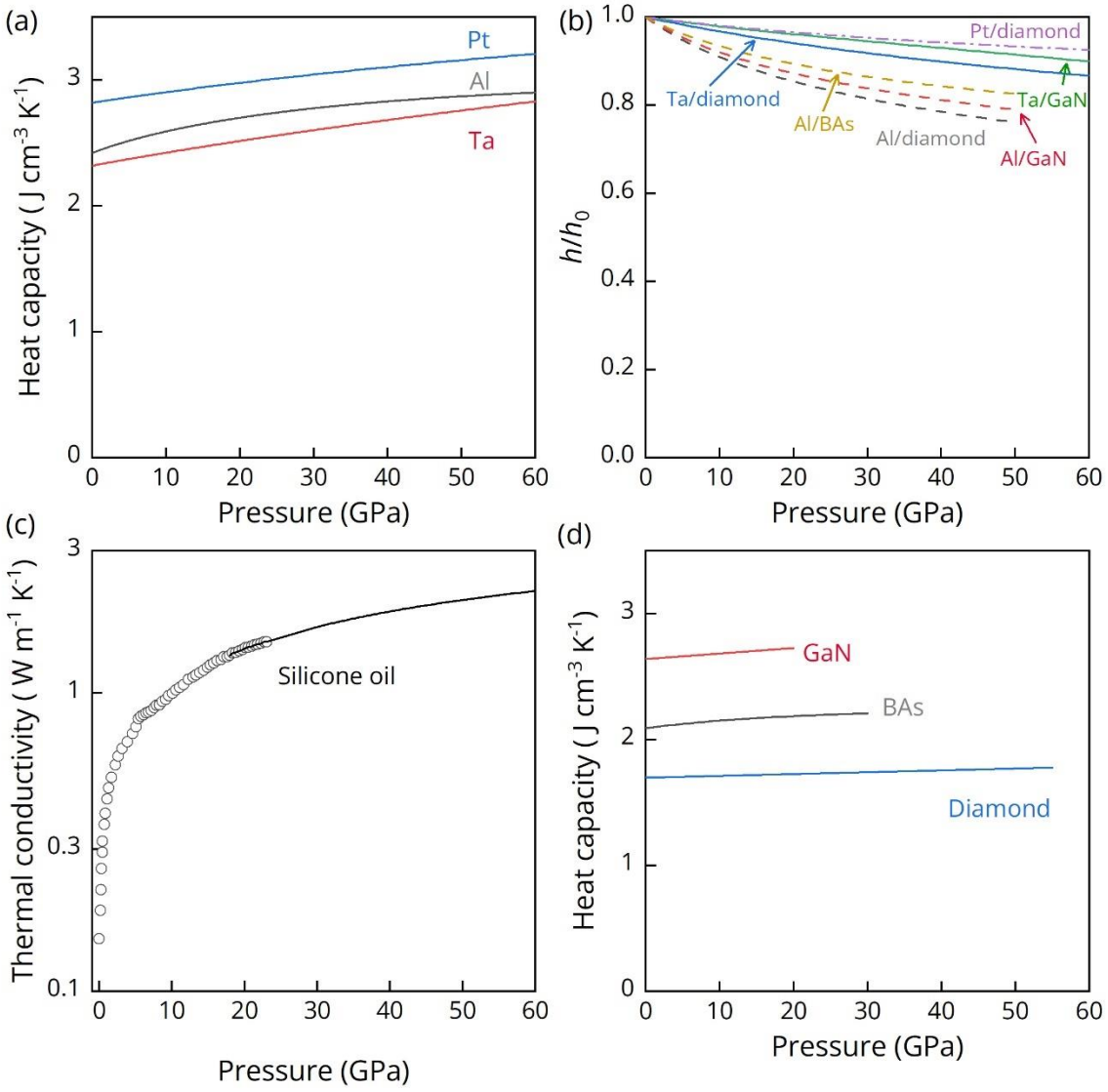

Figure 7.6. Pressure-dependent parameters in the heat diffusion model.

(a) Heat capacity of Al, Ta, and Pt versus pressure calculated by the Debye model. (b) Transducer thickness changes relative to the ambient value. h_0 is the thickness at ambient conditions and h_P is the thickness at given pressure. (c) Thermal conductivity of silicone oil from Ref. [21]. Circles represent experimental data, and the line shows the extrapolation of the experimental data at high pressure. (d) Heat capacity versus pressure of GaN, BAs, and diamond.

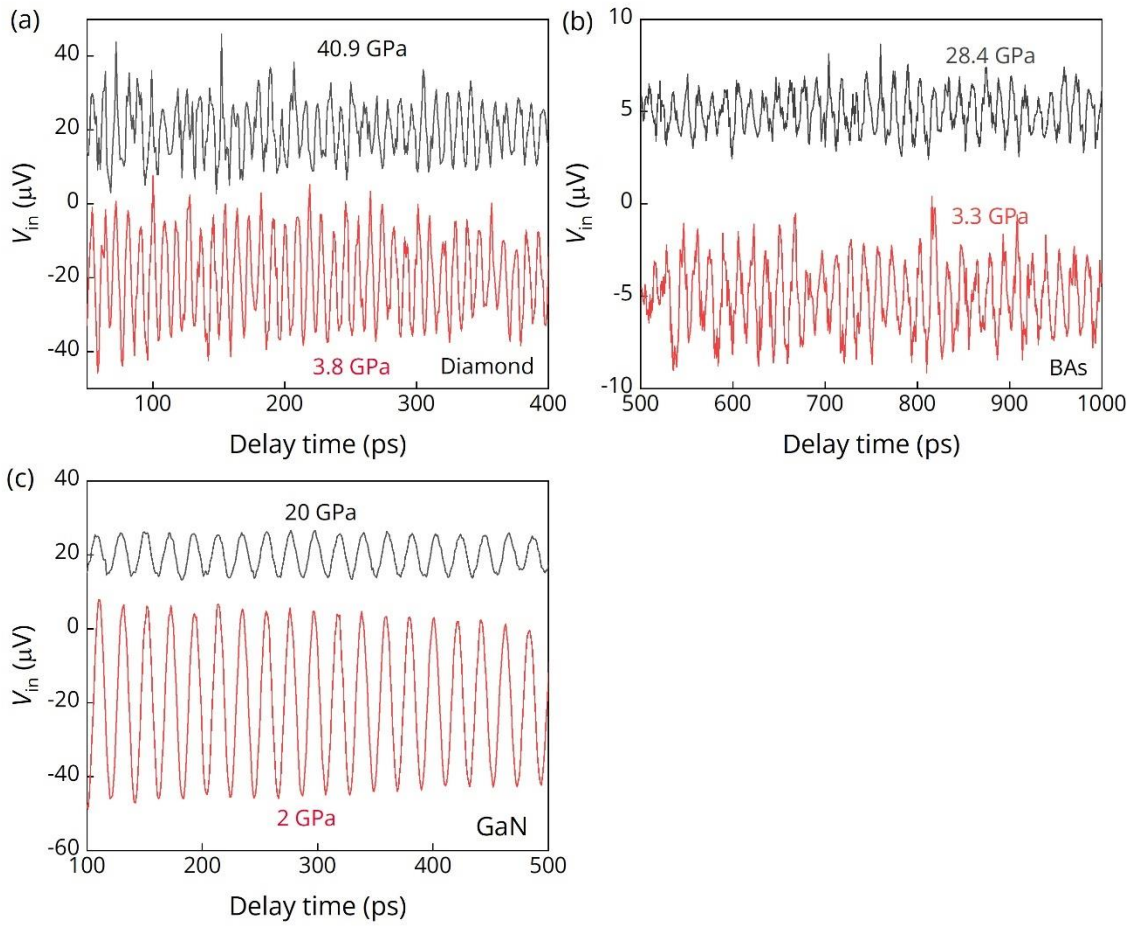

Figure 7.7. Brillouin scattering signals collected on (a) diamond, (b) BAs, (c) GaN. Data collected at different pressures are shifted for clarity.

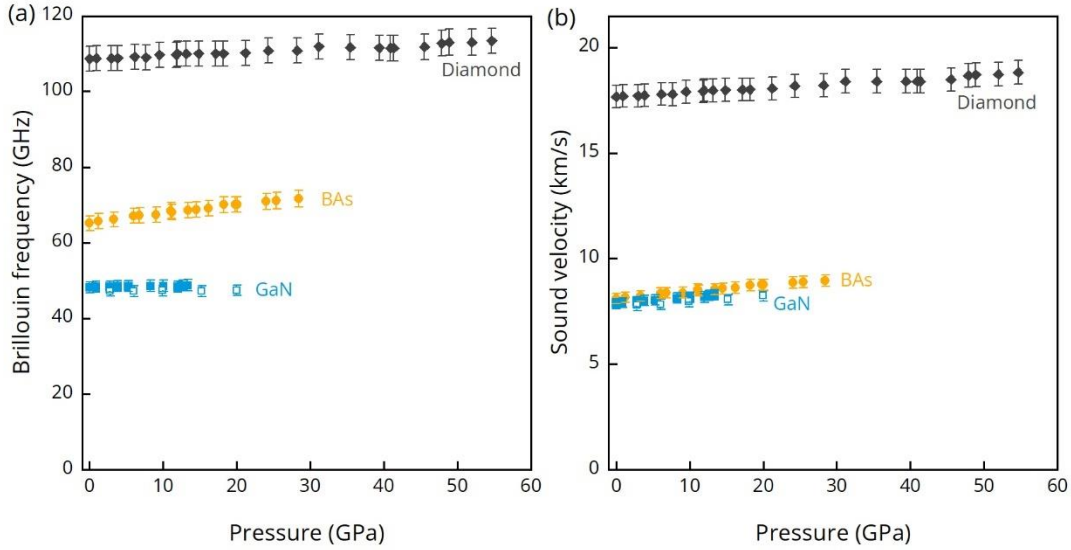

Figure 7.8. Brillouin frequency and sound velocity versus pressure for diamond, BAs, and GaN.

(a) Brillouin frequency versus pressure of diamond, BAs, and GaN. Data of diamond (dark diamonds) and BAs (yellow dots) are collected on a Pt/diamond and an Al/BAs sample, respectively. Data of GaN are collected on an Al/GaN and a Ta/GaN sample, shown as filled and open markers, respectively. (b) Sound velocity versus pressure for diamond, BAs, and GaN calculated from their Brillouin frequency in (a).

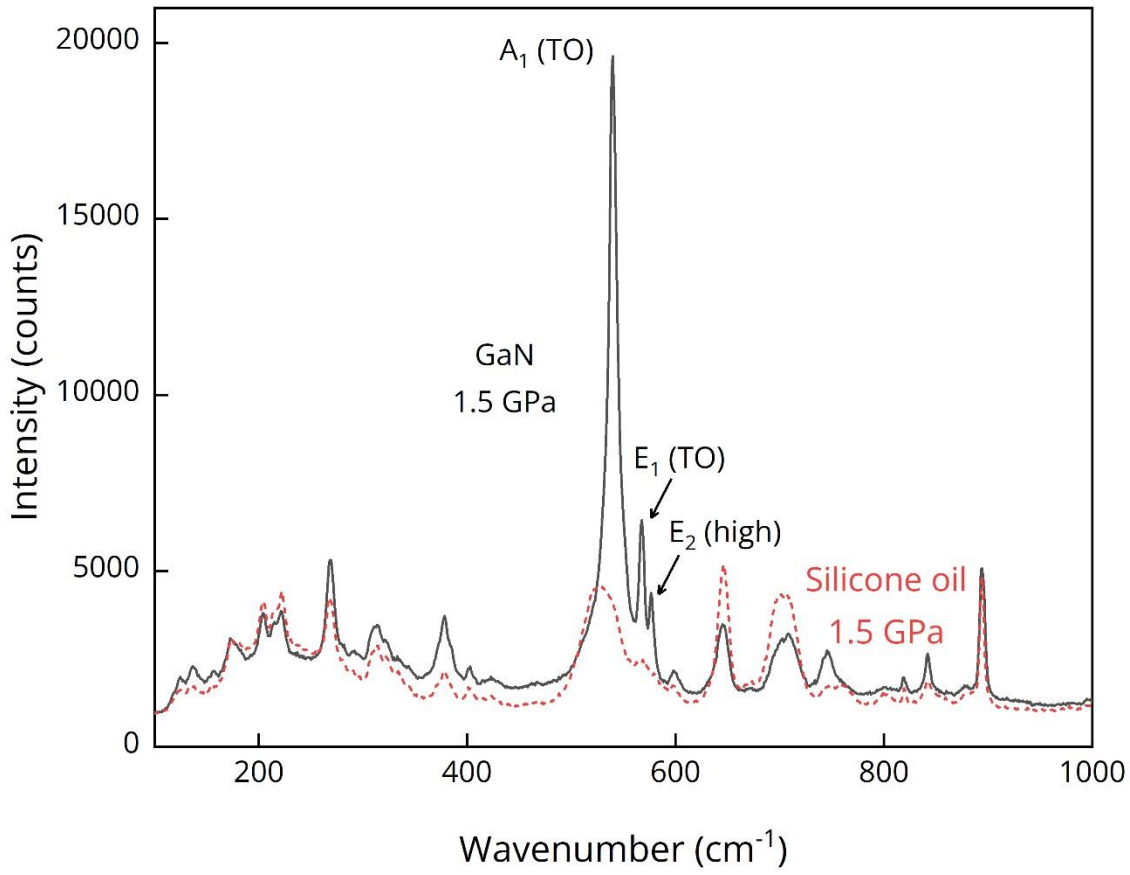

Figure 7.9. Raman spectrum of GaN at 1.5 GPa.

The black solid curve is the Raman spectrum of GaN, and the red dashed curve is the Raman spectrum of silicone oil at 1.5 GPa. Both curves are measured with 20 mW laser power, 60 s collection time, and 6 μm spot size ($1/e^2$ radius). We tracked A_1, E_1, and E_2 peaks as pressure increases. A_1 and E_1 correspond to two transverse optical (TO) phonon modes at the Brillouin zone center.

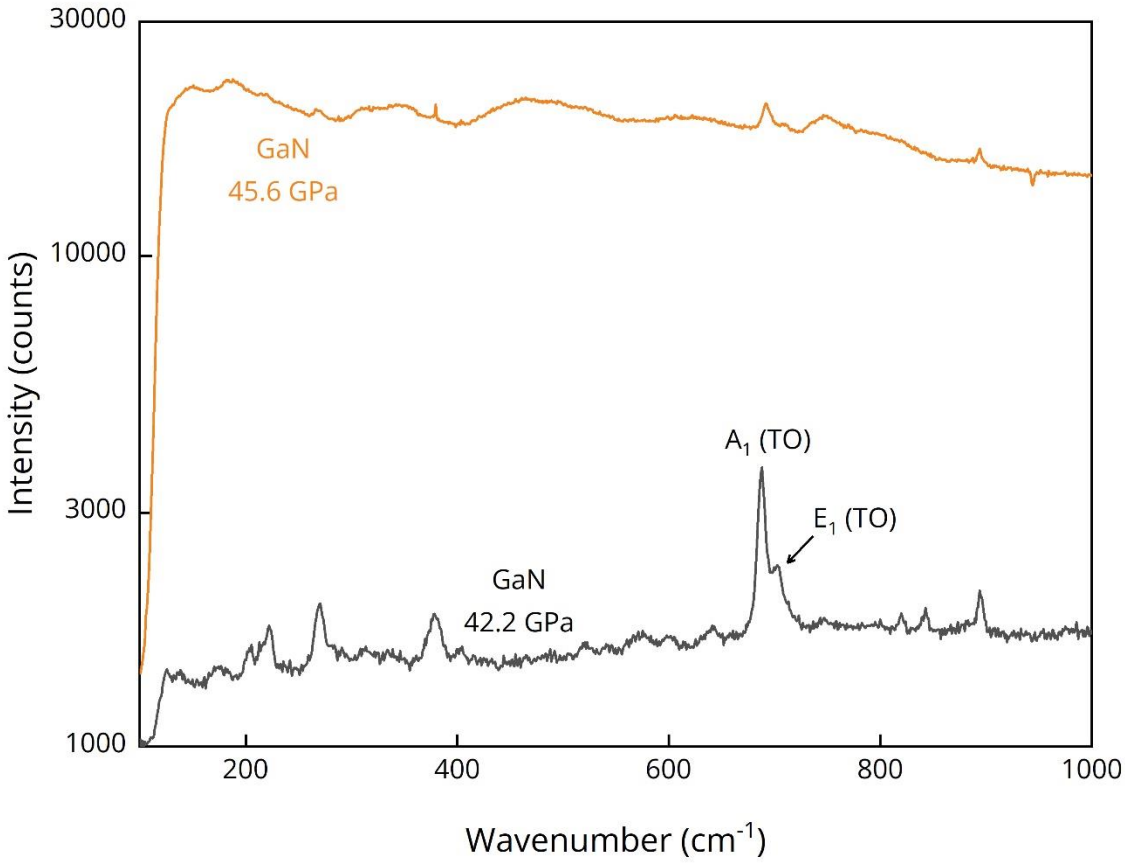

Figure 7.10. Wurtzite to rock salt phase transition in GaN at ~ 45.6 GPa observed using Raman scattering.

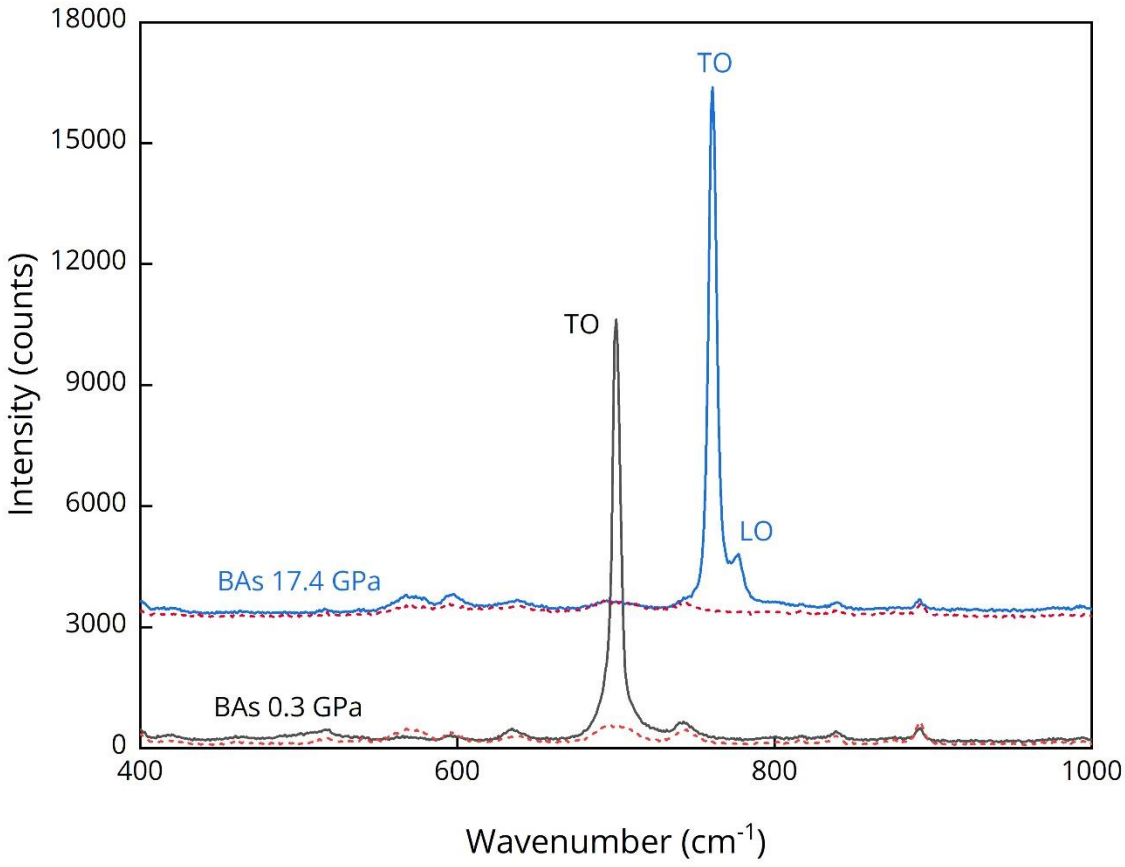

Figure 7.11. Raman spectra of BAs at 0.3 and 17.4 GPa.

Black and blue solid curves are Raman spectra of BAs, and two red dashed lines are the Raman spectra of silicone oil at the corresponding pressure. At low pressure, transverse (TO) and longitudinal optical (LO) phonon modes degenerate at the Brillouin zone center. At high pressure, they split, and we can observe two peaks. All measurements are done with 12 mW laser power, 60 s collection time, and 6 μm spot size ($1/e^2$ radius). Measurements at 17.4 GPa are shifted upward for clarity.

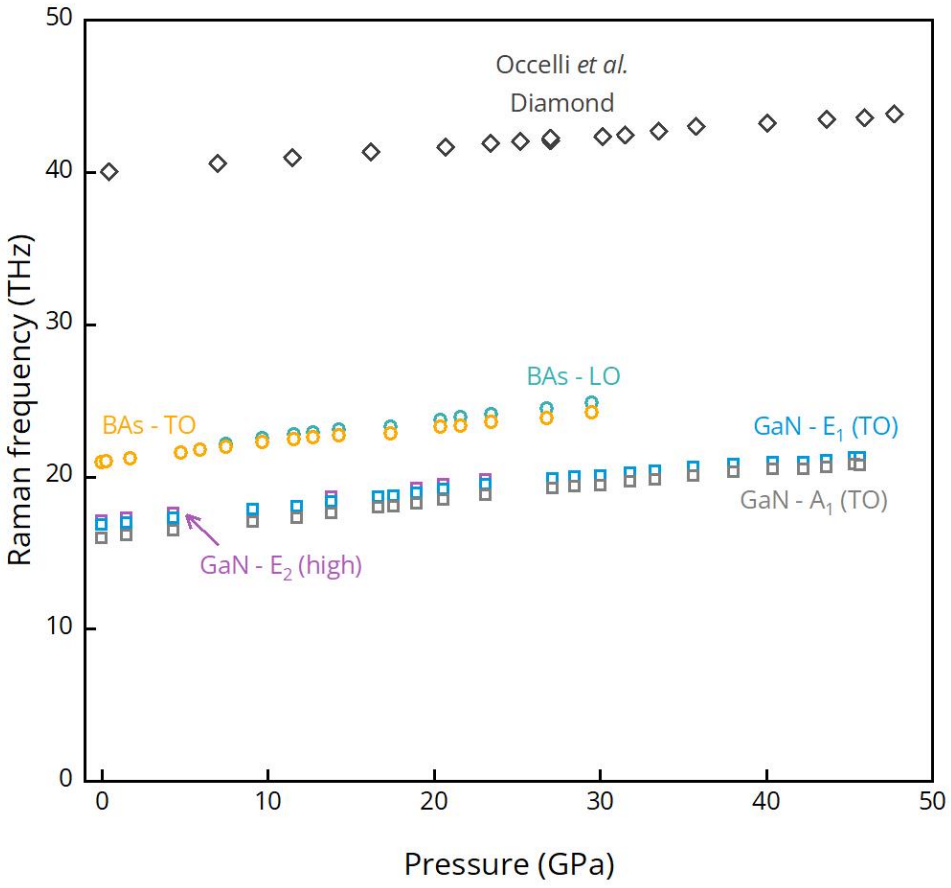

Figure 7.12. Raman frequency versus pressure of diamond, BAs, and GaN.

We tracked three Raman peaks of GaN at high pressure, shown as purple, blue, and gray squares. We stopped tracking certain peaks when they became invisible in the spectrum. Data of diamond is from Ref. [30].

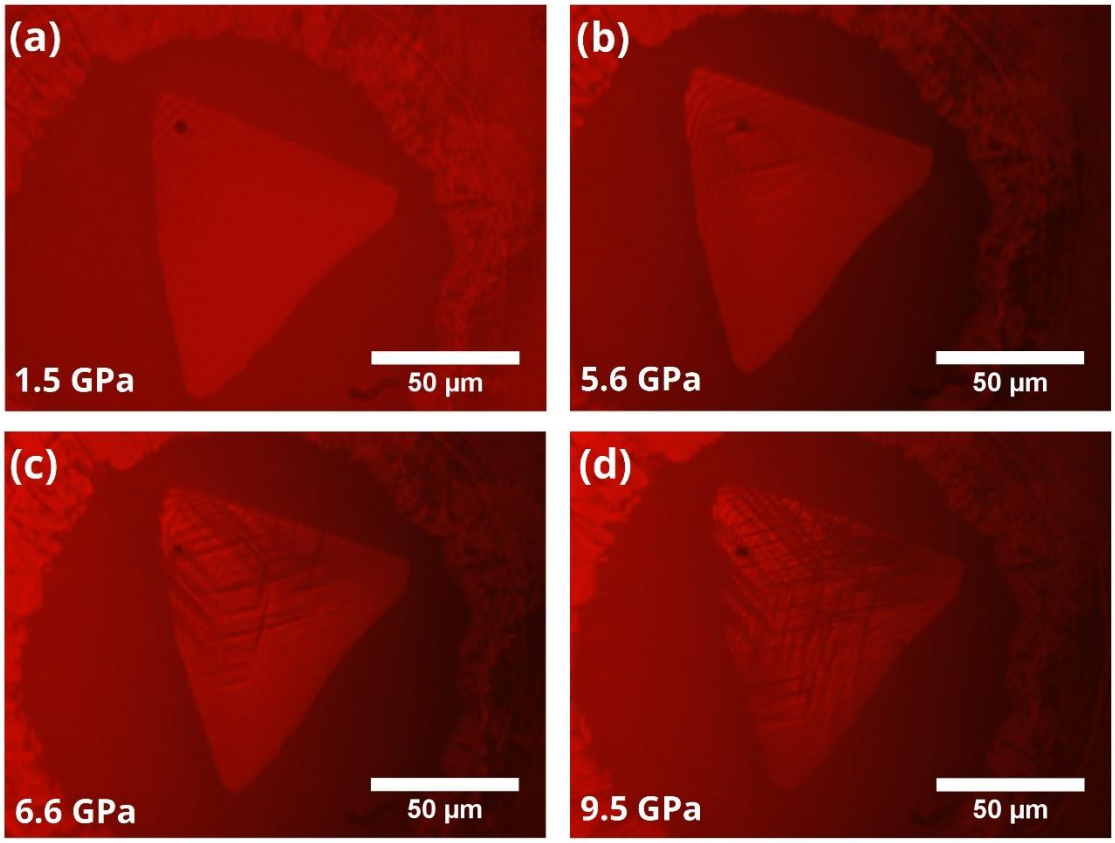

Figure 7.13. Images of the TiN/GaN sample under pressure.

At 1.5 GPa, there are some fringe patterns on the sample surface. This may be due to the buckling of TiN as discussed in Chapter 2. At 6.6 GPa, the TiN transducer cracks due to its isostructural phase transition at 5 – 7 GPa [270,271].

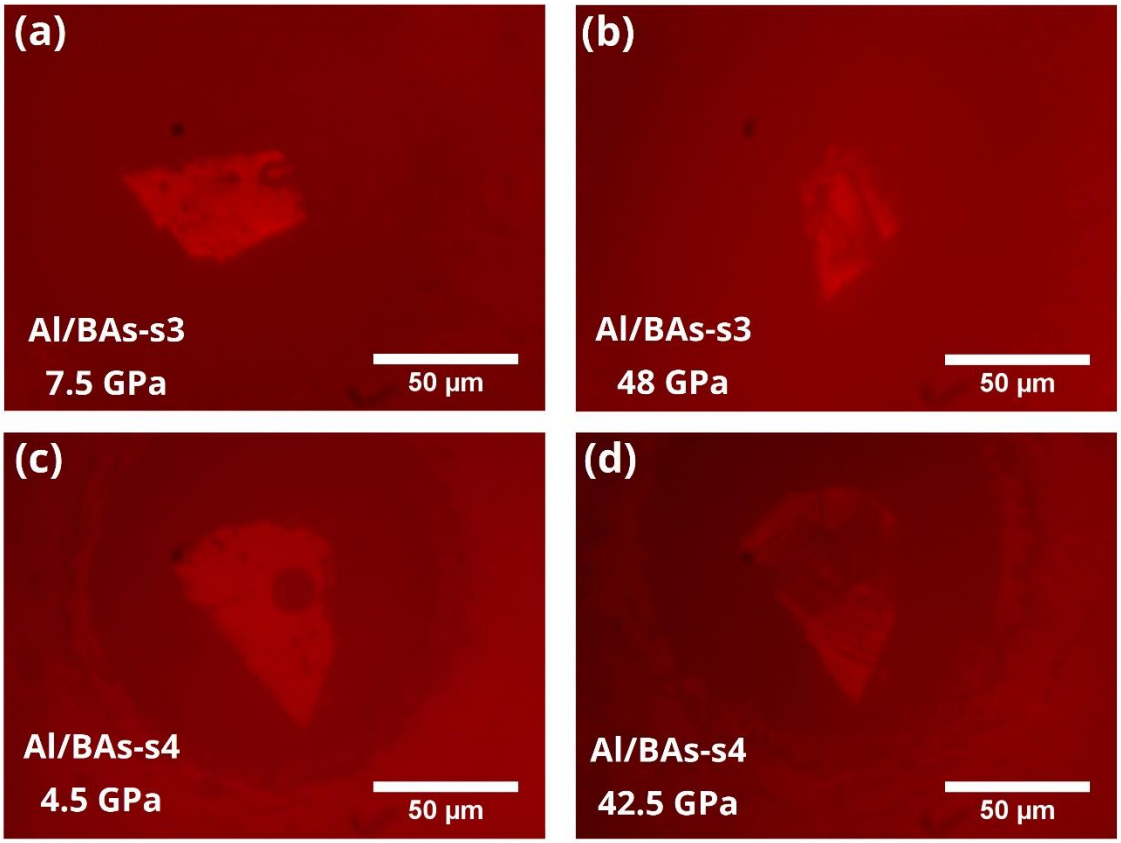

Figure 7.14. Images of Al/BAs-s3 and Al/BAs-s4 samples at high pressure.
The cracks showed up at 30 – 35 GPa and became worse as pressure increased.

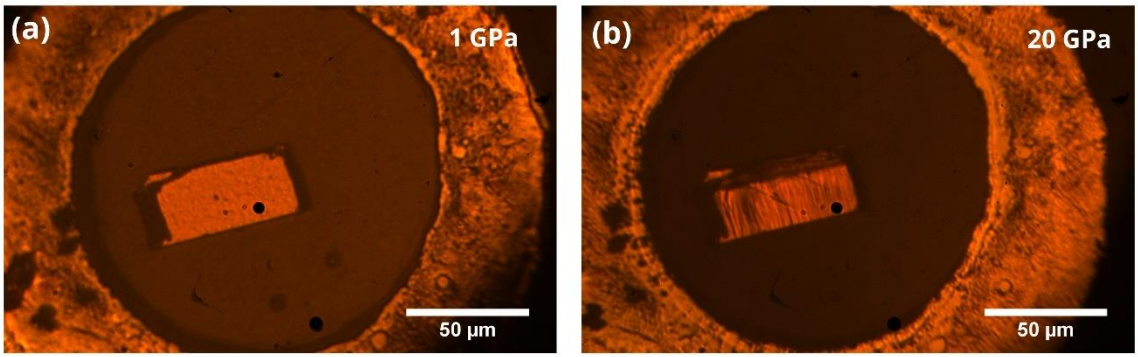

Figure 7.15. Images of the Ta/GaN at (a) 1 and (b) 20 GPa.

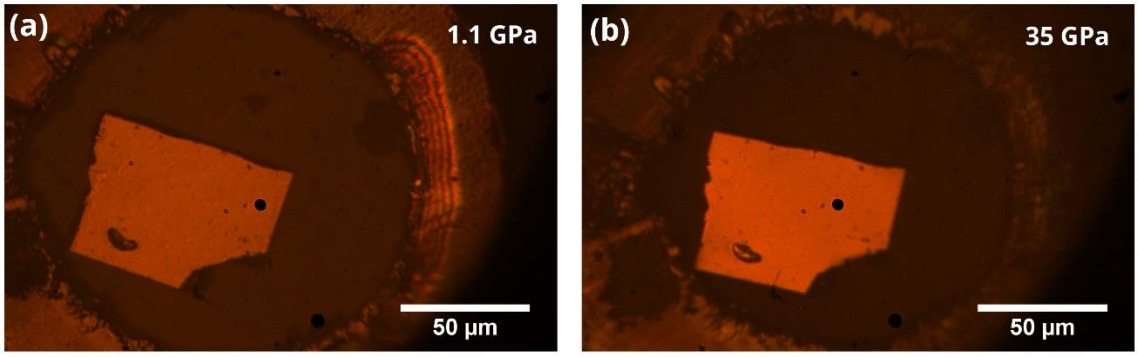

Figure 7.16. Images of the Ta/diamond sample at (a) 1.1 and (b) 35 GPa.

The surface of Ta/diamond sample remains smooth up to 55 GPa.

Chapter 8 Conclusions

In the context of this dissertation, I illustrate that the synergy of time-domain thermoreflectance and scattering techniques, together with tuning phonon dispersion by high pressure, provides an effective experimental avenue for investigating the influence of phonon dispersion on thermal conductivity. Specifically, I studied the pressure dependence of phonon dynamics and thermal conductivity of $SrTiO_3$, $KTaO_3$, BAs, GaN, and diamond up to 20 – 55 GPa. Through systematic analysis of the variation of phonon frequencies and thermal conductivity under pressure, I build connections between the two properties based on the kinetic gas theory for thermal conductivity.

I studied the pressure-dependent thermal conductivity and vibrational dynamics of two perovskites, $SrTiO_3$ and $KTaO_3$, which share similar structural and elastic properties. Despite their structural similarities, $SrTiO_3$ and $KTaO_3$ exhibit contrasting pressure dependence in their thermal conductivity. At 20 GPa, thermal conductivity of $SrTiO_3$ doubles, while that of $KTaO_3$ triples. This divergence stems from distinct pressure-induced alterations in phonon lifetimes. Based on the analysis of the LS equation, at 20 GPa, $SrTiO_3$ experiences a 60% increase in phonon mean free path, while $KTaO_3$ experiences a 100% increase. Additionally, the Grüneisen parameter of low-frequency acoustic phonon in $SrTiO_3$ decreases by 50% at 20 GPa, while that of $KTaO_3$ drops by 80% evident from the Brillouin scattering measurements. Both analyses suggest that changes in phonon lifetimes under pressure predominantly influence the pressure dependence of thermal conductivity in $SrTiO_3$ and $KTaO_3$.

Moving forward, I investigated the pressure dependence of BAs, a material characterized by distinctive phonon dispersion and a complex mechanism of phonon-phonon scattering. The phase space of three-phonon scattering of BAs is very small due to the *a*-*o* gap and acoustic bunching in the phonon dispersion. Subsequently, four-phonon scattering becomes an important scattering

channel in BAs. I observed a pressure-independent thermal conductivity in five BAs samples, each possessing an ambient thermal conductivity of approximately 1000 W m^{-1} K^{-1}. The unique pressure dependence of BAs originates from the competition of three- and four-phonon scattering as pressure varies. With increasing pressure, three-phonon scattering becomes stronger, while four-phonon scattering gets weaker. The resultant interplay between these mechanisms offsets each other, culminating in a pressure-independent thermal conductivity in BAs. This observation aligns well with predictions using first-principles calculation [149].

In the course of my collaboration with Prof. Zhifeng Ren's group at the University of Houston over the past two years, a remarkable discovery unfolded. Contrary to the established upper limit of approximately 1400 W m^{-1} K^{-1} for the thermal conductivity of BAs [109,114,115,219,221], I encountered BAs samples demonstrating an ambient thermal conductivity of 1500 W m^{-1} K^{-1}. Within the dataset of approximately 50 BAs samples that I examined, four of them displayed thermal conductivity over 1400 W m^{-1} K^{-1}. Furthermore, a detailed investigation into the thermal conductivity as a function of temperature for two BAs samples with Λ_{300K} of 1500 W m^{-1} K^{-1} revealed an intriguing $1/T^2$ dependence. This observed stronger temperature dependence surpassed both prior experimental observations ($1/T^{1.3}$ to $1/T^{1.4}$) [109,221] and theoretical predictions ($1/T^{1.7}$ to $1/T^{1.8}$) [114,115]. This enhanced temperature dependence indicates that theoretical predictions using first-principles calculation may have previously underestimated the significance of four-phonon scattering in BAs.

Naturally, I proceeded to conduct thermal conductivity measurements on a BAs sample with Λ_{300K} of 1500 W m^{-1} K^{-1} as a function of pressure, to see what the pressure dependence is for a higher-purity BAs sample. Surprisingly, in contrast to the pressure-independent thermal conductivity I observed on the BAs samples with Λ_{300K} of ~ 1000 W m^{-1} K^{-1}, I observed an

increasing thermal conductivity as pressure increases in the 1500 W m^{-1} K^{-1} BAs sample. At 30 GPa, the relative increase in thermal conductivity is about 50%. These data were all obtained by TDTR with Al as the transducer, for both the 1000 and 1500 W m^{-1} K^{-1} BAs samples. However, when coating a bilayer V/Al transducer on the 1500 W m^{-1} K^{-1} BAs sample, the measured thermal conductivity is pressure-independent. I did not get a chance to do a control measurement for the V/Al bilayer transducer at high pressure, *e.g.*, high-pressure TDTR measurements on MgO with the V/Al bilayer as transducer. With the control measurements, the cause of such discrepancies can be explored.

Moreover, to scrutinize the pressure dependence of other materials characterized by a frequency gap in their phonon dispersion, I conducted measurements on the thermal conductivity and vibrational dynamics of GaN as a function of pressure. As a reference, diamond, devoid of a frequency gap, was used as a control sample. At 20 GPa, both BAs and GaN experience a 7% increase in the longitudinal sound velocity. The zone-center optical phonon mode increases by 10% in BAs, and 15% in GaN. At 20 GPa, thermal conductivity of GaN increases by 55%, and that of BAs increases by only 15 – 35%. Further validation of the pressure dependence of BAs's thermal conductivity is needed. For diamond, at 50 GPa, we observe a 6% increase in the longitudinal sound velocity, 10% increase in zone-center optical phonon mode, and 40% increase in thermal conductivity. Additionally, we observed that the LS equation demonstrates good agreement with GaN, acceptable conformity with diamond, but encountered a substantial discrepancy with BAs.

Chapter 9 References

[1] C. Kittel, *Introduction to Solid State Physics*, 8th ed (Wiley, Hoboken, NJ, 2005).

[2] D. A. Broido, M. Malorny, G. Birner, N. Mingo, and D. A. Stewart, *Intrinsic Lattice Thermal Conductivity of Semiconductors from First Principles*, Applied Physics Letters **91**, 231922 (2007).

[3] Y. Yamada and G. Shirane, *Neutron Scattering and Nature of the Soft Optical Phonon in SrTiO3*, J. Phys. Soc. Jpn. **26**, No. 2 (1969).

[4] C. H. Perry, J. H. Fertel, and T. F. McNelly, *Temperature Dependence of the Raman Spectrum of SrTiO $_3$ and KTaO $_3$*, The Journal of Chemical Physics **47**, 5 (1967).

[5] S. Ghose, M. Krisch, A. R. Oganov, A. Beraud, A. Bosak, R. Gulve, R. Seelaboyina, H. Yang, and S. K. Saxena, *Lattice Dynamics of MgO at High Pressure: Theory and Experiment*, Phys. Rev. Lett. **96**, 3 (2006).

[6] Y. Zhou, Z.-Y. Dong, W.-P. Hsieh, A. F. Goncharov, and X.-J. Chen, *Thermal Conductivity of Materials under Pressure*, Nat Rev Phys **4**, 5 (2022).

[7] L. Lindsay, D. A. Broido, and T. L. Reinecke, *First-Principles Determination of Ultrahigh Thermal Conductivity of Boron Arsenide: A Competitor for Diamond?*, Phys. Rev. Lett. **111**, 2 (2013).

[8] S. Lohrasbi, R. Hammer, W. Essl, G. Reiss, S. Defregger, and W. Sanz, *A Comprehensive Review on the Core Thermal Management Improvement Concepts in Power Electronics*, IEEE Access **8**, 166880 (2020).

[9] G. A. Slack, *Nonmetallic Crystals with High Thermal Conductivity*, Journal of Physics and Chemistry of Solids **34**, 2 (1973).

[10] B. Chen, W. P. Hsieh, D. G. Cahill, D. R. Trinkle, and J. Li, *Thermal Conductivity of Compressed H2O to 22 GPa: A Test of the Leibfried-Schlömann Equation*, Physical Review B - Condensed Matter and Materials Physics **83**, 1 (2011).

[11] J. M. Ziman, *Electrons And Phonons: The Theory of Transport Phenomena in Solids*, 1st ed. (Oxford University Press, London, 1963).

[12] N. L. Vočadlo and G. D. Price, *The Grüneisen Parameter — Computer Calculations via Lattice Dynamics*, Physics of the Earth and Planetary Interiors **82**, 3–4 (1994).

[13] T. Favaloro, J.-H. Bahk, and A. Shakouri, *Characterization of the Temperature Dependence of the Thermoreflectance Coefficient for Conductive Thin Films*, Review of Scientific Instruments **86**, 024903 (2015).

[14] R. B. Wilson, B. A. Apgar, L. W. Martin, and D. G. Cahill, *Thermoreflectance of Metal Transducers for Optical Pump-Probe Studies of Thermal Properties*, Opt. Express **20**, 28829 (2012).

[15] A. Schmidt, M. Chiesa, X. Chen, and G. Chen, *An Optical Pump-Probe Technique for Measuring the Thermal Conductivity of Liquids*, Review of Scientific Instruments **79**, 064902 (2008).

[16] D. Errandonea et al., *Experimental and Theoretical Confirmation of an Orthorhombic Phase Transition in Niobium at High Pressure and Temperature*, Commun Mater **1**, 60 (2020).

[17] H. Cynn and C.-S. Yoo, *Equation of State of Tantalum to 174 GPa*, Phys. Rev. B **59**, 13 (1999).

[18] S. Klotz, J.-C. Chervin, P. Munsch, and G. Le Marchand, *Hydrostatic Limits of 11 Pressure Transmitting Media*, J. Phys. D: Appl. Phys. **42**, 075413 (2009).

[19] M. Rivers, V. Prakapenka, A. Kubo, C. Pullins, C. Holl, and S. Jacobsen, *The COMPRES/GSECARS Gas-Loading System for Diamond Anvil Cells at the Advanced Photon Source*, High Pressure Res. **28**, 273 (2008).

[20] A. F. Goncharov, M. Wong, D. Allen Dalton, J. G. O. Ojwang, V. V. Struzhkin, Z. Konôpková, and P. Lazor, *Thermal Conductivity of Argon at High Pressures and High Temperatures*, Journal of Applied Physics **111**, 112609 (2012).

[21] W.-P. Hsieh, *Thermal Conductivity of Methanol-Ethanol Mixture and Silicone Oil at High Pressures*, Journal of Applied Physics **117**, 23 (2015).

[22] W. P. Hsieh, B. Chen, J. Li, P. Keblinski, and D. G. Cahill, *Pressure Tuning of the Thermal Conductivity of the Layered Muscovite Crystal*, Physical Review B - Condensed Matter and Materials Physics **80**, 1 (2009).

[23] S. Li, Z. Qin, H. Wu, M. Li, M. Kunz, A. Alatas, A. Kavner, and Y. Hu, *Anomalous Thermal Transport under High Pressure in Boron Arsenide*, Nature **612**, 459 (2022).

[24] G. T. Hohensee, R. B. Wilson, and D. G. Cahill, *Thermal Conductance of Metal-Diamond Interfaces at High Pressure*, Nature Communications **6**, 1 (2015).

[25] A. Dewaele, M. Torrent, P. Loubeyre, and M. Mezouar, *Compression Curves of Transition Metals in the Mbar Range: Experiments and Projector Augmented-Wave Calculations*, Phys. Rev. B **78**, 104102 (2008).

[26] G. T. Hohensee, M. R. Fellinger, D. R. Trinkle, and D. G. Cahill, *Thermal Transport across High-Pressure Semiconductor-Metal Transition in Si and Si0.991 Ge0.009*, Physical Review B - Condensed Matter and Materials Physics **91**, 1 (2015).

[27] A. Dewaele, P. Loubeyre, F. Occelli, M. Mezouar, P. I. Dorogokupets, and M. Torrent, *Quasihydrostatic Equation of State of Iron above 2 Mbar*, Phys. Rev. Lett. **97**, 215504 (2006).

[28] W.-P. Hsieh, A. F. Goncharov, S. Labrosse, N. Holtgrewe, S. S. Lobanov, I. Chuvashova, F. Deschamps, and J.-F. Lin, *Low Thermal Conductivity of Iron-Silicon Alloys at Earth's Core Conditions with Implications for the Geodynamo*, Nat Commun **11**, 3332 (2020).

[29] W. Hsieh, F. Deschamps, T. Okuchi, and J. Lin, *Reduced Lattice Thermal Conductivity of Fe-bearing Bridgmanite in Earth's Deep Mantle*, J. Geophys. Res. Solid Earth **122**, 4900 (2017).

[30] F. Occelli, P. Loubeyre, and R. LeToullec, *Properties of Diamond under Hydrostatic Pressures up to 140 GPa*, Nature Mater **2**, 151 (2003).

[31] N. M. Balzaretti and J. A. H. da Jornada, *Pressure Dependence of the Refractive Index of Diamond, Cubic Silicon Carbide and Cubic Boron Nitride*, Solid State Communications **99**, 943 (1996).

[32] A. Dewaele, P. Loubeyre, and M. Mezouar, *Equations of State of Six Metals above 94 GPa*, Phys. Rev. B **70**, 9 (2004).

[33] K.-H. Yang, N.-J. Ho, and H.-Y. Lu, *Plastic Deformation of <001> Single-Crystal SrTiO3 by Compression at Room Temperature*, J. Am. Ceram. Soc. **94**, 3104 (2011).

[34] B. Sun, G. Haunschild, C. Polanco, J. Ju, L. Lindsay, G. Koblmüller, and Y. K. Koh, *Dislocation-Induced Thermal Transport Anisotropy in Single-Crystal Group-III Nitride Films*, Nature Mater **18**, 136 (2019).

[35] Z. Zhang, X. Fan, J. Zhu, J. Zhou, and D. Tang, *An Accurate Method to Determine Nano-Film Thickness in Diamond Anvil Cells for Time Domain Thermoreflectance Measurements*, Review of Scientific Instruments **93**, 043904 (2022).

[36] C. Thomsen, H. J. Maris, and J. Tauc, *Picosecond Acoustics as a Non-Destructive Tool for the Characterization of Very Thin Films*, Thin Solid Films **154**, 217 (1987).

[37] G. T. Hohensee, R. B. Wilson, and D. G. Cahill, *Thermal Conductance of Metal–Diamond Interfaces at High Pressure*, Nat Commun **6**, 1 (2015).

[38] A. Dewaele, F. Datchi, P. Loubeyre, and M. Mezouar, *High Pressure–High Temperature Equations of State of Neon and Diamond*, Phys. Rev. B **77**, 094106 (2008).

[39] J. P. Feser and D. G. Cahill, *Probing Anisotropic Heat Transport Using Time-Domain Thermoreflectance with Offset Laser Spots*, Review of Scientific Instruments **83**, 10 (2012).

[40] J. P. Feser, J. Liu, and D. G. Cahill, *Pump-Probe Measurements of the Thermal Conductivity Tensor for Materials Lacking in-Plane Symmetry*, Review of Scientific Instruments **85**, 104903 (2014).

[41] M. J. Gomez, K. Liu, J. G. Lee, and R. B. Wilson, *High Sensitivity Pump–Probe Measurements of Magnetic, Thermal, and Acoustic Phenomena with a Spectrally Tunable Oscillator*, Review of Scientific Instruments **91**, 2 (2020).

[42] W.-P. Hsieh and D. G. Cahill, *Ta and Au(Pd) Alloy Metal Film Transducers for Time-Domain Thermoreflectance at High Pressures*, Journal of Applied Physics **109**, 11 (2011).

[43] L. A. Clevenger, A. Mutscheller, J. M. E. Harper, C. Cabral, and K. Barmak, *The Relationship between Deposition Conditions, the Beta to Alpha Phase Transformation, and Stress Relaxation in Tantalum Thin Films*, Journal of Applied Physics **72**, 4918 (1992).

[44] W.-P. Hsieh and D. G. Cahill, *Ta and Au(Pd) Alloy Metal Film Transducers for Time-Domain Thermoreflectance at High Pressures*, Journal of Applied Physics **109**, 113520 (2011).

[45] Y. Wang, J. Y. Park, Y. K. Koh, and D. G. Cahill, *Thermoreflectance of Metal Transducers for Time-Domain Thermoreflectance*, Journal of Applied Physics **108**, 043507 (2010).

[46] M. Guennou, P. Bouvier, J. Kreisel, and D. Machon, *Pressure-Temperature Phase Diagram of SrTiO 3 up to 53 GPa*, Phys. Rev. B **81**, 5 (2010).

[47] R. G. Greene, H. Luo, A. L. Ruoff, S. S. Trail, and F. J. DiSalvo, *Pressure Induced Metastable Amorphization of BAs: Evidence for a Kinetically Frustrated Phase Transformation*, Phys. Rev. Lett. **73**, 18 (1994).

[48] D. A. Dalton, W.-P. Hsieh, G. T. Hohensee, D. G. Cahill, and A. F. Goncharov, *Effect of Mass Disorder on the Lattice Thermal Conductivity of MgO Periclase under Pressure*, Sci Rep **3**, 2400 (2013).

[49] K. Takemura and A. Dewaele, *Isothermal Equation of State for Gold with a He-Pressure Medium*, Phys. Rev. B **78**, 104119 (2008).

[50] J. H. Rose, J. R. Smith, F. Guinea, and J. Ferrante, *Universal Features of the Equation of State of Metals*, Phys. Rev. B **29**, 2963 (1984).

[51] C.-S. Zha, K. Mibe, W. A. Bassett, O. Tschauner, H.-K. Mao, and R. J. Hemley, *P - V - T Equation of State of Platinum to 80GPa and 1900K from Internal Resistive Heating/x-Ray Diffraction Measurements*, Journal of Applied Physics **103**, 054908 (2008).

[52] H. Cynn, J. E. Klepeis, C.-S. Yoo, and D. A. Young, *Osmium Has the Lowest Experimentally Determined Compressibility*, Phys. Rev. Lett. **88**, 135701 (2002).

[53] Y. Ding, R. Ahuja, J. Shu, P. Chow, W. Luo, and H. Mao, *Structural Phase Transition of Vanadium at 69 GPa*, Phys. Rev. Lett. **98**, 085502 (2007).

[54] R. L. Douglass, *Heat Transport by Spin Waves in Yttrium Iron Garnet*, Phys. Rev. **129**, 1132 (1963).

[55] C. Hess, B. Büchner, U. Ammerahl, L. Colonescu, F. Heidrich-Meisner, W. Brenig, and A. Revcolevschi, *Magnon Heat Transport in Doped L a 2 C u O 4*, Phys. Rev. Lett. **90**, 197002 (2003).

[56] R. Jin, Y. Onose, Y. Tokura, D. Mandrus, P. Dai, and B. C. Sales, *In-Plane Thermal Conductivity of N d 2 C u O 4 : Evidence for Magnon Heat Transport*, Phys. Rev. Lett. **91**, 146601 (2003).

[57] B. Y. Pan, T. Y. Guan, X. C. Hong, S. Y. Zhou, X. Qiu, H. Zhang, and S. Y. Li, *Specific Heat and Thermal Conductivity of Ferromagnetic Magnons in Yttrium Iron Garnet*, EPL **103**, 37005 (2013).

[58] N. Prasai, B. A. Trump, G. G. Marcus, A. Akopyan, S. X. Huang, T. M. McQueen, and J. L. Cohn, *Ballistic Magnon Heat Conduction and Possible Poiseuille Flow in the Helimagnetic Insulator Cu 2 OSeO 3*, Phys. Rev. B **95**, 224407 (2017).

[59] G. S. Dixon, *Lattice Thermal Conductivity of Antiferromagnetic Insulators*, Phys. Rev. B **21**, 2851 (1980).

[60] G. Laurence and D. Petitgrand, *Thermal Conductivity and Magnon-Phonon Resonant Interaction in Antiferromagnetic Fe Cl 2*, Phys. Rev. B **8**, 2130 (1973).

[61] B. Wei, Q. Sun, C. Li, and J. Hong, *Phonon Anharmonicity: A Pertinent Review of Recent Progress and Perspective*, Sci. China Phys. Mech. Astron. **64**, 117001 (2021).

[62] S. Bao et al., *Evidence for Magnon-Phonon Coupling in the Topological Magnet Cu 3 TeO 6*, Phys. Rev. B **101**, 214419 (2020).

[63] C. A. Pocs, I. A. Leahy, H. Zheng, G. Cao, E.-S. Choi, S.-H. Do, K.-Y. Choi, B. Normand, and M. Lee, *Giant Thermal Magnetoconductivity in CrCl 3 and a General Model for Spin-Phonon Scattering*, Phys. Rev. Research **2**, 013059 (2020).

[64] D. R. Ratkovski, L. Balicas, A. Bangura, F. L. A. Machado, and S. M. Rezende, *Thermal Transport in Yttrium Iron Garnet at Very High Magnetic Fields*, Phys. Rev. B **101**, 174442 (2020).

[65] P. A. Sharma, J. S. Ahn, N. Hur, S. Park, S. B. Kim, S. Lee, J.-G. Park, S. Guha, and S.-W. Cheong, *Thermal Conductivity of Geometrically Frustrated, Ferroelectric Y M n O 3 : Extraordinary Spin-Phonon Interactions*, Phys. Rev. Lett. **93**, 177202 (2004).

[66] F. Meier, J. Levy, and D. Loss, *Quantum Computing with Antiferromagnetic Spin Clusters*, Phys. Rev. B **68**, 134417 (2003).

[67] O. Gomonay, T. Jungwirth, and J. Sinova, *High Antiferromagnetic Domain Wall Velocity Induced by Néel Spin-Orbit Torques*, Phys. Rev. Lett. **117**, 017202 (2016).

[68] C. Tzschaschel, K. Otani, R. Iida, T. Shimura, H. Ueda, S. Günther, M. Fiebig, and T. Satoh, *Ultrafast Optical Excitation of Coherent Magnons in Antiferromagnetic NiO*, Phys. Rev. B **95**, 174407 (2017).

[69] M. Fechner, A. Sukhov, L. Chotorlishvili, C. Kenel, J. Berakdar, and N. A. Spaldin, *Magnetophononics: Ultrafast Spin Control through the Lattice*, Phys. Rev. Materials **2**, 064401 (2018).

[70] Y. W. Windsor, D. Zahn, R. Kamrla, J. Feldl, H. Seiler, C.-T. Chiang, M. Ramsteiner, W. Widdra, R. Ernstorfer, and L. Rettig, *Exchange-Striction Driven Ultrafast Nonthermal Lattice Dynamics in NiO*, Phys. Rev. Lett. **126**, 147202 (2021).

[71] T. Jungwirth, X. Marti, P. Wadley, and J. Wunderlich, *Antiferromagnetic Spintronics*, Nature Nanotech **11**, 231 (2016).

[72] G. E. W. Bauer, E. Saitoh, and B. J. Van Wees, *Spin Caloritronics*, Nature Mater **11**, 391 (2012).

[73] S. R. Boona, R. C. Myers, and J. P. Heremans, *Spin Caloritronics*, Energy Environ. Sci. **7**, 885 (2014).

[74] H. Wang, C. Du, P. C. Hammel, and F. Yang, *Antiferromagnonic Spin Transport from Y 3 Fe 5 O 12 into NiO*, Phys. Rev. Lett. **113**, 097202 (2014).

[75] C. Hahn, G. De Loubens, V. V. Naletov, J. Ben Youssef, O. Klein, and M. Viret, *Conduction of Spin Currents through Insulating Antiferromagnetic Oxides*, EPL **108**, 57005 (2014).

[76] H. Wang, C. Du, P. C. Hammel, and F. Yang, *Spin Transport in Antiferromagnetic Insulators Mediated by Magnetic Correlations*, Phys. Rev. B **91**, 220410 (2015).

[77] T. Shang et al., *Effect of NiO Inserted Layer on Spin-Hall Magnetoresistance in Pt/NiO/YIG Heterostructures*, Applied Physics Letters **109**, 032410 (2016).

[78] M. Foëx, *A Type of Transformation Common to Manganous, Ferrous, Cobaltous, and Nickelous Oxides*, Compt. Rend **227**, 193 (1948).

[79] J. R. Tomlinson, L. Domash, R. G. Hay, and C. W. Montgomery, *The High Temperature Heat Content of Nickel Oxide*, Journal of the American Chemical Society **77**, 909 (1955).

[80] H. Kondoh, E. Uchida, Y. Nakazumi, and T. Nagamiya, *Magnetic Anisotropy Measurements of NiO Single Crystal*, Journal of the Physical Society of Japan **13**, 579 (1958).

[81] N. P. Duong, T. Satoh, and M. Fiebig, *Ultrafast Manipulation of Antiferromagnetism of NiO*, Physical Review Letters **93**, 117402 (2004).

[82] Q. Sun, B. Wei, Y. Su, H. Smith, J. Y. Lin, D. L. Abernathy, and C. Li, *Mutual Spin-Phonon Driving Effects and Phonon Eigenvector Renormalization in Nickel (II) Oxide*, Proceedings of the National Academy of Sciences **119**, e2120553119 (2022).

[83] G. A. Slack and R. Newman, *Thermal Conductivity of MnO and NiO*, Physical Review Letters **1**, 359 (1958).

[84] V. P. Zhuze, O. N. Novruzov, and A. I. Shelykh, *THERMAL CONDUCTIVITY NEAR A CONTINUOUS PHASE TRANSITION (EXPERIMENTAL, WITH SODIUM NITRATE, BARIUM TITANATE, MANGANESE TELLURIDE, NICKEL OXIDE, COBALT OXIDE)*, INST SEMICOND LENINGRAD SOVIET PHYS SOLID STATE **11**, 1044 (1969).

[85] F. B. Lewis and N. H. Saunders, *The Thermal Conductivity of NiO and CoO at the Neel Temperature*, Journal of Physics C: Solid State Physics **6**, 2525 (1973).

[86] J. E. Keem and J. M. Honig, *Selected Electrical and Thermal Properties of Undoped Nickel Oxide*, Cindas Report **52**, (1978).

[87] M. Massot, A. Oleaga, A. Salazar, D. Prabhakaran, M. Martin, P. Berthet, and G. Dhalenne, *Critical Behavior of CoO and NiO from Specific Heat, Thermal Conductivity, and Thermal Diffusivity Measurements*, Physical Review B **77**, 134438 (2008).

[88] J. Linnera and A. J. Karttunen, *Lattice Dynamical Properties of Antiferromagnetic MnO, CoO, and NiO, and the Lattice Thermal Conductivity of NiO*, Physical Review B **100**, 144307 (2019).

[89] E. Aytan, B. Debnath, F. Kargar, Y. Barlas, M. M. Lacerda, J. X. Li, R. K. Lake, J. Shi, and A. A. Balandin, *Spin-Phonon Coupling in Antiferromagnetic Nickel Oxide*, Applied Physics Letters **111**, (2017).

[90] O. Arnold, J.-C. Bilheux, J. M. Borreguero, A. Buts, S. I. Campbell, L. Chapon, M. Doucet, N. Draper, R. F. Leal, and M. A. Gigg, *Mantid—Data Analysis and Visualization Package for Neutron Scattering and μ SR Experiments*, Nuclear Instruments and Methods in Physics Research Section a: Accelerators, Spectrometers, Detectors and Associated Equipment **764**, 156 (2014).

[91] D. G. Cahill, *Analysis of Heat Flow in Layered Structures for Time-Domain Thermoreflectance*, Review of Scientific Instruments **75**, 12 (2004).

[92] D. A. Ditmars, C. A. Plint, and R. C. Shukla, *Aluminum. I. Measurement of the Relative Enthalpy from 273 to 929 K and Derivation of Thermodynamic Functions for Al(s) from 0 K to Its Melting Point*, Int J Thermophys **6**, 499 (1985).

[93] H. Seltz, B. J. DeWitt, and H. J. McDonald, *The Heat Capacity of Nickel Oxide from 68-298° K. and the Thermodynamic Properties of the Oxide*, Journal of the American Chemical Society **62**, 88 (1940).

[94] D. S. Kim, O. Hellman, J. Herriman, H. L. Smith, J. Y. Y. Lin, N. Shulumba, J. L. Niedziela, C. W. Li, D. L. Abernathy, and B. Fultz, *Nuclear Quantum Effect with Pure Anharmonicity and the Anomalous Thermal Expansion of Silicon*, Proceedings of the National Academy of Sciences **115**, 1992 (2018).

[95] W. Reichardt, V. Wagner, and W. Kress, *Lattice Dynamics of NiO*, J. Phys. C: Solid State Phys. **8**, 3955 (1975).

[96] Z. Yamani, W. J. L. Buyers, R. A. Cowley, and D. Prabhakaran, *Magnetic Excitations of Spin and Orbital Moments in Cobalt oxideSpecial Issue on Neutron Scattering in Canada.*, Can. J. Phys. **88**, 729 (2010).

[97] X. Wu, Z. Liu, and T. Luo, *Magnon and Phonon Dispersion, Lifetime, and Thermal Conductivity of Iron from Spin-Lattice Dynamics Simulations*, Journal of Applied Physics **123**, 085109 (2018).

[98] H. J. Qin, Kh. Zakeri, A. Ernst, and J. Kirschner, *Temperature Dependence of Magnetic Excitations: Terahertz Magnons above the Curie Temperature*, Phys. Rev. Lett. **118**, 127203 (2017).

[99] M. Grimsditch, L. E. McNeil, and D. J. Lockwood, *Unexpected Behavior of the Antiferromagnetic Mode of NiO*, Phys. Rev. B **58**, 14462 (1998).

[100] T. Kampfrath, A. Sell, G. Klatt, A. Pashkin, S. Mährlein, T. Dekorsy, M. Wolf, M. Fiebig, A. Leitenstorfer, and R. Huber, *Coherent Terahertz Control of Antiferromagnetic Spin Waves*, Nature Photon **5**, 31 (2011).

[101] A. Togo, L. Chaput, and I. Tanaka, *Distributions of Phonon Lifetimes in Brillouin Zones*, Phys. Rev. B **91**, 094306 (2015).

[102] D. G. Cahill and R. O. Pohl, *Thermal Conductivity of Amorphous Solids above the Plateau*, Phys. Rev. B **35**, 4067 (1987).

[103] *The Effect of a Magnetic Field on the Thermal Conductivity of Paramagnetic Crystals: Holmium Ethylsulphate*, Proc. R. Soc. Lond. A **298**, 359 (1967).

[104] L. Mauger, M. S. Lucas, J. A. Muñoz, S. J. Tracy, M. Kresch, Y. Xiao, P. Chow, and B. Fultz, *Nonharmonic Phonons in α -Iron at High Temperatures*, Phys. Rev. B **90**, 064303 (2014).

[105] D. G. Cahill, S.-M. Lee, and T. I. Selinder, *Thermal Conductivity of κ-Al2O3 and α-Al2O3 Wear-Resistant Coatings*, Journal of Applied Physics **83**, 5783 (1998).

[106] S. Yue et al., *High Ambipolar Mobility in Cubic Boron Arsenide Revealed by Transient Reflectivity Microscopy*, Science **377**, 433 (2022).

[107] J. Shin et al., *High Ambipolar Mobility in Cubic Boron Arsenide*, Science **377**, 437 (2022).

[108] F. Tian et al., *Unusual High Thermal Conductivity in Boron Arsenide Bulk Crystals*, Science **361**, 6402 (2018).

[109] J. S. Kang, M. Li, H. Wu, H. Nguyen, and Y. Hu, *Experimental Observation of High Thermal Conductivity in Boron Arsenide*, Science **361**, 6402 (2018).

[110] S. Li, Q. Zheng, Y. Lv, X. Liu, X. Wang, P. Y. Huang, D. G. Cahill, and B. Lv, *High Thermal Conductivity in Cubic Boron Arsenide Crystals*, Science **361**, 6402 (2018).

[111] T. Feng, L. Lindsay, and X. Ruan, *Four-Phonon Scattering Significantly Reduces Intrinsic Thermal Conductivity of Solids*, Phys. Rev. B **96**, 16 (2017).

[112] E. Guzman, F. Kargar, A. Patel, S. Vishwakarma, D. Wright, R. B. Wilson, D. J. Smith, R. J. Nemanich, and A. A. Balandin, *Optical and Acoustic Phonons in Turbostratic and Cubic Boron Nitride Thin Films on Diamond Substrates*, Diamond and Related Materials **140**, 110452 (2023).

[113] T.-H. Liu, B. Song, L. Meroueh, Z. Ding, Q. Song, J. Zhou, M. Li, and G. Chen, *Simultaneously High Electron and Hole Mobilities in Cubic Boron-V Compounds: BP, BAs, and BSb*, Phys. Rev. B **98**, 081203 (2018).

[114] X. Yang, T. Feng, J. Li, and X. Ruan, *Stronger Role of Four-Phonon Scattering than Three-Phonon Scattering in Thermal Conductivity of III-V Semiconductors at Room Temperature*, Phys. Rev. B **100**, 24 (2019).

[115] K. Chen et al., *Ultrahigh Thermal Conductivity in Isotope-Enriched Cubic Boron Nitride*, Science **367**, 6477 (2020).

[116] H. Sun, K. Chen, G. A. Gamage, H. Ziyaee, F. Wang, Y. Wang, V. G. Hadjiev, F. Tian, G. Chen, and Z. Ren, *Boron Isotope Effect on the Thermal Conductivity of Boron Arsenide Single Crystals*, Materials Today Physics **11**, 100169 (2019).

[117] X. Chen et al., *Effects of Impurities on the Thermal and Electrical Transport Properties of Cubic Boron Arsenide*, Chem. Mater. **33**, 17 (2021).

[118] S. Yue et al., *Photoluminescence Mapping and Time-Domain Thermo-Photoluminescence for Rapid Imaging and Measurement of Thermal Conductivity of Boron Arsenide*, Materials Today Physics **13**, 100194 (2020).

[119] J. L. Lyons, J. B. Varley, E. R. Glaser, J. A. Freitas, J. C. Culbertson, F. Tian, G. A. Gamage, H. Sun, H. Ziyaee, and Z. Ren, *Impurity-Derived* p *-Type Conductivity in Cubic Boron Arsenide*, Applied Physics Letters **113**, 251902 (2018).

[120] I. H. Nwigboji, Y. Malozovsky, L. Franklin, and D. Bagayoko, *Calculated Electronic, Transport, and Related Properties of Zinc Blende Boron Arsenide (Zb-BAs)*, Journal of Applied Physics **120**, 145701 (2016).

[121] S. Wang, S. F. Swingle, H. Ye, F.-R. F. Fan, A. H. Cowley, and A. J. Bard, *Synthesis and Characterization of a P-Type Boron Arsenide Photoelectrode*, J. Am. Chem. Soc. **134**, 11056 (2012).

[122] K. Bushick, K. Mengle, N. Sanders, and E. Kioupakis, *Band Structure and Carrier Effective Masses of Boron Arsenide: Effects of Quasiparticle and Spin-Orbit Coupling Corrections*, Applied Physics Letters **114**, 022101 (2019).

[123] S. Chae, K. Mengle, J. T. Heron, and E. Kioupakis, *Point Defects and Dopants of Boron Arsenide from First-Principles Calculations: Donor Compensation and Doping Asymmetry,* Applied Physics Letters **113**, 212101 (2018).

[124] J. Buckeridge and D. O. Scanlon, *Electronic Band Structure and Optical Properties of Boron Arsenide,* Phys. Rev. Materials **3**, 051601 (2019).

[125] H. Zhong, F. Pan, S. Yue, C. Qin, V. Hadjiev, F. Tian, X. Liu, F. Lin, Z. Wang, and J. Bao, *Idealizing Tauc Plot for Accurate Bandgap Determination of Semiconductor with Ultraviolet–Visible Spectroscopy: A Case Study for Cubic Boron Arsenide,* J. Phys. Chem. Lett. 6702 (2023).

[126] B. Abeles, *Lattice Thermal Conductivity of Disordered Semiconductor Alloys at High Temperatures*, Phys. Rev. **131**, 1906 (1963).

[127] P. G. Klemens, *Thermal Resistance Due to Point Defects at High Temperatures*, Phys. Rev. **119**, 507 (1960).

[128] N. K. Ravichandran and D. Broido, *Phonon-Phonon Interactions in Strongly Bonded Solids: Selection Rules and Higher-Order Processes*, Phys. Rev. X **10**, 2 (2020).

[129] F. Tian et al., *Seeded Growth of Boron Arsenide Single Crystals with High Thermal Conductivity,* Appl. Phys. Lett. **112**, 3 (2018).

[130] P. Jiang, X. Qian, and R. Yang, *Tutorial: Time-Domain Thermoreflectance (TDTR) for Thermal Property Characterization of Bulk and Thin Film Materials*, Journal of Applied Physics **124**, 16 (2018).

[131] J. F. Thomas, *Third-Order Elastic Constants of Aluminum*, Phys. Rev. **175**, 955 (1968).

[132] J. S. Kang, M. Li, H. Wu, H. Nguyen, and Y. Hu, *Basic Physical Properties of Cubic Boron Arsenide,* Appl. Phys. Lett. **115**, 12 (2019).

[133] B. Song, K. Chen, K. Bushick, K. A. Mengle, F. Tian, G. A. G. U. Gamage, Z. Ren, E. Kioupakis, and G. Chen, *Optical Properties of Cubic Boron Arsenide*, Applied Physics Letters **116**, 141903 (2020).

[134] S. Mahat, S. Li, H. Wu, P. Koirala, B. Lv, and D. G. Cahill, *Elastic Constants of Cubic Boron Phosphide and Boron Arsenide*, Phys. Rev. Materials **5**, 3 (2021).

[135] A. Rai, S. Li, H. Wu, B. Lv, and D. G. Cahill, *Effect of Isotope Disorder on the Raman Spectra of Cubic Boron Arsenide*, Phys. Rev. Materials **5**, 013603 (2021).

[136] F. Kargar and A. A. Balandin, *Advances in Brillouin–Mandelstam Light-Scattering Spectroscopy,* Nat. Photon. **15**, 720 (2021).

[137] P. Jiang, X. Qian, and R. Yang, *A New Elliptical-Beam Method Based on Time-Domain Thermoreflectance (TDTR) to Measure the in-Plane Anisotropic Thermal Conductivity and Its Comparison with the Beam-Offset Method*, Review of Scientific Instruments **89**, 094902 (2018).

[138] D. G. Cahill et al., *Nanoscale Thermal Transport. II. 2003–2012*, Applied Physics Reviews **1**, 011305 (2014).

[139] B. Sun and Y. K. Koh, *Understanding and Eliminating Artifact Signals from Diffusely Scattered Pump Beam in Measurements of Rough Samples by Time-Domain Thermoreflectance (TDTR)*, Review of Scientific Instruments **87**, 064901 (2016).

[140] G. T. Hohensee, W.-P. Hsieh, M. D. Losego, and D. G. Cahill, *Interpreting Picosecond Acoustics in the Case of Low Interface Stiffness*, Review of Scientific Instruments **83**, 11 (2012).

[141] R. B. Wilson and D. G. Cahill, *Anisotropic Failure of Fourier Theory in Time-Domain Thermoreflectance Experiments*, Nat Commun **5**, 1 (2014).

[142] A. J. Minnich, J. A. Johnson, A. J. Schmidt, K. Esfarjani, M. S. Dresselhaus, K. A. Nelson, and G. Chen, *Thermal Conductivity Spectroscopy Technique to Measure Phonon Mean Free Paths*, Phys. Rev. Lett. **107**, 9 (2011).

[143] R. B. Wilson and D. G. Cahill, *Limits to Fourier Theory in High Thermal Conductivity Single Crystals*, Applied Physics Letters **107**, 203112 (2015).

[144] C. Hua, L. Lindsay, X. Chen, and A. J. Minnich, *Generalized Fourier's Law for Nondiffusive Thermal Transport: Theory and Experiment*, Phys. Rev. B **100**, 8 (2019).

[145] Q. Zheng, S. Li, C. Li, Y. Lv, X. Liu, P. Y. Huang, D. A. Broido, B. Lv, and D. G. Cahill, *High Thermal Conductivity in Isotopically Enriched Cubic Boron Phosphide*, Adv. Funct. Mater. **28**, 43 (2018).

[146] I. Kudman and E. F. Steigmeier, *Thermal Conductivity and Seebeck Coefficient of InP*, Phys. Rev. **133**, A1665 (1964).

[147] A. Jain and A. J. H. McGaughey, *Effect of Exchange–Correlation on First-Principles-Driven Lattice Thermal Conductivity Predictions of Crystalline Silicon*, Computational Materials Science **110**, 115 (2015).

[148] H. Zhou, S. Zhou, Z. Hua, K. Bawane, and T. Feng, *Extreme Sensitivity of Higher-Order Interatomic Force Constants and Thermal Conductivity to the Energy Surface Roughness of Exchange-Correlation Functionals*, Applied Physics Letters **123**, 192201 (2023).

[149] N. K. Ravichandran and D. Broido, *Non-Monotonic Pressure Dependence of the Thermal Conductivity of Boron Arsenide*, Nat Commun **10**, 1 (2019).

[150] S. Hou, B. Sun, F. Tian, Q. Cai, Y. Xu, S. Wang, X. Chen, Z. Ren, C. Li, and R. B. Wilson, *Thermal Conductivity of BAs under Pressure*, Adv Elect Materials 2200017 (2022).

[151] W. Bludau, A. Onton, and W. Heinke, *Temperature Dependence of the Band Gap of Silicon*, Journal of Applied Physics **45**, 1846 (1974).

[152] M. D. Sturge, *Optical Absorption of Gallium Arsenide between 0.6 and 2.75 eV*, Phys. Rev. **127**, 768 (1962).

[153] M. R. Lorenz, G. D. Pettit, and R. C. Taylor, *Band Gap of Gallium Phosphide from 0 to 900°K and Light Emission from Diodes at High Temperatures*, Phys. Rev. **171**, 876 (1968).

[154] H. P. Maruska and J. J. Tietjen, *THE PREPARATION AND PROPERTIES OF VAPOR-DEPOSITED SINGLE-CRYSTAL-LINE GaN*, Applied Physics Letters **15**, 327 (1969).

[155] M. Fava, N. H. Protik, C. Li, N. K. Ravichandran, J. Carrete, A. Van Roekeghem, G. K. H. Madsen, N. Mingo, and D. Broido, *How Dopants Limit the Ultrahigh Thermal Conductivity of Boron Arsenide: A First Principles Study*, Npj Comput Mater **7**, 54 (2021).

[156] G. A. Gamage, H. Sun, H. Ziyaee, F. Tian, and Z. Ren, *Effect of Boron Sources on the Growth of Boron Arsenide Single Crystals by Chemical Vapor Transport*, Appl. Phys. Lett. **115**, 9 (2019).

[157] X. Meng, A. Singh, R. Juneja, Y. Zhang, F. Tian, Z. Ren, A. K. Singh, L. Shi, J. Lin, and Y. Wang, *Pressure-Dependent Behavior of Defect-Modulated Band Structure in Boron Arsenide*, Adv. Mater. **32**, 45 (2020).

[158] H. Ma, C. Li, S. Tang, J. Yan, A. Alatas, L. Lindsay, B. C. Sales, and Z. Tian, *Boron Arsenide Phonon Dispersion from Inelastic X-Ray Scattering: Potential for Ultrahigh Thermal Conductivity*, Phys. Rev. B **94**, 22 (2016).

[159] A. Amith, I. Kudman, and E. F. Steigmeier, *Electron and Phonon Scattering in GaAs at High Temperatures*, Phys. Rev. **138**, A1270 (1965).

[160] E. F. Steigmeier and I. Kudman, *Acoustical-Optical Phonon Scattering in Ge, Si, and III-V Compounds*, Phys. Rev. **141**, 767 (1966).

[161] Q. Zheng, S. Li, C. Li, Y. Lv, X. Liu, P. Y. Huang, D. A. Broido, B. Lv, and D. G. Cahill, *High Thermal Conductivity in Isotopically Enriched Cubic Boron Phosphide*, Adv Funct Materials **28**, 1805116 (2018).

[162] S. Mahat, *APPLICATION OF PICOSECOND INTERFEROMETRY TO CHARACTERIZE PHYSICAL BEHAVIOR OF CRYSTALS*, (n.d.).

[163] X. Chen, C. Li, F. Tian, G. A. Gamage, S. Sullivan, J. Zhou, D. Broido, Z. Ren, and L. Shi, *Thermal Expansion Coefficient and Lattice Anharmonicity of Cubic Boron Arsenide*, Phys. Rev. Applied **11**, 6 (2019).

[164] J. H. Haeni et al., *Room-Temperature Ferroelectricity in Strained SrTiO3*, **430**, 4 (2004).

[165] L. Maerten, A. Bojahr, M. Gohlke, M. Rössle, and M. Bargheer, *Coupling of GHz Phonons to Ferroelastic Domain Walls in SrTiO 3*, Phys. Rev. Lett. **114**, 047401 (2015).

[166] E. F. Steigmeier, *Field Effect on the Cochran Modes in SrTiO_3 and KTaO_3*, Physical Review **168**, 523 (n.d.).

[167] V. Martelli, J. L. Jiménez, M. Continentino, E. Baggio-Saitovitch, and K. Behnia, *Thermal Transport and Phonon Hydrodynamics in Strontium Titanate*, Phys. Rev. Lett. **120**, 125901 (2018).

[168] Y. Fu and D. J. Singh, *Thermal Conductivity of Perovskite KTaO 3 and PbTiO 3 from First Principles*, Phys. Rev. Materials **2**, 094408 (2018).

[169] A. O. Fumega, Y. Fu, V. Pardo, and D. J. Singh, *Understanding the Lattice Thermal Conductivity of SrTiO 3 from an* Ab Initio *Perspective*, Phys. Rev. Materials **4**, 033606 (2020).

[170] R. Shayduk et al., *Femtosecond X-Ray Diffraction Study of Multi-THz Coherent Phonons in SrTiO $_3$*, Appl. Phys. Lett. **120**, 202203 (2022).

[171] W. Hsieh, F. Deschamps, T. Okuchi, and J. Lin, *Reduced Lattice Thermal Conductivity of Fe-bearing Bridgmanite in Earth's Deep Mantle*, J. Geophys. Res. Solid Earth **122**, 7 (2017).

[172] R. A. Cowley, *Lattice Dynamics and Phase Transitions of Strontium Titanate*, Phys. Rev. **134**, A981 (1964).

[173] G. Shirane, R. Nathans, and V. J. Minkiewicz, *Temperature Dependence of the Soft Ferroelectric Mode in KTa O 3*, Phys. Rev. **157**, 396 (1967).

[174] Y. Yamada and G. Shirane, *Neutron Scattering and Nature of the Soft Optical Phonon in SrTiO3*, J. Phys. Soc. Jpn. **26**, 396 (1969).

[175] M. Guennou, P. Bouvier, J. Kreisel, and D. Machon, *Pressure-Temperature Phase Diagram of SrTiO 3 up to 53 GPa*, Phys. Rev. B **81**, 054115 (2010).

[176] M. A. Carpenter, *Elastic Anomalies Accompanying Phase Transitions in (Ca,Sr)TiO3 Perovskites: Part I. Landau Theory and a Calibration for SrTiO3*, American Mineralogist **92**, 309 (2007).

[177] S.-C. Weng et al., *Pressure-Induced Antiferrodistortive Phase Transition in SrTiO $_3$: Common Scaling of Soft-Mode with Pressure and Temperature*, EPL **107**, 36006 (2014).

[178] C. Zhang, F. Li, X. Wei, M. Guo, Y. Wei, L. Li, X. Li, and Q. Zhou, *Abnormal Elastic Changes for Cubic-Tetragonal Transition of Single-Crystal SrTiO $_3$*, Chinese Phys. Lett. **39**, 096201 (2022).

[179] D. G. Cahill, *Analysis of Heat Flow in Layered Structures for Time-Domain Thermoreflectance*, Review of Scientific Instruments **75**, 5119 (2004).

[180] M. J. Gomez, K. Liu, J. G. Lee, and R. B. Wilson, *High Sensitivity Pump–Probe Measurements of Magnetic, Thermal, and Acoustic Phenomena with a Spectrally Tunable Oscillator*, Review of Scientific Instruments **91**, 023905 (2020).

[181] H. K. Mao, J. Xu, and P. M. Bell, *Calibration of the Ruby Pressure Gauge to 800 Kbar under Quasi-Hydrostatic Conditions*, Journal of Geophysical Research **91**, 4673 (1986).

[182] A. Batool, M. A. Faridi, Q. Mahmood, B. Ul Haq, A. Laref, and S. E. Awan, *The Pressure-Induced Indirect to Direct Bandgap Transition and Thermoelectric Response in SrTiO3: An Ab-Initio Study*, Journal of Physics and Chemistry of Solids **123**, 70 (2018).

[183] X. Liu, W. Lv, C. Chen, W. Yang, J. Han, J. Lin, and H. Sun, *Structural, Electronic and Optical Properties of KTaO3 under High Pressure Based on First-Principles*, Materials Science in Semiconductor Processing **138**, 106248 (2022).

[184] R. G. Greene, H. Luo, and A. L. Ruoff, *Al as a Simple Solid: High Pressure Study to 220 GPa (2.2 Mbar)*, Phys. Rev. Lett. **73**, 2075 (1994).

[185] A. Dewaele, P. Loubeyre, and M. Mezouar, *Equations of State of Six Metals above 94 GPa*, Phys. Rev. B **70**, 094112 (2004).

[186] W. P. Hsieh, *Thermal Conductivity of Methanol-Ethanol Mixture and Silicone Oil at High Pressures*, Journal of Applied Physics **117**, (2015).

[187] A. Boudali, M. D. Khodja, B. Amrani, D. Bourbie, K. Amara, and A. Abada, *First-Principles Study of Structural, Elastic, Electronic, and Thermal Properties of SrTiO3 Perovskite Cubic*, Physics Letters A **373**, 879 (2009).

[188] H. Bouafia, S. Hiadsi, B. Abidri, A. Akriche, L. Ghalouci, and B. Sahli, *Structural, Elastic, Electronic and Thermodynamic Properties of KTaO3 and NaTaO3: Ab Initio Investigations*, Computational Materials Science **75**, 1 (2013).

[189] J. P. Feser and D. G. Cahill, *Probing Anisotropic Heat Transport Using Time-Domain Thermoreflectance with Offset Laser Spots*, Review of Scientific Instruments **83**, 104901 (2012).

[190] G. T. Hohensee, W.-P. Hsieh, M. D. Losego, and D. G. Cahill, *Interpreting Picosecond Acoustics in the Case of Low Interface Stiffness*, Review of Scientific Instruments **83**, 114902 (2012).

[191] A. Grzechnik, G. H. Wolf, and P. F. McMillan, *Raman Scattering Study of SrTiO3 at High Pressure*, J. Raman Spectrosc. **28**, 885 (1997).

[192] W. G. Nilsen and J. G. Skinner, *Raman Spectrum of Potassium Tantalate*, The Journal of Chemical Physics **47**, 1413 (1967).

[193] Z. Zhang, K. Yuan, J. Zhu, X. Fan, J. Zhou, and D. Tang, *Thermal Conductivity of $SrTiO_3$ under High-Pressure*, Appl. Phys. Lett. **120**, 262201 (2022).

[194] W.-P. Hsieh, *High-Pressure Thermal Conductivity and Compressional Velocity of NaCl in B1 and B2 Phase*, Sci Rep **11**, 21321 (2021).

[195] G. A. Samara, T. Sakudo, and K. Yoshimitsu, *Important Generalization Concerning the Role of Competing Forces in Displacive Phase Transitions*, Phys. Rev. Lett. **35**, 1767 (1975).

[196] D. A. Dalton, W. P. Hsieh, G. T. Hohensee, D. G. Cahill, and A. F. Goncharov, *Effect of Mass Disorder on the Lattice Thermal Conductivity of MgO Periclase under Pressure*, Scientific Reports **3**, 1 (2013).

[197] O. L. Anderson, *A Simplified Method for Calculating the Debye Temperature from Elastic Constants*, Journal of Physics and Chemistry of Solids **24**, 909 (1963).

[198] L. Feng, T. Shiga, and J. Shiomi, *Phonon Transport in Perovskite $SrTiO_3$ from First Principles*, Appl. Phys. Express **8**, 7 (2015).

[199] S. Sarfraz, S. A. Aldaghfag, M. K. Butt, M. Yaseen, M. Zahid, and A. Dahshan, *Physical Properties of KTaO3 Compound for Optoelectronic and Thermoelectric Applications: A DFT Study*, Materials Science in Semiconductor Processing **148**, 106811 (2022).

[200] A. V. Postnikov, T. Neumann, G. Borstel, and M. Methfessel, *Ferroelectric Structure of KNbO 3 and KTaO 3 from First-Principles Calculations*, Phys. Rev. B **48**, 5910 (1993).

[201] T. Liu, X. Zhao, J. Li, Z. Liu, F. Liscio, S. Milita, B. C. Schroeder, and O. Fenwick, *Enhanced Control of Self-Doping in Halide Perovskites for Improved Thermoelectric Performance*, Nat Commun **10**, 1 (2019).

[202] H. Ohta, *Thermoelectrics Based on Strontium Titanate*, Materials Today **10**, 10 (2007).

[203] C. W. Li, J. Hong, A. F. May, D. Bansal, S. Chi, T. Hong, G. Ehlers, and O. Delaire, *Orbitally Driven Giant Phonon Anharmonicity in SnSe*, Nature Phys **11**, 1063 (2015).

[204] W.-P. Hsieh, *Thermal Conductivity of Methanol-Ethanol Mixture and Silicone Oil at High Pressures*, Journal of Applied Physics **117**, 235901 (2015).

[205] W.-P. Hsieh, F. Deschamps, T. Okuchi, and J.-F. Lin, *Effects of Iron on the Lattice Thermal Conductivity of Earth's Deep Mantle and Implications for Mantle Dynamics*, Proc. Natl. Acad. Sci. U.S.A. **115**, 4099 (2018).

[206] E. Marzotto, W. Hsieh, T. Ishii, K. Chao, G. J. Golabek, M. Thielmann, and E. Ohtani, *Effect of Water on Lattice Thermal Conductivity of Ringwoodite and Its Implications for the Thermal Evolution of Descending Slabs*, Geophys. Res. Lett. **47**, (2020).

[207] K. Chao and W. Hsieh, *Thermal Conductivity Anomaly in (Fe $_{0.78}$ Mg $_{0.22}$)CO $_3$ Siderite Across Spin Transition of Iron*, J. Geophys. Res. Solid Earth **124**, 1388 (2019).

[208] C. Qian, A. M. Gheitaghy, J. Fan, H. Tang, B. Sun, H. Ye, and G. Zhang, *Thermal Management on IGBT Power Electronic Devices and Modules*, IEEE Access **6**, 12868 (2018).

[209] R. C. Willson and H. S. Hudson, *Solar Luminosity Variations in Solar Cycle 21*, Nature **332**, 810 (1988).

[210] G. A. Slack, *Nonmetallic Crystals with High Thermal Conductivity*, Journal of Physics and Chemistry of Solids **34**, 321 (1973).

[211] S. Tamura and H. J. Maris, *Temperature Dependence of Phonon Lifetimes in Dielectric Crystals*, Phys. Rev. B **51**, 2857 (1995).

[212] J. M. Ziman, *Principles of the Theory of Solids*, second (Cambridge University Press, 1972).

[213] C. Kittel, *Introduction to Solid State Physics*, 8th ed (Wiley, Hoboken, NJ, 2005).

[214] D. A. Broido, L. Lindsay, and T. L. Reinecke, *Ab Initio Study of the Unusual Thermal Transport Properties of Boron Arsenide and Related Materials*, Physical Review B - Condensed Matter and Materials Physics **88**, 1 (2013).

[215] L. Lindsay, D. A. Broido, and T. L. Reinecke, *First-Principles Determination of Ultrahigh Thermal Conductivity of Boron Arsenide: A Competitor for Diamond?*, Phys. Rev. Lett. **111**, 025901 (2013).

[216] N. K. Ravichandran and D. Broido, *Phonon-Phonon Interactions in Strongly Bonded Solids: Selection Rules and Higher-Order Processes*, Phys. Rev. X **10**, 021063 (2020).

[217] N. K. Ravichandran and D. Broido, *Non-Monotonic Pressure Dependence of the Thermal Conductivity of Boron Arsenide*, Nature Communications **10**, 1 (2019).

[218] L. Lindsay, D. A. Broido, J. Carrete, N. Mingo, and T. L. Reinecke, *Anomalous Pressure Dependence of Thermal Conductivities of Large Mass Ratio Compounds*, Physical Review B - Condensed Matter and Materials Physics **91**, 1 (2015).

[219] F. Tian et al., *Unusual High Thermal Conductivity in Boron Arsenide Bulk Crystals*, Science **361**, 582 (2018).

[220] J. S. Kang, M. Li, H. Wu, H. Nguyen, and Y. Hu, *Experimental Observation of High Thermal Conductivity in Boron Arsenide*, Science **361**, 575 (2018).

[221] S. Li, Q. Zheng, Y. Lv, X. Liu, X. Wang, P. Y. Huang, D. G. Cahill, and B. Lv, *High Thermal Conductivity in Cubic Boron Arsenide Crystals*, Science **361**, 579 (2018).

[222] J. S. Kang, H. Wu, and Y. Hu, *Thermal Properties and Phonon Spectral Characterization of Synthetic Boron Phosphide for High Thermal Conductivity Applications*, Nano Lett. **17**, 7507 (2017).

[223] Q. Zheng, S. Li, C. Li, Y. Lv, X. Liu, P. Y. Huang, D. A. Broido, B. Lv, and D. G. Cahill, *High Thermal Conductivity in Isotopically Enriched Cubic Boron Phosphide*, Adv. Funct. Mater. **28**, 1805116 (2018).

[224] T. Feng, L. Lindsay, and X. Ruan, *Four-Phonon Scattering Significantly Reduces Intrinsic Thermal Conductivity of Solids*, Physical Review B **96**, 1 (2017).

[225] H. Ma, C. Li, S. Tang, J. Yan, A. Alatas, L. Lindsay, B. C. Sales, and Z. Tian, *Boron Arsenide Phonon Dispersion from Inelastic X-Ray Scattering: Potential for Ultrahigh Thermal Conductivity*, Phys. Rev. B **94**, 220303 (2016).

[226] M. Lax, P. Hu, and V. Narayanamurti, *Spontaneous Phonon Decay Selection Rule: N and U Processes*, Phys. Rev. B **23**, 3095 (1981).

[227] F. Tian et al., *Seeded Growth of Boron Arsenide Single Crystals with High Thermal Conductivity*, Applied Physics Letters **112**, (2018).

[228] H. Sun, K. Chen, G. A. Gamage, H. Ziyaee, F. Wang, Y. Wang, V. G. Hadjiev, F. Tian, G. Chen, and Z. Ren, *Boron Isotope Effect on the Thermal Conductivity of Boron Arsenide Single Crystals*, Materials Today Physics **11**, 100169 (2019).

[229] X. Chen et al., *Effects of Impurities on the Thermal and Electrical Transport Properties of Cubic Boron Arsenide*, Chem. Mater. **33**, 6974 (2021).

[230] G. A. Gamage, H. Sun, H. Ziyaee, F. Tian, and Z. Ren, *Effect of Boron Sources on the Growth of Boron Arsenide Single Crystals by Chemical Vapor Transport*, Appl. Phys. Lett. **115**, 092103 (2019).

[231] J. L. Lyons, J. B. Varley, E. R. Glaser, J. A. Freitas, J. C. Culbertson, F. Tian, G. A. Gamage, H. Sun, H. Ziyaee, and Z. Ren, *Impurity-Derived* p *-Type Conductivity in Cubic Boron Arsenide*, Appl. Phys. Lett. **113**, 251902 (2018).

[232] J. P. Feser and D. G. Cahill, *Probing Anisotropic Heat Transport Using Time-Domain Thermoreflectance with Offset Laser Spots*, Review of Scientific Instruments **83**, (2012).

[233] X. Tang and J. Dong, *Lattice Thermal Conductivity of MgO at Conditions of Earth's Interior*, Proceedings of the National Academy of Sciences **107**, 4539 LP (2010).

[234] R. G. Greene, H. Luo, A. L. Ruoff, S. S. Trail, and F. J. DiSalvo, *Pressure Induced Metastable Amorphization of BAs: Evidence for a Kinetically Frustrated Phase Transformation*, Physical Review Letters **73**, 2476 (1994).

[235] R. G. Greene, H. Luo, and A. L. Ruoff, *Al as a Simple Solid: High Pressure Study to 22t| GPa (2. 2 Mbar)*, **73**, 11 (1994).

[236] S. Daoud, N. Bioud, and N. Bouarissa, *Structural Phase Transition, Elastic and Thermal Properties of Boron Arsenide: Pressure-Induced Effects*, Materials Science in Semiconductor Processing **31**, 124 (2015).

[237] C. Kittel and D. F. Holcomb, *Introduction to Solid State Physics*, Vol. 35 (1967).

[238] X. Wang, V. Ho, R. A. Segalman, and D. G. Cahill, *Thermal Conductivity of High-Modulus Polymer Fibers*, Macromolecules **46**, 4937 (2013).

[239] B. Sun and Y. K. Koh, *Understanding and Eliminating Artifact Signals from Diffusely Scattered Pump Beam in Measurements of Rough Samples by Time-Domain Thermoreflectance (TDTR)*, Review of Scientific Instruments **87**, 064901 (2016).

[240] S. Tamura, *Isotope Scattering of Dispersive Phonons in Ge*, Physical Review B **27**, (1983).

[241] V. G. Hadjiev, M. N. Iliev, B. Lv, Z. F. Ren, and C. W. Chu, *Anomalous Vibrational Properties of Cubic Boron Arsenide*, Phys. Rev. B **89**, 024308 (2014).

[242] S. Daoud, N. Bioud, and N. Lebga, *Elastic and Thermophysical Properties of BAs under High Pressure and Temperature*, Chinese Journal of Physics **57**, 165 (2019).

[243] N. H. Protik, J. Carrete, N. A. Katcho, N. Mingo, and D. Broido, *Ab Initio Study of the Effect of Vacancies on the Thermal Conductivity of Boron Arsenide*, Physical Review B **94**, 1 (2016).

[244] B. Lv, Y. Lan, X. Wang, Q. Zhang, Y. Hu, A. J. Jacobson, D. Broido, G. Chen, Z. Ren, and C.-W. Chu, *Experimental Study of the Proposed Super-Thermal-Conductor: BAs*, Appl. Phys. Lett. **106**, 074105 (2015).

[245] P. Jiang, X. Qian, and R. Yang, *Tutorial: Time-Domain Thermoreflectance (TDTR) for Thermal Property Characterization of Bulk and Thin Film Materials*, Journal of Applied Physics **124**, 161103 (2018).

[246] Y. K. Koh, S. L. Singer, W. Kim, J. M. O. Zide, H. Lu, D. G. Cahill, A. Majumdar, and A. C. Gossard, *Comparison of the 3ω Method and Time-Domain Thermoreflectance for Measurements of the Cross-Plane Thermal Conductivity of Epitaxial Semiconductors*, Journal of Applied Physics **105**, 054303 (2009).

[247] D. G. Cahill and F. Watanabe, *Thermal Conductivity of Isotopically Pure and Ge-Doped Si Epitaxial Layers from 300 to 550 K*, Phys. Rev. B **70**, 235322 (2004).

[248] R. B. Wilson and D. G. Cahill, *Anisotropic Failure of Fourier Theory in Time-Domain Thermoreflectance Experiments*, Nat Commun **5**, 5075 (2014).

[249] A. J. Minnich, J. A. Johnson, A. J. Schmidt, K. Esfarjani, M. S. Dresselhaus, K. A. Nelson, and G. Chen, *Thermal Conductivity Spectroscopy Technique to Measure Phonon Mean Free Paths*, Phys. Rev. Lett. **107**, 095901 (2011).

[250] C. Hua, L. Lindsay, X. Chen, and A. J. Minnich, *Generalized Fourier's Law for Nondiffusive Thermal Transport: Theory and Experiment*, Phys. Rev. B **100**, 085203 (2019).

[251] F. Tian et al., *Mechanical Properties of Boron Arsenide Single Crystal*, Applied Physics Letters **114**, (2019).

[252] B. B. Karki, L. Stixrude, S. J. Clark, M. C. Warren, G. J. Ackland, and J. Crain, *Structure and Elasticity of MgO at High Pressure*, American Mineralogist **82**, 51 (1997).

[253] B. B. Karki, R. M. Wentzcovitch, S. de Gironcoli, and S. Baroni, *High-Pressure Lattice Dynamics and Thermoelasticity of MgO*, Physical Review B **61**, 8793 (2000).

[254] R. Boehler and J. Ramakrishnan, *Experimental Results on the Pressure Dependence of the Gruneisen Parameter: A Review*, Journal of Geophysical Research: Solid Earth **85**, 6996 (1980).

[255] F. Deschamps and W. P. Hsieh, *Lowermost Mantle Thermal Conductivity Constrained from Experimental Data and Tomographic Models*, Geophysical Journal International **219**, S115 (2019).

[256] W. P. Hsieh, M. D. Losego, P. V. Braun, S. Shenogin, P. Keblinski, and D. G. Cahill, *Testing the Minimum Thermal Conductivity Model for Amorphous Polymers Using High Pressure*, Physical Review B - Condensed Matter and Materials Physics **83**, 1 (2011).

[257] A. M. Hofmeister, *Pressure Dependence of Thermal Transport Properties*, Proceedings of the National Academy of Sciences **104**, 9192 LP (2007).

[258] P. Andersson, *Thermal Conductivity under Pressure and through Phase Transitions in Solid Alkali Halides. I. Experimental Results for KCl, KBr, KI, RbCl, RbBr and RbI*, Journal of Physics C: Solid State Physics **18**, 3943 (1985).

[259] N. K. Ravichandran and D. Broido, *Exposing the Hidden Influence of Selection Rules on Phonon–Phonon Scattering by Pressure and Temperature Tuning*, Nat Commun **12**, 3473 (2021).

[260] X. Meng, A. Singh, R. Juneja, Y. Zhang, F. Tian, Z. Ren, A. K. Singh, L. Shi, J. Lin, and Y. Wang, *Pressure-Dependent Behavior of Defect-Modulated Band Structure in Boron Arsenide*, Adv. Mater. **32**, 2001942 (2020).

[261] Q. Zheng, C. A. Polanco, M.-H. Du, L. R. Lindsay, M. Chi, J. Yan, and B. C. Sales, *Antisite Pairs Suppress the Thermal Conductivity of BAs*, Physical Review Letters **121**, 105901 (2018).

[262] M. T. Yin and M. L. Cohen, *Ab Initio Calculation of the Phonon Dispersion Relation: Application to Si*, Physical Review B **25**, 4317 (1982).

[263] R. G. Greene, H. Luo, A. L. Ruoff, S. S. Trail, and F. J. DiSalvo, *Pressure Induced Metastable Amorphization of BAs: Evidence for a Kinetically Frustrated Phase Transformation*, Phys. Rev. Lett. **73**, 2476 (1994).

[264] G. T. Hohensee, R. B. Wilson, and D. G. Cahill, *Thermal Conductance of Metal–Diamond Interfaces at High Pressure*, Nat Commun **6**, 6578 (2015).

[265] J. S. Kang, M. Li, H. Wu, H. Nguyen, and Y. Hu, *Experimental Observation of High Thermal Conductivity in Boron Arsenide*, Science **361**, 575 (2018).

[266] L. Lindsay, D. A. Broido, and T. L. Reinecke, *Thermal Conductivity and Large Isotope Effect in GaN from First Principles*, Phys. Rev. Lett. **109**, 095901 (2012).

[267] S. Khan et al., *Properties for Thermally Conductive Interfaces with Wide Band Gap Materials*, ACS Appl. Mater. Interfaces **14**, 36178 (2022).

[268] S. Hou, R. B. Wilson, and C. Li, *Response of Vibrational Properties and Thermal Conductivity of Perovskites to Pressure*, Materials Today Physics **32**, 101010 (2023).

[269] M. Ueno, M. Yoshida, A. Onodera, O. Shimomura, and K. Takemura, *Stability of the Wurtzite-Type Structure under High Pressure: GaN and InN*, Phys. Rev. B **49**, 14 (1994).

[270] Z. Jing-Geng et al., *Isostructural Phase Transition of TiN under High Pressure*, Chinese Phys. Lett. **22**, 1199 (2005).

[271] P. Cheng, T. Ye, H. Zeng, and J. Ding, *Raman Spectra Investigation on the Pressure-Induced Phase Transition in Titanium Nitride (TiN)*, AIP Advances **10**, 045110 (2020).

[272] D. A. Broido, L. Lindsay, and A. Ward, *Thermal Conductivity of Diamond under Extreme Pressure: A First-Principles Study*, Phys. Rev. B **86**, 115203 (2012).

[273] K. Yuan, X. Zhang, D. Tang, and M. Hu, *Anomalous Pressure Effect on the Thermal Conductivity of ZnO, GaN, and AlN from First-Principles Calculations*, Phys. Rev. B **98**, 144303 (2018).

[274] Q. Zheng, C. Li, A. Rai, J. H. Leach, D. A. Broido, and D. G. Cahill, *Thermal Conductivity of GaN, GaN 71 , and SiC from 150 K to 850 K*, Phys. Rev. Materials **3**, 014601 (2019).

[275] P. Perlin, I. Gorczyca, N. E. Christensen, I. Grzegory, H. Teisseyre, and T. Suski, *Pressure Studies of Gallium Nitride: Crystal Growth and Fundamental Electronic Properties*, Phys. Rev. B **45**, 13307 (1992).

[276] J. A. Van Vechten, *Quantum Dielectric Theory of Electronegativity in Covalent Systems. II. Ionization Potentials and Interband Transition Energies*, Phys. Rev. **187**, 1007 (1969).

[277] P. Perlin, C. Jauberthie-Carillon, J. P. Itie, A. San Miguel, I. Grzegory, and A. Polian, *Raman Scattering and X-Ray-Absorption Spectroscopy in Gallium Nitride under High Pressure*, Phys. Rev. B **45**, 83 (1992).

[278] A. Ward, D. A. Broido, D. A. Stewart, and G. Deinzer, Ab Initio *Theory of the Lattice Thermal Conductivity in Diamond*, Phys. Rev. B **80**, 125203 (2009).